



THÈSE DE DOCTORAT
DE L'UNIVERSITÉ SORBONNE PARIS CITÉ
Préparée à l'Université Paris Diderot

Spécialité : Physique

École doctorale n°564: Physique en Île-de-France

réalisée

au C2N: Centre de Nanosciences et Nanotechnologies
(groupe GOSS)

sous la direction de Loïc LANCO

**A CAVITY-BASED SPIN-PHOTON
INTERFACE**

présentée par

Paul HILAIRE

pour obtenir le grade de :

DOCTEUR DE L'UNIVERSITÉ SORBONNE PARIS CITÉ

présentée et soutenue publiquement au CEA-NanoInnov, le 6 Juin 2019

devant le jury composé de :

| | | |
|--------------------|-------------------------|--|
| Présidente du jury | Mme. Sara DUCCI, | Professeur à l'Université Paris Diderot |
| Rapporteur | M. Guillaume CASSABOIS, | Professeur à l'Université de Montpellier 2 |
| Rapporteur | M. Thierry LAHAYE, | Chargé de Recherche à l'Institut d'Optique |
| Examinateuse | Mme. Maria CHAMMARO, | Professeur à l'UPMC |
| Examinateuse | Mme. Eleni DIAMANTI, | Chargée de recherche à l'UPMC |
| Invité | M. Patrice BERTET, | Chargé de Recherche au CEA |
| Directeur de thèse | M. Loïc LANCO, | Maître de Conférences à l'université Paris Diderot |

Contents

| | |
|--|-----------|
| Remerciements | 1 |
| Résumé | 3 |
| Introduction | 17 |
| 1 Fundamentals on charged quantum dots in pillar micro-cavities. | 21 |
| 1.1 Charges confined in quantum dots. | 21 |
| 1.1.1 Semiconductor quantum dots. | 21 |
| 1.1.2 Charged states in quantum dots. | 22 |
| 1.2 Spin physics in quantum dots. | 28 |
| 1.2.1 Hyperfine interaction with electrons and holes. | 28 |
| 1.2.2 Spin dynamics in quantum dots. | 29 |
| 1.2.3 Spin coherence and relaxation time. | 30 |
| 1.2.4 Spin noise spectroscopy. | 31 |
| 1.2.5 Improving the spin qubit. | 33 |
| 1.3 Quantum optics with spins. | 34 |
| 1.3.1 Spin initialization. | 34 |
| 1.3.2 Spin measurement. | 35 |
| 1.3.3 Spin coherent control. | 37 |
| 1.3.4 Entangling the spin with an emitted photon. | 39 |
| 1.3.5 Entanglement between a spin and a photon incoming from a distant source. . | 42 |
| 1.4 Cavity-QED with quantum dots. | 42 |
| 1.4.1 Optical micro-cavities. | 44 |
| 1.4.2 Deterministic cavity-quantum dot coupling. | 47 |
| 1.4.3 Quantum emitter coupled to a cavity. | 49 |
| 1.5 Single-photon sources. | 53 |
| 1.5.1 Single-photon purity. | 53 |
| 1.5.2 Photon indistinguishability. | 54 |
| 1.5.3 Brightness. | 55 |
| 1.6 Optimal spin-photon interface using cavity-QED. | 56 |
| 1.6.1 Optical response of cavity and cavity-QED devices. | 56 |
| 1.6.2 Cavity-enhanced Kerr rotation. | 57 |
| 1.6.3 Measurement of macroscopic spin-dependent polarization rotation. | 58 |
| 1.7 Conclusion. | 60 |

| | |
|--|------------|
| 2 Polarization Tomography: measurement of input and output coupling in a pillar micro-cavity. | 61 |
| 2.1 Introduction: input and output couplings in pillar microcavities. | 61 |
| 2.2 Polarization response of a pillar microcavity. | 62 |
| 2.2.1 Optical response of a pillar microcavity. | 62 |
| 2.2.2 Mode matching and input coupling in pillar microcavity. | 62 |
| 2.2.3 Elliptical pillar microcavities. | 64 |
| 2.3 Accurate measurement of input/output coupling through polarization tomography. | 67 |
| 2.3.1 Polarization tomography technique. | 67 |
| 2.3.2 Experimental polarization tomography reconstruction. | 70 |
| 2.3.3 Measurement of a high cavity mode coupling. | 72 |
| 2.3.4 Fibered polarization tomography of an elliptical cavity. | 76 |
| 2.4 Polarization rotation as a resource for coupling optimization. | 77 |
| 2.4.1 Presentation of the principle. | 77 |
| 2.4.2 Observation of the cavity mode characteristics. | 77 |
| 2.4.3 Cross-polarized intensity to maximize the cavity coupling. | 78 |
| 2.5 Theory: polarization rotation in free-space and fibered configurations. | 79 |
| 2.5.1 Input-output formalism. | 80 |
| 2.5.2 Imperfect input coupling. | 81 |
| 2.5.3 Single-mode fibered detection. | 82 |
| 2.6 Conclusion. | 84 |
| 3 Quantum-dot induced polarization rotation and depolarization | 85 |
| 3.1 Introduction to quantum-dot induced optical phase shift. | 85 |
| 3.2 Experimental polarization tomography. | 86 |
| 3.2.1 Setup and micropillar sample. | 86 |
| 3.2.2 Principle of quantum dot-induced polarization rotation. | 87 |
| 3.2.3 Neutral quantum dot single-photon emission. | 88 |
| 3.2.4 Reflectivity of a cavity-coupled neutral quantum dot. | 90 |
| 3.2.5 Reconstruction of the polarization density matrix. | 90 |
| 3.3 Theoretical modelization of a neutral quantum dot-cavity device. | 93 |
| 3.3.1 Density matrix and open quantum system formalism. | 93 |
| 3.3.2 Cavity-QED model with a 2-level quantum emitter. | 95 |
| 3.3.3 Realistic cavity-QED model of a neutral quantum dot embedded into a mi-cropillar. | 98 |
| 3.3.4 Simulations of noise mechanisms. | 101 |
| 3.3.5 Determination of the dominant noise mechanism. | 103 |
| 3.4 Conclusion. | 105 |
| 4 Optical charge control in a deterministic spin-photon interface. | 107 |
| 4.1 Spin-photon interface with pillar micro-cavities. | 107 |
| 4.2 Deterministic spin-photon coupling in pillar micro-cavities. | 108 |
| 4.2.1 Trion transition identification through magneto-photoluminescence. | 108 |
| 4.2.2 Deterministic spin cavity matching. | 112 |
| 4.3 Optical charge control of the quantum dot. | 113 |
| 4.3.1 Hole trapping through device structure engineering. | 113 |

| | | |
|---|--|------------|
| 4.3.2 | Quasi-resonant excitation scheme. | 114 |
| 4.3.3 | Measurement of the hole trapping efficiency. | 117 |
| 4.4 | Device performances as a single photon source. | 126 |
| 4.4.1 | Quantum dot spectral fluctuations. | 128 |
| 4.5 | Conclusion. | 129 |
| 5 | Measurement back-action induced by a single detected photon. | 131 |
| 5.1 | Introduction: from spin noise spectroscopy to single photon back-action. | 131 |
| 5.2 | Single-photon measurement back-action on the hole spin. | 132 |
| 5.2.1 | Principle of photon measurement back-action on a single spin. | 132 |
| 5.2.2 | Theory: from measurement back action to photon cross-correlations. | 133 |
| 5.2.3 | Classical vs quantum measurement back-action. | 137 |
| 5.2.4 | Experimental evidence of the measurement back-action. | 139 |
| 5.2.5 | Discussion on the "simple picture" model. | 143 |
| 5.3 | Theoretical model of a charged quantum dot coupled to a cavity. | 146 |
| 5.3.1 | Coherent evolution of a cavity-coupled charged quantum dot. | 146 |
| 5.3.2 | Theoretical polarization tomography. | 148 |
| 5.3.3 | Consequence for the measurement back-action. | 153 |
| 5.4 | Cross-correlations under longitudinal magnetic field. | 159 |
| 5.4.1 | Cross-correlations for different magnetic fields. | 160 |
| 5.4.2 | Carrier-spin/nuclear spins interaction at zero magnetic field. | 160 |
| 5.4.3 | Spin relaxation processes with external longitudinal magnetic field. | 162 |
| 5.5 | Conclusion. | 162 |
| Conclusion and Perspectives | | 163 |
| A | Appendix: Initialization 3 level | 173 |
| Appendix: Initialization 3 level | | 173 |
| List of Publications | | 175 |

Remerciements

Pendant ces trois dernières années, j'ai eu l'occasion de découvrir et de fréquenter de nombreuses personnes. J'ai eu la chance de travailler avec certaines d'entre elles tandis que d'autres ont contribué à l'ambiance stimulante tout en étant conviviale et m'ont ainsi beaucoup apporté sur le plan personnel.

Je tiens tout d'abord à remercier les membres de mon jury de thèse qui ont accepté d'évaluer mon travail et ont bien voulu lire et corriger ce manuscrit.

Je remercie bien sûr mon directeur de thèse Loïc Lanco qui m'a donné l'opportunité de travailler sur ce sujet d'une part, mais aussi pour tout ce qu'il m'a appris, pour sa grande disponibilité (malgré sa charge d'enseignement) et ses conseils mais surtout pour son enthousiasme, son optimisme et sa bienveillance qui m'ont rendu cet expériences stimulante et agréable.

Je n'oublie pas non plus Oliver Krebs, pour avoir été mon directeur de thèse pendant le début de ma thèse mais aussi pour sa bienveillance et pour avoir toujours pris le temps (et souvent beaucoup de temps!) pour répondre à mes questions (sur ce domaine mystérieux des spins nucléaires principalement). Je remercie également Pascale Senellart et Daniel Kimura pour leur dynamisme, leur sympathie et leur enthousiasme. Je tiens aussi à remercier Jacqueline Bloch, Alberto Amo et Sylvain Ravets pour nos discussions scientifiques ou non. Je souhaite aussi remercier la direction du laboratoire LPN puis C2N qui m'ont accueilli au laboratoire pendant ma thèse ainsi que le secrétariat, le service informatique, l'atelier mécanique et les membres de la salle blanche, d'où sont sortis les échantillons grâce à l'excellent travail d'Aristide Lemaître et Isabelle Sagnes.

Je remercie Juan qui m'a appris l'optique quantique expérimentale et les jurons espagnols pendant mon stage en Australie et avec qui j'ai eu la chance de travailler à nouveau en France (vu qu'il ne parle pas français, "Thank you, Juan!"). Je n'oublie pas Justin qui m'a très vite familiarisé avec ce sujet malgré la pression de sa fin de thèse. J'ai aussi passé mes journées aux laboratoires en travaillant quotidiennement avec Christian, Carlos puis Clément que je remercie pour leur implication, leur énergie et pour leur excellent niveau scientifique. Je fais toute confiance à Clément et à la nouvelle recrue, Elham, pour la poursuite de ces travaux. J'ai aussi eu l'occasion de travailler avec deux très bons et très motivés stagiaires, Maxime et Warren qui m'ont facilité certains projets. Je remercie aussi Niccolo et Abdou pour la fabrication des magnifiques échantillons que j'ai utilisés pendant ma thèse. Je remercie particulièrement Laoges pour son soutien logistique et sa réponse rapide aux problèmes du labo.

Enfin, je tiens à remercier les autres copains du labo, notamment Valentin (pour, entre autres, les afterworks conviviaux à Orsay) et Guillaume (pour les discussions très intéressantes quoi qu'assez improbables) qui m'ont côtoyé pendant ces trois années et quelque de thèse, vu qu'ils ont commencé et terminé en même temps que moi, je rajoute dans cette catégorie Fabrice (pour entres autres, "son humour quelque peu décalé" pour citer la thèse de Valérian), qui bien qu'ayant commencé un peu avant a eu la gentillesse de nous attendre pour finir! Je remercie également les autres post-

doc et thésards qui sont aussi désormais des amis: Marijana (pour ton franc-parler), Hélène (même si Eustache est moins bien que Nelle!), Marie (pour ta bonne humeur contagieuse), Florian (pour ton endurance!), Martin (encore félicitations pour Clara!), Omar (un co-bureau très sympathique), Lorenzo (pour tes mots d'esprit), Valérian (pour les concerts endiablés), Titta (pour les discussions sur la gastronomie italienne), Nicolas (pour ton second degré), Philippe (même si c'est dommage que tu caches ton accent québécois!).

Je remercie aussi mes amis de tous horizons qui, bien que ne voyant pas trop le sujet de ma thèse, hochaient la tête d'un air approbateur lorsque je leur fournissais des explications à base de vilains mots comme "qubit", et qui, malgré cela, n'ont pas cessé de me voir. Vous m'avez fourni un soutien moral et l'occasion de pas trop penser à ma thèse les week-ends. Je remercie particulièrement mes colocataires, Marine (pour l'animation de la coloc, à toute heure!) et Gabriel (qui m'a appris les joies de la programmation et de SSB) ¹.

Je finirai par remercier profondément ma famille qui m'a toujours soutenu, surtout mes parents, Laurent et Claudine, qui m'ont donné le goût d'apprendre, le goût des sciences et qui m'ont toujours soutenu. Je remercie aussi mes deux petites sœurs, Elise et Claire.

Un grand merci à tous!

¹et à Nelle, pour son soutien moral à toute heure pendant la rédaction!

Résumé

Introduction.

La première révolution quantique désigne la révolution technologique permise au siècle dernier par la compréhension détaillée des phénomènes quantiques à l'état solide, qui a mené, entre autres, à la réalisation des lasers ou des transistors. Aujourd'hui, les phénomènes quantiques les plus fondamentaux tels que la superposition quantique et l'intrication sont explorés avec pour objectif de révolutionner le calcul, la communication et la métrologie. En effet, en encodant l'information non plus sur des systèmes classiques mais sur des systèmes quantiques, il serait possible de simuler efficacement des phénomènes quantiques [1], de résoudre des problèmes inaccessibles pour des ordinateurs classiques [2], de communiquer de façon complètement sécurisée [3] et de réaliser des capteurs dont la précision dépasserait la limite classique [4].

Dans de tels systèmes quantiques, l'information n'est plus codée de manière classique sur des bits, mais sur leurs analogues quantiques, les bits quantiques (qubits), qui sont des systèmes à deux niveaux qui peuvent être préparés dans des états superposés du type:

$$|\Psi\rangle = \alpha|0\rangle + \beta|1\rangle \quad (0.1)$$

où $|0\rangle$ et $|1\rangle$, sont les deux états quantiques possibles et sont équivalents aux bits classiques "0" et "1" et α et β , deux nombres complexes qui caractérisent la superposition quantique. Pour réaliser un ordinateur quantique [2], il est non seulement nécessaire de pouvoir préparer et contrôler un très grand nombre de qubits, mais aussi de réaliser des portes logiques quantiques entre ces qubits, et enfin de pouvoir les mesurer.

Plusieurs systèmes peuvent être utilisés comme qubits, parmi lesquels les atomes et les ions [5, 6]. Ceux-ci ont d'excellentes propriétés et des portes logiques à deux qubits ont pu être réalisés avec une très bonne fidélité. Cependant, la manipulation d'atomes et d'ions est très lourde expérimentalement, ce qui fait qu'il est difficile de concevoir à long terme des ordinateurs basés sur ces technologies. C'est pour cette raison que d'autres systèmes, généralement appelés atomes artificiels à l'état solide, tels que les qubits supraconducteurs [7], les centres NV dans le diamant [8] ou encore les boîtes quantiques semiconductrices [9, 10], sont aussi explorés. Les photons uniques peuvent être aussi utilisés, surtout pour le transfert d'information quantique sur de longues distances [11]. Des travaux théoriques proposent aussi la réalisation d'un ordinateur quantique complètement basé sur des photons uniques et de l'optique linéaire [12]. Les principaux inconvénients de ces propositions sont le manque actuel de sources de photons efficaces, la difficulté d'implémentation de mémoires

quantiques avec des photons, et surtout le fait qu'il est impossible de réaliser des portes logiques déterministes en utilisant uniquement des composants d'optique linéaire.

Pour pallier aux problèmes d'un ordinateur purement quantique photonique, une solution pourrait provenir d'une hybridation avec d'autres atomes artificiels. En effet, les atomes (artificiels ou naturels) sont des émetteurs de photons uniques déterministes qui peuvent donc être utilisés comme sources de photons uniques. De plus, l'interaction non-linéaire entre un atome et un photon permet la réalisation de portes logiques quantiques déterministes entre deux photons [13]. Enfin, l'information quantique d'un photon pourrait être stockée dans un atome. L'hybridation d'un photon avec un atome permettrait aussi de réaliser des répéteurs quantiques permettant d'augmenter les distances de communications [14]. Une telle interface entre un atome artificiel et un photon est donc un enjeu majeur, non seulement pour la conception d'un ordinateur quantique, mais aussi pour les communications quantiques.

Cette thèse, réalisée au Centre de Nanosciences et de Nanotechnologie (C2N) dans le groupe de Pascale Senellart et sous la direction de Loïc Lanco, a pour objectif la réalisation d'une interface efficace entre un qubit à l'état solide et un qubit photonique, encodé en polarisation. Une telle interface est un défi majeur, dans la mesure où il faut considérablement augmenter l'intensité de l'interaction entre un photon et un atome. Une solution permettant d'augmenter cette interaction, est l'usage de micro-cavités qui confinent le champ électromagnétique exactement à la position de l'atome, augmentant ainsi considérablement l'interaction lumière-matière. Le qubit à l'état solide choisi est le spin d'une charge confinée dans une boîte quantique semiconductrice. Ce choix est motivé par les résultats prometteurs concernant l'initialisation [15, 16], le contrôle [17, 18], l'intrication [19, 20, 21] et la mesure [22, 23] de ce type de qubit, ainsi que par sa facilité d'intégration dans des cavités photoniques, qui est par ailleurs le domaine d'expertise du groupe de Pascale Senellart. Ce groupe a notamment réalisé le couplage déterministe d'une boîte quantique dans une cavité micro-pilier [24], permettant la réalisation de source de photons uniques [25, 26]. Un autre résultat, crucial pour cette thèse est la démonstration d'une rotation de polarisation macroscopique induite par un spin unique qui est un premier pas vers la réalisation d'interfaces spin-photon idéales [27].

De telles interfaces doivent non seulement pouvoir être utilisées comme des émetteurs efficaces de photons uniques et indiscernables, mais aussi comme des récepteurs de photons. A cet égard, un photon doit être injecté efficacement dans la cavité, doit interagir efficacement avec l'état de spin et doit être collecté efficacement. Afin de permettre l'injection d'un photon dans la cavité, il faut pouvoir coupler de manière déterministe un mode optique externe avec le mode optique de la cavité. Le phénomène étudié dans cette thèse, à l'origine de l'interaction entre un spin et un photon, est la rotation de polarisation Kerr, induite par un spin unique: après avoir interagi avec le spin, le photon est réfléchi avec une polarisation qui dépend de l'état du spin. Enfin, il faut efficacement collecter la lumière ayant interagi avec le spin. Pour ce faire, il faut faciliter son émission dans le mode de la cavité et favoriser l'extraction des photons dans le micro-pilier dans une direction maîtrisée (notamment par le miroir du haut).

Ce résumé de thèse suit le même ordre que le manuscrit.

- Nous présentons d'abord les propriétés fondamentales des boîtes quantiques chargées et de leur intégration dans des micro-piliers.
- Deuxièmement, nous étudions la réponse en polarisation d'un micro-pilier seul (sans boîte quantique), grâce à une technique de tomographie de polarisation qui permet la reconstruction complète de l'état de polarisation de la lumière réfléchie par le micro-pilier. Cette technique

nous permet de mesurer précisément à la fois l'efficacité d'injection record et d'extraction des photons dans une cavité.

- Troisièmement, la technique de tomographie de polarisation est appliquée à une boîte quantique neutre couplée à un micro-pilier, ce qui permet de démontrer une rotation de polarisation géante (20° en latitude et en longitude) induite par une boîte quantique unique.
- Le quatrième thème de ce manuscrit est la fabrication d'une interface spin-photon déterministe. Nous montrons comment identifier la transition optique correspondant à une charge grâce à une étude de la photoluminescence avec un champ magnétique transverse, et comment la coupler à un mode de cavité grâce à la technique de lithographie in-situ. Nous détaillons aussi les solutions techniques permettant de confiner une charge dans la boîte quantique grâce à un pompage optique et grâce à l'insertion d'une barrière tunnel à proximité de la boîte quantique.
- Pour le dernier thème, nous utilisons les interfaces spin-photon pour démontrer la forte action en retour induite par la mesure d'un photon unique sur le spin d'une boîte quantique. Ce phénomène est le témoin de la forte interaction entre l'état de spin et la polarisation d'un photon (émis par une source externe).

Finalement, nous concluons et discutons des perspectives de ce travail.

Propriétés fondamentales des boîtes quantiques chargées, couplées à des cavités micro-piliers.

Charges confinées dans les boîtes quantiques.

Une boîte quantique [28, 29] est une nanostructure semiconductrice insérée dans un milieu semi-conducteur ayant une bande interdite plus large. Du fait de ses petites dimensions (de l'ordre de la dizaine de nanomètres), une boîte quantique confine les électrons dans les trois dimensions ce qui a pour effet de discréteriser les niveaux d'énergie des électrons ainsi que les transitions optiques entre ces niveaux (voir Fig. 1.1). Pour cette raison, une boîte quantique a un comportement similaire à un atome et est considéré comme un atome artificiel.

La bande de valence d'une boîte quantique est généralement complètement remplie d'électrons tandis que sa bande de conduction est vide. Il est possible de promouvoir un électron de la bande de valence à la bande de conduction, grâce à l'absorption d'un photon correspondant à la transition optique de plus basse énergie: on crée ainsi une paire électron-trou, communément appelé un exciton. Cette paire électron-trou peut se recombiner en émettant un photon unique de longueur d'onde typique égale à 930nm. De plus, il est aussi possible de piéger une charge en excès dans les boîtes quantiques, soit par une technique de pompage optique, soit grâce à un contrôle électrique.

Grâce à ces techniques, un trou ou un électron en excès peuvent être confinés dans une boîte quantique. De telles charges ont un spin : $1/2$ pour l'électron et $3/2$ pour le trou (voir Fig. 1.4). Il est toujours possible d'exciter optiquement une boîte quantique chargée en créant une paire électron-trou en plus de la charge confinée; l'état résultant est nommé un trion. Par contre, les règles de sélection optique vont dépendre du spin: dans le cas d'un trou confiné dans une boîte quantique, si

le spin est $|\uparrow_z\rangle$ (resp. $|\downarrow_z\rangle$), il va être sensible à une lumière polarisée circulairement gauche (resp. droite). Il est aussi possible d'appliquer un champ magnétique externe, soit longitudinalement, c'est-à-dire suivant l'axe de croissance de la boîte quantique (on parle de configuration Faraday), soit perpendiculairement (on parle de configuration Voigt). Ceci a pour effet de modifier les règles de sélection optique d'une boîte quantique chargée en levant la dégénérescence des états de spin d'un trou ou d'un électron, par effet Zeeman et, dans le cas d'un champ magnétique en configuration Voigt, modifier ses états propres et donc la polarisation des transitions optiques.

Les performances d'un spin en tant que qubit sont évaluées par son temps de relaxation T_1 , correspondant aux sauts de spin, et son temps de cohérence T_2 , qui est le temps durant lequel une superposition cohérente d'états de spin peut être réalisée. Ces deux temps sont limités, entre autres, par l'interaction hyperfine du spin de la charge confinée avec les spins nucléaires de la boîte quantique [30]. Ces deux temps caractéristiques peuvent être étudiés par l'étude des fluctuations de polarisation (induite par rotation Kerr ou Faraday) induite par l'interaction de la lumière avec le spin. Cette technique, appelée spectroscopie du bruit de spin [31], permet de mesurer les temps de relaxation (en configuration Faraday) et de cohérence (en configuration Voigt) du spin.

Grâce aux règles de sélection optique, il est possible d'initialiser [15, 32, 16] et de contrôler de manière cohérente [18, 17, 33] le spin d'une boîte quantique (en configuration Voigt uniquement). Il est aussi possible de réaliser un état intriqué entre un spin et un photon [20, 19, 21], mais aussi d'utiliser cette intrication pour réaliser des intrications spin-spin [34, 35] ou bien photon-photon [36]. Néanmoins, dans tous ces cas, le photon intriqué a été émis par la boîte quantique et jusqu'à présent, une intrication entre un spin et un photon émis par une autre source n'a pas été démontrée.

Il est aussi possible de mesurer le spin d'une charge confinée dans une boîte quantique, notamment en utilisant la rotation Faraday [15] ou la rotation Kerr [22]. La rotation Faraday (respectivement la rotation Kerr) est la rotation de polarisation induite quand un photon traverse (resp. est réfléchi par) un milieu magnétique. Dans le cas d'un spin unique, cet effet est très faible et donc l'amplitude de la rotation de polarisation est minime (de l'ordre de la dizaine de microradians). Ces rotations de polarisation ont tout de même été observées au niveau d'un spin unique. L'objectif du travail présenté ici est d'augmenter cet effet pour obtenir idéalement des états de polarisation dépendants de l'état de spin qui sont orthogonaux. Ceci permettrait une mesure non destructive forte du spin grâce à la détection d'un seul photon, et permettrait de créer un état intriqué entre un spin et un photon provenant d'une autre source, qui est à la base de la réalisation de portes logiques photon-photon déterministes. Pour cela, il faut grandement augmenter l'interaction de la boîte quantique avec la lumière, grâce à une cavité.

Boîtes quantiques couplées à des cavités.

Dans ce manuscrit, nous présentons des résultats basés sur une cavité micro-pilier. Ce type de cavité est composé de deux miroirs de Bragg en GaAs et AlAs, séparés par une couche de GaAs qui constitue notre cavité optique. Le confinement latéral du micro-pilier est obtenu grâce à la différence d'indice de réfraction entre le milieu semi-conducteur et le vide. On peut coupler une boîte quantique à un micro-pilier de manière déterministe grâce à la technique de lithographie in-situ [24] (voir Fig. 1.16):

- On réalise par croissance épitaxiale, une cavité planaire qui possède en son centre une couche de boîte quantique (de position et d'énergie aléatoire) et sur sa surface une résine photosensible.

-
- On éclaire de manière non résonante l'échantillon et on observe la photoluminescence des boîtes quantiques grâce à un spectromètre. On se positionne au-dessus d'une boîte quantique qui possède une transition optique à l'énergie désirée en maximisant l'intensité de son signal de photoluminescence.
 - On expose la résine photo-sensible au-dessus de la boîte quantique voulue grâce à un second laser. La durée d'exposition permet de régler l'énergie du mode optique fondamental du micro-pilier en modifiant son diamètre.
 - Enfin on dépose une couche de nitre qui va protéger le micro-pilier, on dissout la résine photosensible et on grave l'échantillon.

Le résultat de cette technologie est la fabrication d'échantillons avec une boîte quantique unique couplée à un micro-pilier de manière déterministe. Cette technique a été significativement améliorée par l'ajout d'un contrôle électrique qui stabilise l'environnement électrique de la boîte quantique et qui permet le réglage fin de sa transition optique [37].

Grâce à ce type d'échantillons, une boîte quantique est interfacée avec un seul mode optique, celui confiné par la cavité. Il est possible de démontrer le couplage fort entre une boîte quantique et une cavité [38, 39, 40]. Il est aussi possible de démontrer l'accélération de l'émission spontanée dans le mode de la cavité, un phénomène appelé l'effet Purcell [41]. Ceci permet la réalisation de source de photons uniques efficaces.

Enfin, une cavité peut grandement augmenter la rotation Kerr induite par un spin unique, afin d'avoir une rotation macroscopique (voir Fig. 1.23). Il est même possible, avec des dispositifs de boîte quantiques couplés à des micropiliers réalisistes, d'avoir des polarisations réfléchies qui sont orthogonales (par exemple polarisée diagonalement si le spin est $|\uparrow\rangle$ et polarisée anti-diagonalement si le spin est $|\downarrow\rangle$) [27]. Dans ce cas, il est possible de mesurer l'état de spin grâce à la mesure de la polarisation d'un photon unique. La détection d'un photon projette le spin par action en retour de la mesure.

Tomographie de polarisation d'une cavité micro-pilier

L'objectif de cette section est de réaliser une mesure précise de l'efficacité de couplage d'un mode optique externe avec le mode optique d'un micro-pilier. Pour ce faire, on étudie la réponse optique d'une cavité micro-pilier, en prenant en compte à la fois l'efficacité de couplage des modes optiques et l'ellipticité du micro-pilier. On introduit la technique de tomographie de polarisation que nous avons développé, permettant la mesure précise d'un couplage record entre la cavité et le mode d'un laser incident. Enfin, on montre d'autres applications de cette étude en polarisation, permettant notamment d'imager le mode de cavité, et de maximiser le couplage des photons incidents avec le micro-pilier.

Réponse optique d'une cavité micro-pilier

Une cavité micro-pilier confine un mode optique d'énergie ω_c . Le confinement n'est pas optimal et la lumière peut s'échapper par le miroir du haut, du bas, et par les côtés. Le mode de la cavité

optique a donc une largeur spectrale $\kappa = \kappa_{top} + \kappa_{bottom} + \kappa_{side} + \kappa_{abs}$, correspondant au taux de fuite des photons intracavités total, κ_{top} , κ_{bottom} , κ_{loss} κ_{abs} étant respectivement les taux de fuite par le miroir du haut, du bas et par les côtés et le taux d'absorption des photons intra-cavités . Dans tous les travaux présentés dans ce manuscrit, les photons sont injectés et collectés par le miroir du haut du micro-pilier. On est donc intéressé par l'efficacité d'extraction par le miroir du haut $\eta_{top} = \kappa_{top}/\kappa$, qui correspond à la probabilité qu'un photon intra-cavité s'échappe par le haut. Le coefficient de réflexion d'une telle cavité pour un laser parfaitement couplé d'énergie ω est donnée par:

$$r_{cav} = 1 - 2\eta_{top} \frac{1}{1 - i\Delta} \quad (0.2)$$

avec

$$\Delta = 2 \frac{\omega - \omega_c}{\kappa} \quad (0.3)$$

Il semble donc possible de déduire précisément l'efficacité d'extraction η_{top} à partir d'une mesure de réflectivité, vu que la réflectivité minimum dépend directement de η_{top} : $R_{min} = |1 - 2\eta_{top}|^2$. Cependant, dans le cas réel, le laser a un mode spatial qui peut être différent de celui de la cavité (voir Fig. 2.1(b)). Il faut donc aussi prendre en compte la lumière réfléchie qui est non-couplée. La réflectivité minimale dans ce cas est donnée par: $R_{min} = (1 - \eta_{in}) + \eta_{in}|1 - 2\eta_{top}|^2$ où η_{in} est l'efficacité de couplage au mode de cavité, c'est-à-dire le recouvrement entre le mode spatial du laser $\Phi_i(x,y)$ et celui de la cavité $\Phi_m(x,y)$:

$$\eta_{in} = \left| \int \int \Phi_m(x,y)^* \Phi_i(x,y) dx dy \right|^2 \quad (0.4)$$

On voit bien que la réflectivité minimum dépend aussi de η_{in} et il est donc impossible de déduire facilement les valeurs de η_{in} et η_{top} à partir d'une mesure de réflectivité.

D'autre part, un micro-pilier obtenu par lithographie optique n'est généralement pas parfaitement circulaire: il possède deux axes propres et confine différemment la lumière polarisée horizontalement (pris comme étant suivant un axe propre de la cavité) et la lumière polarisée verticalement (suivant l'autre axe). Il y a donc deux modes optiques confinés par une cavité à des énergies légèrement différentes $\omega_{c,H} \neq \omega_{c,V}$ (voir Fig. 2.4). Il est possible de montrer qu'un laser polarisé diagonalement $|D\rangle$ (donc qui n'est pas suivant les axes propres de la cavité) est réfléchi avec une polarisation qui peut être différente de sa polarisation incidente: $|\Psi_{refl}\rangle \neq |D\rangle$. Afin de déterminer cette polarisation réfléchie, on utilise la technique de tomographie de polarisation: l'intensité de la lumière réfléchie est mesurée dans trois bases de polarisations correspondant aux polarisations horizontale et verticale, diagonale et anti-diagonale, et circulaire gauche et circulaire droite. Grâce à ces intensités, il est possible de mesurer les paramètres de Stokes $s_{\parallel\perp} = \frac{I_{\parallel} - I_{\perp}}{I_{\parallel} + I_{\perp}}$ (avec I_{\parallel} et I_{\perp} les intensités mesurées dans les bases de polarisations orthogonales \parallel et \perp) qui sont les coordonnées de l'état de polarisation sur la sphère de Poincaré (qui est une manière visuelle de représenter un état de polarisation, voir Fig. 2.5(b)).

Pour ce faire, un laser continu et polarisé diagonalement, scanne en longueur d'onde le mode de cavité. Le mode spatial du laser peut être ajusté à celui de la cavité grâce à un télescope composé de trois lentilles (voir Fig. 2.6). Le laser est ensuite réfléchi par le micro-pilier, et est analysé en polarisation grâce à une lame quart d'onde et une lame demi-onde, un séparateur de polarisation (prisme Wollaston) et deux photodiodes. La caractérisation fine des lames demi-onde et quart d'onde permet de mesurer précisément les intensités réfléchies dans les bases horizontale/verticale, diagonale/anti-diagonale et circulaire gauche/droite.

Mesure précise des efficacités de couplage du micro-pilier.

Expérimentalement, la tomographie de polarisation montre bien la rotation de polarisation induite par l'ellipticité du micro-pilier, mais cette rotation de polarisation s'accompagne aussi d'une dépolarisation (voir Fig. 2.10). On peut montrer que cette dépolarisation est induite par la superposition incohérente (car n'ayant pas le même mode spatial) de la lumière couplée au micro-pilier (et réfléchie avec une polarisation $|\Psi_{refl}\rangle$) et par la lumière non-couplée (réfléchie avec une polarisation diagonale $|D\rangle$). Il est possible de montrer que cette dépolarisation dépend très fortement de l'efficacité d'injection η_{in} (voir Fig. 2.13). Grâce à cette mesure de tomographie de polarisation, il devient possible de mesurer de manière très précise, à la fois l'efficacité d'injection $\eta_{in} = 96 \pm 1\%$ et l'efficacité d'extraction $\eta_{top} = 53 \pm 2\%$. La valeur de l'efficacité d'injection est d'ailleurs le record de couplage obtenu avec une cavité micro-pilier.

Optimisation du couplage entre un mode externe et la cavité.

Par ailleurs, en filtrant uniquement la lumière réfléchie qui possède une polarisation orthogonale à la polarisation incidente du laser, il est possible de sélectionner uniquement la lumière réfléchie qui a été couplée au micro-pilier, étant donné que la lumière non-couplée est réfléchie avec une polarisation identique à la polarisation incidente. Cette lumière couplée au micro-pilier possède le même mode spatial que celui-ci, et peut donc être imagée (voir Fig. 2.16). De plus, l'intensité de la lumière réfléchie avec une polarisation orthogonale au laser est proportionnelle à l'efficacité d'injection η_{in} . En conséquence, en maximisant la lumière réfléchie en polarisation croisée, on maximise le couplage avec le micro-pilier. Cette nouvelle technique permet le couplage fin entre un mode optique externe et le micro-pilier: elle est maintenant utilisée par l'ensemble du groupe travaillant, au C2N, sur des systèmes à base de micro-piliers.

Tomographie de polarisation d'une boîte quantique neutre

Dans la section précédente, nous avons introduit la technique de tomographie de polarisation qui permet de reconstruire expérimentalement la polarisation de la lumière réfléchie par une cavité. Dans cette section, nous utilisons la même technique pour montrer la rotation de polarisation géante induite par une boîte quantique neutre couplée à une cavité micro-pilier. Le même dispositif expérimental est utilisé, mais cette fois-ci le micro-pilier étudié est couplé à une boîte quantique neutre (un exciton) dont la longueur d'onde peut être ajustée finement grâce à un contrôle électrique. Dans cette étude, on met d'abord expérimentalement en évidence la conversion de polarisation induite par la boîte quantique. Grâce à la technique de tomographie de polarisation, on prouve que la boîte quantique induit une rotation de polarisation, avec aussi une dégradation de la pureté de polarisation. Enfin, on construit un modèle exact permettant de reproduire théoriquement les résultats expérimentaux, et d'en déduire le processus incohérent dominant responsable de cette dépolarisation.

Rotation de polarisation induite par une boîte quantique neutre.

Dans cette expérience, le laser continu est polarisé verticalement, c'est-à-dire suivant un axe propre du micro-pilier, ce qui permet d'éviter d'observer la rotation de polarisation uniquement induite par la cavité. La rotation de polarisation induite par une boîte quantique neutre peut s'expliquer par le fait que cette boîte quantique possède en fait deux états excitoniques, accessibles optiquement par deux polarisations linéaires (généralement différentes des polarisations propres de la cavité, voir Fig. 3.2). Ces deux états sont séparés en énergie d'une valeur Δf_{ss} . Lorsqu'un exciton est préparé dans une superposition cohérente de ces deux états, il va alors précesser jusqu'à ce que l'émission spontanée d'un photon ramène la boîte quantique dans son état fondamental. Du fait de l'évolution cohérente de l'état excitonique, le photon peut être émis dans une polarisation différente de la polarisation d'excitation (initialement verticale). On peut donc avoir une conversion d'une polarisation verticale à une polarisation horizontale. Expérimentalement, on démontre que cette conversion de polarisation est bien induite par la boîte quantique en étudiant la lumière réfléchie avec une polarisation orthogonale au laser incident. On réalise une étude des auto-corrélations en intensité $g^{(2)}(t)$ de cette lumière réfléchie grâce à une expérience de Hanbury-Brown-Twiss (HBT), qui permet d'extraire la statistique de la source de photons (voir Fig. 3.5). Expérimentalement, on observe un anti-regroupement (anti-bunching en anglais) des photons à $t = 0$, qui est caractéristique d'une source de photon unique. La conversion de photon de la polarisation incidente verticale vers une polarisation horizontale est donc bien induite par la boîte quantique.

Ensuite, on réalise une tomographie de polarisation afin de reconstruire complètement l'état de polarisation de la lumière réfléchie (voir Fig. 3.8). On observe la rotation de polarisation induite par la boîte quantique sur la sphère de Poincaré. Cette rotation de polarisation est macroscopique (environ 20° à la fois en longitude et en latitude), ce qui montre une forte interaction entre la boîte quantique et le micro-pilier (qui amplifie cette rotation). Toutefois, cette rotation de polarisation s'accompagne aussi d'une dépolarisation de la lumière réfléchie.

Modèle théorique et identification du mécanisme de bruit dominant.

Afin d'expliquer cette dépolarisation, on réalise un modèle exact de notre système de boîte quantique neutre en cavité. Ce modèle s'appuie sur l'hamiltonien de Jaynes-Cummings qui est adapté pour prendre en compte, d'une part l'ellipticité de la cavité et les deux états excités de la boîte quantique, d'autre part les processus incohérents qui sont l'émission d'un photon hors du mode de la cavité, la fuite d'un photon intra-cavité, et le déphasage induit par l'interaction de la boîte quantique avec son environnement. Ce modèle complet est basé sur la résolution d'une équation maîtresse où les processus cohérents sont modélisés par des hamiltoniens et les processus incohérents grâce au formalisme des Lindbladiens. Il permet de réaliser un ajustement théorique des courbes expérimentales. Par une modélisation des différents mécanismes d'interactions entre la boîte quantique et son environnement, on peut aussi déduire que le processus incohérent dominant de la boîte quantique a une origine électrique (voir Fig. 3.14).

Nous avons donc montré ici qu'une boîte quantique unique peut modifier la polarisation de la lumière réfléchie de manière macroscopique et que l'on peut reconstruire cette polarisation réfléchie grâce à une technique de tomographie de polarisation. Cependant, pour réaliser des portes logiques photonique, il faut aussi avoir un degré de liberté supplémentaire (par exemple le degré de liberté du spin) pour pouvoir contrôler cette rotation de polarisation, ce qui n'est pas possible avec une boîte quantique neutre. Il faut donc réaliser une interface entre un photon et le spin d'une charge confinée dans la boîte quantique.

Réalisation déterministe d'une interface spin-photon.

Cette section a pour objectif de présenter une méthode permettant le couplage déterministe d'un photon avec le spin d'une charge confinée dans une boîte quantique, grâce à une cavité micro-pilier couplée à cette boîte quantique. Ceci requiert de coupler efficacement un mode optique externe à une cavité micro-pilier (ce qui a déjà été montré précédemment avec une efficacité de couplage de $\eta_{in} = 96 \pm 1\%$). De plus, il faut augmenter l'interaction entre la boîte quantique chargée et les photons intra-cavités. Pour ce faire, il faut d'une part placer la boîte quantique au centre du micro-pilier, où le champ électrique est le plus intense. Il faut ensuite s'assurer que la transition correspondant au trion est en résonance avec la boîte quantique et aussi qu'une charge est confinée dans la boîte quantique. Il faut aussi pouvoir collecter efficacement les photons s'échappant de la cavité micro-pilier (il faut donc optimiser l'extraction de photon par le miroir du haut, η_{top}).

Couplage déterministe trion-cavité.

La réalisation d'une telle interface est basée sur la technique de lithographie in-situ permettant de positionner une boîte quantique au centre d'un micro-pilier et de coupler une transition de la boîte quantique avec le mode de la cavité. Afin de réaliser une interface entre un trou confiné dans la boîte quantique avec la cavité, il faut aussi d'une part, réaliser des choix technologiques facilitant le confinement d'un trou par la boîte quantique et d'autre part identifier la transition trou-trion positif. Pour faciliter le confinement du trou, on réalise des échantillons comportant une barrière tunnel au-dessus de la couche de boîte quantique (voir Fig. 4.5). Ceci permet de faciliter le piégeage d'un trou en prolongeant la durée de son confinement dans la boîte quantique, et cela crée une asymétrie dans l'échantillon qui fait que l'électron peut tout de même facilement s'échapper. Concernant l'échantillon, on choisit aussi de réduire le nombre de paires sur le miroir de Bragg supérieur: ceci permet de faciliter l'échappement d'un photon intra-cavité par le miroir du haut. Une mesure de réflectivité permet de déduire une efficacité d'extraction des photons par le miroir du haut de $\eta_{top} = 85 \pm 5\%$.

Pour coupler de manière déterministe la transition optique correspondant au trion à la cavité, il faut être capable de l'identifier. Pour cela, on utilise la modification des transitions optiques lorsqu'un champ magnétique transverse est appliqué sur la boîte quantique (voir Fig. 4.1 (a)). Sans champ magnétique extérieur, les deux transitions optiques correspondant au trion sont dégénérées en énergie et ont deux polarisations circulaires (gauche et droite respectivement). Avec un champ magnétique cependant, les transitions correspondant au trion sont au nombre de quatre et ont chacune une énergie différente et une polarisation linéaire. Cet effet est caractéristique d'un trion et permet donc de déterminer sans ambiguïté la transition correspondant au trion. On utilise cette identification du trion pour ensuite réaliser un micro-pilier dont le mode fondamental a pour longueur d'onde celle du trion: $\lambda_{cav} = \lambda_{X^+}$. Ainsi, on obtient une cavité couplée à la transition optique du trion de la boîte quantique (voir Fig. 4.4).

Technique optique du confinement de la charge.

La dernière étape consiste maintenant à s'assurer qu'un trou peut être confiné dans la boîte quantique. En général, ceci peut être réalisé grâce à un contrôle électrique de la boîte quantique [42]. Cependant, pour que cela soit possible il faut réaliser un dopage très proche de la boîte quantique. Dans le contexte d'une boîte quantique couplée à une cavité, ceci peut amener à une absorption de la lumière

intra-cavité par le dopage et donc à une réduction de la qualité du confinement des photons intra-cavités. On choisit donc de réaliser un dopage éloigné de la boîte quantique afin de réduire cette absorption. La contrepartie est qu'il est impossible de contrôler électriquement la charge dans la boîte quantique. On choisit donc de confiner une charge de manière optique [43]: pour ce faire, on génère optiquement une paire électron-trou, jusqu'à ce qu'un électron s'échappe de la boîte quantique par effet tunnel avant d'avoir pu se recombiner radiativement avec le trou. Le trou reste plus longtemps dans la boîte quantique grâce à la barrière tunnel: on se retrouve donc avec un trou unique confiné dans la boîte quantique.

Expérimentalement, on choisit d'utiliser un laser continu en résonance avec une transition p-shell de la boîte quantique (voir Fig. 4.6): contrairement à une excitation non-résonante dans le continuum, ceci permet d'éviter d'injecter optiquement deux trous dans la boîte quantique, étant donné que le confinement d'une charge modifie l'énergie des transitions optiques. Avec cette technique, il devient donc possible de confiner optiquement un trou unique dans la boîte quantique.

Mesure de la probabilité d'occupation du trou.

Pour quantifier cela, on observe la fluorescence résonante de la transition trion grâce à un laser pulsé. On observe le signal réfléchi en polarisation croisée, grâce à un détecteur de photons uniques. Si un photon unique est détecté, cela veut dire que le trion a été optiquement généré par le laser résonant pulsé, et donc qu'un trou est confiné dans la boîte quantique. Ainsi, la fluorescence résonante du trion nous informe sur la présence d'un trou confiné dans la boîte quantique. On peut par exemple réaliser une mesure en temps réel du signal de fluorescence résonante (voir Fig. 4.9). On voit que ce signal présente un comportement "on/off": lorsque le trou n'est pas confiné, la boîte quantique ne peut pas émettre de photons, tandis que lorsque le trou est confiné, on peut observer un signal non nul de fluorescence résonante. Afin de quantifier plus précisément ceci, nous réalisons des mesures d'auto-corrélations en intensité du signal de fluorescence résonante: le signal de fluorescence résonante est séparé en deux grâce à une fibre séparatrice dont les deux sorties sont connectées à des détecteurs de photons uniques (ceci est un dispositif pour réaliser une expérience Hanbury-Brown & Twiss (HBT)). On observe les corrélations entre les deux détecteurs de photons uniques (voir Fig. 4.10). A zéro délai, on observe un anti-regroupement des photons, caractéristique d'une source de photon unique: si un photon est détecté par un détecteur, il est peu probable qu'un autre photon soit observé par l'autre détecteur simultanément. Cependant pour le moment, on est intéressé aux caractéristiques à temps plus long de ces auto-corrélations, où l'on devrait observer l'effet du confinement de la boîte quantique sur le signal de fluorescence résonante. En observant les auto-corrélations à temps long, on observe une exponentielle décroissante. Grâce à un modèle simple, on peut en déduire la probabilité d'occupation du trou (donnée par la valeur à délai nul des auto-corrélations) et le temps de piégeage du trou (donné par l'intersection de la tangente à l'origine avec l'axe des abscisses). On montre qu'on est capable d'avoir une probabilité d'occupation supérieure à 85% sur plusieurs échantillons, avec un temps de confinement du trou supérieur à la μ s. Pour la meilleure interface, on obtient une probabilité d'occupation du trou de $91 \pm 1\%$ et une brillance de la source de photon unique de $33 \pm 5\%$ (voir Fig. 4.13).

Enfin, on peut observer les performances en tant que sources de photons uniques de ces interfaces spin-photon. Pour ce faire, on réalise une expérience HBT, où l'on observe cette fois-ci le comportement à zéro délai. Pour le meilleur échantillon, on observe un anti-regroupement des photons donnant un $g^{(2)}(0) = 1.6 \pm 0.4\%$. Il est aussi possible de mesurer l'indiscernabilité des photons grâce à une expérience de Hong-Ou-Mandel. Cette mesure permet de mesurer une indiscernabilité

(corrigée du $g^{(2)}(0)$) de $99.8 \pm 0.2\%$. Les interfaces spin-photon réalisées sont donc comparables à l'état de l'art des sources de photons uniques.

Action en retour de la mesure induite sur un spin par la détection d'un photon unique

Dans cette section, nous montrons que les interfaces spin-photon présentées précédemment peuvent être aussi utilisées pour manipuler la polarisation des photons, grâce à la rotation Kerr macroscopique induite par un spin unique. Pour ce faire, nous montrons que l'on a une action en retour macroscopique de la mesure de la polarisation d'un photon unique sur le spin: la mesure de la polarisation d'un seul photon induit une projection macroscopique du spin. Ceci est révélateur des fortes corrélations réalisées entre le spin et la polarisation d'un photon réfléchi par l'interface spin-photon.

Pour ce faire, on présente tout d'abord en détail l'action en retour de la mesure et nous mesurons des corrélations entre deux détecteurs de photons uniques mesurant la lumière réfléchie dans deux polarisations orthogonales (la plupart du temps diagonale et antidiagonale). Grâce à un modèle simple que nous présentons, on est capable d'interpréter ces mesures de corrélations pour en déduire la projection du spin induite par la mesure d'un seul photon. Cependant, ce modèle est trop simple pour expliquer dans le détail nos résultats expérimentaux. On le complète donc grâce à un modèle exact qui simule la réponse en polarisation de la boîte quantique et les corrélations mesurées. Ce modèle théorique simule notamment les processus incohérents qui peuvent intervenir sur la boîte quantique.

Mise en évidence du phénomène d'action en retour de la mesure

Afin de comprendre la projection de spin qui peut être induite par une mesure, on réalise un modèle simplifié de notre problème (voir Fig. 5.1). Le trou confiné dans la boîte quantique possède un spin qui peut soit être $|\uparrow_z\rangle$, soit $|\downarrow_z\rangle$. Un faisceau incident polarisé horizontalement est réfléchi par l'interface spin-photon. Grâce à la rotation Kerr amplifiée par la cavité, la lumière est réfléchie avec une polarisation qui dépend du spin: $|\Psi_{\uparrow}\rangle$ si le spin est $|\uparrow_z\rangle$ ou bien $|\Psi_{\downarrow}\rangle$ si le spin est $|\downarrow_z\rangle$. Dans le cas idéal, ces polarisations sont orthogonales $\langle\Psi_{\uparrow}|\Psi_{\downarrow}\rangle=0$ et on suppose $|\Psi_{\downarrow}\rangle=|D\rangle$ et $|\Psi_{\uparrow}\rangle=|A\rangle$. On suppose au départ que l'on n'a aucune information sur le spin et qu'il est donc dans un mélange statistique. Si un photon interagit avec ce spin et est détecté avec une polarisation antidiagonale $|A\rangle=|\Psi_{\uparrow}\rangle$, on sait alors que le spin était dans l'état $|\uparrow_z\rangle$. On acquiert donc de l'information sur le spin et cela a pour effet de le projeter dans l'état $|\uparrow_z\rangle$: il y a une action en retour de la mesure d'un photon sur l'état de spin.

Si les deux états de polarisations $|\Psi_{\uparrow}\rangle$ et $|\Psi_{\downarrow}\rangle$ ne sont pas orthogonaux, la détection d'un photon ne projette pas le spin complètement dans un seul état: la projection de spin n'est alors que partielle.

Pour quantifier cela, on réalise un modèle qui considère les deux états de spin possibles, avec un temps de saut de spin T_S qui permet de passer de l'un à l'autre (voir Fig. 5.1). On peut alors calculer la dynamique d'un spin, donné par:

$$\begin{aligned} P_{\uparrow\uparrow}(t) &= \frac{1}{2} + \left(P_{\uparrow\uparrow}(0) - \frac{1}{2} \right) e^{-\frac{2t}{T_S}} \\ P_{\downarrow\downarrow}(t) &= \frac{1}{2} + \left(P_{\downarrow\downarrow}(0) - \frac{1}{2} \right) e^{-\frac{2t}{T_S}} \end{aligned} \quad (0.5)$$

On voit donc que l'état final est toujours $P_{\uparrow\uparrow}(\infty) = P_{\downarrow\downarrow}(\infty) = \frac{1}{2}$ et que lorsqu'on part d'un état initial $P_{\uparrow\uparrow}(0) \neq P_{\downarrow\downarrow}(0) \neq \frac{1}{2}$, le spin retourne vers cet état final au bout d'un temps $\frac{T_S}{2}$.

Afin d'observer cette dynamique, il faut voir son effet sur la polarisation des photons et notamment sur des corrélations croisées entre deux détecteurs observant des polarisations orthogonales (diagonale et antidiagonale). Les corrélations croisées dans la base de détection "D/A" sont données par:

$$\begin{aligned} g_{DA}^{(2)}(t) &= \frac{\langle a_D^\dagger(t)a_A^\dagger(0)a_A(0)a_D(t) \rangle}{\langle a_D^\dagger a_D \rangle \langle a_A^\dagger a_A \rangle} \\ &= \frac{P(D, t | A, 0)}{P(D)} \end{aligned} \quad (0.6)$$

où $P(D, t | A, 0)$ est la probabilité de détecter un photon avec une polarisation diagonale au temps t sachant qu'un photon antidiagonal a été détecté à $t = 0$, et $P(D)$, la probabilité de détecter un photon diagonal sans condition préalable.

Il est possible de relier cette relation à la dynamique du spin:

$$g_{DA}^{(2)}(t) = 1 + \left(g_{DA}^{(2)}(0) - 1 \right) e^{-\frac{2t}{T_S}} \quad (0.7)$$

avec

$$g_{DA}^{(2)}(0) = 1 - (2P_{\uparrow\uparrow|A} - 1)^2 \quad (0.8)$$

A partir d'une mesure des corrélations croisées de la lumière réfléchie, il est donc possible de quantifier la projection du spin induite par la détection d'un photon polarisé anti-diagonalement. On peut donc quantifier l'action en retour de la mesure d'un photon unique à partir d'une mesure de corrélations croisées et notamment de sa valeur à délai nul (voir Fig. 5.3).

Expérimentalement, on peut réaliser une telle mesure et l'on obtient une anti-corrélation à délai nul de $g_{DA}^{(2)}(0) = 80 \pm 1\%$ (voir Fig. 5.6(a)), correspondant à une action en retour de la mesure, induite par la détection d'un seul photon, $P_{\uparrow\uparrow|A} = 72 \pm 1\%$. La détection d'un seul photon permet donc d'obtenir une différence significative par rapport au mélange statistique initial ($P_{\uparrow\uparrow} = 50\%$).

L'intensité de la projection est quantifiée grâce à notre modèle qui, bien que donnant une intuition du phénomène physique de projection du spin induite par la mesure d'un photon, ne permet pas de prendre en compte toute la complexité du problème. En effet, ce modèle a plusieurs limitations:

- Il ne prend pas en compte la probabilité d'occupation du trou qui n'est pas de 100%. Il peut arriver qu'un trou ne soit pas confiné dans la boîte quantique et donc que la lumière incidente ne puisse interagir avec le spin; dans ce cas, la lumière ne subit pas de rotation de polarisation et est donc réfléchie avec une polarisation identique à la polarisation incidente (qui est horizontale).
- Il ne prend pas non plus en compte les mécanismes de bruits qui peuvent avoir lieu au niveau de la boîte quantique. Ces mécanismes peuvent avoir plusieurs origines et peuvent se dérouler avec des temps caractéristiques différents.

Réalisation d'un modèle décrivant fidèlement l'interface spin-photon.

Pour pallier à ces limitations, on réalise un modèle théorique de notre interface spin-photon capable de prendre en compte soit un bruit magnétique, soit un bruit électrique qui possèdent un temps caractéristique soit très faible ($< 100\text{ps}$) soit très long (bien plus long que les autres temps caractéristiques du système). Avec ce système, on prédit la réponse en polarisation de notre interface spin-photon, ce qui permet de simuler l'expérience de tomographie de polarisation de la lumière réfléchie, mais aussi de quantifier l'anti-corrélation que l'on observe sur les corrélations croisées expérimentales. On peut montrer que l'on peut simuler de manière satisfaisante la tomographie de polarisation avec n'importe quel bruit (voir Fig. 5.13) mais qu'il est possible d'avoir une anti-corrélation seulement pour le bruit électrique se déroulant à temps longs (voir Fig. 5.14). On utilise donc ce dernier pour réaliser la simulation complète de notre système.

Cette simulation permet de prédire à la fois la tomographie de polarisation mais aussi les corrélations croisées à délai nul. Il est intéressant de remarquer que lorsque le laser est en résonance avec la transition du trion, il ne devrait pas y avoir d'anti-corrélations sans bruit électrique (voir Fig. 5.16(a)). Grâce à ce bruit électrique, la transition du trion se retrouve décalée spectralement du laser et il peut y avoir des anti-corrélations. Une expérience de corrélations croisées réalise une moyenne des corrélations pour tous les décalages spectraux et c'est pour cette raison qu'on observe expérimentalement des anti-corrélations.

Effet des fluctuations spectrales sur l'action en retour de la mesure.

La conséquence de ce raisonnement concernant l'action en retour de la mesure est la suivante. Lorsque la transition du trion est idéalement décalée spectralement de la boîte quantique, on devrait pouvoir trouver une base de polarisation telle que les polarisations réfléchies dépendantes du spin sont orthogonales, $\langle \Psi_{\uparrow} | \Psi_{\downarrow} \rangle = 0$. On réalise donc une mesure non-destructive forte du spin dans ces conditions. Cependant, vu que l'on ne contrôle pas le décalage spectral du trion, on ne sait pas dans quel état le spin du trou est mesuré. N'ayant pas accès à l'information du décalage spectral, lorsque le laser est placé en résonance avec l'énergie moyenne du trion, on ne peut pas interpréter le résultat de la mesure. Ceci est différent lorsqu'on réalise une mesure avec le laser décalé spectralement de la transition moyenne du trion (voir Fig. 5.16(b)). Dans ce cas, on peut voir que la détection d'un photon avec une certaine polarisation projette le spin plus favorablement dans un état que dans l'autre. On peut donc réaliser une mesure non-destructive macroscopique d'un spin unique avec la détection d'un photon unique. Les données expérimentales où le laser est décalé spectralement sont en cours d'analyse et ne sont pas présentées dans cette thèse.

Conclusion et perspectives

L'objectif principal de ce travail était la réalisation et l'utilisation d'une interface entre le spin d'une charge confinée dans une boîte quantique et la polarisation d'un photon généré par une source externe. Dans l'idéal, une telle interface doit se comporter comme un atome unidimensionnel, ce qui signifie que le spin doit interagir uniquement avec un seul mode optique externe (celui de la cavité) dans lequel les photons peuvent être à la fois efficacement injectés et collectés. Les photons

doivent donc être à la fois efficacement injectés dans la cavité, interagir optimalement et de manière cohérente avec le spin, et enfin être efficacement collectés.

Pour ce faire, nous avons utilisé des boîtes quantiques couplées à des cavités micropiliers de manière déterministe. Nous avons d'abord introduit une technique de tomographie de polarisation permettant de reconstruire l'état de polarisation de la lumière réfléchie par ces dispositifs de cavité-QED. Grâce à cette technique, nous avons mesuré, avec une excellente précision, une efficacité d'injection record (96%) ainsi que le taux d'extraction de photons par le miroir du haut [44]. Nous avons aussi complètement reconstruit la rotation de polarisation induite par une boîte quantique unique et identifié le processus incohérent dominant qui réduit la qualité de l'interaction lumière-matière dans nos dispositifs. Cependant la boîte quantique utilisée pour ce résultat n'était pas chargée et donc son état fondamental n'avait pas de degré de liberté de spin.

La deuxième partie de ce travail est donc la fabrication et l'utilisation d'interface spin-photon. Ces nouveaux dispositifs utilisent une barrière tunnel qui empêche les trous de s'échapper de la boîte quantique: lorsqu'on crée une paire électron-trou, l'électron s'échappe rapidement et il reste alors uniquement un trou dans la boîte quantique. Ces échantillons utilisent aussi la technique de lithographie in-situ, qui est améliorée afin de coupler de manière déterministe la transition du trion d'une boîte quantique, en l'identifiant préalablement par sa photoluminescence sous fort champ magnétique transverse. En utilisant un pompage optique, nous avons démontré une probabilité d'occupation de $91 \pm 1\%$ d'un seul trou confiné dans la boîte quantique. De plus, nous avons montré l'intérêt de ces dispositifs pour la réalisation de source de photons uniques, car la collection de photons uniques est optimisée. Le résultat final de ce manuscrit est la démonstration de l'action en retour de la mesure sur le spin induite par la détection d'un unique photon. Ceci est réalisé grâce à la rotation de polarisation induite par un spin unique, amplifiée grâce à la cavité.

Les perspectives de ce travail sont les suivantes. Premièrement, nous continuons l'analyse des données expérimentales présentées précédemment afin de comprendre mieux les processus incohérents et la dynamique du spin. Un second objectif est la démonstration de la mesure non-destructive du spin unique grâce à la détection d'un seul photon.

On peut enfin poursuivre ces recherches en suivant trois axes de développement. Le premier axe est l'amélioration du dispositif afin d'augmenter l'interfaçage entre le spin et la polarisation du photon. Ceci passe par une réduction des sources de bruits qui sont les causes principales de limitations de l'interface spin-photon. Une première solution envisagée est de réduire les fluctuations spectrales induites par le piégeage du trou, soit en modifiant le pompage optique soit en optant pour des échantillons avec contrôle électrique de l'état de charge de la boîte quantique. Une autre solution consiste en un contrôle actif (ou passif) de la position spectrale de la transition trion.

Un deuxième axe de développement est l'utilisation des interfaces spin-photon pour l'étude de la physique du spin et de la mesure quantique. On espère générer et observer une précession de spin cohérente en configuration Voigt. Nous voulons aussi pouvoir mesurer en temps réel l'état de spin de la boîte quantique. Enfin, on peut utiliser ces interfaces pour étudier des aspects fondamentaux de la mesure en physique quantique, notamment la décohérence induite par la mesure ou bien l'effet Zénon quantique.

Le dernier axe de développement est orienté vers les applications concernant la technologie quantique. Pour ce faire, il faut réaliser une intrication entre un spin et un photon généré par une source externe, grâce à la rotation de polarisation géante induite par le spin. Cette intrication permettrait la réalisation de portes logiques spin-spin ou bien photon-photon ainsi que des états clusters.

Introduction

Quantum technologies:

In the XXth century, the fine understanding of microscopic quantum interactions led to a better comprehension of solid-state physics and to a succession of technological breakthroughs, such as the development of lasers and transistors. This is often referred as the first quantum revolution.

In the early 1980s, Richard Feynman had the intuition that only a computer in which information is processed quantum mechanically can efficiently simulate a quantum system [45]. It should benefit from two purely quantum mechanical features: quantum superposition and entanglement. This motivated a new field of research called quantum information, which studies how information can be encoded, manipulated, transferred, and read out quantum mechanically. The implementation of technologies based on quantum information is expected to give rise to a second quantum revolution [46]. Four fields of applications of quantum information can be foreseen:

- Quantum simulation, which consists in the efficient simulation of quantum systems benefiting from the laws of quantum mechanics [1].
- Quantum sensing, where the measurement accuracy is improved below the standard quantum limit thanks to quantum systems [4].
- Quantum communications, which aims at the transfer of quantum information, with applications in cryptography [3, 47].
- Quantum computing, whose main objective is the realization of a universal quantum computer [2, 48].

For quantum computers, the fundamental unit of information is no longer a classical bit but a quantum bit (qubit), which is a two-level system that can be prepared in a quantum superposition, such as:

$$|\Psi\rangle = \alpha|0\rangle + \beta|1\rangle \quad (0.9)$$

where $|0\rangle$ and $|1\rangle$ are the two possible states, that are equivalent to the classical bits "0" and "1" and α and β (such that $|\alpha|^2 + |\beta|^2 = 1$) are the complex numbers that describe the quantum superposition and contains the quantum information. To be considered as useful for quantum computation, a physical system should fulfill five criteria, defined by *DiVincenzo* (2000) [2]:

- Scalability: a sufficiently high number of qubits is required for quantum computing. The physical system should therefore be able to provide as many qubits as required.
- Initialization: the physical system requires the possibility to be initialized in a perfectly determined state such as $|0, 0, 0, 0, \dots 0\rangle$.

-
- Coherence time. It should be much longer than the operation time, so that a high number of operations can be realized within the qubit coherence time.
 - Gating operations: a quantum computer requires a universal set of operations that consists in all single-qubit unitary gates and a single universal two-qubit gate such as a CNOT gate.
 - Measurement: all qubits of the physical system should be measured individually.

In addition, DiVincenzo added two criteria to be able to perform quantum communications:

- The ability to convert stationary qubits into flying qubits.
- The faithful transfer of flying qubits over long distances.

The most natural set of qubits available in nature are photons, atoms and ions. Atoms [6] and ions [5, 49, 50] provide long coherence time and high two-qubit gate fidelities. However, atoms or ions are experimentally complicated to manipulate. This is the reason why a wide variety of solid-state artificial atoms are explored, such as superconducting qubits [7], colored-centers in diamond [8], or semiconductor quantum dots [9, 10]. In all these systems, the number of qubits that has been manipulated is still too small [51] for the realization of a quantum computer more powerful than classical computers.

Concerning photons, photonic qubits are ideal for sending information over long distances and are at the core of most quantum communication protocols [11]. In addition, they preserve their coherence, and single-qubit operations can be easily implemented. For these reasons, it was proposed to build universal quantum computers solely-based on single photons and linear optics [12], called a Linear-Optics Quantum Computer (LOQC). Its main drawbacks are that the widely-used Spontaneous Parametric Down Conversion (SPDC) single-photon generation is not efficient enough, that photons are not ideal for quantum memories, and that it is impossible to deterministically realize photon-photon gates with only linear optics. Concerning quantum communications, photons are also sensitive to fiber losses which reduce their application range or requires free-space communications [52, 53].

Interfacing photons and (artificial) atoms:

A hybrid system where artificial atoms are interfaced with photons might overcome the limitations related to LOQC [54]. Indeed, the non-linear interaction of a photon with a quantum emitter can be used to implement deterministic photon-photon gates [13] and artificial atoms can be used to store the quantum information [55]. Concerning quantum communications, quantum repeater protocols [14], where the photon state is encoded onto a solid-state memory at intermediate nodes, can also be used to significantly reduce the effective propagation distances of photons and therefore enhance the quantum communication range. Such interfacing between photons and artificial atoms is therefore crucial not only for quantum computing but also for quantum communications.

The practical implementation of these protocols requires interactions between photons and artificial atoms that are much stronger than what is experimentally achieved. This challenge can be overcome thanks to cavity-Quantum ElectroDynamics (cavity-QED): by using microcavities, the electromagnetic field is confined at the artificial atom position which significantly enhances the light-matter interaction.

This thesis has been carried out in the group of Pascale Senellart (at Centre de Nanosciences de Nanotechnologies, C2N), under the supervision of Loïc Lanco. In this work, an interface between a flying qubit and a stationary qubit is explored: our flying qubit is the polarization of a single-photon, while our stationary qubit is the spin degree of freedom of a charge confined in a quantum dot. This

choice is motivated by the promising results concerning the initialization [15, 16], control [17, 18], entanglement [19, 20, 21] and read out [22, 23] of such spins, that make them promising solid-state qubits.

A second motivation is that semiconductor quantum dots can be integrated in semiconductor nanostructures such as microcavities to maximize their interaction with photons. The integration of quantum dots in microcavities is the field of expertise of Pascale Senellart's group, which has achieved the deterministic coupling of single quantum dots and pillar microcavities [24], with applications including the generation of non classical light [56, 25, 26]. In these devices, the strong light-matter coupling regime was also demonstrated [39] as well as the macroscopic spin-dependent polarization rotation of photons [27].

The main objective of my research is the realization and the use of a spin-photon interface. In this respect, photons require to be deterministically injected into the pillar cavity, must efficiently interact with a charged quantum dot via spin-dependent polarization rotation and then must be efficiently collected. During this work, I have addressed these three challenges. I have demonstrated the near optimal injection of photons into the cavity and measured this cavity-coupling accurately. I have also shown a giant optical phase shift induced by a single neutral quantum dot coupled to a cavity. Besides, I have developed a technique to deterministically identify and select the charged state optical transition, and to optically confine a single hole in order to produce deterministic spin-photon interfaces. The final results of my thesis is the demonstration of the quantum measurement back-action induced on a single spin with a single detected photon.

This manuscript is organized as follows:

- **In Chapter 1,** we introduce the fundamental properties of self-assembled InAs quantum dots and more specifically the spin properties of singly-charged quantum dots. We show how the spin of a charge confined in a quantum dot is interacting with its environment and can be optically manipulated. The second part of this chapter focuses on the fundamental concepts of the integration of quantum dots into microcavities. We also present the in-situ lithography technique allowing to deterministically couple a single quantum dot into a micropillar and we detail the applications of these devices as single-photon sources and spin-photon interfaces.
- **In Chapter 2,** we study the polarization response of pillar microcavities thanks to a polarization tomography approach that allows representing the polarization state in the Poincaré sphere. We show that we can measure with record accuracy the cavity coupling parameters by analyzing the polarization of the reflected light in the Poincaré sphere and more specifically its polarization purity. This technique leads to the demonstration of a record high injection coupling efficiency with a micropillar cavity. In addition, this resulted in the development of an optical coupling procedure that is now used in the everyday life of our lab.
- **In Chapter 3,** the polarization tomography approach is extended to a cavity-QED device, that consists of a cavity-coupled neutral quantum dot. We demonstrate experimentally the giant rotation of polarization (20° both in latitude and longitude) induced by a single neutral quantum dot, measured in the Poincaré sphere by polarization tomography. The main limitations of this rotation of polarization are the interactions with the environment that reduce the quality of the light-matter interface by inducing depolarization for the reflected photons. Together with numerical simulations, based on a master equation describing our cavity-QED device, we are able to discriminate the origin of the dominant noise mechanisms at play on the device under study, thus demonstrating that the tomography approach provides a comprehensive

measurement tool in the general framework of light-matter interfaces.

- **In Chapter 4**, we show how spin-photon interfaces can be deterministically fabricated. We identify the optical transition corresponding to a singly-charged quantum dot state by observing the evolution of the photoluminescence of a quantum dot under in-plane magnetic field. The deterministic spatial and spectral matching with the pillar microcavity is achieved using the in-situ lithography technique. The single hole confinement is obtained under quasi-resonant excitation thanks to a tunneling barrier that prevents the hole from escaping the quantum dot. Thanks to this technique we demonstrate a hole occupation probability of more than 85% on multiple devices. The performances of such spin-photon interfaces are then evaluated in the framework of single-photon sources.
- **In Chapter 5**, we are interested in the giant spin-dependent rotation of polarization that allows the mapping of the spin state onto the polarization photon qubit. We demonstrate the macroscopic measurement back-action on the spin induced by a single photon detection. This is an interesting result as it shows that we can achieve strong correlations between a quantum dot spin and a pre-existing photon, which is crucial for the implementation of quantum computing and quantum communication. We also explore the implications of this promising result on the investigation of the interaction of a single spin with its nuclear environment.

Finally, we discuss the on-going data analysis. The perspectives offered by such spin-photon interfaces are also discussed with applications on the study of fundamental quantum measurements and for quantum technologies.

Chapter 1

Fundamentals on charged quantum dots in pillar micro-cavities.

The spin of a carrier confined in a self-assembled quantum dot is a promising device for the development of quantum-computing and quantum-communication technologies [2, 57, 3]. Indeed, it can act as a quantum bit (also called qubit), the most fundamental unit of quantum information. The manipulation of such a qubit can be performed optically, but the light-matter interaction is not strong enough to optimally interface a single photon with a single spin. A solution to overcome this challenge lies in the field of cavity Quantum ElectroDynamics (cavity-QED) where the light-matter interaction is drastically enhanced by the confinement of the electromagnetic field.

The objective of the present chapter is to introduce spin states in self-assembled quantum dots and show how they can be interfaced with light using microcavities. The first part of this chapter is focused on semiconductor quantum dots. The different charged states that can be confined in a quantum dot are first introduced. We then take a closer look at their interactions with the nuclear spins. We also show how the spin of a confined carrier can be optically initialized, manipulated, entangled with spins or photons, and read out. The second part of this chapter deals with the cavity-enhanced light-matter interaction in the objective of increasing the interaction between a single photon and a single spin. We present applications of such cavity-QED devices first to produce single photons, and then to develop a spin-photon interface based on cavity-enhanced Kerr polarization rotation.

1.1 Charges confined in quantum dots.

In this section, self-assembled quantum dots [28, 29] are presented in detail. We also show how they can be experimentally fabricated. Finally, we present how charges can be controllably confined in a quantum dot, to obtain a spin qubit that can be controlled with photons, via optical selection rules.

1.1.1 Semiconductor quantum dots.

A self-assembled Quantum Dot (QD) is a semiconductor nanostructure embedded in a wider bandgap semiconductor matrix. Figure 1.1(a) shows a transmission electron microscope (TEM) image of a InGaAs quantum dot embedded in a GaAs matrix. The wetting layer, constituted by a monolayer of InAs in between bulk GaAs layers, is a consequence of the growth technique.

Growth: In this work, the quantum dots are grown using the Stranski-Krastanov technique [58, 59, 60]. InAs is epitaxially grown layer-by-layer on a GaAs substrate. These two materials have slightly different lattice constants (6.06 Å for the InAs and 5.65 Å for the GaAs) which leads to an accumulation of strain during the growth. When the InAs layer is too thick (about 1.7 monolayers), it becomes energetically favorable to create nucleations of InAs. By continuing the epitaxial growth, the InAs aggregates around these nucleations and leads to the creation of InAs islands with typical heights of a few nm, and diameters of a few tens of nm, which are denoted as quantum dots. They are then enclosed in a capping layer of GaAs. In all this manuscript, the quantum dots under study are also annealed at high temperature (850 – 900°) [61] to adjust their energies by interdiffusion of GaAs and InAs at the quantum dot interface. By diffusion of GaAs in the quantum dot, the quantum dot potential barrier is reduced leading to higher optical transition energies. Another consequence of the annealing is that the quantum dots are bigger and nearly have a rotational symmetry along the growth axis.

Artificial atoms: Due to their small sizes, quantum dots confine electrons and holes in the three dimensions, therefore leading to discrete electronic energy levels. At cryogenic temperature ($T \approx 4K$), this also results in sharp optical transitions between these discrete energy levels, corresponding to the absorption or the emission of a single photon. For these reasons, a quantum dot behaves similarly to an atom and as a result, is often called a solid-state artificial atom [62]. The energy levels of a quantum dot are sketched in Fig. 1.1(b). For undoped semiconductors, the valence band is generally completely filled with electrons while the conduction band is generally empty. The electronic levels in the bulk GaAs semiconductor are not discretized and therefore a photon with an energy higher than typically 1.5 eV can non-resonantly promote an electron from the GaAs bulk valence band to its conduction band. Similarly, because the electronic levels in the wetting layer are also not discretized, it is also possible to non-resonantly promote an electron from the valence to the conduction band thanks to a photon of typical energy above 1.45 eV. On the contrary, the quantum dot presents discrete energy levels depicted by horizontal bars in the sketch of Fig. 1.1(b). The lower energy optical transition (typically 1.33 eV) corresponds to the promotion of the higher energy valence electron to the lower energy conduction state in the quantum dot. The resulting state is an electron in the conduction state and a missing electron in the valence state, denoted as a hole. The resulting electron-hole pair is generally called a neutral exciton, although in quantum dots, electron-hole pairs are confined by the quantum dot potential and not by the electron-hole binding energy, as in "true" excitons [63]. The neutral exciton is one of the numerous states that can be populated in a quantum dot, as seen in the following section.

1.1.2 Charged states in quantum dots.

Optical observation of charged states.

As observed previously, it is possible to promote optically electrons from the valence to the conduction band, thus creating electron-hole pairs. However, a wide variety of states can be obtained in quantum dots. Originally, these states have been evidenced using optical non-resonant excitation (generally with incoming photons exciting the GaAs bulk or the InAs wetting layer) and observing the QD photoluminescence [29, 64, 65, 66]. The non-resonant excitation generates electrons and holes inside the quantum dot. The electron (resp. the hole) can also escape the quantum dot leading to a resident hole (resp. electron), inside the quantum dot and therefore different optical transitions

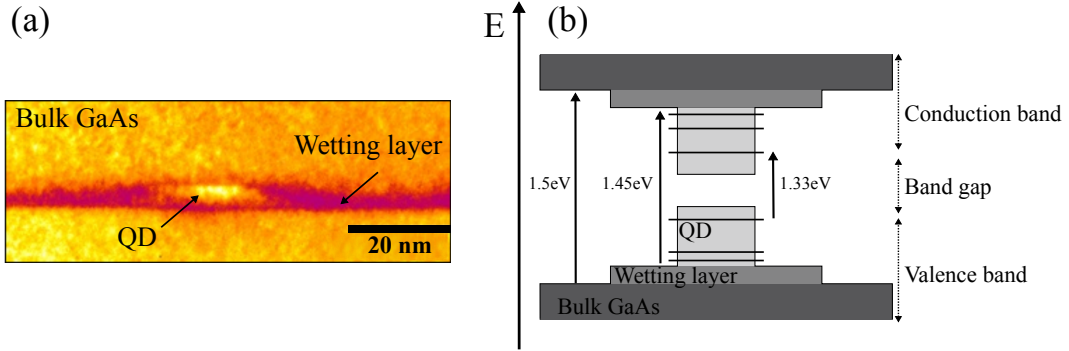


Figure 1.1: (a) Transmission electron microscopy image of a single quantum dot. (b) Energy levels and typical optical transition energies (at cryogenic temperatures) of a self-assembled *InAs* quantum dot, its wetting layer and the *GaAs* semiconductor matrix.

corresponding to different QD charge states. Such photoluminescence can be spectrally analyzed in wavelength, as displayed in Fig. 1.2 (a), evidencing different optical transition wavelengths corresponding to different quantum dot charge states. In the example presented in Fig. 1.2 (a), three optical transitions are clearly observed. Each corresponds to the radiative decay of an electron from the conduction band to the valence band.

Some of the possible optical transitions are illustrated in Figs. 1.2 (b-e). Both the excited and ground states are sketched. In Fig. 1.2(b), the excited state corresponds to an electron-hole pair, also called an exciton (X). It radiatively decays by emitting a single photon with energy $\hbar\omega_X$ into the crystal ground state (*cgs*), where there are no excess charges at all. It is also possible to have two electron-hole pairs inside the quantum dot, a bi-exciton (XX), such as depicted in Fig. 1.2(c). One pair radiatively decays by emitting a single photon with energy $\hbar\omega_{XX}$ and the resulting state is an exciton. Figs. 1.2(d) and (e) display excited states where an excess charge is present together with the electron-hole pair. Such states are denoted positive (X^+) or negative (X^-) trion depending if the excess charge is a hole or an electron. After photon emission, the ground state is a charged quantum dot, where the excess charge remains.

Control of the charge state.

In the spectrum presented in Fig. 1.2 (a), it is possible to show that the three optical transitions correspond to a biexciton (XX), an exciton (X) and a trion (CX). It is therefore possible to populate an excess charge ground state inside the quantum dot using non-resonant excitation. However, in general, this excess charge is only produced with reduced probability because other QD states can also be populated. Other techniques are used to control the ground charge states. A first solution is to dope the *GaAs* matrix with n-type or p-type impurities. By growing a doped layer a few nanometers near the quantum dot, with adjusted density, it is possible to obtain the desired charge inside the quantum dot [67, 68]. However, in that case, the number of resident charge inside the quantum dot is not deterministically controlled and the desired number of resident charges is only obtained statistically over different QD samples.

This technique has been greatly improved by the control of the electron chemical potential, by applying an external bias voltage in a Schottky diode structure [69, 42], such as presented in Fig. 1.3(a). The applied bias voltage modifies the electronic energy levels of the quantum dot that needs

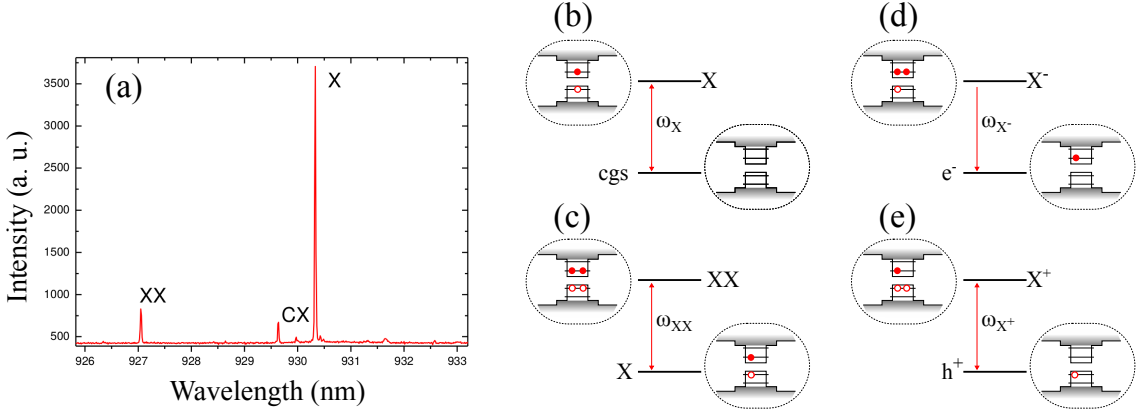


Figure 1.2: (a) Typical photoluminescence spectrum of a single quantum dot in a planar cavity. Three distinct optical transitions are observed, each corresponding to a different quantum dot transition (from left to right: a bi-exciton (XX), a charged exciton (CX), also called a trion, and an exciton (X)). (b-e) Sketch of typical optical transitions from an excited state (upper bar) to a ground state (lower bar). The corresponding charge states are also illustrated: only excess electrons (full circles) in the conduction band and holes (empty red circles) in the valence band are represented. The optical transitions are: (b) the exciton transition (with energy $\hbar\omega_X$), (c) the bi-exciton transition ($\hbar\omega_{XX}$), (d) the negative trion ($\hbar\omega_{X^-}$) and (e) the positive trion ($\hbar\omega_{X^+}$).

to be compared to the Fermi energy of the semiconductor: by setting the electronic levels above or below the Fermi energy, it is possible to control deterministically the number of charges inside the quantum dot as observed in Fig. 1.3(b) [42]. In the following, we are interested in the properties of the charge carrier that can be confined inside the quantum dot.

Charge carriers in quantum dots.

Charge carriers that can be confined inside the quantum dot are constituted of excess electrons in the conduction state or holes (which are missing electrons) in the valence state. The simplest quantum dot charged states are the singly-charged states constituted of a single electron, or a single hole, confined inside the quantum dot (see Fig. 1.4 (a)). The electron spin is $1/2$ and therefore, the relevant electron spin states $|\uparrow_z\rangle, |\downarrow_z\rangle$ have spin projections $\pm 1/2$. The quantum dot hole states have a spin $3/2$ and therefore spin projections $\pm 1/2$ and $\pm 3/2$. The states $|\uparrow_z\rangle, |\downarrow_z\rangle$ with spin projections $\pm 3/2$ are called the heavy holes while the states with spin projection $\pm 1/2$ are called light holes [70].

In bulk semiconductors, heavy-holes and light-holes are energy-degenerate. However, the shape of quantum dots is such that the QD height is typically an order of magnitude smaller than the QD lateral dimensions. Therefore, charges are more confined vertically than laterally: this implies a lift of degeneracy of the light-holes and heavy-holes [72], so that in practice, only the heavy holes can be populated. In the following, we therefore only consider the heavy hole states with spin $3/2$ and spin projections $\pm 3/2$ and we neglect the light-hole states with spin $3/2$ but spin projections $\pm 1/2$. Consequently, the relevant charge states are $|\uparrow_z\rangle$ and $|\downarrow_z\rangle$ with respective spin projections $1/2$ and $-1/2$ for the electron and $|\uparrow_z\rangle$ and $|\downarrow_z\rangle$ with respective spin projections $3/2$ and $-3/2$ for the heavy

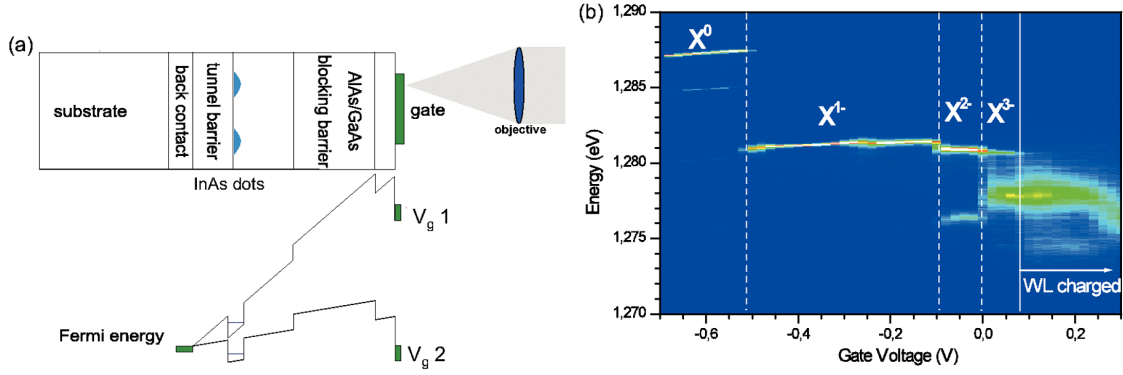


Figure 1.3: From Ref. [42] (Petroff's group) : (a) Scheme of InAs quantum dots embedded in a charge-tunable device, where depending on the applied voltage V_{g1} or V_{g2} , the Fermi energy is above or below the electronic level of the quantum dot. Therefore, by applying a voltage bias, it is possible to trap an electron inside the quantum dot. (b) Photoluminescence of a single quantum dot under different external applied voltages. With higher voltage, the quantum dot efficiently trap electrons, which results in different charge states of the quantum dot and therefore in different transition energies. (Figure extracted from Ref. [70].)

hole.¹

Optical selection rules.

The singly-charged states can be optically excited by creating an electron-hole pair alongside the first confined charge (as seen in Fig. 1.4) (b,c)). Due to the Pauli exclusion principle, the two holes of a positive trion X^+ are in a singlet state $|\uparrow\downarrow\rangle$, and the trion spin state is identical to its electron spin which is either $1/2$ (for $|\uparrow_z\rangle$) or $-1/2$ (for $|\downarrow_z\rangle$). Another consequence of the cylindrical symmetry of a quantum dot, illustrated in Figure 1.4 (b), is that it sets the growth axis (denoted z) as a preferred direction along which optical selection rules connect the hole $|\uparrow_z\rangle$ (respectively $|\downarrow_z\rangle$) and the trion states $|\uparrow\downarrow\uparrow_z\rangle$ (respectively $|\downarrow\uparrow\downarrow_z\rangle$) with left-handed (right-handed) circular polarization, as displayed in Fig. 1.4(b). The polarization of the trion transitions is due to angular momentum conservation. For example for the trion transition $|\uparrow\downarrow\uparrow_z\rangle \rightarrow |\uparrow_z\rangle$, the excited and ground states have spin $1/2$ and $3/2$ respectively. It therefore emits a photon with spin -1 , which corresponds to a left-handed circularly polarized photon.

Interestingly, thanks to the degeneracy between states $|\uparrow_z\rangle$, $|\downarrow_z\rangle$ and $|\uparrow\downarrow\uparrow_z\rangle$, $|\downarrow\uparrow\downarrow_z\rangle$ (in the absence of magnetic field), it is possible to rewrite the same optical selection rules using different basis states. For example, the spin states expressed along the x-axis are:

$$\begin{aligned} |\uparrow_x\rangle &= \frac{1}{\sqrt{2}} (|\uparrow_z\rangle + |\downarrow_z\rangle) \\ |\downarrow_x\rangle &= \frac{1}{\sqrt{2}} (|\uparrow_z\rangle - |\downarrow_z\rangle) \end{aligned} \quad (1.1)$$

¹In reality, due to the quantum dot mechanical strains, there is still a residual heavy-hole light-hole mixing such that the accessible states are mixed typically with 10% of light-hole that has implications on its optical selection rules and its interaction with the environment as will be detailed in Sec. 1.2.

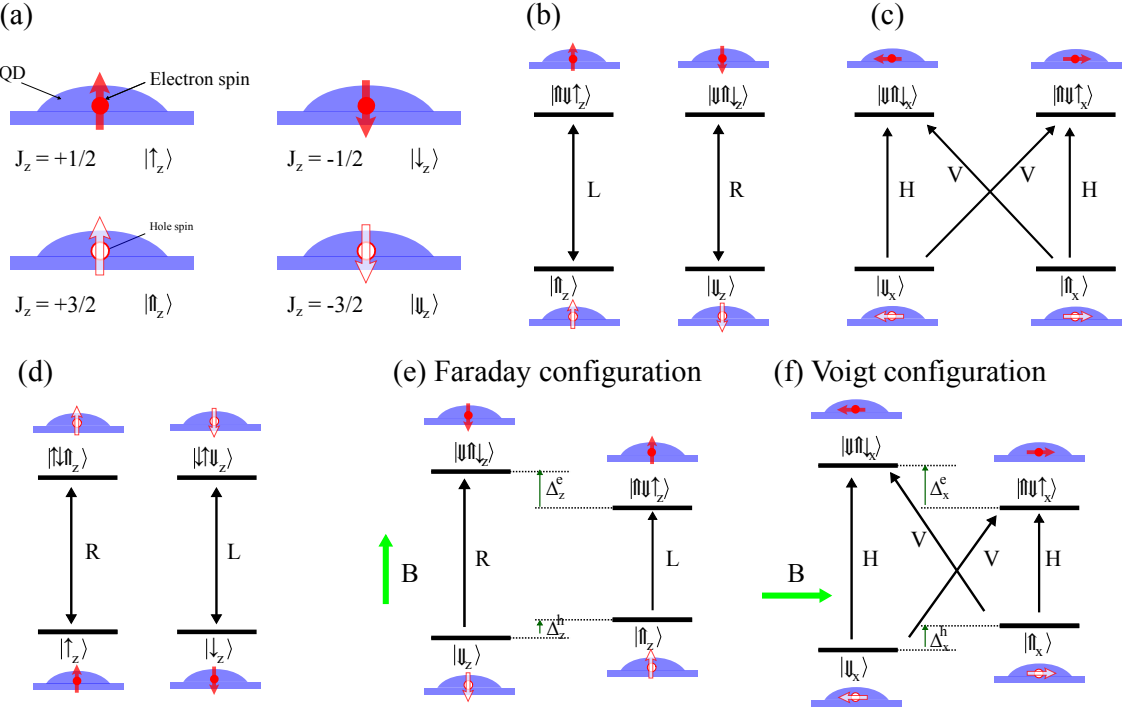


Figure 1.4: (a) Sketch representing spin projections along the growth axis (z-axis) for an electron (top panel) and a hole (bottom panel). (b) Optical selection rules of a positive trion (b). The spin projections are also represented using the sketches in (a). (c) Same optical selection rules of a positive trion but represented with spin projections expressed along the x-axis (without magnetic field). (d) Optical selection rules of a negative trion. (e) Optical transition of a positive trion under magnetic field in Faraday configuration (longitudinal magnetic field) [71]. The magnetic field induces a Zeeman splitting between the hole states (Δ_z^h) and between the trion states (Δ_z^e). (f) Optical transition of a positive trion under magnetic field in Voigt configuration (transverse magnetic field) [71]. The magnetic field induces a Zeeman splitting between the hole states (Δ_x^h) and between the trion states (Δ_x^e).

and similar expressions for the trion states.

At zero magnetic field, the optical trion transitions, expressed with spin projections along the x-axis, are represented in Fig. 1.4 (c). The trion and hole states are connected by linearly-polarized optical transitions:

$$\begin{aligned} |H\rangle &= \frac{1}{\sqrt{2}} (|L\rangle + |R\rangle) \\ |V\rangle &= \frac{-i}{\sqrt{2}} (|L\rangle - |R\rangle) \end{aligned} \quad (1.2)$$

There are similar selection rules for an electron in the ground state as displayed in Fig. 1.4 (d). The negative trion state X^- is constituted of two electrons (that are in a singlet state $|\uparrow\downarrow\rangle$) and a single hole. Therefore its spin is governed by the hole spin with spin projections $3/2$ (for $|\uparrow_z\rangle$) or $-3/2$ (for $|\downarrow_z\rangle$). Consequently, depending on its hole spin state, the trion radiatively decays by emitting a circularly-polarized photon with either left or right helicity, due to angular momentum conservation,

as shown in Fig. 1.4 (d).

Optical selection rules with external magnetic field

An interesting property of quantum dots is that their optical properties are modified when an external magnetic field is applied. Indeed, the spin of an electron is interacting with a magnetic field \vec{B} with an interaction hamiltonian:

$$H = g\mu_B \vec{S} \cdot \vec{B} \quad (1.3)$$

where g is the electron Landé-factor, \vec{B} is the magnetic field, \vec{S} is the spin vector operator and $\mu_B = \frac{q\hbar}{2m_e}$ is the Bohr magneton (with q the charge, \hbar the Planck constant and m_e the mass of the electron). The spin vector operator is defined by $\vec{S} = S\hbar\vec{\sigma}$ with S the spin projection and with the Pauli vector operator $\vec{\sigma} = \sigma_x\vec{x} + \sigma_y\vec{y} + \sigma_z\vec{z}$.

The interaction hamiltonian for a hole is slightly different because the spin is more sensitive to a magnetic field along the QD growth direction. Therefore, there are in fact two Landé factors [73]: g^\perp for an in-plane magnetic field and g^\parallel for longitudinal magnetic field (i. e. along the growth axis). The interaction hamiltonian for a hole is therefore:

$$H = \hbar\mu_BS(g^\perp\sigma_xB_x + g^\perp\sigma_yB_y + g^\parallel\sigma_zB_z) \quad (1.4)$$

The consequence of these interactions is that they lift the spin state degeneracy by inducing a Zeeman splitting Δ^h for the hole spin states and Δ^e for the electron spin states. This also modifies the optical selection rules of the quantum dot as can be seen in Fig. 1.4 (e) and (f). These figures display the optical selection rules of a positively-charged quantum dot; similar axes are obtained for a negatively-charged quantum dot (that we do not show here).

An external magnetic field is generally applied either along the growth axis (Faraday configuration) or it can be orthogonal to the growth axis (Voigt configuration). In the Faraday configuration, the magnetic field induces Zeeman splittings Δ_z^h and Δ_z^e onto the hole and the trion states, but the eigenstates are still the spin projections along the z-axis, i. e. $|\uparrow_z\rangle$ and $|\downarrow_z\rangle$ (resp. $|\uparrow\downarrow\uparrow_z\rangle$ and $|\downarrow\uparrow\downarrow_z\rangle$) for the hole (resp. trion). Therefore the trion transitions are still circularly-polarized, as can be seen in Fig. 1.4 (e).

Conversely, in Voigt configuration, the system rotational symmetry is broken and the eigenstates are along an in-plane axis, denoted x-axis [74], the new symmetry axis, imposed by the external magnetic field: $|\uparrow_x\rangle$, $|\downarrow_x\rangle$ for the hole eigenstates and $|\uparrow\downarrow\uparrow_x\rangle$, $|\downarrow\uparrow\downarrow_x\rangle$ for the trion eigenstates.¹

The in-plane magnetic field also induces a Zeeman splitting for the trion states and for the hole states. Therefore, for a high in-plane magnetic field ($B_x > 1\text{T}$ typically), a trion decays into a hole by emitting a single photon with four combinations of linear polarizations and energies, as illustrated in Fig. 1.4 (f).

In the overall, in the presence or absence of magnetic field, the confined electron or hole provides a spin that can be optically manipulated thanks to well-defined optical selection rules. In the following section, we are interested in the spin properties of such charge carriers.

¹To be more accurate, the spin eigenstates are generally not along the external magnetic field axis but can be in another in-plane axis. Consequently, the expression of the spin eigenstates should be: $|\uparrow_x\rangle = \frac{1}{\sqrt{2}}(|\uparrow_z\rangle + e^{i\theta}|\downarrow_z\rangle)$ and $|\downarrow_x\rangle = \frac{1}{\sqrt{2}}(|\uparrow_z\rangle - e^{i\theta}|\downarrow_z\rangle)$, with a phase θ determined by the geometry of the quantum dot and the orientation of the external magnetic field [74].

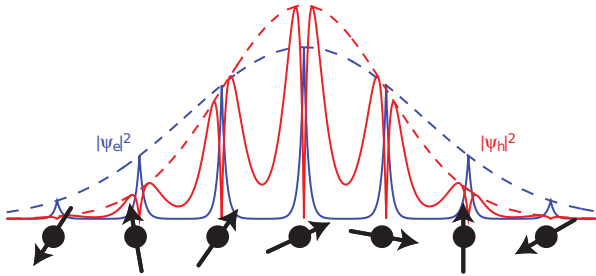


Figure 1.5: From Ref. [82] (Warburton's group): Schematic of the electron and hole wave functions. The electron wave function (blue line) is based on s-orbitals which are localized at each atomic site of a unit cell, where a nuclear spin (represented by a black circle and an arrow) is localized. The hole wave function (red line) is based on p-orbitals whose wave functions are equal to zero at each nuclear site. Therefore, the hyperfine interaction is much stronger for electrons than for holes. The envelope of the wave functions $|\Psi_e|^2$ and $|\Psi_h|^2$ are represented in dashed line.

1.2 Spin physics in quantum dots.

The spin state of an electron or a hole generally fluctuates over time mainly because of its interplay with the environment caused by phonon-assisted spin flips [75, 76] and nuclear spin interactions [30, 77, 78]. The hyperfine interaction with nuclei is the dominant incoherent process at low magnetic field (typically below a few tens of mT) while phonon-assisted spin flips are dominant at high magnetic field (typically above $1T$). In this work, we will study the spin physics at low magnetic field and are therefore mainly interested in the hyperfine interaction that is detailed in the following.

1.2.1 Hyperfine interaction with electrons and holes.

An InGaAs quantum dot is constituted of $10^4 - 10^6$ nuclei of In, Ga and As which all have a non-zero nuclear spin ($9/2$ for In and $3/2$ for Ga and As) [70]. All these spins are generally randomly oriented. Because of the strong confinement of the charge carrier wave function inside the quantum dot (over typically $N \approx 10^5$ lattice sites), the fluctuations of the hyperfine interaction of the charge and the nuclei are drastically enhanced. It is a close-to-ideal realization of the central spin problem [79, 80, 81] where one single central spin (the carrier spin) is interacting with a spin bath of nuclear spins that are totally random. There are two main contributions to the hyperfine interaction:

- Fermi-contact interaction, which is only relevant when there is an overlap between the carrier wave function and the nuclear lattice site, so for s-type wave functions.
- The dipole-dipole interaction, that is effective even when there is no overlap of the wave function with the nuclear spin site. It is an order of magnitude weaker than the Fermi-contact interaction and is the dominant hyperfine interaction for p-type wave functions.

The nature of the hyperfine interaction is different for electrons and for holes, because, as shown in Fig. 1.5, the electron and the hole wave functions are different. This figure shows that the electron has an s-type orbital that is strongly localized on the lattice site and consequently is dominantly interacting with nuclei via Fermi-contact interaction. The hyperfine interaction for an electron is

governed by the Fermi-contact hamiltonian:

$$H_{hf}^e = V \sum_{j=1}^N C_j^e \left| \Psi_e(\vec{R}_j) \right|^2 (I_x^j S_x + I_y^j S_y + I_z^j S_z) \quad (1.5)$$

with N the number of nuclei, V the unit cell volume, C_j^e the coupling constant, $\left| \Psi_e(\vec{R}_j) \right|^2$ the envelop of the wave function for the site j , and \vec{I} and \vec{S} the nuclear and electron spins.

On contrary, for a pure heavy hole, the wave function is not localized on the lattice site and therefore the Fermi-contact interaction is suppressed. Thus, the heavy hole is only sensitive to the dipole-dipole interaction. Consequently holes are much less sensitive to nuclei than electrons and their hyperfine interaction hamiltonian has an Ising form:

$$H_{hf}^{hh} = V \sum_{j=1}^N C_j^{hh} \left| \Psi_h(\vec{R}_j) \right|^2 I_z^j S_z \quad (1.6)$$

with C_j^{hh} the coupling constant, and $\left| \Psi_h(\vec{R}_j) \right|^2$ the envelop of the hole wave function at site j . As can be observed, the heavy hole is only sensitive to the spin projection along the growth (z) axis. The dipole-dipole interaction is an order of magnitude smaller so that $|C_j^e/C_j^{hh}| \approx 10$ [73].

To account for the light-hole heavy-hole mixing, a more realistic hamiltonian needs to be taken into account:

$$H_{hf}^h = V \sum_{j=1}^N \left| \Psi_h(\vec{R}_j) \right|^2 (C_j^{h,z} I_z^j S_z + C_j^{h,x} I_x^j S_x + C_j^{h,y} I_y^j S_y) \quad (1.7)$$

Consequently, due to the light-hole mixing, a quantum dot hole is also sensitive to the transverse components of the nuclear spins. This sensitivity is still much smaller than for the longitudinal component because $|C_j^{h,z}| >> |C_j^{h,x}|, |C_j^{h,y}|$ [82].

1.2.2 Spin dynamics in quantum dots.

The spin dynamics of a single charge spin interacting with a nuclear spin bath is described by the Merkulov-Efros-Rosen model [30], with interactions occurring at three different characteristic timescales, illustrated in Fig. 1.6:

- (i) The carrier spin is interacting with the nuclear spins by Fermi-contact interactions for electron spins and by dipole-dipole interaction for heavy holes [82]. In the mean field approach, the carrier spin is affected by a mean nuclear spin polarization (which is not zero due to spin fluctuations of magnitude $\approx 1/\sqrt{N}$). It acts similarly to an effective magnetic field called the Overhauser field, $\vec{B}_N^{(e)}$, which is typically of $|B_N^{(e)}| \approx 20mT$ [83] for an electron spin. This Overhauser field is oriented in a random direction and the electron spin is precessing about it. For an electron, this leads to a typical dephasing time of the order of $1ns$ [84]. For a hole, the hyperfine interaction is weaker and can also be described by a Overhauser field $\vec{B}_N^{(h)}$ which is weaker than the electron Overhauser field ($|B_N^{(h)}| < |B_N^{(e)}|$) and is anisotropic (because the hyperfine in-plane coupling constants $|C_j^{h,x}|$ and $|C_j^{h,y}|$ are smaller than the longitudinal coupling constant $|C_j^{h,z}|$). Therefore the typical hole dephasing time is longer, typically $100ns$ [85].

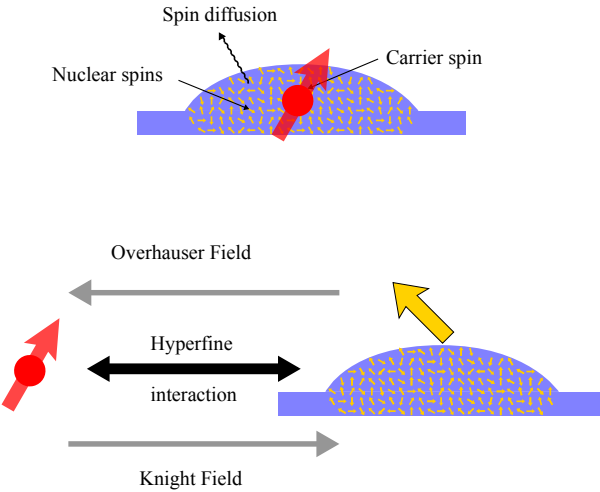


Figure 1.6: Top panel: sketch representing the confined carrier spin inside the quantum dot (red arrow) interacting with all the nuclear spins (yellow arrows). The nuclei are also interacting weakly with spins outside of the quantum dot, leading to spin diffusion. Bottom panel: the hyperfine interaction between the carrier spin and the nuclei can be pictured by the carrier spin precession around the Overhauser field (yellow arrow) and by the nuclear spin precession around the carrier spin (Knight field).

- (ii) The nuclei are also affected by the electron or the hole spin, acting as an effective magnetic field, the Knight field \vec{B}_K , around which they are also precessing. This leads to an uncontrolled modification of the Overhauser field orientation and intensity. The fluctuations of the Overhauser field are occurring typically at the microsecond timescale.
- (iii) The third interaction concerns the nuclear spin interacting with nuclei at the vicinity of the quantum dot. It corresponds to diffusion of the angular momentum outside the quantum dot and occurs at a timescale of typically $100\mu\text{s}$. We will not consider further this effect as it is not relevant for the study of the spin relaxation at short timescales.

Consequently, the charge spin is precessing quickly around the Overhauser field (1ns for an electron and 100ns for a hole), whose direction fluctuates at intermediate timescale ($1\mu\text{s}$). The total angular momentum is preserved for a timescale of $100\mu\text{s}$. Because the nuclear spins are in general not controlled, this hyperfine interaction limits the spin performances.

1.2.3 Spin coherence and relaxation time.

A spin state is completely described by its density matrix:

$$\rho_{\text{spin}} = \begin{pmatrix} \rho_{\uparrow\uparrow} & \rho_{\uparrow\downarrow} \\ \rho_{\downarrow\uparrow} & \rho_{\downarrow\downarrow} \end{pmatrix} \quad (1.8)$$

The diagonal terms $\rho_{\uparrow\uparrow}$ and $\rho_{\downarrow\downarrow}$ represent the probabilities to measure the state in spin \uparrow and \downarrow respectively. The off-diagonal terms $\rho_{\uparrow\downarrow}$ and $\rho_{\downarrow\uparrow}$, with $\rho_{\uparrow\downarrow} = \rho_{\downarrow\uparrow}^*$, represent the quantum coherence of the state: for a completely mixed state $\rho_{\uparrow\downarrow} = \rho_{\downarrow\uparrow} = 0$ while $|\rho_{\uparrow\downarrow}| = |\rho_{\downarrow\uparrow}| = \sqrt{\rho_{\uparrow\uparrow}\rho_{\downarrow\downarrow}}$ for a pure state.

Because of the interactions with its environment and mainly with the nuclear spins, the carrier spin fluctuates, such that the spin state cannot be controlled over long timescales, which translates mathematically in a modification of the above-mentioned spin density matrix. Consequently, the spin is a quantum memory with limited performances because the information can be stored only for limited time. In order to quantify the efficiency of this quantum memory, two figures of merit are generally introduced: the relaxation time T_1 , which characterizes the dynamics of the population terms $\rho_{\uparrow\uparrow}$ and $\rho_{\downarrow\downarrow}$ and the coherence time T_2 , which characterizes the dynamics of the coherence terms $\rho_{\uparrow\downarrow}$ and $\rho_{\downarrow\uparrow}$ [86, 87].

Relaxation time T_1 .

The relaxation time T_1 is defined as the average transition time from one spin state to the other. It corresponds to the timescale at which spin flips occur, that erase the information about the spin population. It therefore corresponds to the timescale at which the spin population terms $\rho_{\uparrow\uparrow}$ and $\rho_{\downarrow\downarrow}$ are modified by the environment. It is possible to show that spin flips with timescale T_1 also modifies the coherence terms $\rho_{\uparrow\downarrow}$ and $\rho_{\downarrow\uparrow}$ with timescale T_1 and therefore constitutes a theoretical maximum of the coherence time: $T_2 = T_1$. In general however, other processes limit the spin qubit coherence time by inducing dephasing on the spin qubit such that $T_2 < T_1$.

Coherence time T_2 and dephasing time T_2^* .

When a spin is prepared in a quantum superposition between the two spin states, such as $|\psi\rangle = \frac{1}{\sqrt{2}}(|\uparrow_z\rangle + e^{i\alpha}|\downarrow_z\rangle)$, the quantum superposition is described by the phase α between the two states. The coherence time can be defined as the time during which the phase α remains well defined. A perfectly isolated quantum memory has its coherence time bounded by T_1 . However, this phase can be blurred by other dephasing processes characterized by a dephasing time T_2^* that acts only on the coherence (off-diagonal) terms of the spin density matrix, $\rho_{\downarrow\uparrow}$ and $\rho_{\uparrow\downarrow}$. The coherence time is given by:

$$\frac{1}{T_2} = \frac{1}{T_2^*} + \frac{1}{T_1} \quad (1.9)$$

It corresponds to the time during which a pure quantum state remains well defined and can be manipulated. For example, it corresponds to the typical time during which the coherent Larmor precession of the spin qubit around an applied magnetic field remains visible. It is generally limited by the hyperfine interaction to a few nanoseconds for an electron and typically a few hundred nanoseconds for the hole [85], corresponding to the timescales of the fast spin precession around the static but randomly oriented Overhauser field.

1.2.4 Spin noise spectroscopy.

A widely used technique to access the spin properties of an ensemble of quantum dot spins is the spin noise spectroscopy [83, 31, 88, 89]. Optical spin noise spectroscopy is based on the Faraday/Kerr polarization rotation induced by spins: an optical beam is reflected or transmitted with its polarization rotated in a direction that depends on the spin orientations. The Faraday and Kerr rotation will be discussed in more details in Sec. 1.3.2. The spin noise spectroscopy technique consists in deducing the spin characteristics from the polarization fluctuations of an optical beam that is either reflected or transmitted by the spin ensemble (see Fig. 1.7 (a)).

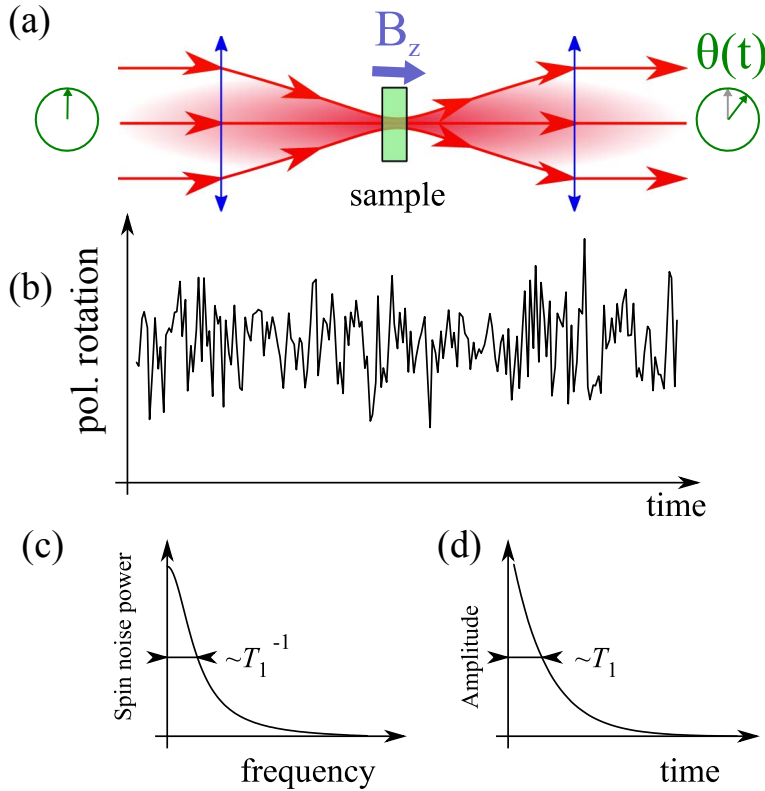


Figure 1.7: From Ref. [93] (Zapasskii's group): (a) Typical spin noise spectroscopy experiment: an optical beam is focused onto a sample containing an ensemble of spins that induces polarization rotation. (b) Typical time trace of the polarization rotation of the optical beam that was reflected or transmitted by the sample, in an experiment performed under longitudinal magnetic field. (c) Spectrum and (d) Autocorrelation function of the polarization rotation signal.

A time trace of the polarization rotation signal is acquired as observed in Fig. 1.7(b). The key idea is that, due to the *fluctuation-dissipation theorem*, information about the spin dynamics are imprinted in the polarization fluctuations noise spectrum, and can be accessed by Fourier transforming the time trace of the polarization rotation signal. The Fourier transform of the signal presented in Fig. 1.7(b) is observed in Fig. 1.7(c). It has typically a Lorentzian shape whose width corresponds to the inverse of the spin relaxation time. It is also possible to access the spin coherence time with this technique, with an external transverse magnetic field. An alternative to the Fourier transform is to calculate the correlations of the optical signal $\langle I(\tau)I(0) \rangle$ (where $I(t)$ is the light intensity at time t) to access an equivalent of the spin correlations, displayed in Fig. 1.7 (d). These two techniques are equivalent due to the *Wiener-Khinchine theorem* and the latter is used in Chap. 5.

Because the Faraday/Kerr rotation induced by a single spin is very small, spin noise spectroscopy has first been applied to ensemble of spins from atomic gases [90] to solid-state systems [91, 83, 89]. Only recently, this technique has been extended to the observation of a single quantum dot hole spin by Dahbashi *et al.* (2014) [92] (Oestreich's group), thanks to the enhancement of Kerr rotation induced by a planar cavity.

1.2.5 Improving the spin qubit.

The spin coherence time determines the time during which a spin qubit can be used to realize quantum operations (that are detailed later in Sec. 1.3), and therefore, must be as long as possible. To avoid the decoherence induced by the hyperfine interaction, one strategy is to develop devices using materials that does not have nuclear spins, such as Silicium or C^{13} -free Carbon. Such strategy is followed in gated electronic quantum dots [94, 95], where a coherence time of $40\mu s$ has been reported, or with colored-center quantum emitters [8] where the coherence time can reach nearly $1s$ at $77K$. As we work with III-V semiconductors with non-zero nuclear spins, other strategies need to be found to improve the coherence of our QD spin qubits.

Magnetic field screening: By applying an external magnetic field, the carrier spin is precessing around the sum of the Overhauser field and the applied magnetic field. When the applied magnetic field is much more intense than the Overhauser field, the effect of the nuclear spins on the carrier spin is reduced: only the fluctuations of the Overhauser field along the external magnetic field orientation induces a dephasing. With such technique, under high transverse magnetic field (a few Teslas), a coherence time of the order of the microsecond timescale can be reached for holes [82], because of the strong anisotropy of the hole Overhauser field.

Spin Hahn echo: Another strategy is to dynamically decouple the spin qubit from its nuclear environment so that the coherence time is not limited by dephasing induced by the random but static Overhauser field. The simplest decoupling protocol is the Hahn echo sequence [96, 17]. It is based on the optical coherent control of a spin, which is presented in details later in Sec. 1.3.3. The key idea is that opposite spins are precessing at the same speed but in opposite directions under the same total magnetic field \vec{B}_{tot} consisting of an external magnetic field and the Overhauser field: $\vec{B}_{tot} = \vec{B}_{ext} + \vec{B}_N$. Therefore, assuming that the Overhauser field is random but static, a pure quantum state precesses around a constant external magnetic field \vec{B}_{tot} for a given time T . At this time, it is possible to coherently inverse the spin state (by using what is called a π -pulse as seen Sec. 1.3.3 for more details) so that it precesses in the opposite direction. Assuming that the Overhauser field is always constant, the initial spin state is recovered at time $2T$.

For the Hahn echo technique, the π -pulse refocuses the dephasing induced by the Overhauser field and consequently, the coherence time T_2 is not sensitive to the fast dephasing induced at the timescale where the Overhauser field is considered random but static (first timescale (i) in the discussion of Sec. 1.2.2). It is only sensitive to the Overhauser field fluctuations (which correspond to the timescale (ii) in the discussion of Sec. 1.2.2) [97]. It is therefore possible to reach coherence times of the order of the microsecond thanks to that technique [17, 98], by dynamically decoupling the spin from its environment.

Engineering the nuclear bath environment: The charge carrier spin coherence time can also be improved by engineering the nuclear spin bath to reduce its fluctuations and therefore control the hyperfine interaction. The spin fluctuations can be reduced by polarizing all the nuclear spins in the same direction. Indeed, as the spin fluctuations σ are proportional to $\sqrt{1 - \langle P_s \rangle^2}$ (with P_s the nuclear spin polarization), the entropy of the nuclear spin bath can be reduced by polarizing all the spins. Experimentally, this technique called Dynamical Nuclear Polarization (DNP), is realized by using the electron spin to optically pump the nuclear spins: nuclear spin polarization of approximately

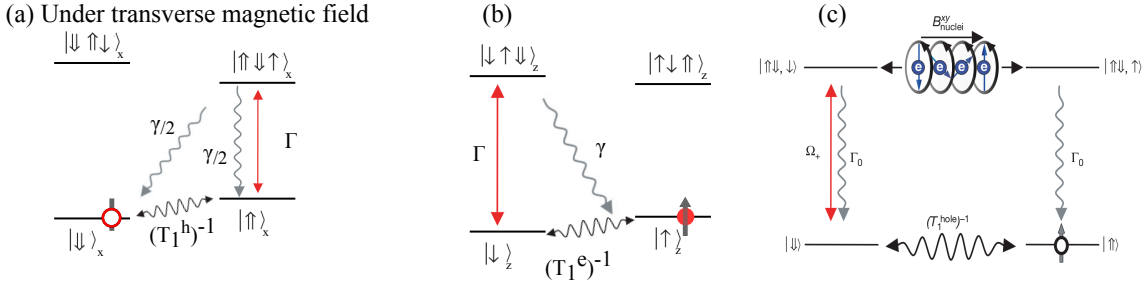


Figure 1.8: Principle of spin initialization under transverse magnetic field (a) and under longitudinal magnetic field for an electron (b) and with or without longitudinal magnetic field for a hole (c). (a) The initialization in transverse magnetic field is similar for the two charge carriers. One of the trion transitions is resonantly excited and eventually decays in the other spin ground state, which is efficiently initialized. (b) The $|\downarrow\rangle \rightarrow |\downarrow\uparrow\downarrow\rangle$ transition is excited with a circularly polarized pump. Eventually the $|\uparrow\rangle$ state is populated by a forbidden diagonal transition. If the diagonal transition rate γ is greater than the spin flip rate $(T_1^e)^{-1}$, the spin state $|\uparrow\rangle$ state is initialized. (c) From Ref. [16]: the $|\downarrow\rangle \rightarrow |\downarrow\uparrow\downarrow\rangle$ transition is excited with a circularly polarized pump. Eventually, an electron spin flip occurs and populate the $|\uparrow\downarrow\uparrow\rangle$ that decays by emitting a single photon. The final state is $|\uparrow\rangle$. It is efficiently initialized if the electron spin flip rate, $(T_1^e)^{-1}$, is greater than the hole spin flip rate, $(T_1^h)^{-1}$.

60% can be achieved [99, 100, 101], which is still not sufficient to significantly improve the charge spin coherence time [102].

Other complex techniques to reduce the nuclear spin bath fluctuations, are also explored: the objective is to reduce the nuclear spin bath fluctuations without dynamically polarizing all the nuclei [103]. These complex methods are beyond the scope of this manuscript but lead to improvements by several orders of magnitude of the electron spin coherence time [68, 104]. Such engineering of the nuclear spin bath is also a step toward its control and use to store quantum information, as shown in a recent paper by *Gangloff et al. (2019)* [105] (Atatüre's group).

1.3 Quantum optics with spins.

To be useful for quantum information processing protocols, it is necessary to be able to prepare qubits, coherently manipulate them, entangle them together and measure them within their coherence time. Such tasks have already been performed with quantum dot spins and are reviewed in this section.

1.3.1 Spin initialization.

The spin can be initialized via optical pumping, benefiting from the selection rules of the trion system. Spin initialization was demonstrated without (only for the hole) and with in-plane or longitudinal magnetic field.

Let us consider first the spin initialization under a strong in-plane magnetic field (see Fig. 1.8(a)). The spin initialization procedure is detailed for a hole spin but is identical for an electron spin. To initialize the spin in the $|\downarrow\downarrow_x\rangle$ eigenstate, the $|\uparrow\uparrow_x\rangle \rightarrow |\uparrow\downarrow\uparrow\downarrow_x\rangle$ transition is excited by a CW laser. If the spin was in the $|\uparrow\uparrow_x\rangle$ state, the trion state $|\uparrow\uparrow\downarrow\downarrow_x\rangle$ is eventually populated. This excited state decays

with equal probability either in the desired $|\Downarrow_x\rangle$ or the unwanted $|\Uparrow_x\rangle$ states. If the resulting spin state is $|\Uparrow_x\rangle$, the resonant laser populates again the trion state $|\Uparrow\Downarrow\Uparrow_x\rangle$ and eventually it decays back into the wanted state $|\Downarrow_x\rangle$. Because the trion transitions $|\Downarrow_x\rangle \rightarrow |\Uparrow\Downarrow\Uparrow_x\rangle$ and $|\Downarrow_x\rangle \rightarrow |\Downarrow\Uparrow\Downarrow_x\rangle$ are energy detuned from the laser, the trion is not populated and therefore the spin stays in its $|\Downarrow_x\rangle$ state until a spin flip transfers it back onto states $|\Uparrow_x\rangle$ at rate $\frac{1}{T_1^h}$. Therefore, by continuously pumping one of the optical transitions, the spin is eventually initialized in the other spin eigenstate with near unity efficiency [32]. This was first demonstrated using the electron spin by *Xu et al.* (2007) (Gammon's group).

The electron spin initialization has also been demonstrated, with near-unity fidelity, under longitudinal magnetic field by *Atature et al.* (2006) [15] (Imamoglu's group). A laser resonantly excites the trion transition with circular polarization, so that only one spin state is optically active; in Fig. 1.8 (b), the $|\Downarrow_z\rangle \rightarrow |\Downarrow\Uparrow\Downarrow_z\rangle$ trion transition is excited with a circularly-left polarized pump. The pumping scheme is based on the forbidden diagonal transition that populates the other spin state $|\Uparrow_z\rangle$, with spontaneous emission rate γ much smaller than the normal decay transition Γ . This transition should be forbidden in the case of a pure heavy-hole trion state but is authorized due to the slight light hole-heavy hole mixing. Even though the spontaneous emission rate in the forbidden transition is much smaller than in the normal decay transition ($\gamma \ll \Gamma$), by constantly exciting the trion transition, the trion eventually decays into the $|\Uparrow_z\rangle$ state. When the state $|\Uparrow_z\rangle$ is populated, because of its polarization, the laser pump cannot generate a trion anymore and thus the spin should stay initialized in $|\Uparrow_z\rangle$. However, due to the hyperfine interaction, it will eventually experience spin flips with a rate $1/T_1^e$. This spin flip rate should be smaller than the forbidden transition spontaneous decay rate so that spin initialization can be achieved. This is only possible by reducing the spin-flip rate by applying a longitudinal magnetic field above $200mT$: the initialization of an electron spin without any applied external magnetic field is not possible.

Finally, a similar scheme has been used for the initialization of a hole spin in *Gerardot et al.* (2008) [16] (Warburton's group), providing efficient hole spin initialization in the absence of magnetic field. In the case of a hole spin, one spin state (in Fig. 1.8 (c), it is the $|\Downarrow_z\rangle$ state) is resonantly excited with circular polarization. The excited trion state has an electron spin and thus, is much more sensitive to spin flips than the ground hole state. If this trion state experiences a spin flip, it decays into the opposite spin state ($|\Uparrow_z\rangle$ in Fig. 1.8 (c)). Because the hole spin flips are much less probable than the trion spin flips, 99% hole spin initialization have been reported without external magnetic field. This scheme also works with an applied longitudinal magnetic field.

1.3.2 Spin measurement.

To use a spin as a qubit, we must be able to read out its state. A quantum dot spin state can be optically measured with different techniques that are all based on the trion optical selection rules, in different magnetic field configurations.

The trion spontaneous emission carries information about the spin state in its polarization, and if an external magnetic field is applied, in its photon energy. Consequently by measuring the emitted photon either in polarization or in energy, it is possible to read out the spin state. Measurement of a single spin based on the resonance fluorescence of a trion has been demonstrated for an electron [106] and a hole [18] spin confined in a quantum dot. It is also possible to measure the spin state by observing a transmission difference induced by an electron [107] or a hole spin [16, 108]. To illustrate this, let us consider the optical selection rules in Voigt configuration, presented in Fig. 1.4(f), and consider that we want to measure the hole spin state. If a laser resonantly excites the trion transition

$|\uparrow\downarrow_x\rangle \rightarrow |\uparrow\downarrow\uparrow_x\rangle$, and that a vertically-polarized photon is detected with energy corresponding to the $|\downarrow\downarrow_x\rangle \rightarrow |\uparrow\downarrow\uparrow_x\rangle$ transition, it means that the spin state was in $|\uparrow_x\rangle$ before the measurement (otherwise the trion state $|\uparrow\downarrow\uparrow_x\rangle$ could not have been populated and could not lead to the emission of such photon). However, with this method, the spin state is destroyed by the measurement because, after the measurement, the spin state is in $|\downarrow_x\rangle$ that is different from the one indicated by the outcome of the measurement ($|\uparrow_x\rangle$).

To use the spin as a quantum memory, it is interesting to find a way to measure the state non destructively, so that the spin state directly after the measurement is exactly the same as indicated by the outcome of the measurement. Such measurement is called a Quantum Non Demolition (QND) measurement [109, 110, 111] and can be experimentally achieved using the spin-dependent polarization rotation induced by a single spin. Pioneer works have demonstrated the rotation of polarization induced by a single spin both in transmission [23] and in reflection [22].

The rotation of polarization induced by the light reflection or transmission onto a magnetic material has been first observed by Kerr and Faraday. Such effect has been observed with large ensembles of spins, such as ferromagnets. However, a single spin can also induce rotation of polarization, though its effect has a much smaller amplitude. Enhancing the spin-dependent polarization rotation and using it to non-destructively measure a single spin is a central part of the work presented in this manuscript, and more specifically in Chap. 5. In the following, we will explain qualitatively the rotation of polarization induced by a single spin and show in details the experiments that have observed such polarization rotation.

Principle of spin-dependent polarization rotation.

The spin-dependent polarization rotation is called Faraday rotation in transmission and Kerr rotation in reflection. The underlying phenomenon is similar in both cases. Due to the optical selection rules in Faraday configuration, presented in Sec. 1.1.2, each spin state is optically active with only one circular polarization. Let us consider that the spin is prepared in its $|\uparrow_z\rangle$ state. An incident laser with linear polarization, assumed to be horizontal, is sent onto a charged quantum dot. This linear polarization is a superposition of the two circular polarizations so that $|H\rangle = \frac{1}{\sqrt{2}}(|R\rangle + |L\rangle)$. Because the spin is prepared in the $|\uparrow_z\rangle$ state, only the left-handed circular polarization is interacting with the quantum dot. The left polarization is experiencing a dephasing $\varphi_{L\uparrow}$, after being transmitted or reflected by the quantum dot, as shown in Fig. 1.9. Now, because the quantum dot is transparent for the right polarization, after being reflected or transmitted, the light experiences another dephasing $\varphi_{R\uparrow}$, that is in general different from $\varphi_{L\uparrow}$. Hence, when the spin is prepared in the $|\uparrow_z\rangle$, the transmitted (or reflected) polarization $|\Psi_{\uparrow}\rangle = \frac{1}{\sqrt{2}}(e^{i\varphi_{R\uparrow}}|R\rangle + e^{i\varphi_{L\uparrow}}|L\rangle)$ is different from its incident horizontal polarization. The light has experienced a $\theta_{\uparrow} = (\varphi_{L\uparrow} - \varphi_{R\uparrow})/2$ rotation of polarization induced by the quantum dot, as illustrated in Fig. 1.9.

If the spin is in the other state $|\downarrow_z\rangle$, the role of the circular polarization is now reversed: the quantum dot is interacting with the circular-right polarization and transparent with the circular-left polarization. Therefore the rotation of polarization is occurring in the other direction: $\varphi_{L\uparrow} = \varphi_{R\downarrow}$ and $\varphi_{R\uparrow} = \varphi_{L\downarrow}$, and thus $\theta_{\downarrow} = -\theta_{\uparrow}$. Consequently, depending on the spin state, the light polarization is rotated in opposite directions.

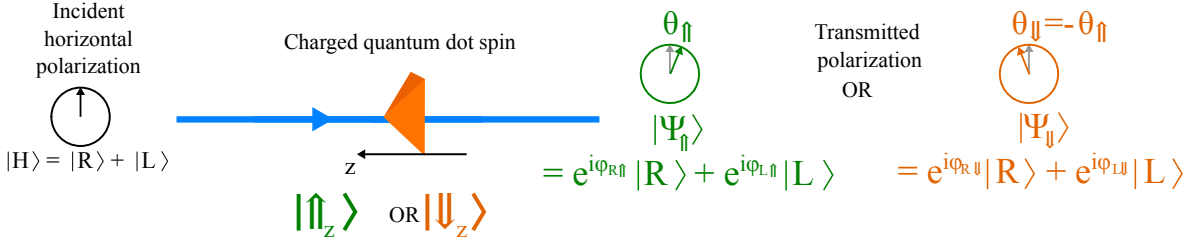


Figure 1.9: Schematic of Faraday rotation. The incident linear polarization is rotated after the interaction with the charged quantum dot. The polarization rotation depends on the spin state of the charge trapped in the quantum dot.

Experimental demonstration of single-spin-induced Faraday and Kerr rotations.

The experimental demonstration of the Faraday or Kerr rotation induced by a single spin is challenging experimentally because the rotation angle is expected to be very small. The first demonstrations were therefore obtained on spin ensembles (this effect is indeed at the core of the spin noise spectroscopy technique presented in Sec. 1.2.4). The first measurements of single-spin-induced polarization rotation were achieved by *Berezovsky et al. (2006)* (Awschalom's group) for Kerr rotation and *Atature et al. (2007)* (Imamoglu's group) for Faraday rotation.

For the Faraday rotation demonstration, the spin-dependent polarization rotation has been demonstrated for a quantum dot embedded in a Schottky structure. The transmitted light has been analyzed in polarization through a polarizing beam splitter and two photodiodes, as shown in the scheme in the top panel of Fig. 1.10(a). The difference in intensity in the two photodiodes, observed in Fig. 1.10(b), has a dispersive shape, expected for spin-induced Faraday polarization rotation. This difference in signal intensity between the two detectors is converted into a rotation angle that reaches $15\mu\text{rad}$ for the proper laser-quantum dot detuning.

For the Kerr rotation demonstration, the sample used is a quantum dot coupled to a planar cavity with $Q = 120$ quality factor (see Fig. 1.10(c)). In such sample, the Kerr rotation reaches $100\mu\text{rad}$. Though very interesting, the rotation angle is still limited and we will see later (in Sec. 1.6) how it can be amplified using pillar micro-cavities.

1.3.3 Spin coherent control.

To be able to perform quantum processing with quantum dot spins, it is necessary to perform any single qubit coherent operation within the spin coherence time. Such coherent control can be performed using energy levels in a Λ -configuration, as is represented in Fig. 1.11 (a) and as is experimentally achievable using one of the excited trion states under Voigt magnetic field. In this case, the magnetic field is considered along the x-axis with intensity B_x and the eigenstates of the charge spin are also along this axis: $|\uparrow_x\rangle$ and $|\downarrow_x\rangle$. Any spin state can be represented in the Bloch sphere as represented in Fig. 1.11 (b), where all pure quantum superpositions of spin states are represented by a vector reaching the sphere surface. The spin state needs to be coherently manipulated, which means that the spin vector needs to be rotated to any position in the Bloch sphere surface. To perform such coherent control it is sufficient to be able to realize a rotation R_z along the z-axis of the Bloch sphere (see Fig. 1.11 (b)) and a rotation R_x along the x-axis of the Bloch sphere (see Fig. 1.11 (c)). The experimental implementation of these rotations is detailed now.

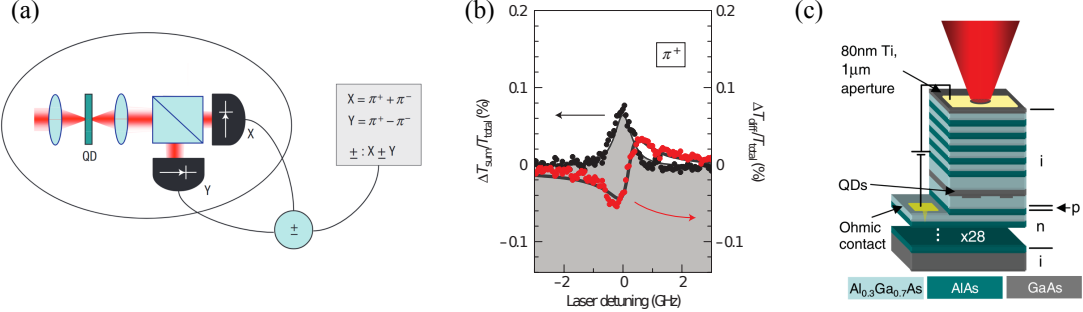


Figure 1.10: (a,b) From Ref. [23] (Imamoglu's group). (a) Experimental setup where the incident laser is focused onto a single charged quantum dot. The transmitted light is analyzed in polarization to measure the Faraday rotation. (b) Differential transmission of a single-electron-charged quantum dot using a linearly-polarized laser probe. The black points represent the sum of the two detector signals, proportional to the absorptive response, while the red points represent the difference of the two detector signals, proportional to the dispersive response, evidencing the polarization rotation. (c) From Ref. [22] (Awschalom's group). Schematic of the quantum dot coupled to a cavity.

Rotation around the z-axis: It is possible to implement a relative phase shift between the spin state $|\uparrow_z\rangle$ and $|\downarrow_z\rangle$ thanks to an optical pulse. The spin can, for example, be prepared in the $|\downarrow_x\rangle$ state (using the initialization technique presented previously) that can be rewritten in the z-axis basis: $|\downarrow_x\rangle = \frac{1}{\sqrt{2}}(|\uparrow_z\rangle - |\downarrow_z\rangle)$. A short laser pulse (a few picoseconds), circularly-polarized and detuned from the trion transitions, induces a phase shift Φ between the states $|\uparrow_z\rangle$ and $|\downarrow_z\rangle$, such that after the pulse, the spin state is $\frac{1}{\sqrt{2}}(|\uparrow_z\rangle - e^{i\Phi}|\downarrow_z\rangle)$. This results in a rotation R_z of the spin state around the z-axis in the Bloch sphere. The short pulse allows for the fast manipulation of the spin state well below its coherence time. By varying the power of the laser, the angle of the rotation R_z is varied as can be seen in Fig. 1.11 (d), which describes the experimental result of *De Greve et al. (2011)* [18] (Yamamoto's group). In this work, the state is first prepared optically in the $|\downarrow_x\rangle$ eigenstate. A short, detuned, circularly-polarized laser pulse with given incoming power realizes the R_z rotation. The spin state is then read out in the x-axis spin projection basis, and the population in the $|\uparrow_x\rangle$ state is represented (in a. u.) as a function of the rotation laser power. The population can be completely reversed for a given pulsed laser power, the so-called π -pulse (which indeed corresponds to a $\Phi = \pi$ phase shift, as $|\uparrow_x\rangle = \frac{1}{\sqrt{2}}(|\uparrow_z\rangle + |\downarrow_z\rangle) = \frac{1}{\sqrt{2}}(|\uparrow_z\rangle - e^{i\pi}|\downarrow_z\rangle)$). It clearly exhibits oscillations that shows that the R_z rotation angle can be controlled, via the applied phase shift $e^{i\phi}$, by the laser power.

Rotation around the x-axis: Thanks to the transverse magnetic field, an R_x rotation is induced by the difference in energy for the two spin eigenstates, $|\uparrow_x\rangle$ and $|\downarrow_x\rangle$. Indeed, the time evolution of a given spin state $|\psi(0)\rangle = \alpha|\uparrow_x\rangle + \beta|\downarrow_x\rangle$ is $|\psi(t)\rangle = \alpha e^{-i\hbar\omega_{\uparrow_x}t}|\uparrow_x\rangle + \beta e^{-i\hbar\omega_{\downarrow_x}t}|\downarrow_x\rangle$. Because the energies of the charge spin eigenstates ω_{\uparrow_x} and ω_{\downarrow_x} are different, the energy splitting induces a Larmor precession of the spin qubit around the magnetic field direction, with a Larmor angular frequency $\Omega_L = \omega_{\uparrow_x} - \omega_{\downarrow_x}$ corresponding to the Zeeman splitting between the two eigenstates.

Fig. 1.11(e) shows such R_x rotation, as observed by *De Greve et al. (2011)*. The state is first initialized and then prepared (using a first $\pi/2$ -pulse for R_z rotation) in a coherent superposition of $|\uparrow_x\rangle$ and $|\downarrow_x\rangle$. It then precesses around the x-axis around the Bloch sphere. A second laser pulse

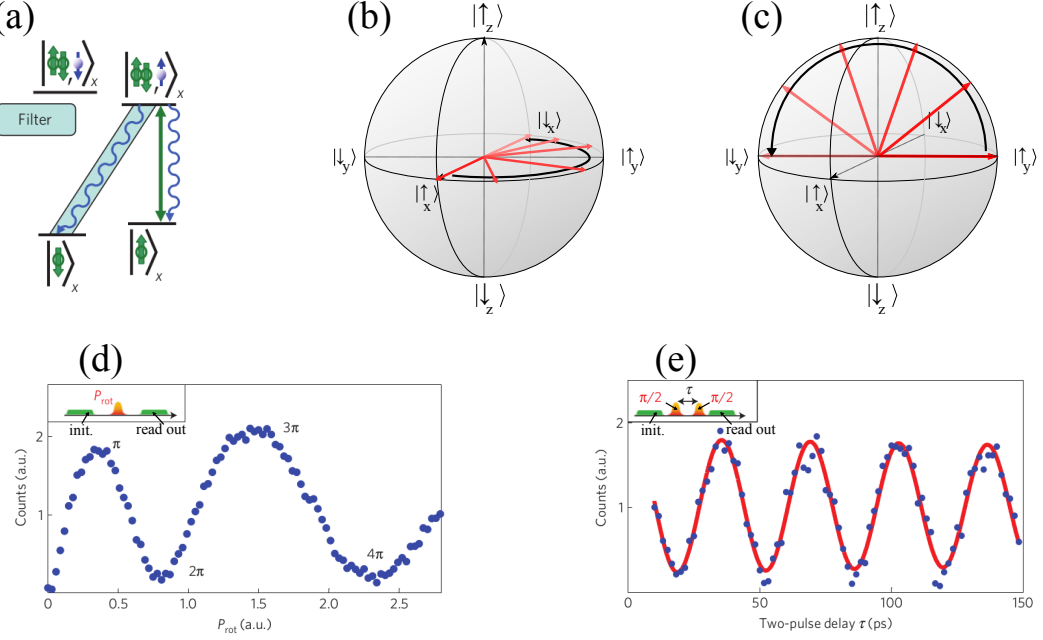


Figure 1.11: From Ref. [18] (Yamamoto’s group): coherent control of a spin state. (a) Sketch of the optical manipulation scheme. The resonant pump laser (green arrow) is used to initialized and read out the spin state. A filter is used to spectrally filter out the laser from the trion transition $|\uparrow\downarrow\uparrow_x\rangle \rightarrow |\downarrow_x\rangle$, which allows measuring the spin state. (b) Schematic of the R_z rotation induced by the pulsed laser. (c) Schematic of the R_x rotation induced by the magnetic field spin precession (Ramsey oscillations). (d) Rabi oscillations between the two spin states as a function of the power of the driving laser. (e) Ramsey oscillations induced by the Larmor spin precession along the transverse magnetic field. The driving laser induces a $\pi/2$ rotation pulse that set the spin in a quantum superposition of $|\uparrow\rangle$ and $|\downarrow\rangle$, which precesses around the external magnetic field ($B_x = 8\text{T}$) until the arrival of a second $\pi/2$ -pulse.

rotates again the spin by $\pi/2$ around the z-axis: if the spin is in $|\uparrow_y\rangle$ (respectively $|\downarrow_y\rangle$), it is then rotated in state $|\downarrow_x\rangle$ (respectively $|\uparrow_x\rangle$). The state is then read out in the x-axis spin projection basis: $|\uparrow_x\rangle$ and $|\downarrow_x\rangle$. Fig. 1.11(e) displays the population of the $|\uparrow_x\rangle$ spin state as a function of the waiting time between the two $\pi/2$ -pulses for a $B_x = 8\text{T}$ magnetic field. It shows that the rotation of the spin state along the x-axis is achieved within a few tens of picoseconds.

These two results show that the coherent control can be achieved in the tens of picoseconds timescale, much shorter than the spin coherence time.

1.3.4 Entangling the spin with an emitted photon.

The last crucial challenge to use a quantum dot spin in a quantum computer is the ability to entangle it with other qubits. Because spins are only interacting with their nearest neighbors, a first strategy is to put other qubits in their neighboring environment. As was discussed previously, a promising result lies in the interface of a quantum dot electron spin with its nuclear spin bath, that can be used as a quantum memory [105]. A second approach is to position quantum dots close one to another so that they can interact. This is the strategy followed by gate-defined quantum dots [9, 95]. For self-

assembled quantum dots, this can be achieved by growing a second quantum dot layer on top of the first one, such that two vertically-stacked quantum dots are interacting via coherent tunneling. The resulting system is called a quantum dot molecule [112, 108]. The main drawback of such quantum dot molecule is that the interaction between the quantum dots cannot be switched off.

A third approach, detailed below, lies in the use of the optical selection rules to create entanglement between the quantum dot spin and a single emitted photon. The interest of such platform is that it can be then used to produce entanglement between remote memory qubits or multi-partite photon entanglement. The spin-photon entanglement and its applications are discussed in the following.

Spin-photon entanglement.

The demonstration of the spin-photon entanglement relies on the optical selection rules of a quantum dot under Voigt external magnetic field, to entangle the quantum dot spin with the polarization and the energy of the emitted photon. The quantum dot is prepared in one of its ground spin state, say $|\uparrow\downarrow_x\rangle$, using the spin initialization technique discussed previously. Then a trion state, say $|\uparrow\downarrow\uparrow_x\rangle$, is populated using a resonant short π -pulse. As seen in Fig. 1.12 the trion spontaneously emits a photon to decay into the two spin ground states with equal probabilities. The emitted photon can be horizontally-polarized and have an energy $\hbar\omega_H$ corresponding to the $|\uparrow\downarrow\uparrow_x\rangle \rightarrow |\uparrow_x\rangle$ transition, leading to a spin in state $|\uparrow_x\rangle$ after the emission. It can also be vertically-polarized, with an energy ω_V corresponding to the $|\uparrow\downarrow\uparrow_x\rangle \rightarrow |\downarrow_x\rangle$ transition leading to a spin in state $|\downarrow_x\rangle$. The final state is therefore an entangled state of spin and photon: $|\Phi\rangle = \frac{1}{\sqrt{2}}(|\uparrow_x\rangle|H, \omega_H\rangle + |\downarrow_x\rangle|V, \omega_V\rangle)$. As can be seen in the expression of $|\Phi\rangle$, the information encoded on the photon qubit is redundant in energy and in polarization. Therefore, to demonstrate the entanglement, the redundant information should be erased either in polarization (for example with a diagonal polarizer) or in energy (for example with a frequency conversion setup).

Experimentally, such entanglement has been demonstrated by combined measurements of the spin state and the photon states in various groups by *Gao et al. (2012)*[20] (Imamoglu's group), *DeGreve et al. (2012)* [19, 113] (Yamamoto's group) and by *Schaibley et al. (2013)*[21] (Sham's group).

Photon-photon entanglement.

It is possible to go beyond the spin-photon entanglement to generate an entanglement between photons. To do so, the spin state is repeatedly pumped to emit spin-entangled photons. A proof of concept of this technique has been demonstrated by *Schwartz et al. (2016)* [36] (Gershoni's group), using a dark exciton spin. This state is similar to an electron or hole spin qubit that is precessing along a weak transverse magnetic field. The magnetic field is not strong enough to break the zero-magnetic-field optical selection rules, so that the ground states and excited states are connected by circularly polarized photons as in Fig. 1.4. By exciting the dark exciton with linearly-polarized light with a repetition rate synchronized to three quarters of the Larmor precession period, *Schwartz et al.* were able to polarization-entangle two photons with the dark exciton spin, thus generating a linear cluster state [114]. A cluster state is a multi-partite maximally entangled state which is resistant to qubit loss: if a photon is lost, the remaining photons are still maximally entangled.

These cluster states are a very important resource as they are at the core of proposals using measurement-based quantum computing and quantum communications protocols [115, 116, 117, 118]. In addition, two recent theoretical works propose the use of solid-state quantum emitters to

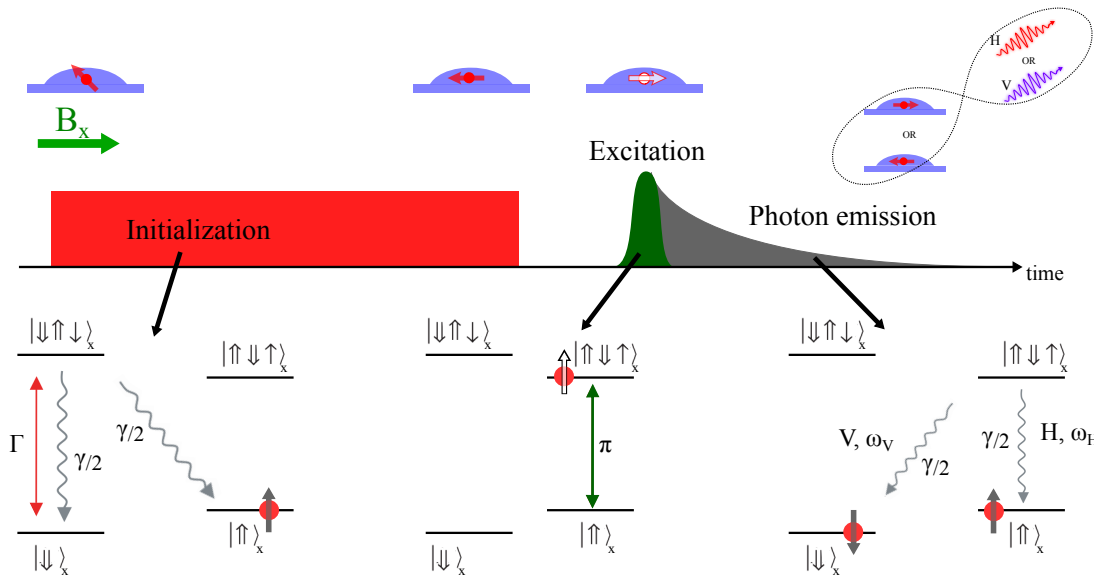


Figure 1.12: Protocol to entangle a quantum dot electron spin and an emitted photon in the presence of a transverse magnetic field B_x . First, a laser is used to initialize the spin in its eigenstate $|\uparrow_x\rangle$. A second laser resonantly excites a quantum dot transition $|\uparrow_x\rangle \rightarrow |\uparrow\downarrow\uparrow_x\rangle$. Then the trion decays into one of its eigenstate by emitting a photon. If the photon is horizontally-polarized (respectively vertically-polarized) with energy ω_H (resp. ω_V), the spin is in its $|\uparrow_x\rangle$ (resp. $|\downarrow_x\rangle$) state. The final state is entangled: $\Psi_{ent} = \frac{1}{\sqrt{2}} (|\uparrow_x\rangle|H, \omega_H\rangle + |\downarrow_x\rangle|V, \omega_V\rangle)$

produce a two-dimensional cluster state [119] (which is an array of maximally-entangled qubits) that are crucial for the realization of measurement-based universal quantum computing, and of all-photonic quantum repeaters [118, 120] for quantum communications.

Spin-spin entanglement.

Instead of using the spin-photon entanglement resource to produce photon-photon entanglement, it is possible to use it to generate spin-spin entanglement. The spin-photon entanglement discussed previously has been used to realize a heralded entanglement between two distant spins in *Delteil et al.* (2015)[34] (Imamoglu's group) and in *Stockill et al.* (2017) [35] (Atatüre's group), using the entanglement protocol detailed in *Cabrillo et al.* (1999)[121] (Zoller's group). The scheme used is based on the spin-photon entanglement presented in Fig. 1.12 and therefore requires a transverse magnetic field with spin eigenstates along the magnetic field x-axis. Two quantum dot spins are prepared in the down state, $|\Psi_{init}\rangle = |\downarrow_1, \downarrow_2\rangle_x$, and are both weakly excited, by a Ti-Sapphire pulsed laser, to emit a spin-entangled photon with small probability (see Fig. 1.13). If a photon is emitted by one quantum dot, it has 50% probability to convert the spin into the up state, depending on its energy or polarization. The emitted photon is passing through a beamsplitter, a polarizer and a spectral filter so that the which-path information of the photon is erased, and so that we do not know by which quantum dot a photon was emitted.

The state before photon measurement is then: $|\Psi_{int}\rangle = |\downarrow_1, \downarrow_2\rangle|0\rangle + \epsilon(|\uparrow_1, \downarrow_2\rangle + e^{i\theta}|\downarrow_1, \uparrow_2\rangle)|1\rangle$, where the emission of two photons, and thus the reversal of both QD spins, has been neglected because of the weak excitation. $|0\rangle$ and $|1\rangle$ denote the presence or the absence of a photon at the

photodiodes (see Fig. 1.13). The crucial point is that if a photon has been detected, the quantum dot spins are entangled: $|\Psi_{ent}\rangle = \frac{1}{\sqrt{2}}(|\uparrow\downarrow_1, \downarrow\uparrow_2\rangle + e^{i\theta}|\downarrow\downarrow_1, \uparrow\uparrow_2\rangle)$. This is due to the fact that it is impossible to know which quantum dot spin had generated the photon. With such protocol, the fidelity of the entangled state relies on the erasure of the which-path information of the photon and therefore on the ability of the two quantum dots to emit indistinguishable photons. This technique is also very sensitive to the non-zero probability that each quantum dot emits one photon at the same time, which limits its entanglement rate efficiency (the best entanglement rate measured so far is 7.3 kHz of spin-spin entanglements [35]).

1.3.5 Entanglement between a spin and a photon incoming from a distant source.

Previously, we have discussed techniques to generate spin-photon, photon-photon and spin-spin entanglement protocols that are based on the emission of a single photon by the quantum dot. So far, entanglement between a quantum dot spin and a single photon produced from another source has not been demonstrated.

Still, several theoretical works propose to generate entanglement between a pre-existing photon and a quantum dot spin [13, 122]. Some proposals are based on the Faraday or Kerr rotation [123, 124], where the reflected or transmitted photon polarization is rotated depending on the spin state. This technique can also be extended to generate a deterministic photon-photon gate (that works even for temporally distant photons), to entangle distant spins [125] or photons [126]. In order to generate spin-photon entanglement using Faraday (or Kerr) rotation, the spin needs to be prepared in a quantum superposition of $|\uparrow\rangle$ and $|\downarrow\rangle$. A single photon with horizontal polarization is transmitted (or reflected) with rotated polarization $|\Psi_\uparrow\rangle$ if the spin is $|\uparrow\rangle$ and $|\Psi_\downarrow\rangle$ if the spin is $|\downarrow\rangle$. The final state is therefore entangled: $|\Psi_{ent}\rangle = \frac{1}{\sqrt{2}}(|\uparrow\rangle|\Psi_\uparrow\rangle + |\downarrow\rangle|\Psi_\downarrow\rangle)$.

In order to obtain maximally entangled state, the transmitted (or reflected) photon polarizations need to be orthogonal: $\langle\Psi_\uparrow|\Psi_\downarrow\rangle = 0$. Yet, as was discussed previously, the Faraday rotation and the Kerr rotation induced by a single spin are very small, less than $100\mu\text{rad}$. In order to be useful for spin-photon entanglement protocols, the rotation needs to be significantly amplified. The use of solid-state microcavities to amplify the light-matter interaction and thus, the Faraday and Kerr rotation, is explored in the last section of this chapter.

1.4 Cavity-QED with quantum dots.

In the previous section, we have presented results concerning the optical manipulation of a quantum dot. These manipulations were carried out in an homogeneous electromagnetic environment (quantum dots in a bulk material) where the light-matter interaction is inefficient. In this section, we see how an engineered electromagnetic environment can enhance the light-matter interaction, using optical micro-cavities to confine the electromagnetic field in a smaller mode volume and for a longer time. The radiative properties of a quantum emitter positioned at the center of such cavity, are completely modified. The use of cavities can drastically enhance the quantum dot spontaneous emission rate [127], a phenomenon called the Purcell effect [128, 129]. More importantly, the acceleration can strongly favor the emission of photons in a single confined cavity mode, as opposed to randomly-oriented emission in the three directions of space.

This engineering of the light-matter interaction gave rise to a very active field of research called cavity-Quantum ElectroDynamics (cavity-QED). Among various applications, cavity-QED is crucial for quantum communications and the implementation of a solid-state quantum network [3]. Indeed,

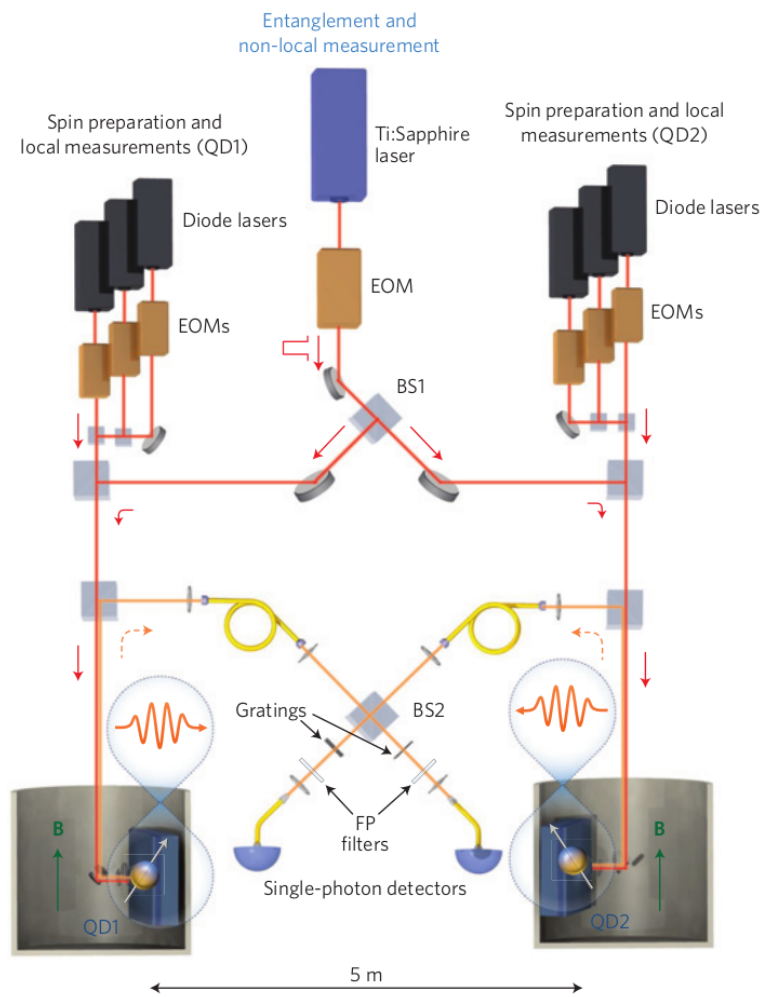


Figure 1.13: From Ref. [34] (Imamoglu's group): experimental setup used to demonstrate spin-spin entanglement. Two quantum dots in Voigt geometry are positioned in two cryostats. The quantum dots are resonantly excited by a Ti:Sapphire laser to create single photons that are passing through a beam splitter and are detected by two photodiodes.

such a quantum network requires an interface between quantum nodes and quantum channels. The quantum nodes are stationary qubits (such as quantum dot spins), which are used as quantum memories or as computational nodes, while flying qubits (such as photons) coherently transmit the quantum information from one node to another.

In this section, we first present the main optical micro-cavities that have been used with quantum dots, with a particular focus on pillar microcavities that are used in this work. Then, we show how a quantum dot can be deterministically coupled to a cavity. Finally, we show how a cavity modifies the quantum emitter properties and allows developing an efficient spin-photon interface: a cavity-QED system that can efficiently couple a spin qubit and a photonic qubit.

1.4.1 Optical micro-cavities.

In the context of light-matter interaction, optical microcavities [130] have been introduced to control and enhance the interaction with an emitter. The two figures of merit that quantify this are the mode volume (generally expressed in units of $(\lambda/n)^3$ where λ is the electromagnetic field wavelength and n is the material refractive index) and the quality factor Q (defined as $Q = \omega_c/\kappa$ where ω_c is the cavity mode angular frequency and κ is the rate at which photons escape the cavity). The quality factor is linked to the mean photon lifetime inside the cavity ($Q = \omega_c T_{photon}$).

Historically, three main types of microcavities have been proposed to interface photons with a quantum dot:

- Photonic crystal cavities [131, 132, 133, 134] are constituted of an intentional defect in the periodic structure of a photonic crystal. This defect confines the electromagnetic field in a small mode volume (typically of the order of $(\lambda/n)^3$) in a cavity with potentially very high quality factor ($Q = 10^5 - 10^6$).
- Microdisks [135, 136, 137] are constituted of a thin semiconductor disk suspended on a small post. The structure confines the electromagnetic field in an optical mode called a whispering-gallery mode. High quality factors (above 10^5) have been achieved as well as mode volumes typically around $8(\lambda/n)^3$.
- Micropillars [138, 139] will be presented in more details later. They present quality factors that can reach 10^5 [140, 141] and mode volumes around $16(\lambda/n)^3$.

An interesting feature of these pillar microcavities is that they can easily be coupled to an external electromagnetic field. Consequently, they constitute an excellent platform to efficiently interface light and matter, which have been widely used for different applications such as VCSELs [142], cavity polaritons [143, 144] or photon-phonon interfaces [145, 146]. In the following, we show how pillar microcavities confine the electromagnetic field, starting from distributed Bragg reflectors.

Distributed Bragg Reflectors.

Distributed Bragg Reflectors (DBR) are alternated stackings of layers of two different semiconductors with respective refractive indexes n_1 and n_2 (Fig. 1.14(a)). It is possible to engineer a DBR structure to obtain maximum reflection at the wavelength λ_{DBR} . The condition to fulfill is: $\lambda_{DBR}/4 = e_1 n_1 = e_2 n_2$, where e_1 and e_2 are the respective layer widths of each semiconductor material. Indeed, each layer induces a phase shift on the electromagnetic field that can be either reflected or transmitted at each layer interface. It can be shown that the phase shift induced by each layer leads

to a destructive interference for the transmitted component and to a constructive interference for the reflected components. This leads to a high DBR reflectivity at wavelength λ_{DBR} . The electromagnetic field is also completely reflected for a large spectral band around λ_{DBR} , whose width depends on the difference of refractive index ($\Delta\lambda = 4\frac{\lambda_{DBR}}{\pi}\frac{|n_1-n_2|}{n_1+n_2}$). The simulated reflectivity of a DBR as a function of the photon wavelength is displayed in Fig. 1.14(b). The DBR spectral forbidden band $\Delta\lambda$ is clearly evidenced.

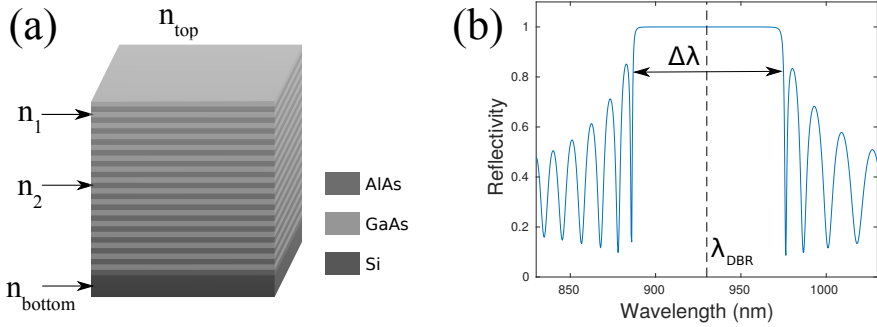


Figure 1.14: (a) Distributed Bragg Reflectors made of GaAs/AlAs layer pairs. (b) Simulated DBR reflectivity constituted of 50 layer pairs of GaAs/AlAs centered at $\lambda_{DBR} = 930\text{nm}$.

Planar Cavity.

By adding a "cavity" layer with thickness λ_{DBR}/n , in between two DBRs, as illustrated in Fig. 1.15(a), the electromagnetic field can be confined vertically in this layer as observed in Fig. 1.15(b). In this figure, the electric field intensity is plotted as a function of the position in the planar structure. We observe that the electromagnetic field is confined vertically inside the structure with maximum intensity at the center of the cavity layer, as can be seen in the zoom in the cavity layer. This is expected for an electromagnetic field wavelength corresponding to the layer thickness as the structure acts as a Fabry-Perot cavity, thus confining the field in the vertical direction. The consequence in the optical response is the apparition of a reflectivity dip inside the photonic crystal forbidden band at the wavelength λ_{DBR} , as displayed in Fig. 1.15(c). This Fabry-Perot cavity is also called a "planar" cavity because the electromagnetic field is confined vertically in all the λ_{DBR}/n cavity layer, but is not confined in the two transverse directions. Fig. 1.15(d) displays a zoom in the reflectivity spectrum, plotted as a function of the detuning between the laser angular frequency, ω , and the cavity mode angular frequency ω_c . The reflectivity dip presents a Lorentzian shape whose width is given by the cavity damping rate κ_{planar} , which corresponds to the rate at which the intracavity photons escape the cavity (Fig. 1.15(d)). The more layer pairs in the DBRs, the higher the quality factor and therefore the thinner the cavity mode linewidth.

Pillar microcavity.

With a planar cavity, the electromagnetic field is confined vertically, but not in the lateral directions. Higher confinement can be obtained by constraining the electromagnetic field in the three dimensions and therefore, by laterally confining the electromagnetic field. This can be achieved by reducing the cavity lateral dimensions to obtain a pillar microcavity whose diameter is sufficiently small so that a discrete cavity mode appears. Indeed, due to the difference of refractive index between the pillar

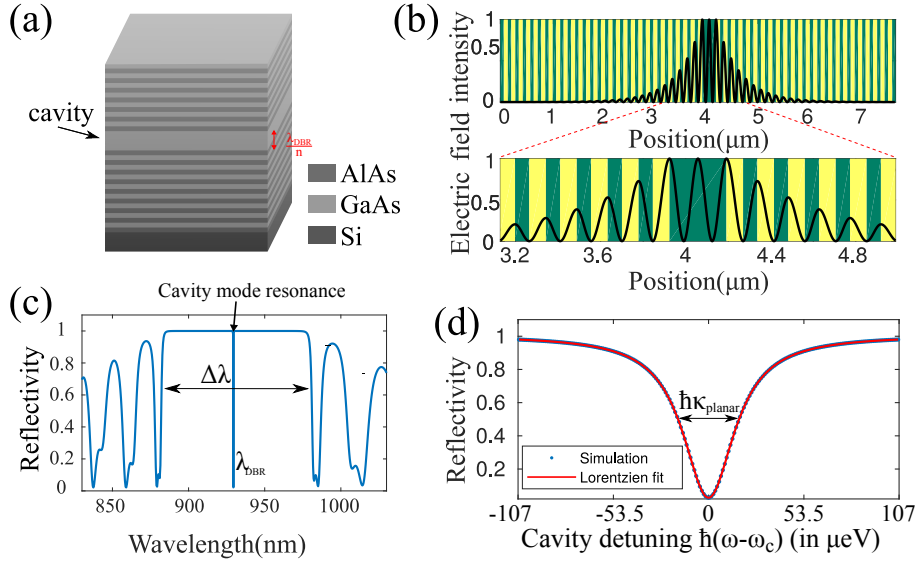


Figure 1.15: (a) Planar cavity: inside the DBR structure, a *GaAs* layer of thickness λ/n_{GaAs} is positioned. This layer confines the electromagnetic field in the vertical direction. (b) Simulated electric field intensity inside the planar cavity structure. The electric field is confined at the cavity layer position. The bottom plot is a zoom in the cavity region (in green the *GaAs* layers, in yellow the *AlAs* layers). (c) Simulated reflectivity of a planar cavity with 23 (resp. 27) pairs of *GaAs/AlAs* at the top (resp. bottom) of a λ/n_{GaAs} thick layer of *GaAs*. The cavity results in a reflectivity dip inside the DBR stop band. (d) Zoom on the reflectivity dip, as a function of the cavity detuning, fitted with a Lorentzian curve.

and vacuum, the electromagnetic field is now also confined laterally, as in an optical fiber. Such confined mode can be obtained with a pillar microcavity whose diameter is typically a few μm . The smaller the pillar radius, the smaller the mode volume so the higher the confinement. However, due to the surface roughness, a smaller radius also involves more optical losses from the pillar sides and therefore a smaller quality factor. Therefore, an optimization must be found to maximize both the quality factor and the confinement.

In the overall, the damping rate for a pillar microcavity is given by:

$$\kappa = \kappa_{top} + \kappa_{bottom} + \kappa_{loss} \quad (1.10)$$

with κ_{top} , κ_{bottom} the damping rates from the top and bottom of the pillar microcavity, and κ_{loss} the damping rate associated both with lateral optical losses and photon absorption.

Another crucial quantity for this manuscript is the top mirror output coupling defined by:

$$\eta_{top} = \frac{\kappa_{top}}{\kappa} \quad (1.11)$$

It is the probability that an intracavity photon escapes from the top mirror. If the top mirror output coupling tends to 1, the photons confined in the cavity mode are always extracted from the top mirror.

1.4.2 Deterministic cavity-quantum dot coupling.

In order to maximally enhance the light-matter interaction, the quantum dot must be positioned at the center of the pillar microcavity where the confined electromagnetic field is the most intense. In this respect, the fabrication process of quantum dots constitutes another challenge: the Stranski-Krastanov method produces quantum dots at random positions and with random emission energies. It is therefore challenging to deterministically insert and couple quantum dots to a cavity. To overcome this challenge, complex growth techniques have been developed to control the quantum dot spatial position. Site-controlled quantum dots have already been positioned in cavities and waveguides [147, 148] but their optical properties are still limited as compared to self-assembled quantum dots [149]. Another strategy, pioneered in Pascale Senellart's group since 2008, lies in the deterministic spatial and spectral positioning of the cavity to maximally couple it to a single self-assembled quantum dot. The idea is to identify the position of a quantum dot in a planar cavity and deterministically etch a micropillar around it, with the cavity mode matching the emission energy. This approach, called in-situ lithography, is presented in detail below.

Growth: The first fabrication step is the growth of a planar cavity sample which consists of a λ – GaAs cavity embedding a low density layer of *InGaAs* quantum dots and surrounded by 2 distributed Bragg reflectors (DBRs) (*GaAs* and $Al_{0.9}Ga_{0.1}As$, with typically 30 and 20 pairs for the bottom and top mirrors). The growth is performed by Aristide Lemaître, using Molecular Beam Epitaxy (MBE), a technique that allows the epitaxial growth of atomically-thin layers and semiconductor heterostructures.

In-situ lithography: The second fabrication step is the low temperature in-situ lithography. This is performed by Niccolo Somaschi and Abdelmounaim Harouri using the technique developed in the team in 2008 [24] and improved in 2014 [37] (see Fig. 1.16(a)). The planar cavity sample is spin-coated with a positive photoresist layer (see Fig. 1.16(b)). It is placed on a 3-axis piezo controller inside a cryostat at low temperature (typically 8K) and a red laser (750 to 850nm) is focused on the sample surface, with a microscope objective, to non-resonantly excite the single quantum dots located at the laser spot position. The photoluminescence is then analyzed with a spectrometer, allowing to select a quantum dot with good optical properties. The focused gaussian laser is positioned at the exact location of the selected quantum dot by maximizing the QD photoluminescence intensity. A pillar must be etched at the position of maximum photoluminescence intensity: to do so, a green laser is then used to expose the photoresist that is used to design the pillar micro-cavity shape. The two laser optical beams must be optimally superposed and focused on the exact same spot on the sample surface, in order to expose the photoresist exactly on top of the quantum dot. With this technique, quantum dots are deterministically positioned at the pillar center with typically 50nm accuracy.

In addition to spatial matching, this in-situ lithography step can be used at the same time for spectral matching: this is obtained by adjusting the cavity mode energy thanks to its dependence on the pillar radius [24]. The laser exposure time is used to adjust the pillar radius and therefore the cavity mode energy, with a typical uncertainty of $\approx 0.65\text{meV}$ [24].

Etching: The final fabrication step is the etching process realized by Isabelle Sagnes. The areas of the positive photoresist that have been exposed are dissolved, leaving holes in the photoresist at the desired location (see Fig. 1.16(c) i.). A layer of Ni is deposited onto the whole structure (see Fig. 1.16(c) ii.). The remaining photoresist is lifted-off: the Ni layer remains only on the area

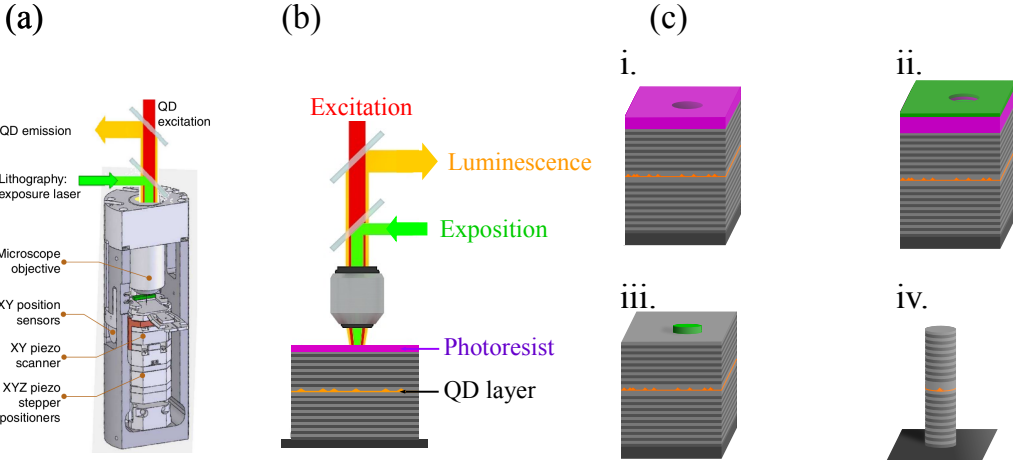


Figure 1.16: (a) From [37]: Setup of in-situ lithography. (b) A planar cavity with a quantum dot layer and a photoresist is scanned laterally by a non-resonant laser. Quantum dots positions and emission energies are analyzed through photoluminescence. When a suitable quantum dot is found, a green laser exposes the photoresist layer with a 50-nm accuracy on top of the targeted quantum dot. This photoresist will be later used for chloride reactive ion etching. (c) Etching process. i. Development of the photoresist layer previously exposed by in-situ lithography. ii. Deposition of Ni layer. iii. Lift-off of the residual photoresist. iv. Etching of the pillar.

previously exposed to the green laser (see Fig. 1.16(c) iii.). This layer acts as a shield preventing the protected area to be removed during the final etching. The dry etching technique performed is chloride reactive ion etching (see Fig. 1.16(c) iv.). After this final step, the resulting sample is composed of deterministically-coupled single quantum dot-pillar micro-cavities.

Improved design: electrically-contacted cavities. In 2014, a new structure was implemented around the micropillar to electrically-contact the cavity-QED device. In this respect, as presented in Fig. 1.17(a), the bottom mirror has a gradual n-doping profile while the top mirror has a p-doping profile, allowing the structure to be electrically-contacted. As shown in Fig. 1.17(b) and (c), each micropillar is connected to a large diode gold surface thanks to four ridges and a circular frame. The electrical contact allows the fine tuning of the quantum dot transitions through the confined Stark effect. This transition fine-tuning operates typically on a range of $\approx 1.4\text{meV}$ [37] which generally compensates the uncertainty on the cavity mode energy. In addition, it stabilizes the electric environment of the quantum dot (as seen in Fig. 1.17(a)) and therefore, reduces the energy fluctuations of a quantum dot transition.

Consequently, the in-situ lithography technique allows the creation of deterministically-coupled quantum dot-pillar devices, both in position and in energy. In Chapter 4, we will show how this technique can be improved to deterministically identify and couple the desired QD charge state. In the following, we study the optical properties of coupled quantum dot-cavity devices.

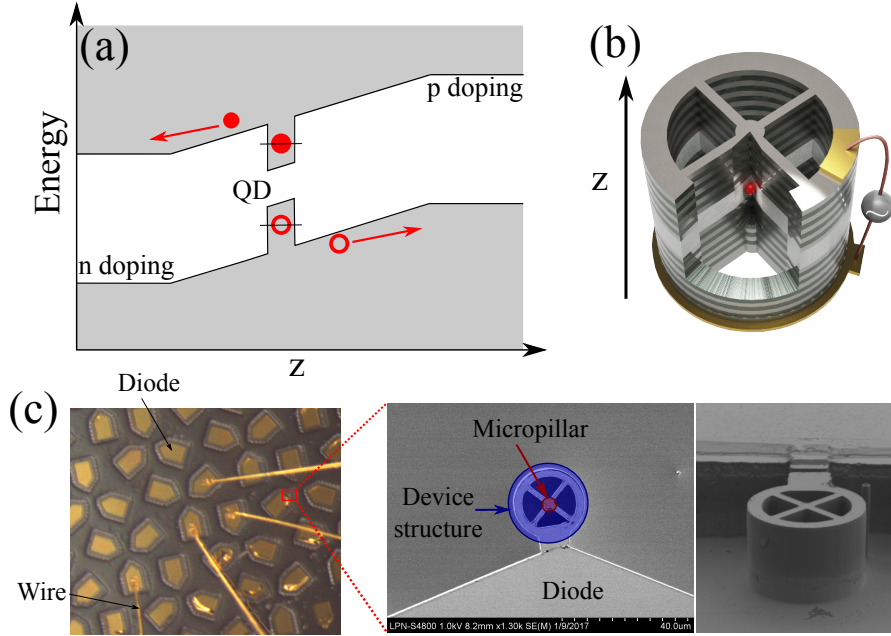


Figure 1.17: (a) Cavity structure. The n-doping and p-doping region tilt the forbidden band so that fluctuating charges remains far from the quantum dot, which stabilizes the electrical fluctuations. (b) Sample scheme. (c) Sample picture. Left panel: $100\mu m$ wide diodes covered with gold surface are electrically-contacted thanks to wires. Middle and right panel: a quantum dot-pillar device (red circle) is connected to an electrically-contacted diode thanks to four ridges and a circular frame (blue circle).

1.4.3 Quantum emitter coupled to a cavity.

The use of cavities strongly modifies the emission properties of a quantum dot because it favors the quantum dot interaction with the confined electromagnetic mode of the cavity. The ideal interaction of a two-level quantum emitter with a single perfectly confined cavity mode is well described by the Jaynes-Cummings Hamiltonian. In reality, a cavity mode is never perfectly confined and a quantum emitter is never interacting only with one single electromagnetic field, so that a more accurate description needs to go beyond the Jaynes-Cummings Hamiltonian approach.

Jaynes-Cummings Hamiltonian.

The Jaynes-Cummings Hamiltonian describes the interaction of a single quantum emitter, described as a two-level system, with a single electromagnetic mode. It is decomposed in three parts: the cavity hamiltonian H_c , the quantum emitter hamiltonian H_{QD} and the light-matter interaction hamiltonian H_{int} :

$$H_{JC} = H_c + H_{QD} + H_{int} \quad (1.12)$$

The cavity hamiltonian is:

$$H_c = \hbar\omega_c \hat{a}^\dagger \hat{a} \quad (1.13)$$

where $\hbar\omega_c$ is the confined electromagnetic mode energy, \hat{a}^\dagger and \hat{a} are the operators describing the creation and annihilation of photons inside the cavity, and the vacuum energy has been taken as the

reference energy. $\hat{a}^\dagger \hat{a}$ correspond to the intracavity photon number operator, so the eigenstates of the cavity hamiltonian are the Fock states $|0\rangle, |1\rangle, \dots, |n\rangle$ of intra-cavity photons.

The quantum dot is described by a two level system with a fundamental state $|g\rangle$ and an excited state $|e\rangle$. The fundamental state is taken as the reference energy, so that the quantum dot is described by:

$$H_{QD} = \hbar\omega_{QD} |e\rangle\langle e| \quad (1.14)$$

where $\hbar\omega_{QD}$ is the energy difference between the ground and excited states.

In addition, the cavity and the quantum dot are interacting via [150, 151]:

$$H_{int} = \hbar g (\hat{\sigma}^- \hat{a}^\dagger - \hat{\sigma}^+ \hat{a}) \quad (1.15)$$

where $\hbar g$ is the light-matter coupling constant of the system, $\hat{\sigma}^+ = |e\rangle\langle g|$, and $\hat{\sigma}^- = |g\rangle\langle e|$.

The total hamiltonian H_{JC} can be diagonalized with eigenenergies:

$$E_{\pm,n} = \hbar \left(n\omega_c - \frac{\omega_c - \omega_d}{2} \pm \sqrt{ng^2 + (\omega_c - \omega_d)^2} \right) \quad (1.16)$$

where n is the number of excitations of the system. When $\omega_c = \omega_d = \omega$, the total eigenenergies are:

$$E_{\pm,n} = \hbar \left(n\omega \pm \sqrt{ng^2} \right) \quad (1.17)$$

which are different from the eigenenergies of the cavity or the quantum dot alone. In all this thesis, we will work with $\hbar = 1$ units, so that we equally use pulsations and energies. The expressions of the eigenenergies mean that the system eigenstates are mixed light-matter states, the so-called polaritons that are quasi-particles of light and exciton. For example, the eigenstates associated to $E_{-,1}$ and $E_{+,1}$ are:

$$\begin{aligned} |\Psi_+\rangle &= \frac{1}{\sqrt{2}} (|0,e\rangle + |1,g\rangle) \\ |\Psi_-\rangle &= \frac{1}{\sqrt{2}} (|0,e\rangle - |1,g\rangle) \end{aligned} \quad (1.18)$$

where $|0,e\rangle$ corresponds to zero intracavity photon and the quantum dot in its excited state while $|1,g\rangle$ corresponds to a quantum dot in its ground state and one intracavity photon.

Fig. 1.18(a) represents the Jaynes-Cumming ladder, which is the typical energy distribution of the eigenstates for the Jaynes-Cumming hamiltonian. If the system is prepared in an initial state corresponding to a vacuum state for the cavity and an excited state for the quantum dot, $|0,e\rangle$, the system is not in an eigenstate and therefore is coherently evolving to $|1,g\rangle$, and back to $|0,e\rangle$, etc... This time evolution corresponds to subsequent emissions and absorptions of a single photon into the cavity. This is displayed on Fig. 1.18(b), where the population of states $|1,g\rangle$ and $|0,e\rangle$ are oscillating at the Rabi frequency g .

Weak and strong coupling regime.

In general, the coherent evolution presented in Fig. 1.18(b) does not continue for a long time and the photon is either emitted in another mode than the cavity mode, or a photon escapes from the cavity. Such processes cannot be described with a hamiltonian and we will see in Chapter. 3 (and in Chapter. 5) how they can be theoretically described. In the following, we give a qualitative description of a more realistic cavity-QED device.

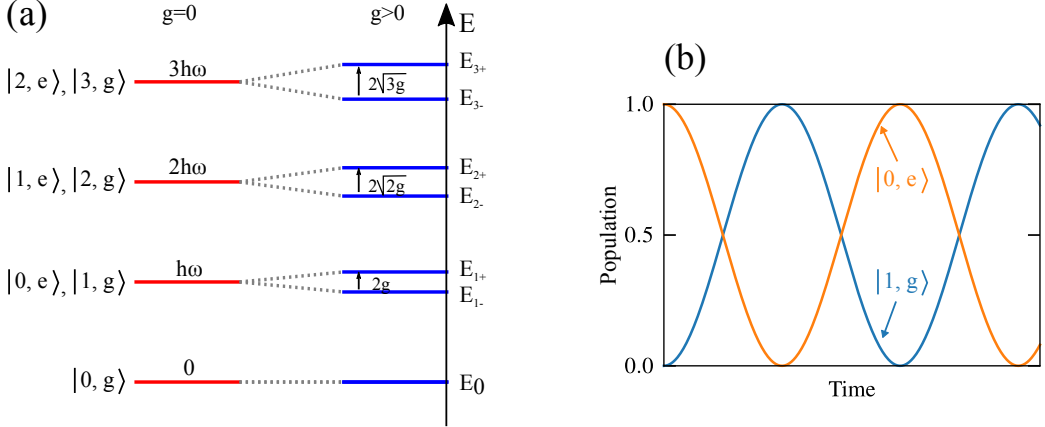


Figure 1.18: (a) Energy level of a cavity-QED device for $\omega_{QD} = \omega_c = \omega$. When the cavity and the quantum dot are not coupled ($g = 0$), the states $|n, g\rangle$ and $|n - 1, e\rangle$ are degenerate. When the cavity and the quantum dot are coupled ($g > 0$), the degeneracy is lifted and the eigenstates E_{n+} and E_{n-} are separated by $2\sqrt{ng}$: the energy level structure is the so-called Jaynes-Cumming ladder. (b) Occupation probabilities for the state $|0, e\rangle$ (in orange) and for the state $|1, g\rangle$ (in blue). It shows a coherent exchange of excitation between the quantum dot and the cavity.

The dissipative effects that need to be taken into account are shown in Fig. 1.19. The first dissipative effect is that the cavity is not perfectly isolated, so photons can escape the cavity from the top and bottom mirrors and from the side. The rate at which photons escape the cavity is given by κ_{top} , κ_{bottom} and κ_{side} , for the top, bottom and side of the micropillar respectively. A photon can also be absorbed by the micropillar material at a rate κ_{abs} . Therefore, the total rate at which a photon escapes the cavity is given by $\kappa = \kappa_{top} + \kappa_{bottom} + \kappa_{side} + \kappa_{abs}$.

In addition, the quantum dot is not always emitting a photon into the cavity mode. It is also possible that it spontaneously decays by emitting a photon in other modes, with rate γ_{sp} . Therefore, the spontaneous decay is acting on the quantum dot populations, by inducing a radiative decay from state $|e\rangle$ to $|g\rangle$. Such emitted photons are also lost for the system composed of the cavity and the quantum dot.

The quantum dot can also interact incoherently with its environment with a pure dephasing rate γ^* . This pure dephasing rate acts on the relative phase between the quantum dot states $|e\rangle$ and $|g\rangle$, preventing them to be in a pure coherent superposition such as $\alpha|g\rangle + \beta|e\rangle$. The total quantum dot decoherence rate is given by $\gamma = \gamma^* + \frac{\gamma_{sp}}{2}$.

The cavity loss rate κ and the quantum dot decoherence rate γ have to be compared to the rate of coherent quantum dot-cavity interactions, given by g . In general, two regimes are distinguished [151, 152].

Strong coupling regime: When the coupling strength g is greater than the incoherent processes $4g > \kappa$ and $4g > \gamma$, it is still possible to observe the Rabi oscillations, but these oscillations are now damped (as illustrated in Fig. 1.20 (a)). Also, the two eigenstates of the system $E_{+,1}$ and $E_{-,1}$ are resolved, meaning that the energy splitting $2\hbar g$ between these two states is greater than their linewidth $\frac{\kappa+\gamma}{2}$, and therefore a photoluminescence spectrum presents two distinct peaks.

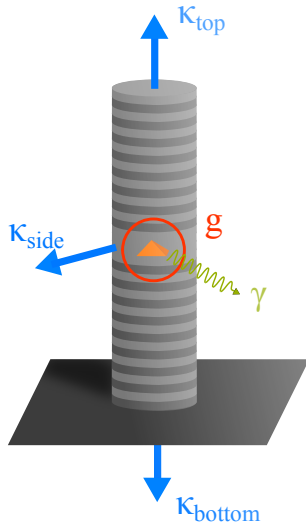


Figure 1.19: Scheme representing the principal cavity-QED parameters: g is the light-matter coupling, γ is the decoherence rate and κ_{top} , κ_{bottom} and κ_{side} are the cavity damping rates from the top, bottom and sides of the pillar.

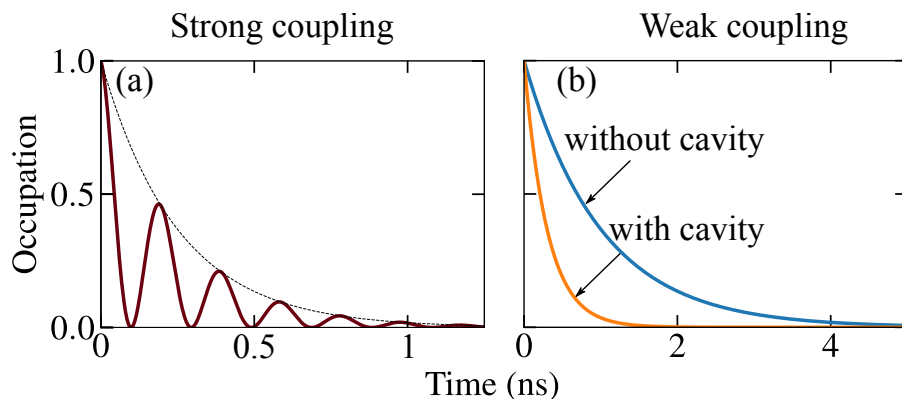


Figure 1.20: (a) Occupation probability of the quantum dot excited state in the strong coupling regime. The Rabi oscillations are visible but are damped. (b) Occupation probability of the quantum dot excited state in the weak coupling regime with and without cavity coupling. There is no Rabi oscillation anymore. Even in that regime a cavity modifies the quantum dot exciton state by reducing its lifetime due to Purcell effect.

Weak coupling regime: When the incoherent processes are faster than the light matter coupling, the Rabi oscillations do not occur anymore: photons escape the cavity too quickly to be reabsorbed by the quantum dot. Still, the cavity enhances the spontaneous emission into the cavity mode, a phenomenon known as the Purcell effect, and therefore, the QD excited state lifetime decreases, as illustrated in Fig. 1.20(b). The emission rate into the cavity mode, given by $\Gamma = 4g^2/\kappa$, needs to be compared to the quantum dot spontaneous emission in bulk γ_{sp} : the Purcell factor is the ratio between these two quantities: $F_p = \Gamma/\gamma_{sp}$. Consequently, an important figure of merit is the probability that the quantum dot emits into the cavity mode, $\beta = \frac{\Gamma}{\Gamma + \gamma_{sp}} = \frac{F_p}{F_p + 1}$.

The strong coupling regime has been reached with quantum dots in various groups [38, 134, 153] but the weak coupling regime is also interesting. By enhancing the emission of the quantum dot into the cavity mode, it is possible to favor one leaky channel to maximize the collection of the photons from the cavity, for example, from the top or bottom mirror of the pillar micro-cavity. In that case, it is possible to obtain a cavity-QED device close to the one-dimensional (1D) atom model [154, 155] where one atom is interacting with one single photonic channel with 100% efficiency. In this model, the cavity-QED device and its input or output channels can be considered as an isolated system. In this context, another important figure of merit is the top mirror output coupling $\eta_{top} = \kappa_{top}/\kappa$, which characterizes the probability for an intracavity photon to escape the cavity from the top mirror. It can therefore be interesting to increase on purpose the top mirror cavity damping rate κ_{top} in order to maximize the top mirror output coupling, $\eta_{top} = \kappa_{top}/\kappa \rightarrow 1$.

In the work of this thesis, the cavity-devices used are fabricated with the objective of approaching the behavior of an ideal weakly-coupled 1D-atom. In the following, we show two applications of these cavity-QED devices as single-photon sources and as spin-photon interfaces.

1.5 Single-photon sources.

For the development of solid-state photonic quantum networks [3], natural or artificial atoms should be efficiently interfaced with single photons. The atom-photon interaction is enhanced by inserting the atom in an optical cavity, resulting in a cavity-QED device. This device can operate both as an emitter and a receiver of single photons [156]: in this section, we focus on the emission of single photons.

For quantum information processing, an optimal single-photon source should provide on-demand photons that are pure and indistinguishable, at high repetition rates [157]. The single-photon purity and indistinguishability of the photons is necessary for the quality of the quantum optics experiments, while the high repetition rate and photon brightness is crucial for multi-photons experiments, where integration times scale exponentially with the number of photons [12, 157].

1.5.1 Single-photon purity.

The purity of a single-photon source quantifies the probability that the source emits multiple-photons at the same time. In this respect, the use of solid-state quantum emitters is interesting due to its atom-like transitions which ensures that only one photon is emitted at the same time, at a given energy. This single-photon purity is generally quantified by measuring the intensity correlations of the emitted light, the $g^{(2)}(t)$ [158, 159]:

$$g^{(2)}(t) = \frac{\langle \hat{a}^\dagger(t)\hat{a}^\dagger(0)\hat{a}(0)\hat{a}(t) \rangle}{\langle \hat{a}^\dagger(t)\hat{a}(t) \rangle \langle \hat{a}^\dagger(0)\hat{a}(0) \rangle} \quad (1.19)$$

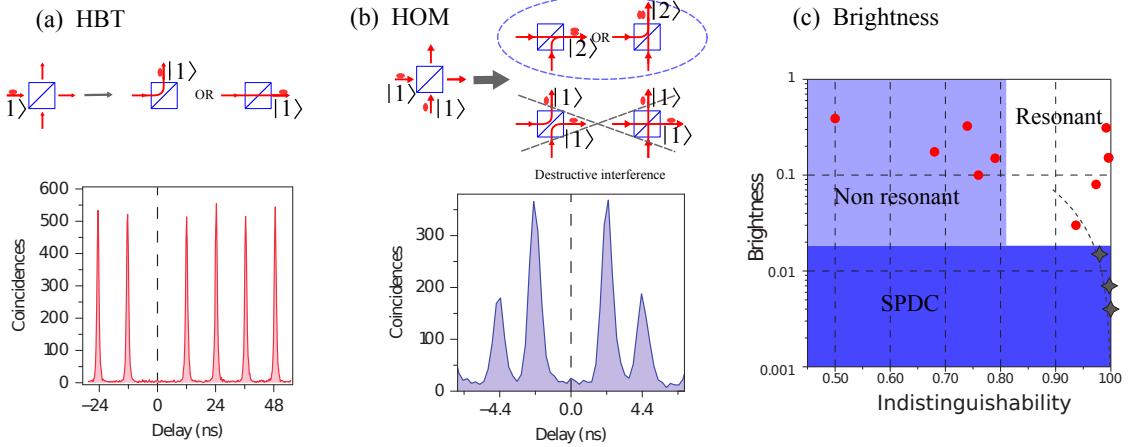


Figure 1.21: From Ref. [26](C2N): (a) Top panel: Hanbury-Brown and Twiss experiment where a single-photon source is sent on a beamsplitter, and measured by single photon detectors at the output ports of the beamsplitter. The correlations between the two detectors are represented in the bottom panel for pulsed single photons. (b) Top panel: Hong-Ou-Mandel interference where two photons are sent at each input port of the beam splitters. Indistinguishable photons leave the beam splitter together and cannot be detected at the same time by both photodiodes. Bottom panel: correlations between the two detectors. (c) Comparison between Spontaneous Parametric Down Conversion (SPDC) sources (grey symbols) and state-of-the-art quantum dot single-photon sources (red circles) [25, 26, 160, 161, 162].

It can be shown that the zero-delay intensity auto-correlation function $g^{(2)}(0)$ can be zero only for a source of single photons. Quantum dots have been shown to be single photon sources with low multi-photon probability [136, 159]. Experimentally, it is measured with a Hanbury-Brown and Twiss (HBT) setup, constituted of a beam splitter and two single-photon avalanche photodiodes, as shown in the top panel of Fig. 1.21 (a). If the source emits photons one-by-one, a photon can only be detected by one of the two detectors, and therefore, $g^{(2)}(0) = 0$. The lower panel of Fig. 1.21 displays the result of a HBT experiment (with pulsed excitation) obtained with an electrically-contacted QD-cavity device fabricated in Pascale Senellart's group [26]. There is no coincidence peak at zero delay, thus indicating a pure single photon source. In Chap. 4 and in Chap. 5, we will describe in more details the intensity auto-correlations function and see that its value at $t \neq 0$ provides also interesting information.

1.5.2 Photon indistinguishability.

For high quality quantum optics experiments with single photons, the successively emitted photons also need to be indistinguishable, and therefore must be emitted with identical polarizations and wave packets. This is crucial so that photons interfere optimally together. Even when the photon wavepackets have identical spectral and temporal profiles, their indistinguishability is limited by $T_2/(2T_1)$, where T_2 is the coherence time and T_1 the lifetime of the single photon source. In the

ideal case, the coherence time is maximum and equal to $T_2 = 2T_1$,¹ but when there is pure dephasing, $1/T_2 - 1/(2T_1) = \gamma^*$, the indistinguishability is not optimal: $T_2/2T_1 < 1$. The use of a cavity, which decreases the photon lifetime by Purcell effect, reduces the influence of the dephasing mechanisms and therefore improves the photon indistinguishability. The experimental measurement of the photon indistinguishability is carried out thanks to a Hong-Ou-Mandel setup (as shown in the top panel of Fig. 1.21 (b)), where two single photons are interfering onto a 50:50 beamsplitter, and where correlations between the detectors positioned at the output ports of the beamsplitter are measured. Indistinguishable photons interfere in such a way that they are exiting the beamsplitter by the same output. Consequently, for perfectly indistinguishable photons, the zero-delay coincidences between the two photon detectors should be zero, as seen in the bottom panel of Fig. 1.21 (b) which displays the result of a HOM measurement with the same electrically-contacted QD-cavity device as in Fig. 1.21 (a) [26]. Near unity indistinguishability have been reported in multiple groups [163, 164, 161, 26, 162].

1.5.3 Brightness.

Finally, to be used at high repetition rates, the accelerated spontaneous emission reduces the photon lifetime so that such single photon source can be operated in the GHz regime [165]. But to be useful for quantum information applications, the photons need also to be efficiently collected, which is not trivial because, without an engineered environment, a quantum dot emits single photons in all directions. Having on-demand single-photon sources requires that a single emission channel is favored compared to all others, which is possible thanks to the use of a cavity. The use of high quality factor cavities, greatly improves the probability to emit the photons in a single optical mode [166, 25, 26, 162]. To quantify it, we introduce the brightness, which is the probability that a single photon is collected (by a lens placed above the micropillar top mirror) when the source is triggered [167].

The brightness depends on the quantum dot state occupation probability P_s . Indeed, to convert a laser pulse into a single photon, the state that is excited by the laser should be the one that is optically active. The photon should also be emitted in the cavity mode to be efficiently collected, hence the brightness should also depend on the cavity mode emission probability, $\beta = \frac{F_p}{F_p+1}$ (see Sec. 1.4.3). It is therefore also necessary to increase as much as possible the Purcell factor. Then the photon should escape the cavity from a given output port of the cavity. In this work, we are working with the top mirror as the privileged output port of the pillar microcavity. Therefore the brightness B is equal to: $B = P_s \beta \eta_{top}$. In the last decade, the use of cavities has greatly enhanced the collection efficiency so that high brightnesses have been reported. Fig. 1.21 (c) shows the brightness and indistinguishability of different single-photon sources (with $g^{(2)}(0) < 5\%$). On the bottom of the graph, the commercially available Spontaneous Parametric DownConversion (SPDC) sources presents high indistinguishability but intrinsically low brightness ($B < 2\%$). They are compared to the quantum-dot-based sources (from Senellart's group [25, 26], Reitzenstein's group [160] and Pan's group [161, 162]) which under resonant pumping present both high indistinguishability (above 95%) and high brightness (above 10%).

¹This equality is different from the case of a spin qubit, $T_2 = T_1$ (see Sec. 1.2.3), because only transitions from the QD excited state $|e\rangle$ to the fundamental state $|g\rangle$ occur contrary to a spin where spin flips can occur for the two spin states (i.e. from $|\uparrow\rangle$ to $|\downarrow\rangle$ and from $|\downarrow\rangle$ to $|\uparrow\rangle$).

1.6 Optimal spin-photon interface using cavity-QED.

For solid-state quantum networks, a cavity-QED device should not only operate as an emitter but also as a receiver of single photons. As a receiver, it should allow manipulating the (natural or artificial) atom state with single photons [168] and, reciprocally, manipulating the single photon state with the atom [169, 54, 170]. In this respect, pillar microcavities have demonstrated intrinsically good performances, allowing high input/output coupling efficiencies and enhancing drastically the light-matter interaction. Incoming photons can be efficiently coupled to a microcavity [44], and it has been shown that a quantum dot coupled to such microcavities can be controlled with incoming fields of a few photons [171, 172, 173]. Reciprocally, a cavity-coupled quantum-dot modifies drastically the properties of the incoming photons [174, 175]. A cavity-QED device can, for example, filter the single-photon component of a coherent optical beam [173], which is potentially useful to produce path-encoded photon-photon gates, where a photon is either transmitted or reflected depending on the presence or absence of a second photon.

In the framework of this thesis, another key feature lies in the fact that quantum dots also modify the incoming photon polarization by inducing a giant polarization rotation. Kerr and Faraday rotations have been detailed in Sec 1.3.2, but their amplitude was too small to efficiently interface the quantum dot spin and the photon polarization. The cavity-enhanced light-matter interaction presented in this section should greatly amplify the polarization rotation induced by a single spin, so that it can be macroscopic. In the ideal case, the two reflected polarizations should be orthogonal so that the spin state is perfectly encoded onto the polarization state of the photon.

In this section, we first show, using a semi-classical model, how a quantum dot drastically modifies the optical properties of a cavity. Then we see how this is related to spin dependent polarization rotation. Finally, we detail experimental and theoretical results concerning the single-spin induced Kerr rotation and how ideal spin-photon interfaces should be accessible with realistic devices.

1.6.1 Optical response of cavity and cavity-QED devices.

A microcavity results in a reflectivity dip at the confined electromagnetic mode wavelength, as represented in Fig. 1.15 (d). The reflection coefficient of a cavity alone is then completely modified in resonance with the confined mode. As will be detailed later in Chap. 2, the reflection coefficient is given as a function of the incident photon energy ω :

$$r_{cav}(\omega) = 1 - 2\eta_{top} \frac{1}{1 - i\Delta} \quad (1.20)$$

with $\Delta = 2\frac{\omega - \omega_c}{\kappa}$, where ω_c is the cavity mode energy. The reflection coefficient is a complex number whose amplitude and phase are represented in Fig. 1.22 (a) (for $\eta_{top} = 85\%$ and $\kappa = 400\mu\text{eV}$). The reflection coefficient amplitude has a Lorentzian shape centered on the cavity mode and, at resonance, the cavity induces a π phase shift onto the reflection coefficient.

When a two-level system is in resonance with the cavity mode, it strongly modifies the reflection coefficient. Using a semi-classical approach, that is valid under small excitation power and when there is no pure dephasing ($\gamma^* = 0$) occurring on the quantum dot [176], it can be shown that the reflection coefficient is [124, 177, 178]:

$$r_{QD}(\omega) = 1 - 2\eta_{top} \frac{1}{1 - i\Delta + 2C \frac{1}{1 - i\Delta'}} \quad (1.21)$$

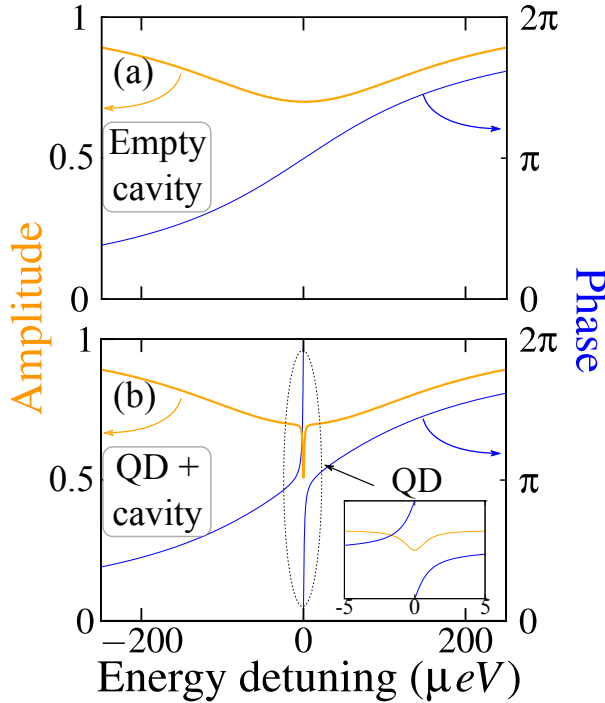


Figure 1.22: Simulated phase (blue) and amplitude (orange) of the reflection coefficients of a cavity (a) and a cavity coupled to a quantum dot (b), for different laser-cavity detunings. Inset: Zoom in the quantum dot behavior: it induces a π phase-shift on the reflected light at resonance.

where $\Delta' = \frac{\omega - \omega_{QD}}{\gamma_{sp}}$, where ω_{QD} is the quantum dot energy, and $C = \frac{g^2}{\kappa\gamma}$ is the cooperativity. Using the same cavity parameters as before and realistic quantum dot parameters ($\gamma_{sp} = 0.6\mu\text{eV}$ and $g = 17\mu\text{eV}$), the reflection coefficient is displayed in Fig. 1.22 (b). This reflection coefficient can be compared to the previous one. The behavior of the reflection coefficients are similar, except close to the quantum dot resonance where both their amplitude and phase are drastically different. In resonance with the quantum dot, the reflection coefficient amplitude presents a small dip which translates to a reflectivity dip.¹ The change in phase is even clearer: the quantum dot induces a π -phase shift onto the reflection coefficient. This phase shift plays a central role in the macroscopic Kerr rotation that is detailed in the following.

1.6.2 Cavity-enhanced Kerr rotation.

The reflection coefficient presented previously was obtained with an ideal two-level quantum emitter in resonance with the cavity. For a charged quantum dot, the quantum emitter is a four-level system with the optical selection rules presented in Fig. 1.4. The quantum dot can be seen as a two-level system interacting with only the left-handed circular polarization, alongside with another two-level system interacting with only the right-handed circular polarization.

Fig. 1.23 shows that this results in spin-dependent Kerr rotation as explained in the following. As presented in Fig. 1.23, we consider an incident horizontal polarization $|H\rangle = \frac{1}{\sqrt{2}}(|R\rangle + |L\rangle)$, and

¹For different parameters, for example higher coupling strength g and lower top-mirror output coupling η_{top} , the quantum dot response can also be a reflectivity peak.

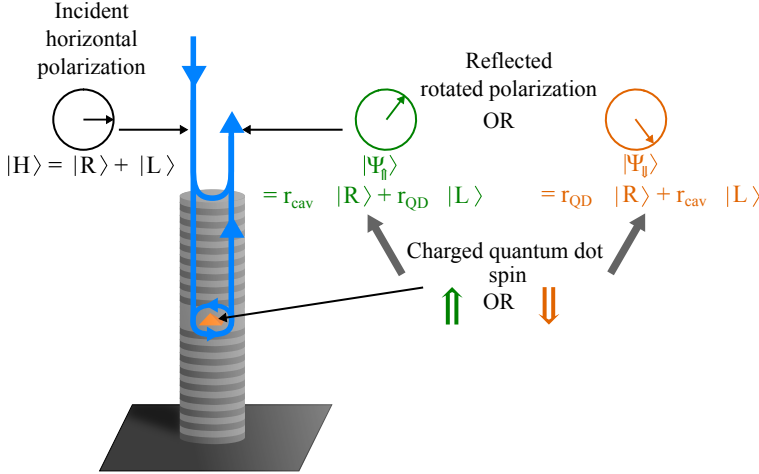


Figure 1.23: Kerr rotation induced by a cavity-coupled quantum dot spin.

we first consider the case where the spin is \uparrow_z . The $|\uparrow_z\rangle$ spin state is transparent for circular-right polarization component, which is therefore reflected with reflection coefficient $r_{cav}(\omega)$ (described by Eq. 1.20). Conversely, for the circular-left polarization, the cavity is populated by a two-level quantum emitter and is therefore reflected with the $r_{QD}(\omega)$ reflection coefficient (described by Eq. 1.21). When the spin is in its $|\uparrow_z\rangle$ state, since $r_{cav}(\omega) \neq r_{QD}(\omega)$, the reflected polarization $|\Psi_{\uparrow}\rangle \propto r_{cav}|R\rangle + r_{QD}|L\rangle$ is rotated as compared to the horizontal incident polarization $|H\rangle$.

Now if the spin is \downarrow_z , the quantum dot is transparent for circular-left polarization and optically active for circular-right polarization. It also results in a rotated polarization $|\Psi_{\downarrow}\rangle$ that is different, not only to the horizontal incident polarization but also to the $|\Psi_{\uparrow}\rangle$ polarization, as seen in Fig. 1.23. Indeed, $|\Psi_{\uparrow}\rangle \propto r_{cav}|R\rangle + r_{QD}|L\rangle$ and $|\Psi_{\downarrow}\rangle \propto r_{QD}|R\rangle + r_{cav}|L\rangle$ are different when $r_{cav} \neq r_{QD}$.

The fact that r_{cav} and r_{QD} can be completely different in phase, even for realistic cavity-QED parameters, illustrates why the Kerr rotation can be strongly amplified, compared to the QD intrinsic Kerr rotation magnitude described in Sec. 1.3.2. As shown in the next section, with cavity-enhanced spin photon interaction, macroscopic Kerr rotation has been experimentally demonstrated in C2N during the PhD thesis of Justin Demory.

1.6.3 Measurement of macroscopic spin-dependent polarization rotation.

In the following, the results from *Arnold et al. (2015)* [27] are detailed, demonstrating a 6° macroscopic Kerr rotation induced by a quantum dot hole spin coupled to a pillar microcavity. Fig. 1.24 is a sketch of the experimental setup. In this experiment, a CW laser resonantly pumps the hole spin with circular polarization, to initialize it either in spin \uparrow_z or in spin \downarrow_z , using the technique already described in Sec. 1.3.1. Then a second CW laser resonantly scans the quantum dot wavelength with linear $|H\rangle$ polarization: it is reflected with a spin-dependent polarization $|\Psi_{\uparrow}\rangle$ or $|\Psi_{\downarrow}\rangle$. The reflected light is analyzed in polarization thanks to a polarizing beamsplitter and two avalanche photodiodes, in order to measure its rotated angle. To discriminate the circularly-polarized pump from the horizontally-polarized probe, the latter is modulated in intensity thanks to an Electro-Optical Modulator (EOM) and the two photodiodes are connected to lock-in amplifiers. The rotation measured on the linear probe is presented in Fig. 1.24 as a function of the probe photon energy and of the

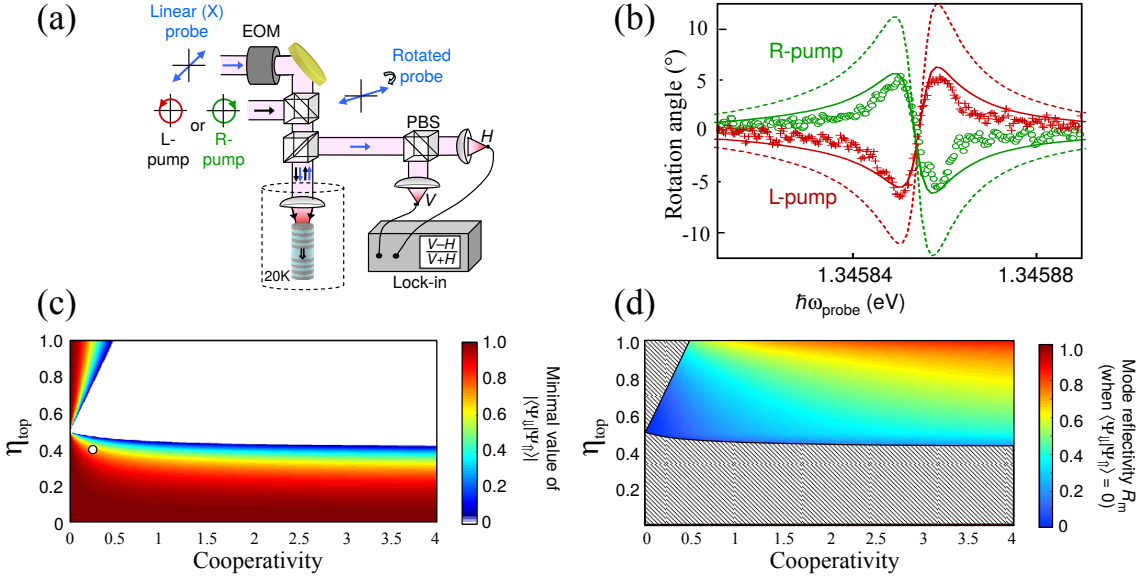


Figure 1.24: From Ref. [27](C2N): (a) Experimental setup for spin pumping and to demonstrate the macroscopic Kerr rotation measurement. (b) Rotation angle as a function of the probe laser-cavity detuning for circular-left (red) and circular-right (green) pump laser. The solid lines are the theoretical fit with partial spin initialization and the dashed lines are the predictions with perfect spin initialization. (c) Minimum value of $|\langle \Psi_{\uparrow} | \Psi_{\downarrow} \rangle|^2$ as a function of the cooperativity and the top-mirror output coupling. Orthogonal states ($\langle \Psi_{\uparrow} | \Psi_{\downarrow} \rangle = 0$) can be obtained for a wide set of parameters (white region of the colorplot). (d) Maximum reflectivity obtained when $\langle \Psi_{\uparrow} | \Psi_{\downarrow} \rangle = 0$, as a function of the cooperativity and the top mirror output coupling.

pump polarization (and, thus, of the prepared spin state). For a given laser-quantum dot wavelength detuning, the rotation reaches $\pm 6^\circ$ depending on the pump polarization, three orders of magnitude higher than the previous state-of-the-art [22]. Such high polarization rotation has also been obtained in *Androvitsaneas et al. (2016)* [179] (Rarity's group).

These results showed for the first time that a macroscopic polarization rotation can experimentally be obtained with a single spin. This is crucial to enable the single shot, non destructive measurement of a single spin. Still, this polarization rotation amplitude is not sufficient to perform a strong projective measurement or to maximally entangle a spin and a single incoming photon. It is therefore important to know whether these applications are achievable with realistic QD-micropillar device. In this respect, a crucial figure of merit is the scalar product between the two spin-dependent polarization states, $|\langle \Psi_{\uparrow} | \Psi_{\downarrow} \rangle|$. In the ideal case, $|\langle \Psi_{\uparrow} | \Psi_{\downarrow} \rangle| = 0$, the two polarizations are completely orthogonal. In that case, the measurement of a photon with polarization $|\Psi_{\uparrow}\rangle$ projects the spin in $|\uparrow_z\rangle$ with 100% probability. In addition, a single photon interacting with a spin prepared in a state superposition $\frac{1}{\sqrt{2}}(|\uparrow_z\rangle + |\downarrow_z\rangle)$ is reflected with its polarization that is entangled to the spin state: $|\Psi_{ent}\rangle = \frac{1}{\sqrt{2}}(|\uparrow_z\rangle|\Psi_{\uparrow}\rangle + |\downarrow_z\rangle|\Psi_{\downarrow}\rangle)$, which is maximally entangled provided that $|\langle \Psi_{\uparrow} | \Psi_{\downarrow} \rangle| = 0$. Therefore $|\langle \Psi_{\uparrow} | \Psi_{\downarrow} \rangle|$ quantifies the maximal fidelity of a quantum measurement or of an entangling gate.

The minimum spin-dependent polarization state overlap $|\langle \Psi_{\uparrow} | \Psi_{\downarrow} \rangle|$ is theoretically calculated as a function of the cooperativity $C = \frac{g^2}{\kappa\gamma}$ and of the top-mirror output coupling $\eta_{top} = \frac{\kappa_{top}}{\kappa}$. It shows that

orthogonal spin-dependent polarizations can be obtained in a large region of cooperativity (typically above 0.5) and top-mirror output coupling above 0.5 as shown in Fig. 1.24 (c). In this region, for a given laser quantum dot detuning, the spin-dependent reflected polarizations $|\Psi_{\uparrow}\rangle$ and $|\Psi_{\downarrow}\rangle$ are orthogonal.

In order to realize an efficient spin-photon interface, the photons must also be efficiently extracted. Therefore, a second crucial number is the reflectivity at the laser-quantum dot detuning for which $\langle\Psi_{\uparrow}|\Psi_{\downarrow}\rangle = 0$, denoted R . This reflectivity quantifies the "success probability" of the entangling spin-photon gate. Fig. 1.24 (d) shows the dependence of this reflectivity with the cooperativity and the top-mirror output coupling. As can be seen in this figure, even though it is possible to have orthogonally-polarized state for small cooperativity and $\eta_{top} \approx 50\%$, in this case the reflectivity is very small: the photon escapes the cavity through other channels, therefore reducing the success probability of generating an entangled-state between the spin and an incoming photon. Conversely, for high cooperativity ($C \gg 1$) and high top mirror output coupling ($\eta_{top} \rightarrow 1$), the device can provide at the same time a unity fidelity for the measurement/entanglement process (through $|\langle\Psi_{\uparrow}|\Psi_{\downarrow}\rangle| = 0$) and a unity success probability (through $R \rightarrow 1$). This would constitute the building block for truly deterministic spin-photon gates, and subsequently photon-photon or spin-spin gates [124, 123].

1.7 Conclusion.

In this chapter, we have seen that quantum dot spins are promising qubits for the implementation of quantum computers. These qubits can be optically initialized, measured and coherently manipulated at a much faster rate than their coherence time, which is limited due to the hyperfine interaction with nuclei. They can also be entangled with emitted photons and therefore constitute promising quantum nodes of a quantum network.

Still, in the realization of quantum communication protocols and photon-photon gates, a major goal consists in entangling a spin with previously-existing photons, a feature that has never been achieved yet. In this respect, a technique based on Faraday or Kerr rotation can be used: the photon polarization is rotated depending on the spin state. However, the experimentally achievable polarization rotation is very small for quantum dots in bulk semiconductors.

Consequently, the light-matter interaction should be enhanced. In this respect, the use of pillar microcavities increases the polarization rotation induced by a single spin by several orders of magnitude. Previous results obtained at C2N [27] have shown that a macroscopic polarization rotation is achievable, and that orthogonal spin-dependent polarization states should be obtained with realistic cavity-QED parameters.

In this work, we study such spin-photon interfaces. We show in the first two chapters how the polarization reflected by a cavity-QED device can be experimentally reconstructed, for an empty cavity and for a cavity coupled to an exciton transition (neutral quantum dot). Such reconstruction is particularly important as it allows characterizing the purity of the polarization qubit, which is not always in a pure quantum state. Then, we show how efficient spin-photon interfaces can be deterministically fabricated. And finally, we show that the spin is efficiently coupled to a single photon by observing the measurement back action induced on a single spin by a single photon detection event.

Chapter 2

Polarization Tomography: measurement of input and output coupling in a pillar microcavity.

2.1 Introduction: input and output couplings in pillar microcavities.

A major potential application of pillar microcavities is the development of efficient interfaces between an electromagnetic mode and a single artificial atom.

To be useful for these applications, a single photon should be efficiently coupled to a cavity and deterministically interact with a single artificial atom such as a semiconductor quantum dot. In this respect, as seen in Sec 1.4.1, a pillar microcavity can drastically amplify the light-matter interaction. In this context, pillar microcavities have already allowed enhancing the light-matter interaction, which have led to the observation of the Purcell acceleration of the spontaneous emission into the cavity mode [127], and to the realization of the strong coupling with a single quantum dot [38]. Efficient coupling of a cavity and a quantum dot is crucial and will be discussed in more details in the next chapters.

However, to perform as efficient interfaces, micropillar cavities must not only confine the electromagnetic field, but also allow the efficient injection and collection of every photons into and from the cavity, via careful optical alignment. Ideally, such interfaces should behave as a one-dimensional atom [154, 155] where the natural or artificial atom is only interacting with a single optical mode, so that photons can be injected and collected with 100 % efficiency. Compared to other types of cavities, the main advantage of micropillars is that they can be easily coupled to a single optical beam: they efficiently couple to a free-space gaussian beam and they can also be engineered to favor one single output channel to facilitate the photon collection. The best input coupling is obtained when the external beam is matched both spatially and spectrally with the confined cavity field. So far, the experimental measurement of this mode matching is generally estimated by observing the incident laser and cavity modes far-field spatial profile with an uncertainty typically higher than 5% [171].

In this chapter, the polarization response of an elliptical pillar microcavity is first investigated. Second, the polarization tomography technique is introduced and used to quantify with unprecedented accuracy, a record high injection efficiency and the top mirror output coupling. Third, the cavity-induced rotation of polarization is used to optimize the cavity coupling alignment. Finally, a theoretical model is developed to evidence the spatial profile influence on the reflected photons

polarization.

2.2 Polarization response of a pillar microcavity.

In this section, we are interested in the polarization response of an elliptical pillar microcavity. First, we investigate the reflection coefficient of a cavity for a perfectly mode-matched external laser beam. Then, we study the effect of an imperfect input coupling onto the pillar reflectivity. Finally, we highlight how the absence of rotational symmetry can induce a polarization rotation onto the reflected light.

2.2.1 Optical response of a pillar microcavity.

In the following, we are interested in the optical response of a pillar microcavity in reflectivity. This response is completely characterized by the complex reflection coefficient r_{cav} . This number is describing the interference between the light that is directly reflected by the top mirror, and the light injected into the cavity and then escaping it through the top mirror (see Fig. 2.1 (a)). Consequently, it depends on the laser energy ω and the cavity parameters: the cavity energy ω_{cav} , the damping rate κ and the top mirror output coupling η_{top} . A semi-classical calculation (detailed in Sec. 2.5) shows that it can be written as:

$$r_{cav} = 1 - 2\eta_{top} \frac{1}{1 - i\Delta} \quad (2.1)$$

with Δ , the normalized cavity detuning:

$$\Delta = 2 \frac{\omega - \omega_{cav}}{\kappa} \quad (2.2)$$

The total reflectivity R_{cav} is the reflection coefficient norm squared:

$$R_{cav} = |r_{cav}|^2 = \left| 1 - 2\eta_{top} \frac{1}{1 - i\Delta} \right|^2 \quad (2.3)$$

From these equations, the reflection is clearly a complex number, so it will modify both the phase and the intensity of the reflected light.

From Eq. 2.3, we deduce that the reflectivity minimum is obtained when the laser is in resonance with the cavity mode: $\omega = \omega_{cav}$, ie. $\Delta = 0$. Its value is:

$$R_{min} = |1 - 2\eta_{top}|^2 \quad (2.4)$$

It reaches zero when $\eta_{top} = 0.5$. In that case the light directly reflected from the top mirror and the one escaping the cavity completely interfere destructively.

2.2.2 Mode matching and input coupling in pillar microcavity.

When an intracavity photon escapes the cavity from the top mirror, it is emitted vertically (along the z-axis) with a normalized transverse spatial profile $\Phi_m(x, y)$ of the mode electric field (see Fig. 2.1). Due to its cylindrical shape, the pillar is a waveguide similar to an optical fiber and consequently the cavity mode spatial profile is similar to the one of a single-mode fiber; it can be approximated to a gaussian beam.

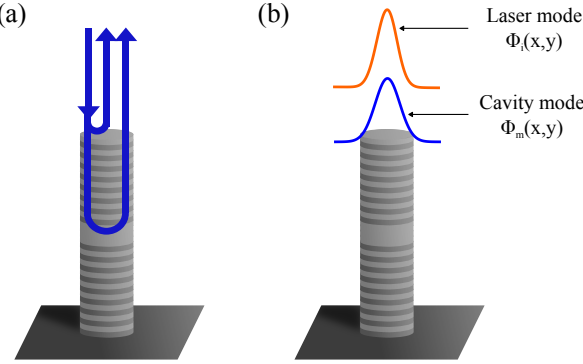


Figure 2.1: (a) Interference scheme between the light directly reflected by the top Bragg mirror and the light injected into and reextracted from the cavity through the device top mirror. (b) Normalized transverse spatial profile of the incoming laser $\Phi_i(x,y)$, and of the cavity mode $\Phi_m(x,y)$. For maximum injection into the cavity, these two spatial profiles should be identical.

Consequently, to efficiently inject a photon into the cavity, not only should it be spectrally matched to the cavity mode but also its incoming spatial profile $\Phi_i(x,y)$ should be identical to the cavity mode $\Phi_m(x,y)$. We call input coupling, and denote η_{in} , the overlap between the photon spatial profile and the cavity mode spatial profile.

$$\eta_{in} = \left| \int \int \Phi_i(x,y)^* \Phi_m(x,y) dx dy \right|^2 \quad (2.5)$$

The spatial profiles are normalized such that:

$$\int \int \Phi_j(x,y)^* \Phi_j(x,y) dx dy = 1 \quad (2.6)$$

for $j = i, m, \dots$. In all this chapter, we will use a subscript "i" to denote the incoming laser and "m" to denote the cavity mode.

Thanks to that normalization, the input coupling η_{in} is a real number between 0 and 1. It quantifies the light injection efficiency into the cavity. If $\eta_{in} = 0$, the incoming light has a completely different spatial profile and cannot enter into the cavity. In such a case, we will consider that the light is completely reflected by the pillar DBR structure.

If $\eta_{in} = 1$, the incoming light has the same spatial profile as the cavity mode. In such a case, the incoming light is reflected with the reflection coefficient discussed previously in Eq. 2.1. In the general case however, the incoming light has a spatial profile $\Phi_i(x,y)$ different from $\Phi_m(x,y)$ so that $0 < \eta_{in} < 1$.

The spatial profile $\Phi_i(x,y)$ can be decomposed as:

$$\Phi_i(x,y) = \sqrt{\eta_{in}} \Phi_m(x,y) + \sqrt{1 - \eta_{in}} \Phi_{\neq}(x,y) \quad (2.7)$$

with $\Phi_{\neq}(x,y)$ a spatial profile that is orthogonal to $\Phi_m(x,y)$ so that, by definition:

$$\left| \int \int \Phi_{\neq}(x,y)^* \Phi_m(x,y) dx dy \right|^2 = 0 \quad (2.8)$$

The subscript " m " is used to denote the fraction of incoming light which is not coupled to the cavity mode.

Therefore, the incoming light is decomposed into two components:

- The fraction of the incoming light coupled to the cavity mode, with the same mode profile $\Phi_m(x, y)$ and incoming intensity $I_m^{in} = \eta_{in}I^{in}$, with I^{in} the total incoming intensity. This fraction of the incoming light is reflected with reflection coefficient r_{cav} and consequently with a reflected intensity $I_m = |r_{cav}|^2\eta_{in}I^{in}$
- The fraction of the incoming light that is not coupled with the cavity mode and therefore has a mode profile denoted $\Phi_{\not{m}}(x, y)$ and incoming intensity $I_{\not{m}}^{in} = (1 - \eta_{in})I^{in}$. It is completely reflected, so that the reflected intensity is $I_{\not{m}} = I_{\not{m}}^{in} = (1 - \eta_{in})I^{in}$. (The total reflection is based on the assumption that the incident mode profile is smaller than the pillar surface.)

It is worth noticing that the total reflected light is based on two reflected contributions $I_{\not{m}}$ and I_m which are in orthogonal spatial modes $\Phi_m(x, y)$ and $\Phi_{\not{m}}(x, y)$, and as a result, do not lead to interference in the total reflected intensity. This is true when all the reflected light is collected without spatial selection, which is the case with free-space detection (single-mode fiber detection is discussed later in Sec. 2.3.4 and 2.5.3 and exhibits different results). The total reflectivity is then:

$$R_{tot} = \eta_{in}|r_{cav}|^2 + (1 - \eta_{in}) \quad (2.9)$$

As evidenced in this equation, the imperfect cavity input coupling adds a constant background of uncoupled light $(1 - \eta_{in})I^{in}$ that is completely reflected, thus degrading the true contrast of the real cavity reflectivity. Indeed the minimum reflectivity value is now:

$$R_{min} = (1 - \eta_{in}) + \eta_{in}|1 - 2\eta_{top}|^2 \quad (2.10)$$

It depends not only on η_{top} as before but also on η_{in} . From a reflectivity measurement only, it is not possible to extract the value of the top mirror output coupling η_{top} because of the coupling imperfections. The combined effect of the input and top mirror output couplings on the reflectivity is illustrated in Fig. 2.2. There is indeed a set of different values that gives the same reflectivity minimum R_{min} . In order to measure these couplings independently, one should find another technique than the reflectivity measurement. The technique explored in the following is based on the measurement of the optical response in polarization.

2.2.3 Elliptical pillar microcavities.

In general, micropillars are not perfectly cylindrical. Therefore, there is a lift of degeneracy in polarization of the cavity modes. The cavity mode is then split in two modes of orthogonal linear polarization that we define as horizontal (H) and vertical (V), and whose energy are $\omega_{c,H}$ and $\omega_{c,V}$ (Fig. 2.3). The cavity mode splitting is given by: $\delta\omega = \omega_{c,H} - \omega_{c,V}$. The global cavity energy is defined as the two cavity mode energies mean value: $\omega_c = (\omega_{c,H} + \omega_{c,V})/2$. If the pillar microcavity is perfectly circular, it has a rotational symmetry and is degenerate in polarization: the cavity mode splitting $\delta\omega$ is equal to zero. In general, the pillar microcavities are never perfectly circular and $\delta\omega \neq 0$.

The experimental results of this chapter were taken with a pillar microcavity consisting in a $\lambda - GaAs$ cavity, positioned between two DBR, with 20 (30) pairs of alternating quarter-wavelength thick $GaAs/Al_{0.9}Ga_{0.1}As$ layers for the top (bottom) mirror.

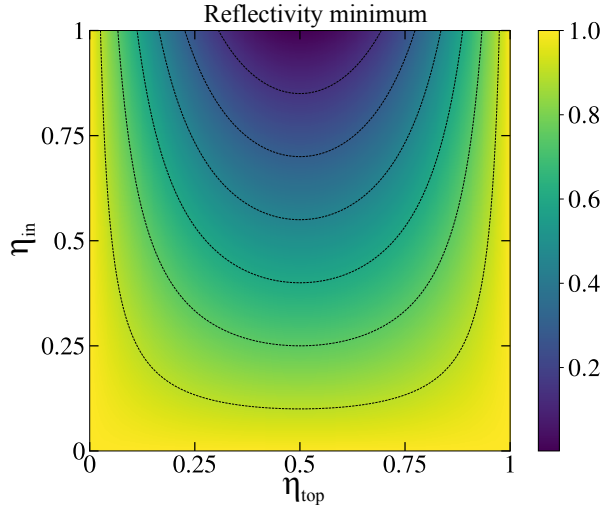


Figure 2.2: Minimum of reflectivity as a function of the input coupling (η_{in}) and the top mirror output coupling (η_{top}). The color scale indicates the reflectivity minimum value. Dashed black lines highlight sets of coupling parameters that gives the same minimum of reflectivity.

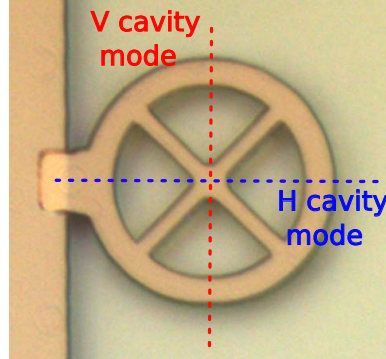


Figure 2.3: Cavity mode of an elliptical micropillar.

The pillar ellipticity is evidenced by measuring the cavity reflectivity under horizontally and vertically polarized excitation. A collimated CW-tunable laser is focused onto a $2.5\mu\text{m}$ -wide pillar. The laser energy ω scans the cavity mode resonance energy ω_c and for each photon energy, we measure the reflectivity, which is the ratio between the reflected and incoming intensities. Results are displayed in Fig. 2.4 where the reflectivity spectrum is displayed for laser energy close to the cavity mode energy ($\omega_c = 1.3365\text{eV}$). The two cavity modes are split by an energy $\delta\omega = 63 \pm 1\mu\text{eV}$ which evidences the cavity ellipticity. The cavity damping rates for the horizontal and vertical polarizations are given by the linewidth of each cavity mode: $\kappa_H = 105 \pm 5\mu\text{eV}$ and $\kappa_V = 86 \pm 5\mu\text{eV}$. The difference of damping rates for the two polarizations can be explained by the pillar ellipticity: the lateral confinement is not the same for the two polarizations. As discussed in Sec. 2.2.2, it is not possible to deduce the top mirror output coupling η_{top} nor the input coupling η_{in} , simply from such reflectivity measurement. This is the focus of the next section.

As deduced from this reflectivity measurement, the reflection coefficients depends on the light

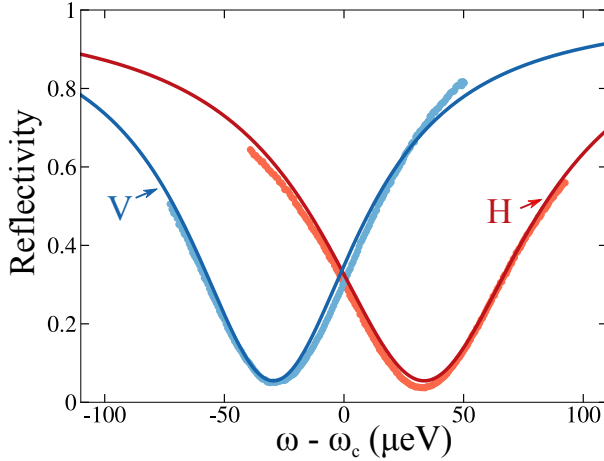


Figure 2.4: Cavity reflectivity for horizontally polarized (red) and vertically polarized (blue) incident light as a function of the laser-cavity detuning energy. Points are experimental data while solid lines are theoretical fits.

polarization and a pillar microcavity has in fact two cavity mode reflection coefficients r_H and r_V for each polarization (assuming $\eta_{in} = 1$):

$$\begin{aligned} r_H &= 1 - 2\eta_{top} \frac{1}{1 - 2i\frac{(\omega - \omega_{c,H})}{\kappa}} \\ r_V &= 1 - 2\eta_{top} \frac{1}{1 - 2i\frac{(\omega - \omega_{c,V})}{\kappa}} \end{aligned} \quad (2.11)$$

They are in general different because $\omega_{c,H} \neq \omega_{c,V}$, so they have different amplitudes and phases.

Consequently, when the cavity is not excited with incident polarization along its cavity axes, horizontally polarized and vertically polarized components are reflected with different reflection coefficients and therefore, the reflected light polarization is rotated. Indeed, let's consider diagonally polarized incoming beam:

$$|\Psi_{in}\rangle = |D\rangle = \frac{1}{\sqrt{2}}(|H\rangle + |V\rangle) \quad (2.12)$$

The incoming beam is composed of horizontal polarization $|H\rangle$ which is reflected with horizontal reflection coefficient: $r_H |H\rangle$, while the vertical polarization is reflected with vertical reflection coefficient: $r_V |V\rangle$.

Consequently, the reflected photons polarization is $|\Psi_m\rangle$:

$$|\Psi_m\rangle = \frac{1}{\sqrt{|r_H|^2 + |r_V|^2}}(r_H |H\rangle + r_V |V\rangle) \quad (2.13)$$

As r_H and r_V are different complex numbers, the reflected polarization can be completely different from the incident diagonal polarization. In the following, we study this cavity-induced rotation of polarization in more details using a technique of polarization reconstruction called polarization tomography, and use it to independently determine the input coupling η_{in} and the top mirror output coupling η_{top} efficiencies.

2.3 Accurate measurement of input/output coupling through polarization tomography.

In this section, the cavity optical response is analyzed in polarization thanks to a technique called polarization tomography. We show that this technique allows the independent and accurate measurement of both the input and output couplings. First, the polarization tomography technique and experimental setups are presented. Second, the reflected polarization is reconstructed for different incident polarizations. Then we show that, thanks to this polarization reconstruction, we can measure with unprecedented accuracy a high $96 \pm 1\%$ input coupling together with a $53 \pm 2\%$ top mirror output coupling. Finally, the same polarization tomography experiment is achieved with single-mode fibered detection.

2.3.1 Polarization tomography technique.

Polarization ellipse representation.

An electromagnetic plane wave can be described by the projections of its electric field in the horizontal-vertical polarization basis E_H and E_V . These two complex numbers characterize the phase and amplitude of the electromagnetic wave in the horizontal-vertical basis. The intensity of horizontally polarized (resp. vertically polarized) light is given by $I_H = |E_H|^2$ (resp. $I_V = |E_V|^2$). The choice of basis is arbitrary and it is possible to choose the diagonal/antidiagonal polarization or the left-handed/right-handed circular polarization basis. For a purely-polarized electromagnetic plane wave, the electric vector generally oscillates in time between the horizontal and the vertical axis. The resulting figure is an ellipse (Fig. 2.5(a)). The complete description of a pure polarization requires two angles: the orientation angle Ψ and the ellipticity angle χ . The orientation angle is the angle between the major ellipse axis and the horizontal axis. The ellipticity angle characterizes the ellipse eccentricity. For a linear polarization, the ellipticity angle is zero ($\chi = 0$), therefore the polarization ellipse is just a line tilted from the horizontal axis by the orientation angle. For example, $\Psi = 0$ corresponds to horizontal polarization, $\Psi = \pi/2$ to vertical polarization and $\Psi = \pi/4$ to diagonal polarization. If $\chi = \pi/4$ (resp. $\chi = -\pi/4$), the light polarization is right-handed (resp. left-handed) circularly polarized.

Poincaré sphere representation.

The polarization ellipse is useful for representing pure polarization states but fails to represent incoherent superpositions of two polarizations. In this chapter and the following, we are interested in the incoherent superposition of polarizations, so we use another representation called the Poincaré sphere (Fig. 2.5(b)). In this representation, pure polarization states are vectors pointing from the center to the sphere surface, and orthogonal polarizations correspond to opposite vectors. The horizontal (H), vertical (V), diagonal (D) and anti-diagonal (A) polarization are positioned on the "equator" while circular-right (R) and circular-left (L) polarizations are at the "north pole" and "south pole", respectively. More generally, any polarization represented with the polarization ellipse representation can be represented by a vector positioned thanks to the orientation and ellipticity angles and reaching the sphere's surface (see Fig. 2.5(b)). The interest of the Poincaré sphere representation is that it also allows to represent an incoherent superposition of polarizations. In that case, it is not possible to clearly define what is the light polarization because of partial depolarization. Partially depolarized light corresponds to a vector that does not reach the surface of the sphere. Completely unpolarized

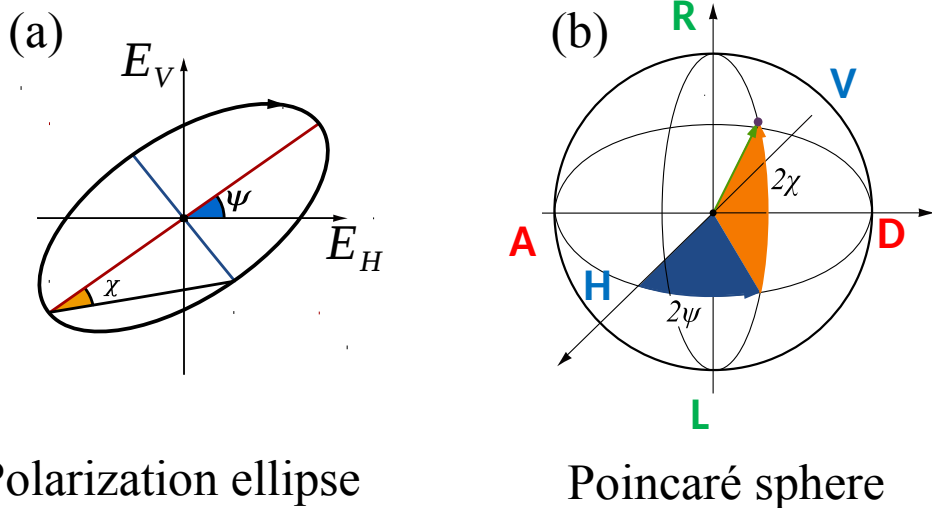


Figure 2.5: Pure polarization state with orientation Ψ and ellipticity χ represented in the polarization ellipse (a) and the Poincaré sphere (b) representations.

light is the limit case where the light is completely depolarized: it is in a balanced incoherent superposition of orthogonal polarizations. This corresponds to the polarization null vector $\vec{0}$ in the Poincaré sphere.

The polarization purity is defined as the norm of the polarization vector in the Poincaré sphere. It quantifies our ability to define the polarization of a given electromagnetic wave. For a pure polarization state, the polarization is well defined, the vector representing the polarization in the Poincaré sphere reaches its surface and therefore the polarization purity is equal to 1. For an incoherent superposition of polarizations, the vector describing the polarization does not reach the surface and therefore the polarization purity is less than one. For a given set of orthogonally-polarized reflected intensities I_{\parallel} and I_{\perp} , we define the Stokes parameter $s_{\parallel\perp}$:

$$s_{\parallel\perp} = \frac{I_{\parallel} - I_{\perp}}{I_{\parallel} + I_{\perp}} \quad (2.14)$$

The Stokes parameter $s_{\parallel\perp}$ corresponds geometrically to the projection of the polarization vector on the axis " \parallel / \perp " in the Poincaré sphere. Consequently, a given polarization is completely described by the set of its three Stokes parameters s_{HV} , s_{DA} and s_{RL} . The polarization purity is given by the Poincaré vector's norm and is therefore equal to $\sqrt{s_{HV}^2 + s_{DA}^2 + s_{RL}^2}$.

In quantum words, the vector can also be seen as a representation of the polarization density matrix ρ . This way, the polarization density matrix can be described by the Stokes parameters:

$$\rho \iff \begin{pmatrix} s_{HV} \\ s_{DA} \\ s_{RL} \end{pmatrix} \quad (2.15)$$

It can be written in the horizontal-vertical basis:

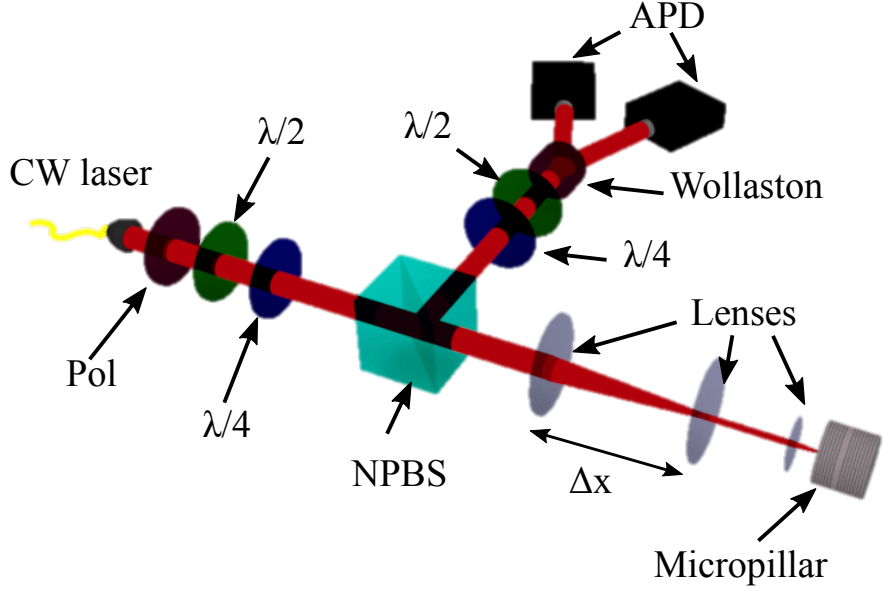


Figure 2.6: Polarization tomography setup. (CW: continuous wave, Pol: polarizer, $\lambda/2$: half waveplate, $\lambda/4$: quarter waveplate, NPBS: non polarizing beam splitter, Wollaston: Wollaston prism, APD: avalanche photodiode)

$$\rho = \begin{pmatrix} \frac{1+s_{HV}}{2} & \frac{s_{DA}+is_{RL}}{2} \\ \frac{s_{DA}-is_{RL}}{2} & \frac{1-s_{HV}}{2} \end{pmatrix} \quad (2.16)$$

For a pure polarization state $|\Psi\rangle$, it can be written as $\rho = |\Psi\rangle\langle\Psi|$.

Presentation of the polarization tomography setup.

In order to reconstruct the polarization density matrix of the reflected light, a possibility is to measure the Stokes parameters. Experimentally, we have designed a polarization tomography setup (Fig. 2.6). A continuous-wave tunable fibered laser resonantly excites the pillar microcavity. The incoming light can be prepared in any polarizations thanks to a set of polarizer and waveplates. Additionally, the incoming laser beam profile $\Phi_i(x,y)$ can be modified in size thanks to a beam adapter made of 3 lenses (with adjustable lens separation Δx). This allows to modify the mode matching with the pillar microcavity. The pillar microcavity is kept inside a helium gas exchange cryostat at a temperature of approximately 10K. The laser is reflected by the pillar microcavity and analysed through a polarization analyser made of 2 accurately characterized waveplates and a Wollaston prism that separate the orthogonal polarizations. The light intensity in each polarization is measured thanks to two free-space avalanche photodiodes. In order to remove as much as possible the detection background, the laser is modulated at a frequency of 70kHz and the two avalanche photodiodes are connected to two lock-in amplifiers.

Thanks to the accurate characterization of the waveplates, it is possible to measure the light intensities reflected by the pillar microcavity in the horizontal/vertical, diagonal/antidiagonal and

circular right/left polarization bases. It is therefore possible to measure the Stokes parameters and completely reconstruct the polarization density matrix of the reflected light.

2.3.2 Experimental polarization tomography reconstruction.

As discussed previously, the input coupling quantifies the proportion of incident light that is interacting with the cavity. Due to the ellipticity of the pillar microcavity, the cavity acts as a birefringent medium that can rotate the polarization of the light that is coupled into and reextracted from it. Thus, the fraction of light that does not couple to the cavity is reflected with the same polarization $|\Psi_{in}\rangle$ while the coupled part can experience a rotation of polarization induced by the cavity, and is thus reflected with polarization $|\Psi_m\rangle$. These two reflected polarizations are reflected in orthogonal spatial modes and consequently are incoherently superposed leading to depolarization of the reflected light. In this section, we will reconstruct the reflected light polarization state and see that we can use this reconstruction to accurately measure the cavity input and output couplings.

Polarization tomography of the reflected light for horizontal/ vertical incident polarization.

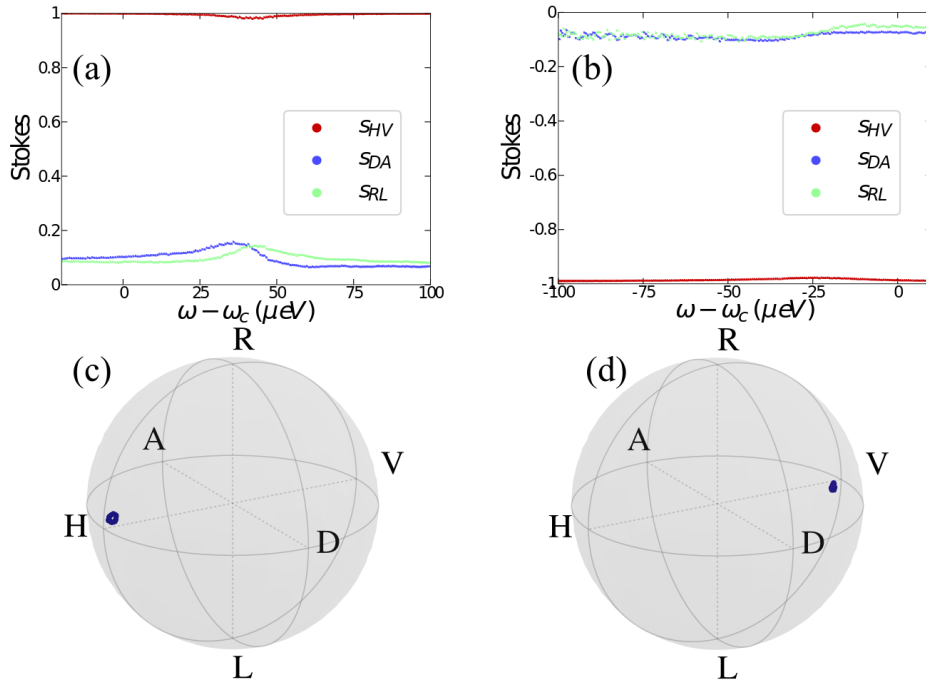


Figure 2.7: Stokes parameters (a) (resp. (b)) of the reflected light for horizontal (resp. vertical) incident polarization. The Stokes parameters value are displayed as a function of the laser energy. (c) (resp. (d)) For each wavelength, the polarization density matrix reconstructed from the Stokes parameters is displayed on the Poincaré sphere. As observed on the Poincaré sphere, with incident polarization along the cavity axis, there is no cavity-induced polarization rotation.

First, the case where the laser excites the cavity along its polarization axes, is explored. There should be no rotation of polarization induced by the cavity. For example, for horizontally polarized

excitation, $|\Psi_{in}\rangle = |H\rangle$, the reflected light should be $|\Psi_m\rangle = r_H/\sqrt{r_H^2}|H\rangle = |H\rangle$.

The total reflectivity was shown in Fig. 2.4. The Stokes parameters s_{HV} , s_{DA} , s_{RL} are measured as a function of the laser-cavity detuning for horizontal incident (Fig. 2.7(a)) and for vertical incident (Fig. 2.7(b)) polarizations.

For incident horizontal polarization, the Stokes parameter s_{HV} is nearly constant equal to 1. s_{DA} and s_{RL} are also roughly constants: this shows that there is no cavity-induced polarization rotation. This means that the laser is reflected with its incident polarization. For all laser wavelength, the reflected polarization is represented in the Poincaré sphere (Fig. 2.7(c)). The reflected polarization is almost identical for all wavelength and is almost horizontal. The same reasoning goes with the polarization reflected from incident vertical polarization excitation (Fig. 2.7(d)).

Still, there are small variations of the three Stokes parameters, that can be due to a small difference between the incident polarization and the cavity polarization axis. Also, with horizontally polarized excitation, s_{DA} and s_{RL} are expected to be zero. The reason why it is not the case experimentally is due to a small tilt between the experimental basis of polarization tomography and the real cavity polarization basis.

Polarization tomography for incident diagonal polarization.

Now, we study what is happening when the cavity is not excited with polarization along its cavity axes. For that purpose, the incident beam is prepared with diagonal polarization:

$$|\Psi_{in}\rangle = |D\rangle = \frac{1}{2}(|H\rangle + |V\rangle) \quad (2.17)$$

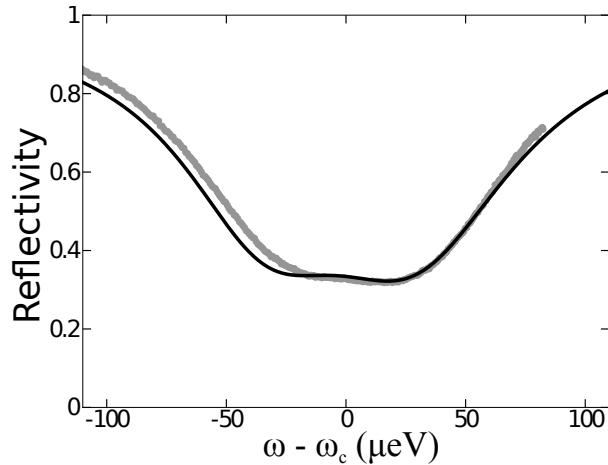


Figure 2.8: Reflectivity of the cavity for diagonally polarized incident light. The points represent experimental data and the solid line represents theoretical fit.

A total reflectivity measurement is displayed in Fig. 2.8 where the total intensity (without selection in polarization $I_{tot} = I_H + I_V$) is normalized by the total incident intensity. The fit displayed in Fig. 2.8 as well as all the fits of this section, will be described later in this chapter. As shown in the experimental data, the cavity response has not the shape of a Lorentzian cavity dip. It demonstrates that the cavity is clearly not excited along its cavity axis. From the discussion in Sec. 2.2.3, a cavity-induced polarization rotation is expected. Fig. 2.9 displays the Stokes parameters as a function of

the laser energy: it clearly shows that there is a polarization rotation of the reflected light. Let us first focus on the evolution of the Stokes parameter s_{DA} . When the laser is far-detuned from the cavity, s_{DA} is close to 1 which means that the reflected polarization is close to the diagonal incident polarization. It is expected because the laser is far-detuned from the cavity, so the incoming beam cannot enter the cavity and therefore, there is no cavity-induced polarization rotation. In resonance with the cavity however, s_{DA} decreases and become negative, so the polarization is quite different from the incident one. Fig. 2.9 also shows variations of the other Stokes parameters, which evidence polarization rotation.

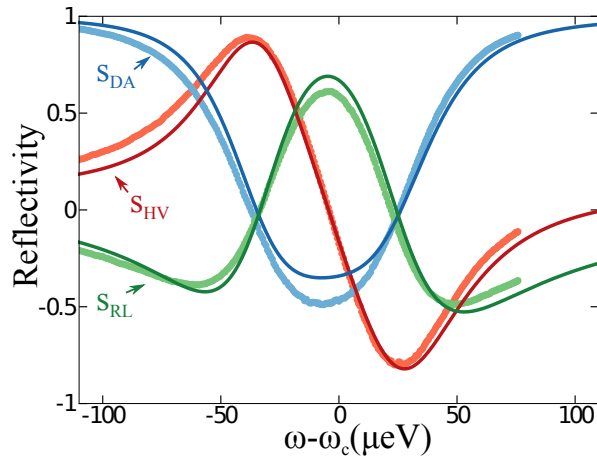


Figure 2.9: Stokes parameters s_{HV} (red), s_{DA} (blue) and s_{RL} (green) of the light reflected by an elliptical micropillar resonantly excited by diagonally polarized light. Points represent experimental data while solid line represent theoretical fits.

In order to visualize the rotation of polarization, Fig. 2.10 displays the polarization density matrix for each wavelength in the Poincaré sphere. Each point corresponds to a given laser-cavity detuning. For strong detunings, the reflected polarization is close to $|\Psi_{in}\rangle \approx |D\rangle$ so there is no polarization rotation. When the laser is tuned into resonance with the cavity energy ω_c , the cavity induces rotation of polarization on the coupled light. This results in a reflected polarization $|\Psi_m\rangle$ very different from the incident polarization. In Fig 2.9, the Stokes parameter s_{DA} is negative in resonance with the cavity, which means that the reflected polarization is closer to $|A\rangle$ than $|\Psi_{in}\rangle \approx |D\rangle$ (which is difficult to visualize in 3D Fig. 2.10). Consequently, there is indeed cavity-induced rotation of polarization. From Fig. 2.10, when the laser is tuned in resonance with the cavity, the reflected polarization cannot be represented by a pure state. This is highlighted by the color scale which displays the polarization purity: when the laser is in resonance with the cavity, the reflected polarization purity decreases to less than 80%.

2.3.3 Measurement of a high cavity mode coupling.

The depolarization discussed previously is a crucial feature in the context of this chapter, as it allows measuring the laser-cavity input coupling efficiency with high accuracy.

Indeed, such depolarization is due to the incoherent superposition of non coupled light, completely reflected with $|\Psi_{in}\rangle$, and the coupled light, which has a rotated polarization $|\Psi_m\rangle$. So for an incident diagonal polarization $|\Psi_{in}\rangle \approx |D\rangle$ with an input coupling η_{in} and intensity I^{in} :

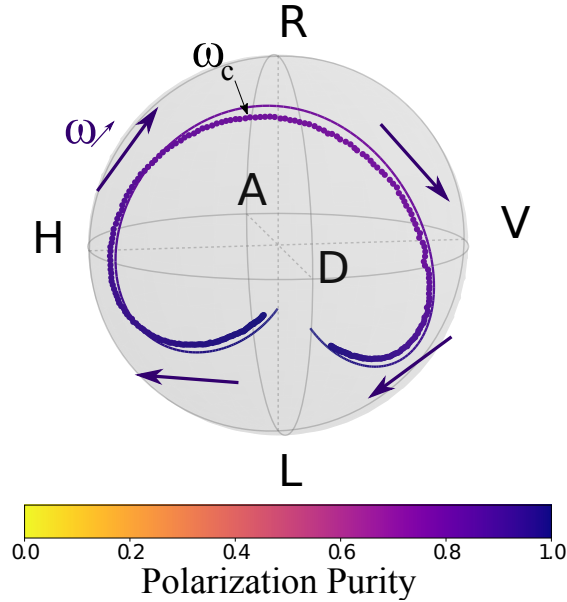


Figure 2.10: Polarization density matrix of the light reflected by an elliptical cavity represented on the Poincaré sphere. The incident polarization is diagonal and each point represents the reflected polarization for a given wavelength. Points are experimental data while the solid line is a theoretical fit. The color of each point represent its polarization purity.

- The uncoupled light with intensity $(1 - \eta_{in})I^{in}$ is completely reflected with polarization $|\Psi_{in}\rangle \approx |D\rangle$ and intensity $I_{\not{H}} = (1 - \eta_{in})I^{in}$.
- The coupled light with intensity $\eta_{in}I^{in}$ is reflected with polarization:

$$|\Psi_m\rangle = \frac{1}{(|r_H|^2 + |r_V|^2)}(r_H|H\rangle + r_V|V\rangle) \neq |\Psi_{in}\rangle \quad (2.18)$$

and intensity $I_m = \eta_{in}R_mI^{in}$ (with R_m , the mode reflectivity).

The intensities of the two beams sum up without interference leading to a total reflectivity:

$$R_{tot} = \frac{I_m + I_{\not{H}}}{I^{in}} \quad (2.19)$$

and a polarization density matrix:

$$\rho = p|\Psi_m\rangle\langle\Psi_m| + (1-p)|\Psi_{in}\rangle\langle\Psi_{in}| \quad (2.20)$$

with p , the proportion of reflected light that is in the same spatial mode as the cavity:

$$p = \frac{I_m}{I_{\not{H}} + I_m} = \frac{\eta_{in}R_m}{(1 - \eta_{in}) + \eta_{in}R_m} \quad (2.21)$$

When the input coupling is optimal ($\eta_{in} = 1$), all the incoming laser is coupled to the cavity mode ($p = 1$), so the reflected light is a pure rotated polarization state $|\Psi_m\rangle$ ($\rho = |\Psi_m\rangle\langle\Psi_m|$).

If the incident laser spatial profile is orthogonal to the cavity mode ($\eta_{in} = 0$), the incident light is not at all coupled to the cavity ($p = 0$), so the reflected polarization is the same as the incident one ($\rho = |\Psi_{in}\rangle\langle\Psi_{in}|$).

In the intermediate case of partial laser-cavity coupling $0 < \eta_{in} < 1$, a fraction p of the reflected light has the cavity mode spatial profile $\Phi_m(x, y)$ and polarization $|\Psi_m\rangle$. The rest of the reflected light is in an orthogonal spatial profile $\Phi_{\perp m}(x, y)$ and has a polarization $|\Psi_{in}\rangle$. Because these two contributions of the reflected light are not in the same spatial profile, they are incoherently superposing which leads to depolarization if the two polarization states $|\Psi_m\rangle$ and $|\Psi_{in}\rangle$ are different. The parameter p , that controls the coupled and uncoupled light contributions (see Eq. 2.20), depends on the cavity reflectivity and on the input coupling η_{in} (see Eq. 2.21). As a result, the polarization purity depends on the input coupling efficiency η_{in} .

In Sec. 2.2.2, we have shown that it is impossible to extract the top mirror output coupling η_{top} and the input coupling η_{in} from a reflectivity measurement. Here, these two coupling parameters seem to have a different influence on the polarization purity, so it may be possible to measure independently η_{in} and η_{top} .

This can be shown by using the model presented in Eqs 2.20, 2.21, 2.19, to fit the experimental data presented in this chapter, namely the reflectivity curves for horizontal, vertical (Fig. 2.4) and diagonal (Fig. 2.8) incident polarizations, and the polarization density matrix presented in Fig. 2.10. Because the cavity mode energies $\omega_{c,H}$, $\omega_{c,V}$ and the cavity damping rates κ_H and κ_V have been extracted from the reflectivity measurements in Fig. 2.4, the only free parameters are the coupling efficiencies η_{top} and η_{in} . The fit result is displayed as a solid line in Fig. 2.4, 2.8 and 2.10. The estimated values for the top mirror output coupling and the input coupling are: $\eta_{top} = 53 \pm 2\%$, $\eta_{in} = 96 \pm 1\%$. Such a moderate top mirror output coupling is expected from the sample number of DBR layer pairs and from the diameter of the pillar that creates additional side losses.

This record input coupling $\eta_{in} = 96\%$ corresponds to the best spatial overlap that we achieved experimentally by careful optical alignment between the freespace optical incident beam and the fundamental cavity mode. This overlap could in principle be improved up to 100% by shaping even more the incoming beam to match perfectly the cavity mode profile. Still, such a high input coupling shows the excellent mode matching between the external electromagnetic field and the cavity mode. This is obtained thanks to the gaussian-like spatial profile of the fundamental mode of a pillar microcavity [180, 181] which is similar to the spatial mode of a single mode fiber.

In addition, the 1% accuracy contrasts with the typical 5% uncertainty of coupling efficiencies estimated by analyzing the input and cavity mode spatial profiles in far-field [182, 171, 172]. This is explained by the strong dependence of the polarization state with the input coupling, as will be highlighted next.

In order to observe this dependence, the experiment is repeated with modified incident beam profile, thus degrading the laser-cavity coupling efficiency. When degrading the cavity coupling, the cavity-induced polarization rotation is reduced and more degradation of the polarization purity is expected. With the same procedure explained before, the Poincaré spheres in Fig. 2.11 were obtained for two other input couplings. As expected, the rotation of polarization is reduced and there is more depolarization. In order to better visualize the depolarization, the polarization purity as a function of the cavity detuning is displayed in Fig. 2.12.

The model presented before is again used to fit the polarization density matrix in the Poincaré sphere (Fig. 2.11) and the polarization purities (Fig. 2.12) for the two other coupling efficiencies. For this new fit, it is worth noting that only the input coupling is considered as a free parameter: all the cavity parameters are fixed (including the top mirror output coupling $\eta_{top} = 53\%$). The resulting

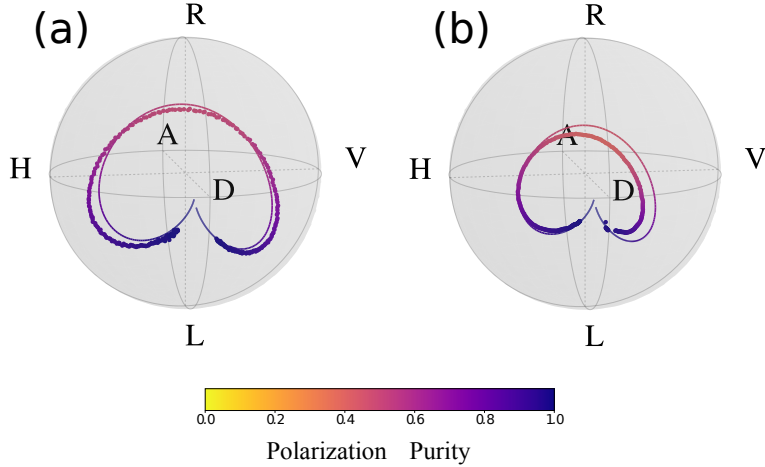


Figure 2.11: Polarization density matrix of the light reflected by the micro-pillar represented in the Poincaré sphere for imperfect coupling and fitted with $\eta_{in} = 85\%$ (a) and $\eta_{in} = 76\%$ (b). Points are experimental data while solid line are fits.

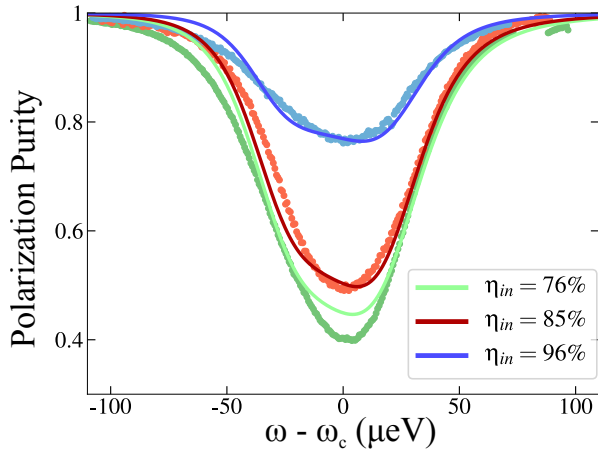


Figure 2.12: Polarization purity of the reflected light for different coupling efficiencies. The blue curves are obtained with best 96% coupling efficiency (it corresponds to the polarization displayed in Fig. 2.10). Red and green curves are obtained with 85% (corresponding to Fig. 2.11(a)) and 76% (corresponding to Fig. 2.11(b)). Points are experimental data and solid lines are theoretical fits.

input couplings measured are $\eta_{in} = 85 \pm 2\%$ (for Fig. 2.11(a)) and $76 \pm 3\%$ (for Fig. 2.11(b)).

Figure 2.13 displays the dependence of the minimum polarization purity with the input coupling, achieved for the laser in resonance with the cavity ($\omega \approx \omega_c$). For high input coupling values (above 80%), the minimum polarization purity is very sensitive to small variations of η_{in} . From the shape of the curve displayed in Fig. 2.13, for a given minimum value of the polarization purity, there are in general two possibilities for η_{in} . However, it is easy to discriminate between the two cases by looking, for example, at the polarizations in the Poincaré sphere. For low values of η_{in} , most of the incident light is not coupled and experiences no rotation of polarization, being then reflected with its incident polarization. For high coupling efficiencies however, most of the light is coupled and experiences

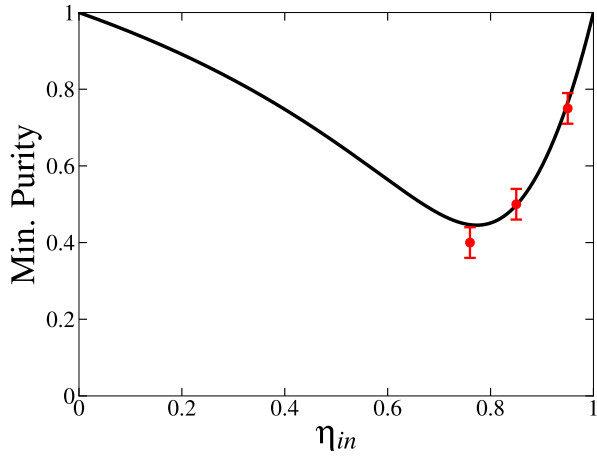


Figure 2.13: Dependence of the polarization purity minimum with the input coupling for the cavity parameters. The red points are the experimental values.

a large rotation of polarization. The sensitivity of the polarization density matrix (and especially its polarization purity) explains why the coupling efficiencies were measured with unprecedented accuracy of 1% for the high (96%) input coupling and 2% for the top mirror coupling.

2.3.4 Fibered polarization tomography of an elliptical cavity.

The experiments carried out previously were realized in free-space. Using a collection fiber however is convenient for plenty of single photon applications [167, 183, 184]. Indeed, after being coupled into a fiber, the photons can be manipulated very easily and with high versatility for different quantum optics experiments that can be free-space, completely fibered or on-chip. It is therefore crucial to efficiently couple the cavity mode (which is the spatial mode of the single photons emitted by a quantum dot embedded in a cavity) into a single mode fiber. Therefore, in this section, we are interested at the optical response in polarization filtered by a single-mode fibered collection. The setup presented in Fig. 2.6 is modified so that the reflected light is passing through a single-mode fiber before being detected by the avalanche photodiodes.

A single mode fiber can be seen as a spatial filter that induces a post-selection on the reflected spatial profile. Previously in Sec. 2.3, we were looking at all the reflected light, without inducing spatial selection onto it. The result was that there was depolarization induced by the different pillar response for the coupled and uncoupled light. These experiments were repeated with this fibered detection and with the same laser-cavity input coupling η_{in} . The polarization density matrix is reconstructed for each wavelength and is displayed in the Poincaré sphere. The results are displayed in Fig. 2.14: for each input coupling, the results for the fibered experiment are plotted together with its free-space counterpart. The main observation is that the light polarization state after fibered selection is always a pure polarization state. Indeed, it stays always on the Poincaré sphere surface, as highlighted by the colorscale showing the polarization purity. Another observation for the case of the maximum input coupling $\eta_{in} = 96\%$ is that the polarization tomography for the free-space and fibered case give qualitatively similar results (apart from the polarization purity) while the results are quite different for the moderate input coupling $\eta_{in} = 76\%$. As a result, the spatial filtering induced by single-mode fibered detection seems to distort the cavity polarization response and does it

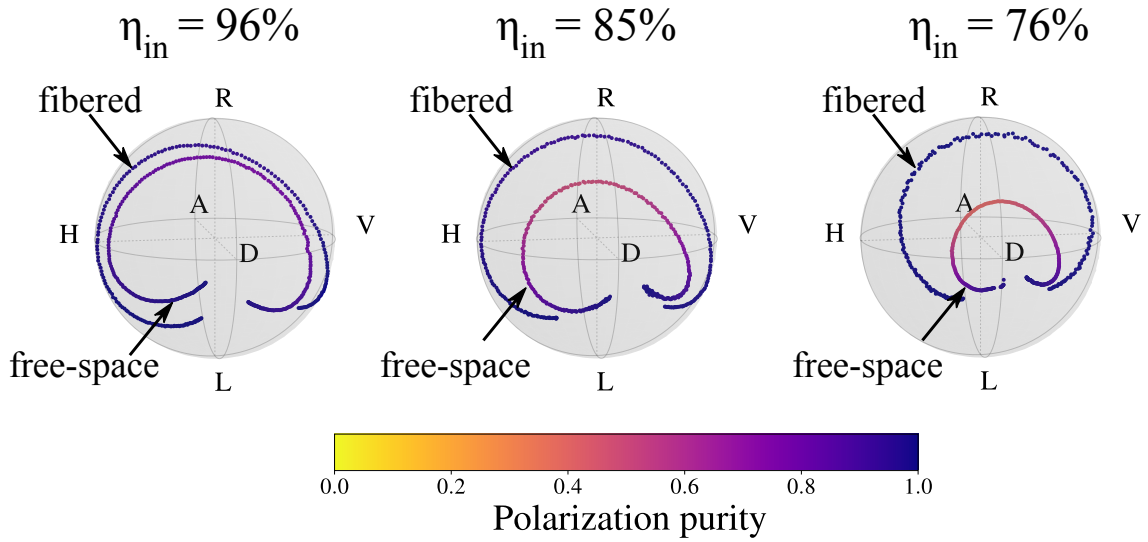


Figure 2.14: Comparison of the polarization tomography with and without fiber single mode selection. The results obtained in Sec. 2.3 for different input couplings are plotted again to be compared to the case where there is a single-mode fiber spatial filtering.

all the more that the incident coupling is not optimal. The explanations of these fibered polarization tomography results will be provided in the theoretical section (Sec. 2.5).

2.4 Polarization rotation as a resource for coupling optimization.

2.4.1 Presentation of the principle.

In the previous section, it has been shown that polarization tomography is a technique that can be used for measuring with unprecedented accuracy the cavity couplings parameters. Here, we show that it can be a tool to maximize the coupling efficiency to the cavity mode. Indeed, the cavity-coupled light can be separated from the uncoupled light because they have different polarizations. By setting a polarizer orthogonal to the uncoupled polarization $|\Psi_{in}\rangle$ (which is the same as the incident polarization), the coupled light with polarization $|\Psi_m\rangle$ is separated from the uncoupled light. Therefore, it is possible to observe only the cavity mode spatial profile $\Phi_m(x,y)$, and to optimize the laser-cavity coupling by shaping the laser mode profile $\Phi_i(x,y)$, to maximize the overlap with the cavity mode.

2.4.2 Observation of the cavity mode characteristics.

Separating the coupled light can be realized with the polarization tomography setup (Fig. 2.6) or its fibered version. For this section, the experimental results were obtained with the setup presented in Fig. 2.15. In this setup, the laser beam is passing through a polarizing beam splitter before and after being reflected by the device. Any linear polarization can be prepared thanks to a half waveplate between the polarizing beam splitter and the device. After being reflected by the device, the photons transmitted by the polarizing beam splitter are automatically orthogonal in polarization to the laser incident polarization $|\Psi_{in}\rangle$ and therefore corresponds to reflected light coupled to the cavity mode.

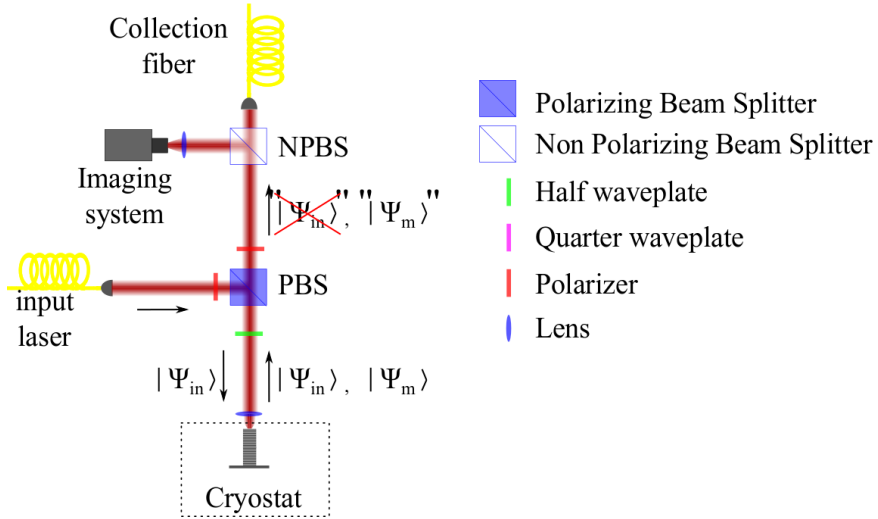


Figure 2.15: Scheme of the optical setup used in this section. Only the cavity-coupled light can be transmitted by the polarizing beam splitter.

Therefore, the coupled light is completely separated from the uncoupled light. In this setup (Fig. 2.15), an imaging system is placed after the polarizing beam splitter, which allows to image the mode directly onto the pillar.

Fig 2.16(a) is an image of the pillar device obtained with small white light intensity: it is possible to observe the typical shape of the electrically contacted pillar devices designed in the group, namely the circle and four ridges structure as well as the diode nearby (on the right).

When the incident resonant laser is switched on, the image (Fig. 2.16(b)) is similar to the previous one except at the center of the four ridges. At this position, the detected light intensity is much higher than previously. This corresponds to the cavity mode which is positioned at the connection between the 4 ridges. In order to have a better visualization, below each image is plotted the intensity detected by the camera along the dashed horizontal red line. Hence, the additional light observed on the image has the cavity mode shape. By doing the difference of image Fig. 2.16(b) and Fig. 2.16(a), we obtain the Fig. 2.16(c). This figure is a visualization of the cavity mode spatial profile.

Therefore, the cavity mode has indeed a nearly-gaussian profile that can be fitted in the horizontal and vertical direction: the double waist w of the cavity mode along the x axis (y axis) is $2w_x = 1.9\mu m$ ($2w_y = 2.3\mu m$). Consequently the cavity mode is not perfectly circular. This analysis of the cavity mode profiles is repeated on different pillar devices and we obtain similar asymmetry. It might be due to the intrinsic pillar ellipticity.

From this we can deduce the incoming laser shape and position required to maximally couple into the pillar microcavity.

2.4.3 Cross-polarized intensity to maximize the cavity coupling.

The last point of this discussion on the observation of the cavity mode is that this cross-polarized technique is also useful to optimize the cavity input coupling and fiber collection.

Indeed, with an incoming laser with given incident polarization $|\Psi_{in}\rangle$ and constant intensity, the reflected intensity cross-polarized to the incident laser depends linearly on the cavity input coupling

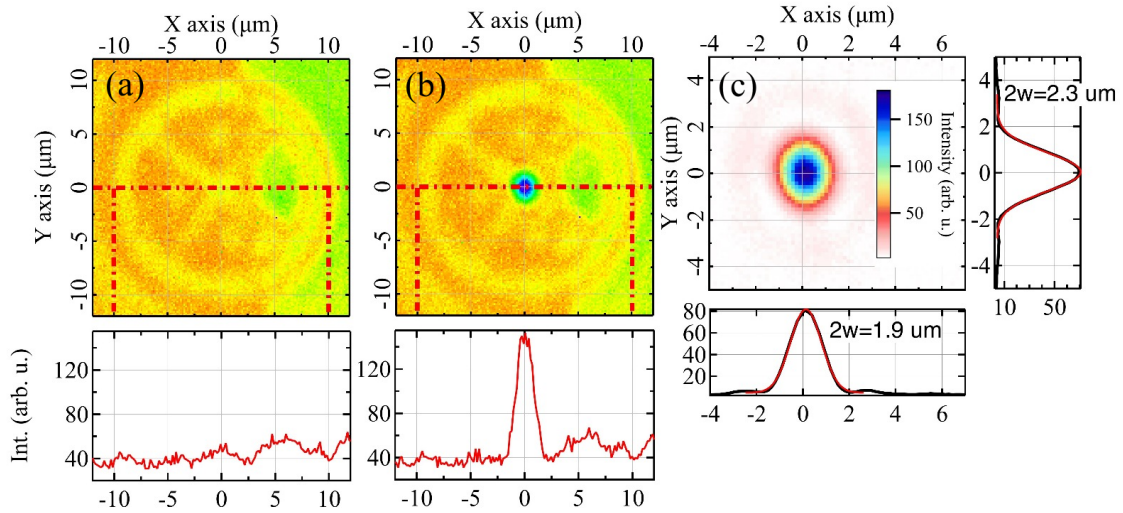


Figure 2.16: Cavity mode imaging. The imaging system with laser off (a) and with the laser on (b) evidencing the cavity mode. The graph below each images represents the light intensity on the red dashed line at $y = 0 \mu\text{m}$ (c) The subtraction of the two images evidencing the cavity mode. The side graphs represent the average intensity for the y axis (right plot) and the x axis (plot below).

η_{in} . Maximizing the cross-polarized intensity (therefore, the light in the collection path of the setup) results in maximizing the coupling. This technique can be used to fine-tune the alignment in order to maximize the coupling η_{in} .

In the case of a setup with single-mode fibered collection, because the photons transmitted by the polarizing beam splitter have the cavity mode profile, the coupling η_{mc} into the collection single-mode fiber can also be optimized by maximizing the intensity into the fiber. A consequence is that under resonant excitation, the only way to maximize the cross-polarized intensity in the collection fiber is by maximizing both the input coupling and the fiber collection coupling with the cavity. This is quite interesting as it provides a quantity that can only be maximized by improving the cavity couplings parameters. This technique is therefore used for alignment fine-tuning on a daily basis in our lab. By observing the cross-polarized intensity before and after the collection fiber, coupling efficiencies of around 90% between the cavity mode and the collection fiber have been achieved.

2.5 Theory: polarization rotation in free-space and fibered configurations.

In order to explain the experimental results and especially the fibered ones (see Sec. 2.3), a more complete model must be built that is based on the input-output formalism. This formalism takes into account the intracavity field and the external incoming and escaping field that are coupled to the cavity mode. Here, it should be generalized to also take into account uncoupled electromagnetic fields. This model will be also used for all the other theoretical simulations done in this thesis. We will first introduce the input-output formalism and then extend it to the case of imperfect input coupling and single-mode fibered collection.

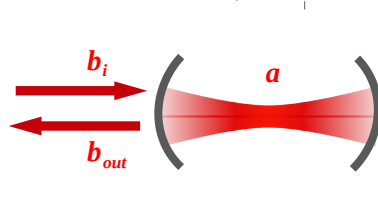


Figure 2.17: Input-output formalism.

2.5.1 Input-output formalism.

The input-output formalism (Fig. 2.17) [185] describes a lossy cavity that is interacting with an external light field mode. In the case of interest here, a laser beam is resonantly exciting a cavity from the top mirror and we are interested with the reflected light. For the moment, we assume that the external field is completely coupled to the cavity mode ($\Phi_i(x, y) = \Phi_m(x, y)$). The input (resp. output) external field operator \hat{b}_{in} (resp. \hat{b}_{out}) corresponds to the incident (escaping) external field that couples with the cavity from the top mirror. It is proportional to the electric field \vec{E}_{in} (resp. \vec{E}_{out}) and is normalized so that $\langle \hat{b}_{in}^\dagger \hat{b}_{in} \rangle$ is in photon per unit of time. The intracavity field is described by the operator \hat{a} (which corresponds to the annihilation operator if the field is quantized). Using these definitions, $\langle \hat{b}_{in}^\dagger \hat{b}_{in} \rangle$ is the flux of incoming photons, $\langle \hat{b}_{out}^\dagger \hat{b}_{out} \rangle$ is the flux of reflected photons and $\langle \hat{a}^\dagger \hat{a} \rangle$ is the mean intracavity photon number. The input-output relation states that:

$$\hat{b}_{out} = \hat{b}_{in} + \sqrt{\kappa_{top}} \hat{a} \quad (2.22)$$

For coherent optical beam, field operators are completely described by their mean values $\hat{a} = \langle \hat{a} \rangle$, $\hat{b}_{in} = \langle \hat{b}_{in} \rangle$ and $\hat{b}_{out} = \langle \hat{b}_{out} \rangle$, so we can introduce the notations $a = \langle \hat{a} \rangle$, $\hat{b}_{in} = b_{in}$, $\hat{b}_{out} = b_{out}$. It can be shown [185, 186, 187, 188], that, for an empty cavity, the intracavity annihilation operator is given by:

$$a = -2 \frac{\sqrt{\kappa_{top}}}{\kappa} \frac{1}{1 - i\Delta} b_{in} \quad (2.23)$$

where Δ is the normalized laser-cavity detuning (Eq. 2.2).

The reflection coefficient r_{cav} is given by:

$$r_{cav} = \frac{b_{out}}{b_{in}} \quad (2.24)$$

With this relation and Eq. 2.23, the cavity reflection coefficient formula given in Eq. 2.1 is obtained.

In the case of an elliptical cavity, this can be extended to the horizontal and vertical polarizations. We use the subscripts "H" and "V" to denote the operators corresponding to the two cavity modes:

$$\begin{aligned} \hat{b}_{out,H} &= \hat{b}_{in,H} + \sqrt{\kappa_{top}} \hat{a}_H \\ \hat{b}_{out,V} &= \hat{b}_{in,V} + \sqrt{\kappa_{top}} \hat{a}_V \end{aligned} \quad (2.25)$$

A pure incident polarization is written $|\Psi_{in}\rangle = 1/\sqrt{|b_{in,H}|^2 + |b_{in,V}|^2} (b_{in,H}|H\rangle + b_{in,V}|V\rangle)$. The output field operators can be described for any polarizations. It is convenient to use other output

operators:

$$\begin{aligned}\hat{b}_{out,D} &= \frac{1}{\sqrt{2}}(\hat{b}_{out,H} + \hat{b}_{out,V}) \\ \hat{b}_{out,A} &= \frac{1}{\sqrt{2}}(\hat{b}_{out,H} - \hat{b}_{out,V}) \\ \hat{b}_{out,R} &= \frac{1}{\sqrt{2}}(\hat{b}_{out,H} + i\hat{b}_{out,V}) \\ \hat{b}_{out,L} &= \frac{1}{\sqrt{2}}(\hat{b}_{out,H} - i\hat{b}_{out,V})\end{aligned}\tag{2.26}$$

With these operators, the intensity reflected in any polarization "j" is given by:

$$I_j = \langle \hat{b}_{out,j}^\dagger \hat{b}_{out,j} \rangle\tag{2.27}$$

So for coherent field, $I_j = |b_{out,j}|^2$. This way, it is possible to compute theoretically the Stokes parameters for orthogonal polarizations "i" and "j":

$$s_{ij} = \frac{I_i - I_j}{I_i + I_j}\tag{2.28}$$

With a perfectly mode-matched cavity, the reflected polarization is in a coherent superposition of horizontal and vertical polarizations and therefore there is no depolarization.

2.5.2 Imperfect input coupling.

Previously, the spatial mode of the cavity and the external modes were considered to be the same. In general, this is not the case: the incident electromagnetic field has a spatial profile $\Phi_i(x,y)$ that is in general different from the cavity spatial profile $\Phi_m(x,y)$. To take into account imperfect cavity mode couplings and to theoretically explain the experimental data, the input output formalism presented previously must be generalized.

The input coupling η_{in} is defined as the overlap between the incident mode and cavity mode spatial profile (see Eq. 2.5). The output beam has a spatial profile $\Phi_{out}(x,y)$ and can be decomposed as:

$$b_{out}\Phi_{out}(x,y) = b_{in}\Phi_i(x,y) + \sqrt{\kappa_{top}}a\Phi_m(x,y)\tag{2.29}$$

with:

$$a = -2\frac{\sqrt{\kappa_{top}}}{\kappa} \frac{1}{1-i\Delta} \sqrt{\eta_{in}} b_{in}\tag{2.30}$$

Indeed, the light intensity inside the cavity depends also only on the part of the incident external light field that has the same spatial overlap with the cavity mode so $|a|^2$ must be proportional to $\eta_{in}I_i = |\sqrt{\eta_{in}}b_{in}|^2$, and consequently a must be proportional to $\sqrt{\eta_{in}}$.

The incoming spatial mode $\Phi_i(x,y)$ can be decomposed using Eq. 2.7 then decomposed such that:

$$\begin{aligned}b_{out}\Phi_{out}(x,y) &= (\sqrt{\eta_{in}}b_{in} + \sqrt{\kappa_{top}}a)\Phi_m(x,y) + \left(\sqrt{1-\eta_{in}}b_{in}\right)\Phi_{\not{m}}(x,y) \\ b_{out}\Phi_{out}(x,y) &= b_{out}^{(m)}\Phi_m(x,y) + b_{out}^{(\not{m})}\Phi_{\not{m}}(x,y)\end{aligned}\tag{2.31}$$

This equation shows that a fraction η_{in} of the incoming beam is overlapping with the cavity mode $\Phi_m(x,y)$ and that the rest of the incoming beam is in a spatial mode $\Phi_{\not{m}}(x,y)$ which is not overlapping

at all with the cavity mode. The reflected field b_{out} has therefore two components corresponding to the coupled light $b_{out}^{(m)}$ and to the uncoupled light $b_{out}^{(\eta)}$.

Let us consider first the coupled part $b_{out}^{(m)}$. It has a spatial profile $\Phi_m(x, y)$ and is governed by Eq. 2.22 which needs to be slightly modified: b_{in} is converted in $\sqrt{\eta_{in}}b_{in}$ because not all the incident light is coupled to the cavity mode:

$$b_{out}^{(m)} = \sqrt{\eta_{in}}b_{in} + \sqrt{\kappa_{top}}a \quad (2.32)$$

with:

$$a = -2\frac{\sqrt{\kappa_{top}}}{\kappa} \frac{1}{1-i\Delta} \sqrt{\eta_{in}}b_{in} \quad (2.33)$$

The uncoupled part is given by $b_{out}^{(\eta)} = \sqrt{1-\eta_{in}}b_{in}$, and therefore, the output uncoupled intensity is given by $(1-\sqrt{\eta_{in}})I_i = |\sqrt{1-\eta_{in}}b_{in}|^2$.

Because, the coupled and uncoupled reflected light are in different spatial profiles $\Phi_m(x, y)$ and $\Phi_{\eta}(x, y)$, the total reflected output flux $|b_{out}|^2$ is given by:

$$|b_{out}|^2 = |b_{out}^{(m)}|^2 + |b_{out}^{(\eta)}|^2 \quad (2.34)$$

$$|b_{out}|^2 = |b_{in}|^2 \left((1-\eta_{in}) + \eta_{in} \left(1 - 2\eta_{top} \frac{1}{1-i\Delta} \right)^2 \right) \quad (2.35)$$

$$|b_{out}|^2 = |b_{in}|^2 ((1-\eta_{in}) + \eta_{in}|r_{cav}|^2) \quad (2.36)$$

Which gives the same result for the total reflectivity $R_{tot} = |b_{out}|^2/|b_{in}|^2$ as in Eq. 2.9 so this model satisfactorily explain the response of a cavity under non optimal input coupling.

In the case of an elliptical cavity, these equations can also be generalized using the same procedure as in Sec. 2.5.1. However, for a polarization "j", the intensity is now given by:

$$\begin{aligned} I_{out,j} &= I_{out,j}^{(m)} + I_{out,j}^{(\eta)} \\ I_{out,j} &= |b_{out,j}^{(m)}|^2 + |b_{out,j}^{(\eta)}|^2 \end{aligned} \quad (2.37)$$

2.5.3 Single-mode fibered detection.

Now, let's consider the case where the detection uses a single-mode fiber. Only the reflected light with the same spatial mode as the fiber $\Phi_c(x, y)$ is collected. Let us define the overlapping functions corresponding respectively to the overlap between the collection mode (or more accurately, the collection fiber mode propagated to the cavity position, see Figure 2.18) and the input mode and between the collection mode and the cavity mode:

$$\eta_{ic} = \left| \int \int \Phi_i(x, y) \Phi_c(x, y)^* dx dy \right|^2 \quad (2.38)$$

$$\eta_{mc} = \left| \int \int \Phi_m(x, y) \Phi_c(x, y)^* dx dy \right|^2 \quad (2.39)$$

Only the reflected light with the same spatial profile as the collection fiber $\Phi_c(x, y)$ is taken into account. The flux of reflected light collected by the fiber is named b_{coll} . In the Equation 2.22, the

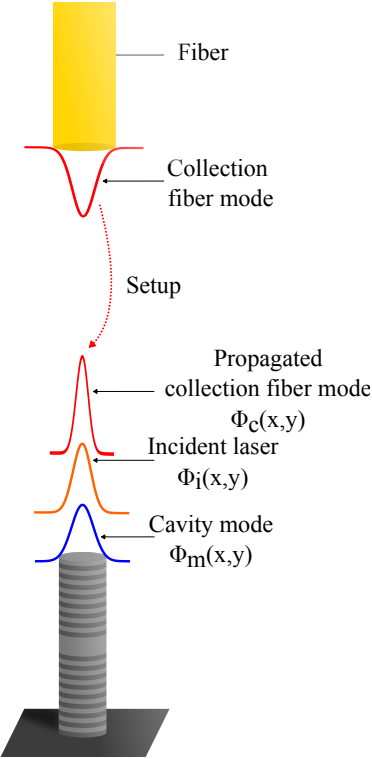


Figure 2.18: Scheme representing all relevant mode profiles at the pillar position.

incident and cavity mode profiles need to be modified into their overlap with the collection fiber profile:

$$b_{coll} = b_{in} \sqrt{\eta_{ic}} + \sqrt{\kappa_{top}} a \sqrt{\eta_{mc}} \quad (2.40)$$

It can be rewritten as:

$$b_{coll} = b_{in} \sqrt{\eta_{ic}} \left(1 + \sqrt{\kappa_{top}} \sqrt{\frac{\eta_{mc}}{\eta_{ic}}} \frac{a}{b_{in}} \right) \quad (2.41)$$

The intra-cavity field a is still given by Eq. 2.33. So, the flux of photons b_{coll} is given by :

$$b_{coll} = b_{in} \sqrt{\eta_{ic}} \left(1 - 2\eta_{top} \sqrt{\frac{\eta_{in}\eta_{mc}}{\eta_{ic}}} \frac{1}{1-i\Delta} \right) \quad (2.42)$$

The reflection coefficient after fiber, $r = b_{coll}/b_{in}$, is:

$$r = r_{cav}^{(eff)} \sqrt{\eta_{ic}} \quad (2.43)$$

Where $r_{cav}^{(eff)}$ is similar to the theoretical reflection coefficient of a cavity with an *effective* top mirror output coupling:

$$\eta_{top}^{(eff)} = \eta_{top} \sqrt{\frac{\eta_{in}\eta_{mc}}{\eta_{ic}}} \quad (2.44)$$

This also can be extended to an elliptical cavity with output flux operators $b_{coll,H}$ and $b_{coll,V}$. As was observed experimentally in Figure 2.14, the polarization reconstruction of reflected light with single-mode fibered selection evidences that the reflected light is completely pure in polarization.

This shows that the horizontally-polarized and vertically-polarized fractions of the collected light are in the same spatial mode and thus, are coherently superposing, leading to a pure polarization state. Up to a normalization factor η_{ic} , corresponding to the overlap between the incident laser spatial profile and the collection fiber spatial profile, the cavity response after spatial filtering behaves exactly as a perfectly mode-matched cavity with an effective top mirror output coupling that depends on the coupling efficiencies of the different light field spatial profiles. This can be observed in Fig. 2.14: the fibered spatial selection modifies the reflection coefficient so that it is similar to a perfectly coupled cavity.

In the context of quantum dots coupled to cavities, because fibered detection remove the cavity coupling-induced depolarization, if depolarization is still measured, it should be induced by noise mechanisms induced on the quantum dot.

In addition, having an effective top mirror output coupling means that it is possible to modify the interference strength between the directly reflected light and the light that enters the cavity and escapes from the top mirror. As can be seen in *Arnold et al.*[27], the top mirror coupling is a crucial figure of merit for spin-dependent polarization rotation induced by a charged quantum dot, so it is interesting to be able to effectively control it with such considerations. There is an important drawback of this technique though: controlling the effective top mirror output coupling requires to modify the relative overlaps between each mode profiles, thus reducing the micropillar reflectivity and consequently, reducing the probability to collect the reflected photons.

2.6 Conclusion.

In this chapter, we have presented the polarization tomography technique and have shown the link between the cavity coupling parameters and the optical polarization response, both experimentally and theoretically. The cavity mode profile was imaged experimentally and a record high input coupling of 96% was measured with unprecedented $\pm 1\%$ accuracy. In addition, with single-mode fibered collection, we have shown that the input and output fiber-cavity couplings does not degrade the polarization purity but modify the effective top mirror output coupling which can be useful for cavity-QED problems.

In the next chapter, the same polarization tomography technique is used on a quantum dot-cavity device, in order to demonstrate the macroscopic quantum-dot induced polarization rotation.

Chapter 3

Quantum-dot induced polarization rotation and depolarization

3.1 Introduction to quantum-dot induced optical phase shift.

For the development of solid-state photonic quantum networks [3], cavity-QED devices should operate both as emitters and as receivers of single photons [156]. The single-photon emitter aspect of the cavity-QED devices is explored in the next chapter.

As a receiver, a cavity-QED device should allow manipulating the atom state with single photons [168] and, reciprocally, manipulating the single photon state with the atom [169, 54, 170]. In this respect, pillar microcavities have demonstrated intrinsically good performances, enhancing drastically the light-matter interaction and allowing high input/output coupling efficiencies. As was discussed in the previous chapter, incoming photons can be efficiently coupled to a microcavity [44]. It has been shown that a quantum dot coupled to such microcavities can be controlled with few-photons incoming fields [171, 172, 173]. Reciprocally, a coupled quantum-dot modifies drastically the properties of the incoming photons [174, 175]. The photon statistics can be completely modified to produce non-classical light [136, 189, 190] which is potentially useful to produce path-encoded photon-photon gates [173]. Quantum dots also modify the incoming photon polarization by inducing a giant polarization rotation. This has been demonstrated in the case of the confined spin of a charged quantum dot device [27] and is a first step toward deterministic polarization-encoded quantum operations between single spins and single photons [124, 123, 191, 192].

This quantum dot-induced macroscopic polarization rotation is the main focus of this chapter. It is usually interpreted by considering the quantum dot as a phase-shifter [177, 179] that modifies the accumulated phase of a photon coupled to a cavity. However, the concept of optical phase shift relies on a semi-classical picture where the quantum emitter response is coherent with the incoming field, i. e. keeps a well-defined phase and amplitude. Yet, generally, the response of a quantum emitter is partially incoherent, so a complete analysis has to include both the coherent and incoherent parts of the optical response of resonantly-excited quantum dots [163, 193, 194]. This implies that the outgoing polarization is generally not a pure polarization state.

In this chapter, we experimentally reconstruct through polarization tomography, the macroscopic QD-induced polarization rotation which is accompanied with a small degradation of the polarization purity. We demonstrate a polarization rotation of more than 20° both in latitude and longitude, induced by a neutral quantum dot, with a polarization purity above 84%. Finally, to theoretically

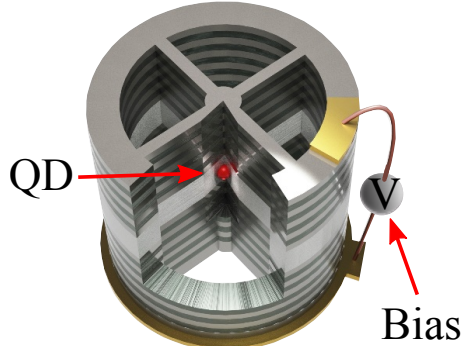


Figure 3.1: Scheme of an electrically contacted pillar microcavity coupled to a neutral quantum dot. The bias voltage is used to tune the quantum dot wavelength by Stark shift.

interpret this polarization tomography, an exact model of the cavity-QED device is introduced. This model evidences the different influences on polarization of various noise mechanisms, allowing to deduce the dominant noise mechanism at play for the device.

3.2 Experimental polarization tomography.

3.2.1 Setup and micropillar sample.

In this section, the polarization rotation induced by a single quantum dot is reconstructed through polarization tomography. This rotation of polarization is increased thanks to the strong interaction with the cavity light field because the quantum dot is deterministically positioned into the pillar microcavity thanks to the in-situ technique (see Sec. 1.4.2 for a detailed presentation of the technique)[24]. Figure 3.1 shows the sample under study in the present chapter, which is an electrically-tunable quantum dot deterministically coupled to a pillar microcavity. The electrical contact allows the electric fine-tuning of the quantum dot emission energy by Stark shift and also, stabilizes the quantum dot electric environment. The quantum dot is neutral which means that its stable fundamental state consists in a valence band completely filled by electrons and an empty conduction band: there are no excess charges inside the quantum dot. This type of quantum dot is optically activated by promoting an electron from the valence band to the conduction band, thus creating an electron-hole pair also called an exciton (see Sec. 1.1.1). The fundamental exciton is obtained by the absorption of a photon of typically $\approx 930\text{nm}$ (927.29nm for this specific sample).

The optical polarization induced by a single neutral quantum dot is investigated here. The experiment is similar to the one carried out in the previous chapter: the cavity-QED device is scanned in wavelength with a CW laser (with a given incident polarization) and the quantum dot-induced polarization rotation is reconstructed thanks to the polarization tomography technique. For this purpose, the cavity-QED device is investigated thanks to the polarization tomography setup already presented in the previous chapter (see Fig. 2.6).

As was evidenced in the previous chapter, a pillar microcavity itself can induce polarization rotation. In order to be sure that the observed polarization rotation is induced by the quantum dot, the incoming polarization is chosen along one of the pillar polarization axes. In that case, there is no cavity-induced polarization rotation, as was demonstrated in the previous chapter (see Fig. 2.7).

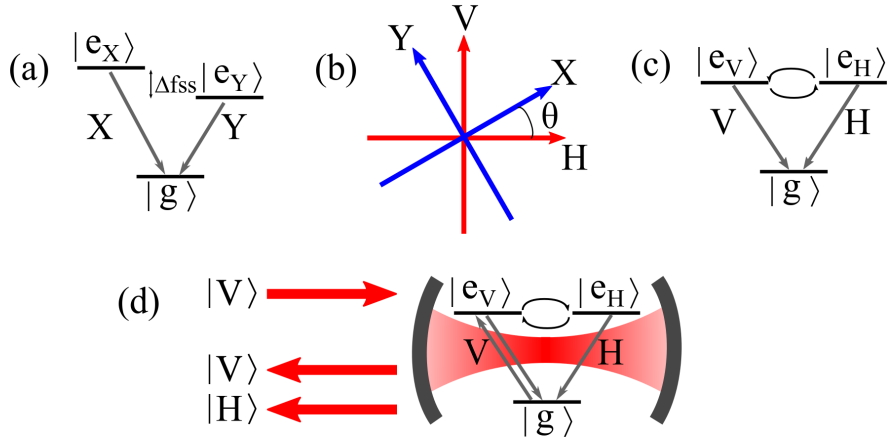


Figure 3.2: (a) Energy levels of a neutral quantum dot. There are two exciton states ($|e_X\rangle$ and $|e_Y\rangle$) separated by a fine structure splitting energy (Δf_{ss}). A quantum dot in the exciton state $|e_X\rangle$ ((resp. $|e_Y\rangle$)) can emit a photon with linear polarization X (resp. Y) to go back to its fundamental mode $|g\rangle$. (b) Polarization ellipse representation (see Fig. 2.5) of the X and Y polarizations. The linear polarizations X and Y are orthogonal and can be different from the cavity polarization axes. (c) Energy levels of a neutral quantum dot rewritten in the basis of cavity eigenaxes "H/V". $|e_H\rangle$ and $|e_V\rangle$ are not eigenstates, and therefore they coherently precess until the emission of a photon. (d) Scheme of the cavity input and output fields. The embedded quantum dot levels are expressed in the basis of the cavity eigenaxes "H/V".

With an incoming polarization along the cavity axis, if any rotation of polarization is observed, it is induced by the quantum dot; the pillar microcavity only amplifies the rotation due to the cavity-enhanced light-matter interaction.

For all the results obtained in this chapter, the incident CW laser is prepared with vertical polarization (Fig. 2.6). The mode matching is not perfectly optimized resulting in a moderate cavity input coupling of $79 \pm 5\%$ (the experiment was carried out before the one in the previous chapter, explaining why the input coupling is not properly optimized and not accurately measured). The reflected light is measured in polarization thanks to the polarization analyzer and with free space avalanche photodiodes.

3.2.2 Principle of quantum dot-induced polarization rotation.

The polarization rotation induced by a neutral quantum dot is explained as follows. Due to the Stranski-Krastanov growth process [28], quantum dots are not perfectly cylindrical. This induces a lift of degeneracy of all integer spin states of a quantum dot. Because an exciton has an integer spin (it is made of a heavy hole of spin $3/2$ and an electron of spin $1/2$), it is therefore energy-splitted as displayed in Fig. 3.2 (a). The two excited states ($|e_X\rangle$ and $|e_Y\rangle$) are generally separated by an energy Δf_{ss} of the order of several tens of μeV , but in this sample it is reduced to $\approx 10\mu\text{eV}$ ($\Delta f_{ss} = 9 \pm 2\mu\text{eV}$ for the quantum dot under study) due to the thermal annealing in the fabrication process. These two states are optically active with orthogonal linear polarizations X, Y. In general, these two polarizations are different from the polarization axes of the cavity (Fig. 3.2 (b)). When the laser is resonantly exciting the quantum dot with vertical polarization, it is populating a state $|e_V\rangle$. However, this state is not an eigenstate of the quantum dot (it is, in general, a superposition of $|e_X\rangle$ and $|e_Y\rangle$), so

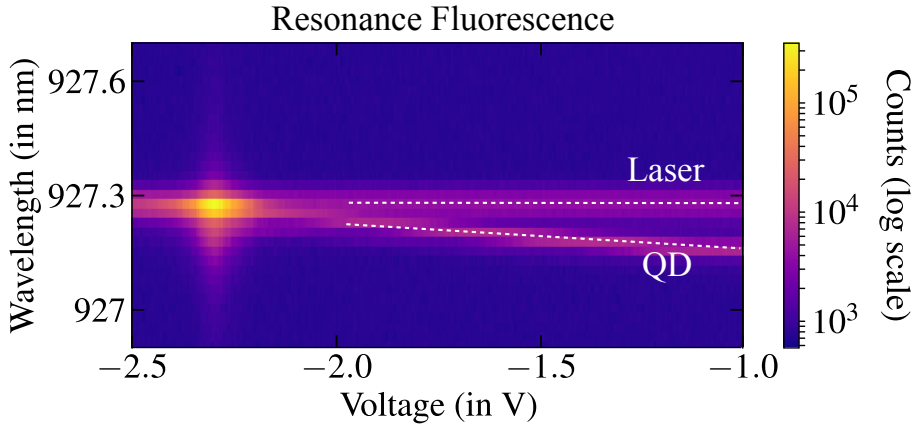


Figure 3.3: Horizontally-polarized resonance fluorescence of the neutral quantum dot as a function of the bias voltage and emission energy. The laser wavelength is set at 927.29nm. The quantum dot wavelength is tuned in resonance with the CW laser by applying -2.33V .

it coherently evolves and oscillates between the states $|e_H\rangle$ and $|e_V\rangle$, interacting with horizontal and vertical polarizations respectively (see Fig. 3.2 (c)). When the exciton is eventually decaying back to the ground state by emitting a photon, this photon can be polarized with not only vertical but also horizontal polarization. So, as shown in Fig. 3.2 (d), a quantum dot-pillar device resonantly excited with vertical polarization reflects photons with both vertical and horizontal polarizations.

3.2.3 Neutral quantum dot single-photon emission.

In the following, as illustrated in Fig. 3.2(d), the incoming laser is prepared with vertical polarization, and we will denote as horizontally-polarized reflected light, and vertically polarized reflected light, the two polarization components of the reflected light. In this section, let us focus on the horizontally-polarized reflected light and show that it has interacted with the quantum dot, by analyzing its single photon-statistics.

The laser is prepared in the low-power regime ($P_{in} = 200\text{pW}$) and at 927.29nm-wavelength, which corresponds to the vertically-polarized cavity mode wavelength. The horizontally-polarized reflected light is observed with a spectrometer. The quantum dot can be tuned in and out of resonance with the laser thanks to the electrical tuning. The results are displayed in Fig. 3.3, showing the cross-polarized reflected intensity for different bias voltages. Let us focus first on what is happening around -1V . At this voltage, there is residual light at the laser wavelength (horizontal line) which corresponds to imperfect extinction of the laser. There is also residual light at the quantum dot wavelength which corresponds to Raman-assisted quantum dot emission. When the voltage is more negative, the quantum dot wavelength is closer to the laser wavelength and at a voltage of -2.33V , the quantum dot is eventually tuned into resonance with the laser, leading to a strong increase of the cross-polarized reflected intensity by almost two orders of magnitude. This demonstrates that the quantum dot indeed scatters photons in the horizontal polarization, cross-polarized to the vertically-polarized laser.

Another evidence that the horizontally-polarized photons are indeed emitted by the quantum dot can be obtained by measuring its photon statistics. Because the radiative decay of a single

quantum dot only produces photons one at a time, two photons cannot be emitted with horizontal polarization at the same time. Consequently, the horizontally-polarized light should have a single photon statistics. The standard metric to access the photon statistics of light is the second order autocorrelation function as a function of time delay τ [158]:

$$g^{(2)}(\tau) = \frac{\langle a^\dagger(0)a^\dagger(\tau)a(\tau)a(0) \rangle}{\langle a^\dagger(0)a(0) \rangle \langle a^\dagger(\tau)a(\tau) \rangle} \quad (3.1)$$

It can be accessed experimentally by a Hanbury-Brown-Twiss (HBT) experiment as displayed in Fig. 3.4 : the quantum dot wavelength is fixed to be in resonance with the laser and the cavity ($\omega_{QD} = \omega_{laser} = \omega_{cav}$) and the horizontally-polarized emitted photons are coupled to a single-mode fiber to be sent to the HBT setup. This setup consists of a fibered beam splitter connected to two fast single photon avalanche photodiodes.

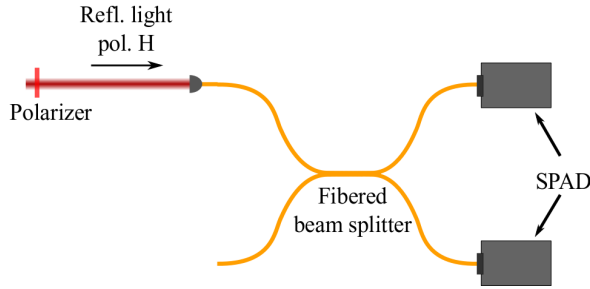


Figure 3.4: Hanbury-Brown-Twiss experimental setup. The emitted light with horizontal polarization is entering a fibered 50:50 beamsplitter. It is detected by two single-photon avalanche diodes (SPAD) which are positioned at each output of the beam splitter.

A single photon statistics is characterized by the value of the intensity correlations at zero delay: $g_H^{(2)}(\tau = 0)$. This quantifies the probability to detect a photon in the first detector exactly when a photon is detected at the same time in the second detector (normalized by the uncorrelated probability of photon detection in the first detector).

For a laser source, the detections in the two photodiodes are completely uncorrelated due to the Poissonian statistics of coherent light ($g_H^{(2)}(0) = 1$).

For thermal light, it is expected to obtain a "bunching" of photons ($g_H^{(2)}(0) = 2$): the detection of a photon is more probable when a first photon is detected in the other photodiode.

Only for single photon statistics, one should see an anti-bunching ($g_H^{(2)}(0) = 0$): when one single-photon is passing through the beamsplitter, only one photon is propagating, either through one detector or the other. So if a photon is detected in one detector it cannot be detected in the other, thus explaining the anti-bunching at zero delay.

The correlations between the two detectors are measured with a time tagging module and are displayed in Fig. 3.5. The theoretical curve presented here is discussed later in Sec. 3.3 (similarly, all theoretical curves will be discussed in Sec. 3.3). In the experimental data, we observe that the $g_H^{(2)}(\tau)$ is constant equal to one, except when the time delay is close to zero. The second order autocorrelation function at time delay $\tau = 0$ is anti-bunched to a raw value of $g_H^{(2)}(0) = 7 \pm 5\%$. This is a clear signature of a single photon source. In addition, this signal is convoluted with the time jitter of the single photon detectors (40ps) and a deconvolution should give a value much closer to zero, which is what is expected for a pure single photon light.

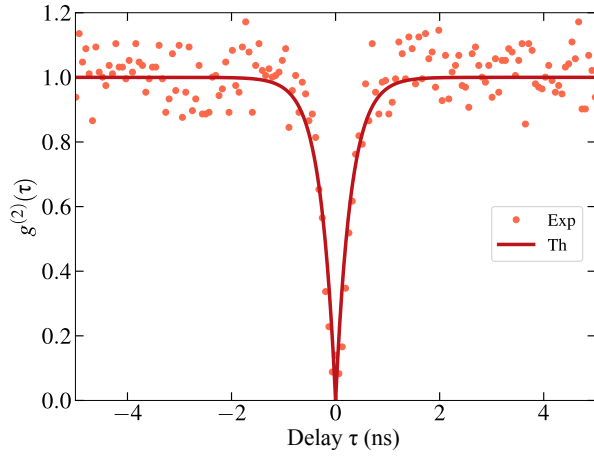


Figure 3.5: Intensity autocorrelation ($g^{(2)}(\tau)$) of the light reflected by the neutral QD-cavity device with horizontal polarization, as a function of the delay τ between detection events. Points are experimental data and the solid line is a theoretical fit that is discussed in Sec. 3.3.3

3.2.4 Reflectivity of a cavity-coupled neutral quantum dot.

The intensity autocorrelation function shows that the horizontally-polarized reflected photons are constituted by the quantum dot resonance fluorescence. Under vertically-polarized excitation, the quantum dot is scattering single photon light into the horizontal polarization, so there is indeed a conversion of polarization from vertical polarization to horizontal polarization.

In this subsection, the amount of light converted in cross-polarization is quantified. To do so, the intensity reflected by the cavity device in horizontal and vertical polarizations is analyzed as a function of the laser detuning. The quantum dot is tuned to be in resonance with the vertical cavity mode. The reflectivity spectrum is displayed in Fig. 3.6. First, let us focus on the vertically-polarized reflected light. As in the previous chapter (Chapter. 2.4), one can observe the cavity reflectivity dip. However, here, the quantum dot optical response leads to a reflectivity peak at the center of the cavity reflectivity dip.

Concerning the horizontally-polarized reflected light, when detuned from the quantum dot, there is negligible reflected light with horizontal polarization. This shows that the cavity is indeed excited along its polarization axis. When in resonance with the quantum dot, incoming vertically-polarized light is scattered into the horizontal polarization. In addition, the peak in reflectivity induced by the quantum dot in horizontal and vertical polarizations are slightly detuned by a few μeV : this is a signature of the fine structure of the exciton state of the quantum dot discussed in Sec. 3.2.2. The amount of horizontally-polarized scattered photons corresponds at best to approximately 10% of the total reflected light. The quantum dot induces a polarization conversion of 10% from vertical to horizontal polarization.

3.2.5 Reconstruction of the polarization density matrix.

As shown previously, the quantum dot induces a conversion of light from the vertical incident polarization by emitting single photons. This emission of single photons is superposed to the vertically-polarized reflected light which still constitutes 90% of the total reflected light.

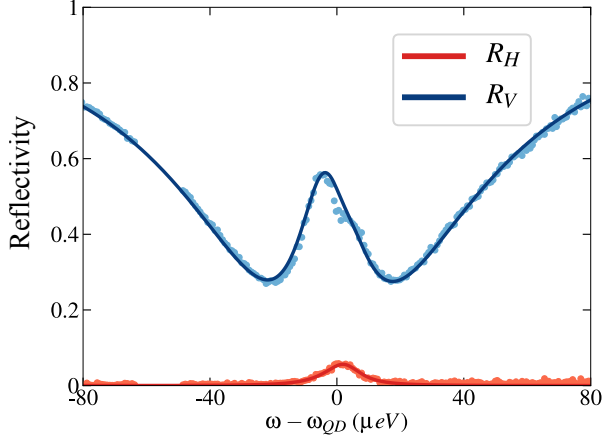


Figure 3.6: Reflectivity of a quantum dot-cavity device under resonant vertically-polarized excitation as a function of the laser quantum dot detuning. The quantum dot is in resonance with the vertically-polarized cavity mode so $\omega_{cV} = \omega_{QD}$. Points are experimental data while solid lines are theoretical predictions that will be discussed in Sec. 3.3.3

A question that arises, is the purity of this polarization superposition. Is it a coherent superposition, that leads to a pure polarization state $\alpha |H\rangle + \beta |V\rangle$, or is it an incoherent superposition, that degrades the polarization purity?

One way to quantify the coherent and incoherent mechanisms at the origin of the polarization conversion, is by reconstructing the polarization density matrix of the reflected light. Indeed, if the horizontally-polarized light incoherently superposes with the vertical polarization, the polarization purity is degraded: there is no rotation of polarization ($s_{DA} = s_{RL} = 0$) and the result is a Poincaré vector that goes inside the Poincaré sphere along the horizontal/vertical axis. If the horizontal polarization is in a coherent superposition with the vertical polarization, this induces a rotation of polarization and thus no degradation of the polarization purity ($s_{DA} \neq 0$ and $s_{RL} \neq 0$ so that $\sqrt{s_{HV}^2 + s_{DA}^2 + s_{RL}^2} = 1$).

The light reflected by the cavity-QED device is analyzed in polarization thanks to the polarization tomography technique discussed in the previous chapter. The light intensity is measured in the Horizontal and Vertical, Diagonal and Antidiagonal, and Right-handed and Left-handed circular polarizations. The Stokes parameters of the reflected light are measured as a function of the laser detuning. The results are displayed in Fig 3.7. The Stokes parameter s_{HV} highlights the polarization conversion from vertical to horizontal polarization: far from resonance, $s_{HV} = -1$ so there is no polarization conversion, and in resonance with the quantum dot, it reaches $s_{HV} = -0.77$ so there is a partial polarization conversion induced by the quantum dot. The Stokes parameters s_{DA} and s_{RL} are also modified by the quantum dot exciton transition, which indicates a quantum dot-induced polarization rotation. From these Stokes parameters, the polarization purity $\sqrt{s_{HV}^2 + s_{DA}^2 + s_{RL}^2}$ is calculated and represented in Fig 3.7. The polarization purity remains high, above 84% for all laser wavelengths.

The polarization of the reflected light is represented in the Poincaré sphere for each wavelength in Fig 3.8. This figure shows a quantum dot-induced polarization rotation of up to 20° both in latitude and longitude. It corresponds to a rotation of polarization induced by a single quantum dot of up

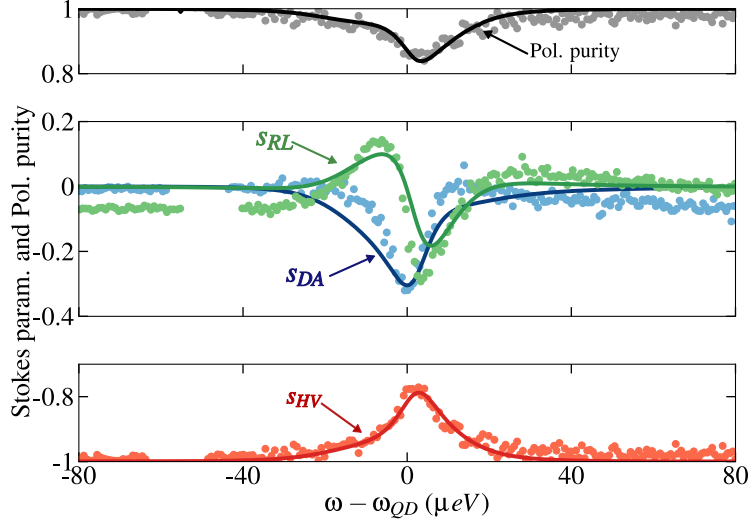


Figure 3.7: Stokes parameters and polarization purity of the light reflected as a function of the laser-quantum dot detuning (with $\omega_{QD} = \omega_{cV}$), using the same experimental conditions as for Fig. 3.6. Points are experimental data while solid lines are theoretical predictions that will be discussed in Sec. 3.3.3

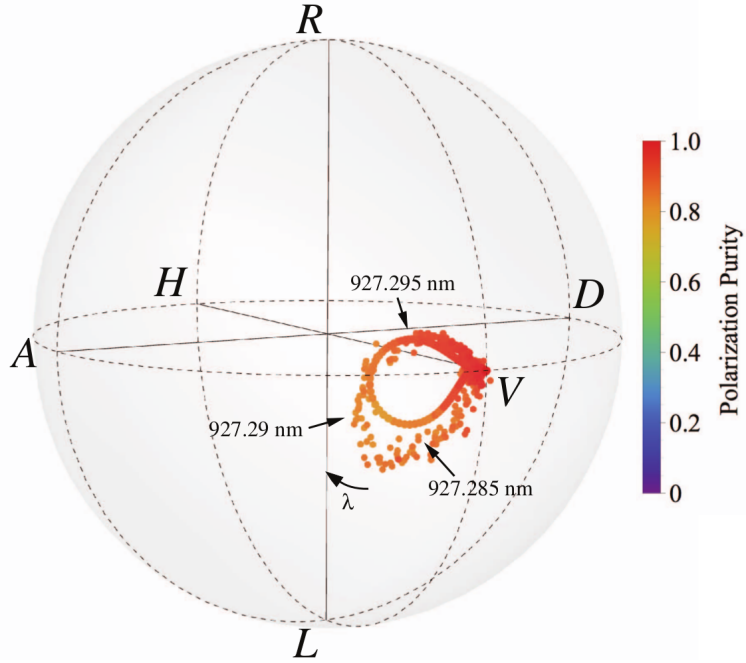


Figure 3.8: Representation of the polarization density matrix of the light reflected by a neutral quantum dot coupled to a pillar microcavity device, for both experimental data (circles) and numerical simulations (solid line). Each point corresponds to the Poincaré vector of the reflected light for a given wavelength. The colorscale shows the polarization purity of each Poincaré vector.

to 10° for the orientation and ellipticity angle (see definition in Fig. 2.5). Consequently, there is a partially coherent superposition of the horizontally-polarized single photons emitted by the quantum dot and the vertically-polarized reflected laser. Yet, the polarization is not completely pure, so there is also part of the horizontal polarization that is incoherently superposed with the vertically-polarized reflected light. To a certain extent, this can be explained by the imperfect input coupling ($\eta_{in} = 79\%$) which was discussed before. However, this is not sufficient to fully explain the degradation of purity observed here. Consequently, it should also be the signature of incoherent processes at play in the quantum dot-cavity device. In order to better understand the mechanisms at play, it is necessary to have a theoretical modelization of the optical response of the quantum dot-cavity device. As discussed in the next section, this model should take into account different noise mechanisms to allow discriminating the main source of decoherence in our system.

3.3 Theoretical modelization of a neutral quantum dot-cavity device.

The theoretical model developped in this section is based on a quantum mechanical description of an atom coupled to a cavity: the Jaynes-Cummings Hamiltonian [150] (see Sec. 1.4.3 for more details). This Hamiltonian describes the coherent interaction of a two-level quantum emitter coupled to a perfectly confined quantized field. Based on this "textbook" model, a more complex model, based on the open quantum system formalism, is constructed that takes into account the light polarization degree of freedom, the three-level structure of the quantum emitter and the resonant laser excitation. Also, it should simulate uncontrolled mechanisms that cannot be described with a hamiltonian.

In the following, we will present the open quantum system formalism and use it to describe the simple case of a two-level atom coupled to a cavity. We will then consider the more realistic case of an exciton quantum dot coupled to an elliptical cavity.

3.3.1 Density matrix and open quantum system formalism.

A pure state can be represented by a wavefunction $|\psi_s\rangle$. However, when the system is interacting with its environment or when classical processes come at play, we have an incomplete knowledge of this wavefunction and have to describe the system with a statistical superposition of this pure state with given probabilities. This statistical approach consists in considering the density matrix ρ of the system which is given by:

$$\rho = \sum_s p_s |\psi_s\rangle\langle\psi_s| \quad (3.2)$$

This considers that the state prepared is in a statistical mixture of the states $|\psi_s\rangle$ with a probability p_s . The density matrix formalism is convenient because it allows us to quantify our lack of knowledge about a quantum state.

For an isolated quantum system, the evolution is given by the Hamiltonian of the system \hat{H}_{tot} . The evolution of an isolated system can be described with the Schrödinger equation, that can be generalized to describe the evolution of the density matrix, with:

$$\dot{\rho} = -i[\hat{H}_{tot}, \rho] \quad (3.3)$$

The expectation value of an operator is given by:

$$\langle \hat{A} \rangle = Tr[\hat{A}, \rho] = \sum_i p_i \langle \psi_i | \hat{A} | \psi_i \rangle \quad (3.4)$$

and its time evolution is:

$$\frac{d\langle \hat{A} \rangle}{dt} = -i\langle [\hat{A}, \hat{H}] \rangle \quad (3.5)$$

The interest of the density matrix formalism lies in the description of incoherent and dissipative processes which are typical when the system is coupled to the environment, and that cannot be described with a hamiltonian. To simulate these incoherent processes, we can use the Markovian approximation in which the correlations between the system and the environment dissipate much faster than the coherent evolution timescales of the system [152]. The fluctuations generated by interactions with the environment are assumed not to be correlated in time (the environment quickly "forgets" its interaction with the system). Under this approximation, the incoherent processes are taken into account thanks to collapse operators \hat{C}_{if} that transforms a state $|i\rangle$ into a state $|f\rangle$ at a rate γ_{if} :

$$\hat{C}_{if} = \sqrt{\gamma_{if}} |f\rangle \langle i| \quad (3.6)$$

For each collapse operator, a superoperator $\hat{L}_{if}(\rho)$ [195], called Lindbladian, is associated and given by [196, 197]:

$$\hat{L}_{if}(\rho) = \frac{1}{2}(2\hat{C}_{if}\rho\hat{C}_{if}^\dagger - \hat{C}_{if}^\dagger\hat{C}_{if}\rho - \rho\hat{C}_{if}^\dagger\hat{C}_{if}) \quad (3.7)$$

The first term describes the increasing probability to be in state $|f\rangle$ provided that we are in state $|i\rangle$: $\hat{C}_{if}\rho\hat{C}_{if}^\dagger = \gamma_{if} \langle i | \rho | i \rangle |f\rangle\langle f|$. The last two terms describe the decreasing probability to be in state $|i\rangle$.

The evolution of the density matrix is given by the master equation:

$$\dot{\rho} = -i[\hat{H}_{tot}, \rho] + \sum_{if} \hat{L}_{if}(\rho) \quad (3.8)$$

To be able to use the master equation, one needs to identify the different contributions of the total hamiltonian and the different incoherent processes that are represented thanks to the collapse operators.

Concerning the total hamiltonian \hat{H}_{tot} , it can be decomposed into different contributions:

$$\hat{H}_{tot} = \hat{H}_{cav} + \hat{H}_{int} + \hat{H}_{QD} + \hat{H}_{pump} + \hat{H}_B \quad (3.9)$$

where:

- \hat{H}_{cav} is the hamiltonian describing the cavity alone.
- \hat{H}_{pump} is the hamiltonian describing the interaction between the resonant laser and the cavity.
- \hat{H}_{QD} is the hamiltonian describing the quantum dot alone.
- \hat{H}_{int} is the hamiltonian describing the interaction between the intracavity field and the quantum dot.
- \hat{H}_B is the hamiltonian describing the interaction between the quantum dot and a magnetic field (it is not taken into account here but will be in Chapter 5).

The incoherent processes need also to be determined:

$$\sum_{if} \hat{L}_{if}(\rho) = \hat{L}_{cav}(\rho) + \hat{L}_{sp}(\rho) + \hat{L}_{deph}(\rho) \quad (3.10)$$

where $\hat{L}_{cav}(\rho)$ simulates the cavity photon losses, $\hat{L}_{sp}(\rho)$ simulates the quantum dot spontaneous emission out of the cavity mode and $\hat{L}_{deph}(\rho)$ simulates the quantum dot dephasing.

In the following, each hamiltonian and Lindbladian are detailed to construct the model that fits the experimental data presented in Sec. 3.2, and determines the dominant noise mechanism.

3.3.2 Cavity-QED model with a 2-level quantum emitter.

The objective of this section is to simulate the optical response of a quantum dot coupled to a cavity close to resonant excitation. Consequently, the external incident field has a pulsation ω which is close to ω_{cav} . For all the theoretical modelizations, a simplification can be made by using the rotating wave approximation (RWA) [150, 152] that will not be detailed in this manuscript. The objective of this subsection is to build a simplified model of the optical response for a quantum dot approximated by a 2 level-system inside a polarization-degenerate cavity. This model does not take into account the polarization degree of freedom that will be introduced later on.

Modelisation of a cavity.

A cavity confines the electromagnetic field in the 3 spatial directions. The confined field can be described into modes of a given energy ω_{mode} that behave as harmonic oscillators. Only the fundamental mode, that has an energy ω_{cav} , is considered.

The cavity energy levels are represented in Figure 3.9. The Fock states $|N\rangle$ (where N is the number of photons in the cavity) constitute the eigenstates of the intracavity quantized field. $|0\rangle$ corresponds to an empty cavity which is in its fundamental state, $|1\rangle$ corresponds to one single photon in the cavity (the first excitation of the cavity) and so on and so forth... Furthermore, \hat{a}^\dagger is the creation operator that increases by 1 the number of intra-cavity photons connecting $|N\rangle$ and $|N+1\rangle$, and \hat{a} , the annihilation operator, destroys a photon in the cavity. The relations defining these operators are the following:

$$\begin{aligned}\hat{a}^\dagger |N\rangle &= \sqrt{N+1} |N+1\rangle, \\ \hat{a} |N\rangle &= \sqrt{N} |N-1\rangle\end{aligned}\tag{3.11}$$

A quantum description of the cavity can be done thanks to the hamiltonian \hat{H}_{cav} given by (in the RWA)[150, 152]:

$$\hat{H}_{cav} = (\omega_{cav} - \omega) \hat{a}^\dagger \hat{a}\tag{3.12}$$

This is sufficient to describe an isolated perfect cavity. However, in general cavities have losses and thus photons can enter or escape from the top, the bottom or the side of the cavity. To describe a cavity resonantly excited from the top mirror, let us introduce the input (resp. output) external field operator \hat{b}_{in} (resp. \hat{b}_{out}) that corresponds to the incident (reflected) external field that couples with the cavity from the top mirror. It is proportional to the electric field \vec{E}_{in} (resp. \vec{E}_{out}), and normalized such that $\langle \hat{b}_{in}^\dagger \hat{b}_{in} \rangle$ (resp. $\langle \hat{b}_{out}^\dagger \hat{b}_{out} \rangle$) represent a flux of incoming (resp. reflected) photons, and is in photons per unit of time. The definition of the field operators \hat{b}_{in} , \hat{b}_{out} is similar to the one in the previous chapter.

The hamiltonian that describes the interaction between the cavity and the external electromagnetic field is given by [185]:

$$\hat{H}_{pump} = -i\sqrt{\kappa_{top}}(\hat{b}_{in} \hat{a}^\dagger - \hat{b}_{in}^\dagger \hat{a})\tag{3.13}$$

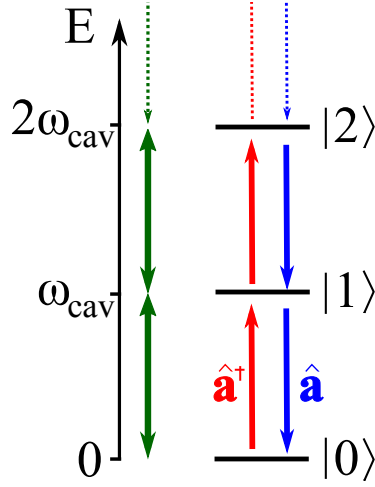


Figure 3.9: Scheme of the energy levels of a cavity. The cavity eigenstates $|N\rangle$ are equally separated in energy by ω_{cav} and are interconnected by the creation (\hat{a}^\dagger) and annihilation (\hat{a}) operators. The fundamental state $|0\rangle$ corresponds to no photon inside the cavity, and each Fock state $|N\rangle$ corresponds to N intracavity photons.

In addition, one needs to take into account the cavity losses thanks to a Lindblad superoperator $\hat{L}_{cav}(\rho)$ which depends on the collapse operator:

$$\hat{C}_{cav} = \sqrt{\kappa} \hat{a} \quad (3.14)$$

where κ is the total damping rate of the cavity and \hat{a} the annihilation operator. It takes into account the finite lifetime of photons inside the cavity.

The intracavity photons escape the cavity by the top or bottom mirror, or from the side of the cavity. The input-output formalism introduced in Chapter 2 is used to obtain the cavity optical response in reflection. In the following, the external field and the cavity spatial mode are supposed perfectly mode-matched, so that only the simpler case where:

$$\hat{b}_{out} = \hat{b}_{in} + \sqrt{\kappa_{top}} \hat{a} \quad (3.15)$$

is considered (where κ_{top} represents the top mirror damping rate, see Sec. 2.2).

Thanks to the input-output formalism, the two hamiltonians \hat{H}_{cav} and \hat{H}_{pump} , the Lindbladian $\hat{L}_{cav}(\rho)$ and the master equation (3.8), one can already simulate the optical response of an empty cavity. The response is identical to the one obtained with a semi-classical approach as was done in Chapter 2. For example, Fig. 3.10 compares the reflectivity of an empty cavity as simulated by semi-classical simulations (with a reflection coefficient given by Eq. 2.1) and by the present model. The agreement between the semi-classical and the quantum mechanical method is expected as there is no interaction with a quantum emitter for the moment: for a cavity, if the incident field is coherent, then the internal and reflected fields are also coherent.

Modelization of a 2-level quantum emitter.

A quantum dot coupled to the cavity is now introduced in the model. For the moment, we consider a simplified model, presented in Figure 3.11, where the quantum dot can either be in its fundamental

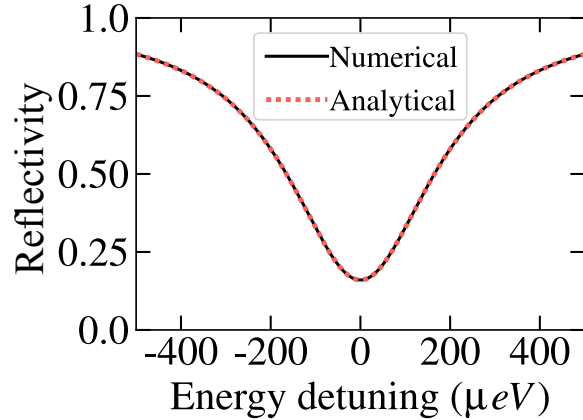


Figure 3.10: Comparison of the simulation of a cavity reflectivity spectrum using the semi-classical approach (analytical) and the exact master equation (numerical)

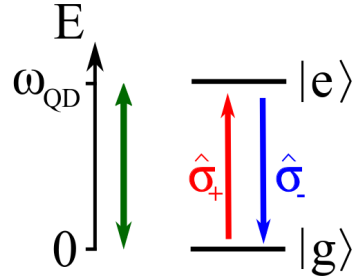


Figure 3.11: Scheme of a two-level quantum emitter. The ground state $|g\rangle$ is connected to the excited states $|e\rangle$ by the operators $\hat{\sigma}_+$ and $\hat{\sigma}_-$.

state $|g\rangle$ or in an excited state $|e\rangle$ (the exciton). A more realistic model will be introduced in the next section. Let us introduce the quantum dot excitation operator $\hat{\sigma}_+$ that converts the fundamental state into the excited state:

$$\hat{\sigma}_+ = |e\rangle \langle g| \quad (3.16)$$

and $\hat{\sigma}_- = \hat{\sigma}_+^\dagger$ that converts the excited state into the fundamental state. The excited state has an energy ω_{QD} higher than the fundamental state (the fundamental state energy is zero-valued by convention.) so that the hamiltonian that describes the quantum dot alone (within the RWA)[150, 152], is:

$$H_{QD} = (\omega_{QD} - \omega) \hat{\sigma}_+ \hat{\sigma}_- \quad (3.17)$$

The quantum dot is also interacting with light inside the cavity. One photon can be absorbed by the quantum dot in its ground state and one photon can be emitted inside the cavity by the quantum dot in its excited state. This is taken into account thanks to the interaction hamiltonian H_{int} , that was already discussed previously in Sec. 1.4.3:

$$H_{int} = ig(\hat{a}^\dagger \hat{\sigma}_- - \hat{a} \hat{\sigma}_+) \quad (3.18)$$

where g is the light matter coupling constant of our system. So the coherent processes can be fully described by the total hamiltonian:

$$H_{tot} = H_{cav} + H_{QD} + H_{int} + H_{pump} \quad (3.19)$$

In addition to the loss of an intracavity photon, there are also incoherent processes acting on the quantum dot. The first one is the quantum-dot spontaneous emission of a photon outside of the cavity mode. It is characterized by the spontaneous emission rate γ_{sp} , and described by the collapse operator:

$$\hat{C}_{sp} = \sqrt{\gamma_{sp}} \hat{\sigma}_- \quad (3.20)$$

In addition, the exciton of the quantum dot is also interacting with its environment (charges, nuclei and phonons...) and lose its quantum coherence by doing so. The loss of coherence can be characterized by the pure dephasing rate γ^* and it is described by the collapse operator:

$$C_{deph} = \sqrt{2\gamma^*} \hat{\sigma}_+ \hat{\sigma}_- \quad (3.21)$$

As $\hat{\sigma}_+ \hat{\sigma}_- = |e\rangle\langle e|$ corresponds to a transition from the excited state to itself, this process does not change the state's population but it decreases the coherence between the ground and the excited state: it converts the density matrix from an ideal quantum superposition to a mixed state. A more detailed discussion about the noise mechanisms is provided later in this chapter. From the collapse operators \hat{C}_{sp} and \hat{C}_{deph} , one can create the Lindbladians \hat{L}_{sp} and \hat{L}_{deph} using Eq. 3.7.

The system of a 2-level quantum dot coupled to a cavity is completely described by the total hamiltonian defined in Eq. 3.19 and the Lindbladians \hat{L}_{cav} , \hat{L}_{sp} , \hat{L}_{deph} thanks to the master equation (Eq. 3.8).

3.3.3 Realistic cavity-QED model of a neutral quantum dot embedded into a micropillar.

The previous model of a 2-level quantum dot embedded into a cavity is not sufficient to take into account the rotation of polarization induced by a quantum dot, as it does not take into account the polarization degree of freedom. As was seen in Sec. 3.2, a neutral quantum dot induces rotation of polarization because it has in fact two excited states. These two states, denoted $|e_X\rangle$ and $|e_Y\rangle$, are split by an energy Δf_{ss} and optically addressable thanks to linear polarizations X and Y (that are orthogonally polarized). In addition, we have seen that, in general, the pillar microcavities are not polarization-degenerate and have also two orthogonal linear polarizations axes H and V. These two polarization splittings have to be taken into account in the theoretical model that describes the real cavity-QED device.

Modelization of elliptical cavities.

In order to take into account the polarization axes of the cavity, one can simply model one cavity mode for the polarization H and one for the polarization V, as illustrated in Figure 3.12. The operators \hat{a}^\dagger , \hat{a} , the energy ω_{cav} , and the intracavity eigenstates $|N\rangle$ are defined for each cavity by adding a subscript "H" or "V" to distinguish the two cavity modes.

The resulting hamiltonian, is the sum of the two hamiltonians for each cavity:

$$H_{cav} = H_{cav,H} + H_{cav,V} = (\omega_{cav,H} - \omega) \hat{a}_H^\dagger \hat{a}_H + (\omega_{cav,V} - \omega) \hat{a}_V^\dagger \hat{a}_V \quad (3.22)$$

The elliptical cavity Lindbladian is also simply the sum of the two cavity mode Lindbladians:

$$\hat{L}_{cav} = \hat{L}_{cav,H} + \hat{L}_{cav,V} \quad (3.23)$$

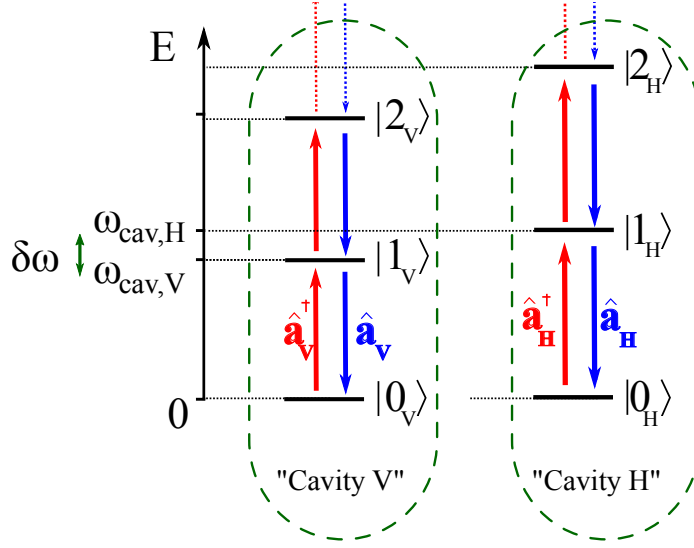


Figure 3.12: Scheme of the energy level of the non-degenerate cavity. It is very similar to Fig. 3.9, but there are now two cavity modes, one for each polarization, which are energy split by the cavity splitting $\delta\omega$, and confine photons with different polarizations and different energies $\omega_{cav,H}$ and $\omega_{cav,V}$.

with $\hat{L}_{cav,H}$ and $\hat{L}_{cav,V}$ made with collapse operators $C_{cav,H} = \sqrt{\kappa_{top}}\hat{a}_H$ and $C_{cav,V} = \sqrt{\kappa_{top}}\hat{a}_V$ respectively.

Polarization needs also to be taken into account for the external fields: $\hat{b}_{i,V}$ (respectively $\hat{b}_{i,H}$) is the operator describing the vertically-(resp. horizontally-) polarized incident field and $\hat{b}_{out,V}$ (resp. $\hat{b}_{out,H}$), the output field operators for vertical (resp. horizontal) polarization.

In addition, one can note that the external field operators can be described for any polarization. Using the equations of Sec. 2.5.1, it is possible to compute the reflected intensity in any polarizations and thus, to reconstruct the complete polarization state.

Modelization of a real neutral quantum dot.

In order to take into account the fine structure splitting of the quantum dot, a more realistic model is presented in Fig. 3.13. In this model, the quantum dot is considered now as a 3-level system with two excited states $|e_X\rangle$ and $|e_Y\rangle$. We use subscripts "X" and "Y" to distinguish these two states. The hamiltonian of the quantum dot alone is now:

$$H_{QD} = H_{QD,X} + H_{QD,Y} = (\omega_{QD,X} - \omega)\hat{\sigma}_{+,X}\hat{\sigma}_{-,X} + (\omega_{QD,Y} - \omega)\hat{\sigma}_{+,Y}\hat{\sigma}_{-,Y} \quad (3.24)$$

Finally, the hamiltonian describing the interaction between the light and the quantum dot needs also to be modified. One photon with polarization X (respectively. Y) can excite the quantum dot in its state $|e_X\rangle$ (resp. $|e_Y\rangle$). So let us define \hat{a}_X^\dagger (resp. \hat{a}_Y^\dagger) and \hat{a}_X (resp. \hat{a}_Y) the creation and annihilation operators corresponding to intracavity photons with polarization X (resp. Y). The interaction hamiltonian is now:

$$H_{int} = H_{int,X} + H_{int,Y} = ig(\hat{a}_X^\dagger\hat{\sigma}_{-,X} - \hat{a}_X\hat{\sigma}_{+,X}) + ig(\hat{a}_Y^\dagger\hat{\sigma}_{-,Y} - \hat{a}_Y\hat{\sigma}_{+,Y}) \quad (3.25)$$

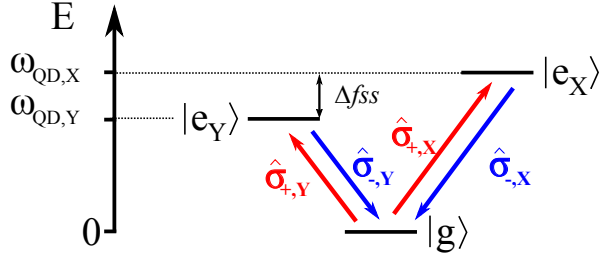


Figure 3.13: Scheme of the energy levels of a neutral quantum dot. The ground state $|g\rangle$ is connected to the two excited states $|e_Y\rangle$ and $|e_X\rangle$ by the operators $\hat{\sigma}_{+,X}$ and $\hat{\sigma}_{+,Y}$ respectively and are separated by an energy corresponding to the fine structure splitting $\Delta fss = \omega_{QD,X} - \omega_{QD,Y}$.

\hat{a}_X^\dagger , \hat{a}_Y^\dagger , \hat{a}_X and \hat{a}_Y require to be defined. In general, they are different from the operators defined with H, V polarizations and we introduce θ , the angle between the polarization axes "H" and "X" (see Fig. 3.2(b)). This way annihilation operators are linked through:

$$\begin{aligned}\hat{a}_X &= \cos(\theta)\hat{a}_H + \sin(\theta)\hat{a}_V \\ \hat{a}_Y &= -\sin(\theta)\hat{a}_H + \cos(\theta)\hat{a}_V\end{aligned}\quad (3.26)$$

The same relations hold for the creation operators.

Concerning the incoherent processes, the spontaneous emission can be taken into account with a Lindbladian $\hat{L}_{sp} = \hat{L}_{sp,X} + \hat{L}_{sp,Y}$ where $\hat{L}_{sp,i}$ is made with the collapse operator $\hat{C}_{sp,i} = \sqrt{\gamma_{sp}}\hat{\sigma}_{-,i}$ (for $i = X, Y$).

Taking into account the pure dephasing is more complicated as it depends on the noise mechanism that is simulated. This will be the topic of the Subsection. 3.3.5. For the moment, we take a pure dephasing \hat{L}_{deph} that is defined thanks to the collapse operator (we will see that it corresponds to a model of an electric or temperature induced interaction with the environment, in the assumption of very fast fluctuations).

$$\hat{C}_{deph} = \sqrt{2\gamma^*}(\hat{\sigma}_{+,X}\hat{\sigma}_{-,X} + \hat{\sigma}_{+,Y}\hat{\sigma}_{-,Y}) \quad (3.27)$$

Finally, with all these equations, this complete model is able to realistically simulate a neutral quantum dot coupled to a pillar microcavity and it was used to fit the experimental data of the previous sections. The reflectivity curves (Fig. 3.6), the Stokes parameters and the polarization purity (Fig. 3.7), the Poincaré sphere (Fig. 3.8) were fitted with the same set of parameters.

The experimental second order correlations (Fig. 3.5) were also fitted with the same set of parameters, using the equation:

$$g^{(2)}(t) = \frac{\langle \hat{b}_{out,H}^\dagger(t)\hat{b}_{out,H}^\dagger(0)\hat{b}_{out,H}(0)\hat{b}_{out,H}(t) \rangle}{\langle \hat{b}_{out,H}^\dagger(t)\hat{b}_{out,H}(t) \rangle \langle \hat{b}_{out,H}^\dagger(0)\hat{b}_{out,H}(0) \rangle} \quad (3.28)$$

For the fit, the following parameters are taken as fixed parameters. The incoming light is vertically polarized with a measured incident power of $P_{in} = 200\text{pW}$ with an input coupling of $\eta_{in} = 79 \pm 5\%$ with the cavity. The cavity parameters were fixed with independent cavity reflectivity measurements for horizontal and vertical incident polarizations. They show that the cavity has a splitting of $\delta\omega = 70\mu\text{eV}$, a total damping rate of $\kappa = 106 \pm 4\mu\text{eV}$ and a top mirror output coupling $\eta_{top} = 55 \pm 5\%$. The vertical cavity mode has an energy of $\omega_{cav,V} = 1.3371\text{eV}$ (which corresponds

to a photon wavelength of $\lambda_{cav,V} = 927.29\text{nm}$). The quantum dot is set in resonance with the vertical cavity mode ($\omega_{QD} = (\omega_{QD,X} + \omega_{QD,Y})/2 = \omega_{cav,V}$).

The free parameters of the fit are the quantum dot parameters: the light-matter coupling g , the quantum dot fine structure splitting Δf_{ss} , the angle between the cavity and quantum dot axes θ , the QD spontaneous emission γ_{sp} and its pure dephasing γ^* . The fit shows that the quantum dot has a fine structure splitting of $\Delta f_{ss} = 9 \pm 2\mu\text{eV}$, a spontaneous emission rate of $\gamma_{sp} = 0.6 \pm 0.3\mu\text{eV}$ (which corresponds to a spontaneous emission lifetime of 1ns, comparable to what is observed in bulk), and a pure dephasing rate of $\gamma^* = 3.7 \pm 0.5\mu\text{eV}$. Its axes are rotated by an angle of $\theta = 17 \pm 5^\circ$ with the cavity axis. The cavity-quantum dot light-matter coupling constant is $g = 18 \pm 3\mu\text{eV}$.

The error bars were computed by simulating a wide range of parameters and calculating the sum of squared errors between experimental data and simulated ones. The experimental data compared with the simulation are the intensities reflected in horizontal and vertical polarizations (and therefore the Stokes parameter s_{HV}), the polarization purity, and the Stokes parameters s_{DA} and s_{RL} . Because the polarizations considered experimentally as diagonal, antidiagonal and circular-left and right might be slightly rotated from the actual ones of the cavity, experimental data are fitted with a relative weight four times smaller for the s_{DA} and s_{RL} curves than for s_{HV} and the polarization purity curves (which are more accurately determined experimentally).

The values extracted from the fit are typical for a quantum dot coupled to a cavity. The high value of the light-matter coupling g is typical for the samples produced in the group as the quantum dot has been deterministically coupled to the cavity, thus maximizing the light-matter coupling. However, because the sample is electrically contacted, the electric environment should be stabilized and we should expect less pure dephasing than observed. This is discussed next.

3.3.4 Simulations of noise mechanisms.

If the light reflected by the quantum dot-cavity device was entirely coherent [163, 164], it would have been completely defined by the complex mean values of the output fields $b_{out,H} = \langle \hat{b}_{out,H} \rangle$ and $b_{out,V} = \langle \hat{b}_{out,V} \rangle$ with total intensities $\langle \hat{b}_{out,H}^\dagger \hat{b}_{out,H} \rangle = |b_{out,H}|^2$ and $\langle \hat{b}_{out,V}^\dagger \hat{b}_{out,V} \rangle = |b_{out,V}|^2$. These complex numbers have perfectly defined phases and amplitudes, so the reflected state $|\Psi_{out}\rangle$ is a pure polarization state:

$$|\Psi_{out}\rangle \propto b_{out,H} |H\rangle + b_{out,V} |V\rangle \quad (3.29)$$

Experimentally, we have observed in Figure 3.8, that the quantum dot induces depolarization, which shows that the quantum dot has also an incoherent optical response. This is in fact induced by its interaction with the environment theoretically modeled by the pure dephasing incoherent process. The environment can induce uncontrolled electric or magnetic instabilities (or more complex mechanisms) that induce dephasing, so that the reflected photons are not entirely coherent. In this section, different noise mechanisms are simulated to fit the data. The simulations of the noise mechanisms are done by modifying the collapse operator \hat{C}_{deph} in the Lindbladian \hat{L}_{deph} introduced before that simulates quantum dot interactions with its environment.

Correlated noise.

In Subsection. 3.3.2, the collapse operator describing the two-level quantum dot dephasing process is:

$$\hat{C}_{deph} = \sqrt{2\gamma^*} \hat{\sigma}_+ \hat{\sigma}_- \quad (3.30)$$

This collapse operator is based on the operator $\hat{\sigma}_+ \hat{\sigma}_- = |e\rangle\langle e|$ that does not change the population between the excited and the ground states. However, it induces random jumps of the relative phase between $|e\rangle$ and $|g\rangle$ which are equivalent to random energy fluctuations between the ground and excited states.

In the more realistic model where there are two excited states $|e_X\rangle$ and $|e_Y\rangle$, there are different ways to generalize this collapse operator.

A first possibility is to use the following equation, corresponding to "correlated" noise:

$$\hat{C}_{deph} = \hat{C}_{corr} = \sqrt{2\gamma^*}(\hat{\sigma}_{+,X}\hat{\sigma}_{-,X} + \hat{\sigma}_{+,Y}\hat{\sigma}_{-,Y}) \quad (3.31)$$

It can also be written as $\sqrt{2\gamma^*}(|e_X\rangle\langle e_X| + |e_Y\rangle\langle e_Y|)$.

This collapse operators does not create phase fluctuations in between the two excited states $|e_X\rangle$ and $|e_Y\rangle$, but creates phase fluctuations between the ground state $|g\rangle$ and the two excited states. In the Markovian approximation, this is equivalent to fluctuating energies $\omega_{QD,X}$ and $\omega_{QD,Y}$, with always the same equal fluctuations in energy. This corresponds to perfectly correlated energy fluctuations for the two excited states: the two excited states are modified in a similar fashion.

This well describes electric instabilities [198]. Indeed, an electric field induces a Stark shift that increases or decreases the energy of all the quantum dot transitions. The change in energy is the same for all transitions so instabilities of the electric field induce correlated fluctuations.

For the temperature instabilities, the temperature dilates the quantum dot and therefore the confinement of the electric charges inside the quantum dot. Again, this change is done in a similar fashion so that the fluctuations are correlated. So, such collapse operator also simulates temperature instabilities.

Anti-correlated noise.

The excited state $|e_X\rangle$ and $|e_Y\rangle$ are superpositions of states $|\uparrow\downarrow\rangle$ and $|\downarrow\uparrow\rangle$ (with \uparrow / \downarrow the hole spin and \uparrow / \downarrow the electron spin), that have opposite spins. A magnetic field induces a Zeeman splitting, that corresponds to anti-correlated energy fluctuations: if the energy of the state $|e_X\rangle$ is increasing, therefore the energy of the state $|e_Y\rangle$ is decreasing by the same amount of energy (and conversely). So magnetic instabilities correspond to anti-correlated energy fluctuations of the two excited states [199]. This can be modeled with a collapse operator which simulates phase fluctuations between the ground and the two excited states, with opposite sign for each excited states. Such a collapse operator is the anti-correlated collapse operator, defined as:

$$\hat{C}_{deph} = \hat{C}_{anti} = \sqrt{2\gamma^*}(\hat{\sigma}_{+,X}\hat{\sigma}_{-,X} - \hat{\sigma}_{+,Y}\hat{\sigma}_{-,Y}) \quad (3.32)$$

It can also be written as $\sqrt{2\gamma^*}(|e_X\rangle\langle e_X| - |e_Y\rangle\langle e_Y|)$.

Cross-dephasing noise.

The previous noise mechanisms correspond to correlated or anti-correlated noise mechanisms. We can also take into account uncorrelated noise mechanisms where the fluctuations of one excitonic transition do not depend on the fluctuations of the other. This can be done by using two independent Lindbladians for each exciton states: $\hat{L}_{deph,X}$ and $\hat{L}_{deph,Y}$. These Lindbladians are calculated thanks to the two collapse operators:

$$\begin{aligned} \hat{C}_{deph,X} &= \sqrt{2\gamma^*}\hat{\sigma}_{+,X}\hat{\sigma}_{-,X} \\ \hat{C}_{deph,Y} &= \sqrt{2\gamma^*}\hat{\sigma}_{+,Y}\hat{\sigma}_{-,Y} \end{aligned} \quad (3.33)$$

These uncorrelated fluctuations, also called cross-dephasing noise, are more exotic but can be used to simulate polarization-dependent interaction with phonons [200] and anisotropic fluctuating fields induced by localized charges [201].

3.3.5 Determination of the dominant noise mechanism.

All the noise mechanisms explicated previously can, in principle, be held responsible for a decrease of purity induced on the reflected photons, because they are inducing decoherence. However, to a certain extent, the nature of the noise is "printed" on the depolarization and one can deduce the dominant noise mechanism by observing the intensity and the polarization purity of the reflected light.

The three models of noise presented before are used to fit the data of normalized intensity reflected in the vertical and horizontal polarization. This is shown in Fig. 3.14(a) and (b) where the experimental points of the reflectivity spectrum are well fitted with the 3 models of noise. As a result, it is difficult to extract the noise mechanisms, only from a reflectivity spectrum. In Fig. 3.14(c), the results of the fits on the purity of the reflected light are displayed. The three fits give significantly different results on the purity of the reflected light. The models corresponding to anticorrelated noise or cross-dephasing noise do not fit well the polarization purity: both lead to much more expected depolarization at the energy of the quantum dot. Only the electric/temperature noise model fits best the polarization purity experimental data.

One reason to qualitatively explain why the electric/temperature noise results in reduced depolarization is the following. $|e_H\rangle$ and $|e_V\rangle$ are quantum superpositions of the quantum dot eigenstates $|e_X\rangle$ and $|e_Y\rangle$. Therefore, phase fluctuations between $|e_X\rangle$ and $|e_Y\rangle$ induces incoherent conversion from state $|e_H\rangle$ and $|e_V\rangle$. This decreases the Stokes parameter s_{HV} without polarization rotation and thus, leads to depolarization. For correlated noise, the phase between $|e_X\rangle$ and $|e_Y\rangle$ is kept constant and consequently, leads to reduced depolarization compared to the anti-correlated and cross-dephasing noises.

By fitting the reflectivities and then comparing the purity, one can think that we induce a bias in the fit results of the polarization purity. Another method is to fit the reflectivity curves and the polarization purity altogether. This is done again by minimizing the squared deviations to experimental data. The results are displayed in Fig. 3.15. In this case, the polarization purity fits are improved for all noise mechanisms. More specifically, the cross-dephasing noise fit is qualitatively close to the electric noise. The fit for anticorrelated noise is not as good as the other ones. The fits are also qualitatively equivalent for the reflectivity in vertical polarization. However, both the anticorrelated and cross-dephasing noises fail to fit the resonance fluorescence intensity in the horizontal polarization: the two fits give significantly smaller reflected intensities than what is observed experimentally. Only the correlated noise mechanism model is able to fit all the reflectivities and polarization purity experimental data. Consequently, it is impossible to fit the experimental data with another noise model than the correlated noise.

In conclusion, it is possible to deduce the dominant noise mechanism of a quantum dot from its optical response in polarization. This result is all the more important that it is based on a cavity-QED simulation that can be extended to other quantum emitters and thus, is not restricted only to quantum dot-based cavity-QED devices.

A first question that arises is the origin of the correlated noise. Indeed, the cryostat is an helium flow cryostat which has temperature instabilities measured with a thermometer of $\approx 10^{-3}\text{K}$ per second at most. This seems not enough to explain the instabilities observed. Concerning the correlated

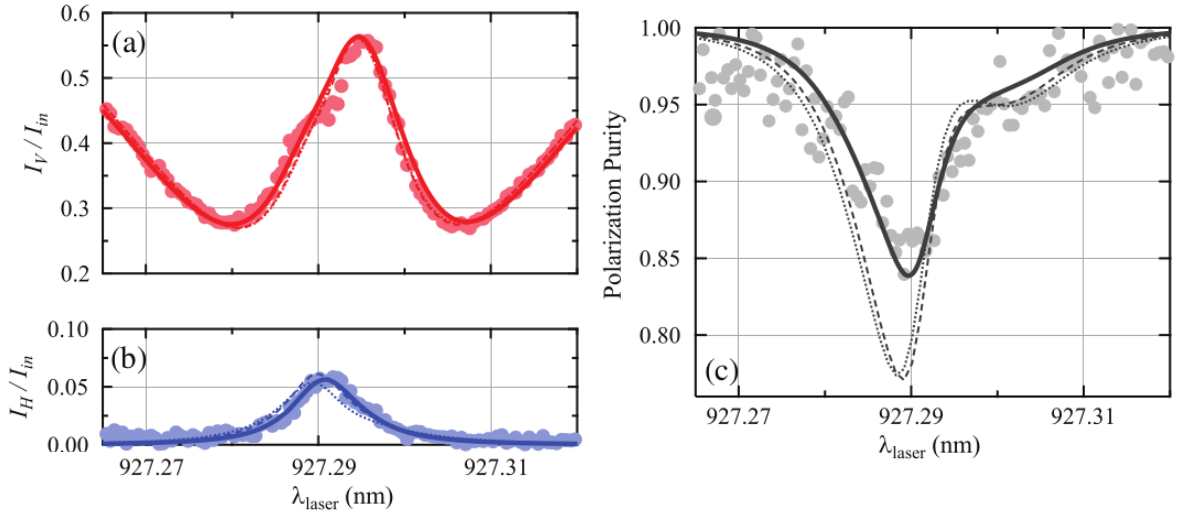


Figure 3.14: Experimental and simulated intensities in vertical (a) and horizontal (b) polarizations, modeled with various decoherence mechanisms. (c) Experimental and simulated polarization purity, modeled with the same set of decoherence mechanisms. Points: experimental data. Solid line: correlated noise. Dotted line: cross-dephasing noise. Dashed line: anticorrelated noise.

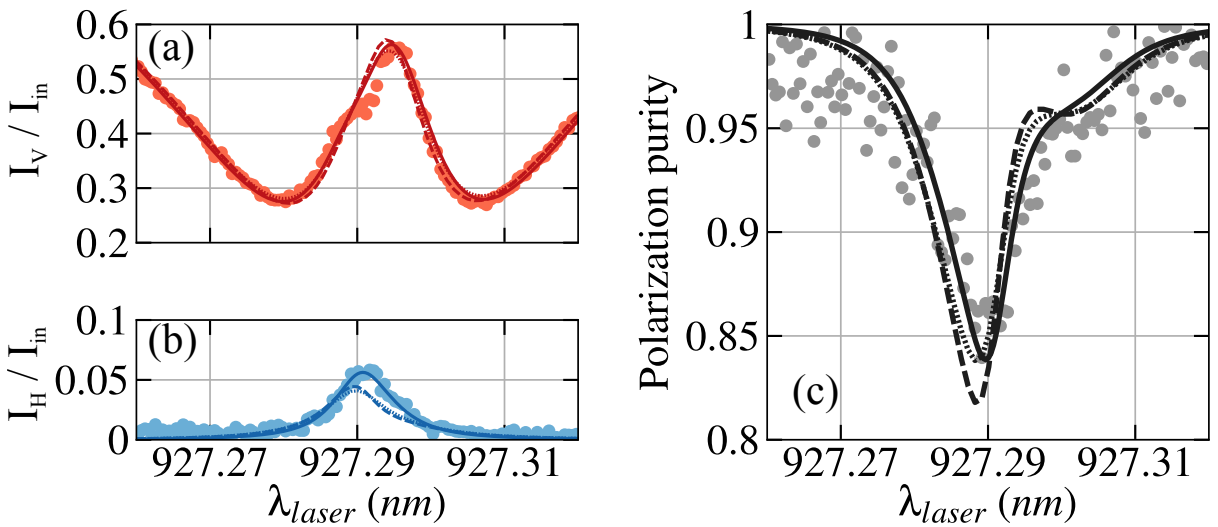


Figure 3.15: In this figure, the fits were obtained by jointly fitting all experimental curves (a), (b) and (c). (a) and (b) Experimental and simulated intensities in H and V polarizations, modeled with various decoherence mechanisms. (c) Experimental and simulated polarization purity, modeled with the same set of decoherence mechanisms. Circles: experimental data. Solid line: correlated noise. Dotted line: cross-dephasing noise. Dashed line: anticorrelated noise.

noise, electrically-contacted samples have been implemented to stabilize the electric environment of the quantum dot and suppress this noise. This is a reason why they can be used for producing high indistinguishability single photon sources [26]. The sample under study is also an electrically contacted device, however it has been widely tested and damaged so that current is passing through the diode when an electric field is applied. The quantum dot is tuned in resonance with a bias voltage above 2V that leads to $\approx 10^{-1}$ mA of current passing through the diode. This current is certainly responsible for the electric fluctuations observed in the experimental data, as it modifies the electronic environment of the quantum dot, and thus the quantum dot transitions by Stark shift.

Finally, a second question that arises is the timescale of these electric fluctuations. The use of a pure dephasing collapse operator is a widely-used method to simulate the effects of fluctuations [195, 87], though it is rigorously valid only if the energy fluctuations are very fast ($\lesssim 100$ ps) compared to the quantum dot excited lifetime. It is most probable that electric fluctuations occur at longer timescales, and in such a case, the proper modelization technique is to consider an inhomogeneous broadening of the quantum dot transition energy, by averaging the simulated results over different values of ω_{QD} . As this approach yields qualitatively similar results for the simulation of the Stokes parameters, compared to the pure dephasing approach, it is not possible with the data acquired here to discriminate between slow fluctuations and fast fluctuations. In Chap. 5, however, we will see that second order auto-correlation measurements applied to a spin-photon interface allow favoring the hypothesis of slow electric fluctuations.

3.4 Conclusion.

In this chapter, we have completely reconstructed the polarization of the light reflected by a single quantum dot-cavity device. We have shown that the quantum dot induces polarization rotation up to 20° both in latitude and longitude. However, the polarization purity is reduced due to incoherent processes induced mostly by electric instabilities.

Such polarization rotation is useful for the implementation of photon-photon gates. Indeed, in photon-photon gates, the state of a photon is modified depending on the state of another photon. This effect can be induced by photon blockade [202, 203, 204, 205] but can also be implemented on polarization-encoded photon qubits [206, 54]. In this case, the full rotation of polarization induced by a quantum dot is crucial for the implementation of polarization encoded photon-photon gates.

However, due to the fact that there is only one ground state, the polarization rotation is induced only by the excited state and there are time-energy uncertainty limitations that reduce the theoretical efficiency of photon-photon gates using neutral quantum dots [122]. One solution is to use a system that has a ground state with a spin degree of freedom such as a charged quantum dot. Indeed, there is no theoretical efficiency limitation for photon-photon gates using such charged quantum dots [122, 177]. The objective of the next chapter is focused on the practical implementation of such spin-photon interfaces where the quantum dot has an excess hole trapped as its fundamental state. A cavity can be deterministically interfaced with the trion transition which corresponds to the first optical excitation from a hole state. This constitutes a deterministic spin-photon interface.

Chapter 4

Optical charge control in a deterministic spin-photon interface.

4.1 Spin-photon interface with pillar micro-cavities.

For the development of solid-state photonic quantum networks [3], natural or artificial atoms should be efficiently interfaced with single photons. As introduced in Chap. 1, the atom-photon interaction is enhanced by inserting the atom in an optical cavity, resulting in a cavity-QED device. This device can operate both as an emitter and a receiver of single photons [156].

Regarding emission, a good single-photon source should produce deterministically pure and indistinguishable single photons [157]. Quantum dots systems are excellent candidates for this purpose, as they emit pure single photons [136] with near-unity indistinguishability [163, 164, 161, 26, 162]. They can be inserted into high-quality factor cavities [166, 25, 26, 162] which greatly improves the emitted photon collection. Consequently, they are promising single-photon sources.

A cavity-QED device should also acts as a receiver, where the state of an artificial atom manipulates or is manipulated by a single photon. As seen in the previous chapter, such single photon manipulation can be realized in polarization, i. e. the presence of a single neutral quantum dot leads to large polarization rotations for the reflected photons. However, a neutral quantum dot has only one single ground state which, therefore, does not have degrees of freedom to be manipulated. To use cavity-QED devices as efficient receivers, one can use the spin degree of freedom of a charged quantum dot, that is interfaced with the cavity mode.

The realization of such spin-photon interfaces requires to fulfill very demanding challenges. The first challenge is the deterministic coupling of a charged-QD state to the cavity mode. A second challenge is to prepare the quantum dot in a singly-charged state, which can be an excess electron or, as used in this work, an excess hole. Finally, the photon must be efficiently injected and collected from the cavity after interaction. The efficient injection has already been discussed in Chapter. 2. The efficient collection of photons emitted by the quantum dot is one of the final challenges addressed in this chapter.

In this chapter, we demonstrate the fabrication of deterministic spin-photon interfaces with near optimal properties, using a tunneling barrier to facilitate the trapping of a single hole [43]. First, we extend the in-situ lithography technique to deterministically couple a charged quantum dot state to a pillar micro-cavity. We then demonstrate a high occupation probability ($\gtrsim 85\%$) of the charge trapped inside the quantum dot, together with a high brightness on several cavity-QED devices. Fi-

nally, the quantum performances of these devices as emitters are compared to state-of-the-art single-photon sources.

4.2 Deterministic spin-photon coupling in pillar micro-cavities.

In order to fabricate a spin-photon interface deterministically, the cavity must be matched in wavelength with the trion transition. The spatial and spectral coupling of a quantum dot thanks to in-situ lithography has already been detailed in Sec. 1.4.2, but now, the objective is to identify and select the trion transition of the quantum dot, among the other charged states that are observed in a quantum dot photoluminescence spectrum. In this chapter, we use electrically-contacted QD-pillar devices, as described in Chap. 3, yet with a significant difference, following the approach proposed by Finley's group [43], a tunneling barrier is epitaxially-grown directly on top of the quantum dot layer, to facilitate the hole confinement. Such new device structure is detailed in the next section. Here we focus on the deterministic identification of the trion transition, through its photoluminescence dependence with a transverse magnetic field, and on the deterministic coupling of a trion transition to a cavity, thanks to the in-situ lithography technique.

4.2.1 Trion transition identification through magneto-photoluminescence.

Optical response of quantum dot charge states under in-plane magnetic field.

In Sec. 1.1, the trion transitions with and without magnetic field have been detailed and are summarized in Fig. 4.1 (a). At zero external magnetic field, a trion radiatively decays into the hole state by emitting a circularly-polarized photon with either a right-handed or left-handed helicity. There are therefore two trion transitions that are energy degenerate.

When a magnetic field is applied, it induces a Zeeman splitting between hole states and trion states, and it also modifies the system eigenstates and consequently the optical selection rules, as illustrated in the right panel of Figure 4.1(a). For a high in-plane magnetic field ($B_x > 1T$ typically), a trion decays into a hole by emitting a single photon with 4 combinations of linear polarizations and energies, as illustrated in Fig. 4.1(a). This feature is a signature of a trion state.

As a comparison, the example of a neutral quantum dot is illustrated in Fig. 4.1(b) where the exciton is energy-split with or without in-plane magnetic field and always exhibits two different transition energies. Thus, the following section exposes a strategy to identify the trion transition through polarization-resolved spectroscopy under an in-plane magnetic field.

Experimental trion transition identification.

The different responses of the trion and exciton quantum dot states under an in-plane magnetic field is used to identify them, which allows to deterministically couple the trion transition to a pillar micro-cavity. Experimentally, the trion transition needs to be identified on the planar cavity sample before the lithography step (see Sec. 1.4.2, for more details on the in-situ lithography procedure).

The technique relies on the study of the photoluminescence under a strong transverse magnetic field. This is experimentally possible thanks to a new helium-bath cryostat, upgraded with a superconducting magnet that produces a vertical magnetic field that can reach 9T. As illustrated in Fig. 4.2, specific lenses and sample holders allow the study of the sample under strong external magnetic field, not only in Faraday configuration, but also in Voigt configuration. The optical setup has

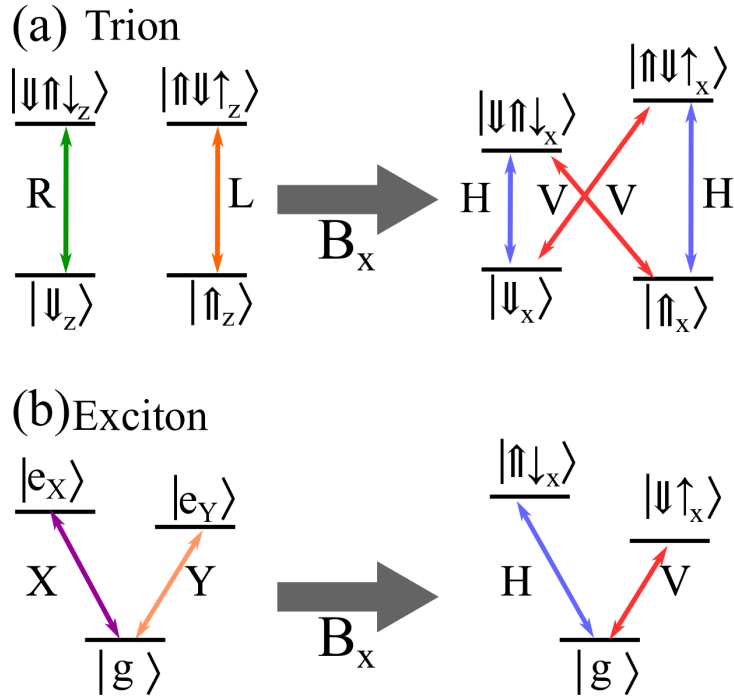


Figure 4.1: (a) Trion transitions with zero external magnetic field and under transverse magnetic field. At zero magnetic field, the trion spin states and the hole spin states are both degenerate in energy. Each trion state decays into one hole state by emitting circularly-polarized photons. With an in-plane magnetic field, the new eigenstates are Zeeman-split and each trion state decays in one hole state or the other by emitting a linearly polarized photon. (b) Exciton transitions at zero and under transverse magnetic field. At zero magnetic field, the excited states $|e_X\rangle$ and $|e_Y\rangle$ are separated by a fine structure splitting and decay into the fundamental state $|g\rangle$ by emitting a linearly polarized photon. When a strong in-plane magnetic field is applied, the splitting between the two excitonic states is increased by Zeeman splitting, and each state decays by emitting a linearly polarized photon with polarization H or V , i. e. parallel or orthogonal to the magnetic field direction.

been completely reconstructed to be adapted to this cryostat, to obtain all the results presented in the present and the next chapters.

Figure 4.3(a) shows a typical photoluminescence spectrum obtained on a quantum dot in such planar cavity sample, under non resonant excitation ($\lambda_{NR} = 850\text{nm}$) and without any applied magnetic field, measured thanks to a spectrometer. There are three dominant transitions observed, at 925.1 nm 925.3 nm and 925.7 nm; the two lower intensity transitions (at 925.5 nm and 926.1 nm) are related to another quantum dot next to the one under study. The 25-pm spectrometer resolution does not permit to resolve the exciton fine structure: consequently, from such spectrum, it is impossible to identify the quantum dot states. When an in-plane magnetic field is applied, the quantum dot transitions observed at $B_x = 0T$ start to be energy splitted. This can be seen in Fig 4.3(b) which displays the evolution of the photoluminescence spectrum (without polarization selection) under an increasing in-plane magnetic field intensity. At $B_x = 4T$ and above, all the transitions are split in two transitions resolved by the spectrometer. At high magnetic field, all the quantum dot transitions observed are also blue-shifted; this is due to the diamagnetic shift [207]. One should expect that the trion transition

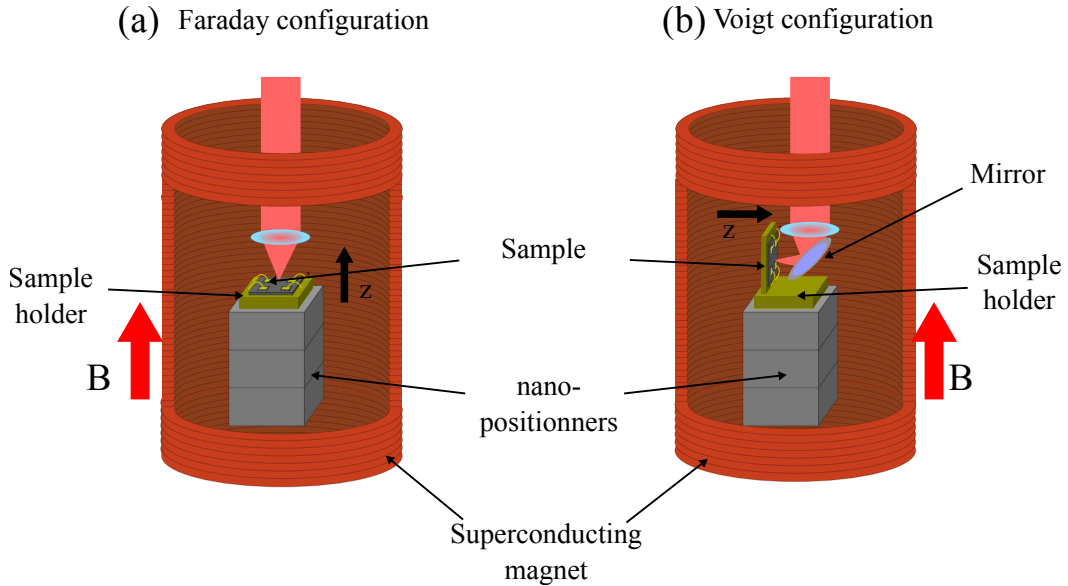


Figure 4.2: Cryostat setup allowing the study of the sample both in Faraday (a) and Voigt (b) configurations, by modifying both the lens and the sample holder. A superconducting magnet generates a magnetic field oriented in the vertical direction. (a) In Faraday configuration, the micropillars and the lens are oriented vertically. (b) In Voigt configuration, the sample holder orients the sample so that the pillars are oriented horizontally. A mirror is added in between the lens and the sample to also orient the beam horizontally.

should split into four different transitions which is not what is observed here. This is due to the limited spectrometer resolution.

To overcome this difficulty, the photoluminescence spectrum is analyzed also in polarization. A half wave plate and a polarizer are inserted before the spectrometer. Fig. 4.3(c) displays the polarization-resolved photoluminescence for the same quantum dot at $B_x = 4T$. The y-axis of this figure, shows the polarization angle at which is observed the quantum dot photoluminescence. The horizontal (vertical) polarization peaks centers are highlighted by white (black) dashed lines. Let's consider first the redder transition from Fig. 4.3 (a). The magnetic field scan and the polarization analysis show that it is split in two transitions with orthogonal linear polarizations, as expected from the polarization selection rules of an exciton, illustrated in Fig. 4.1(b). Fig. 4.3 (b) and (c) show that the redder transition is therefore an exciton. The bluer transition analysis shows that it is split in four transitions with different energies, as can be seen in Fig. 4.3 (b). Among these four, Fig. 4.3 (c) shows that the highest and lowest energy transitions have the same horizontal polarizations, and are orthogonal to the two center transitions which are vertically-polarized. The bluer transition is therefore identified as a trion, as this is the behavior expected from the polarization selection rules of Fig. 4.1 (a). The center transition analysis is more complicated. It is also split in four transitions with similar polarization as the quantum dot trion. However, there is a clear asymmetry in the photoluminescence intensity for these four transitions. This more complex feature can be explained by another quantum dot state such as a bi-trion state X^{2+} (which corresponds to an electron-hole pair and two holes confined inside the quantum dot) [208].

The observed splitting between the two higher and lower energy transitions is small, which is ex-

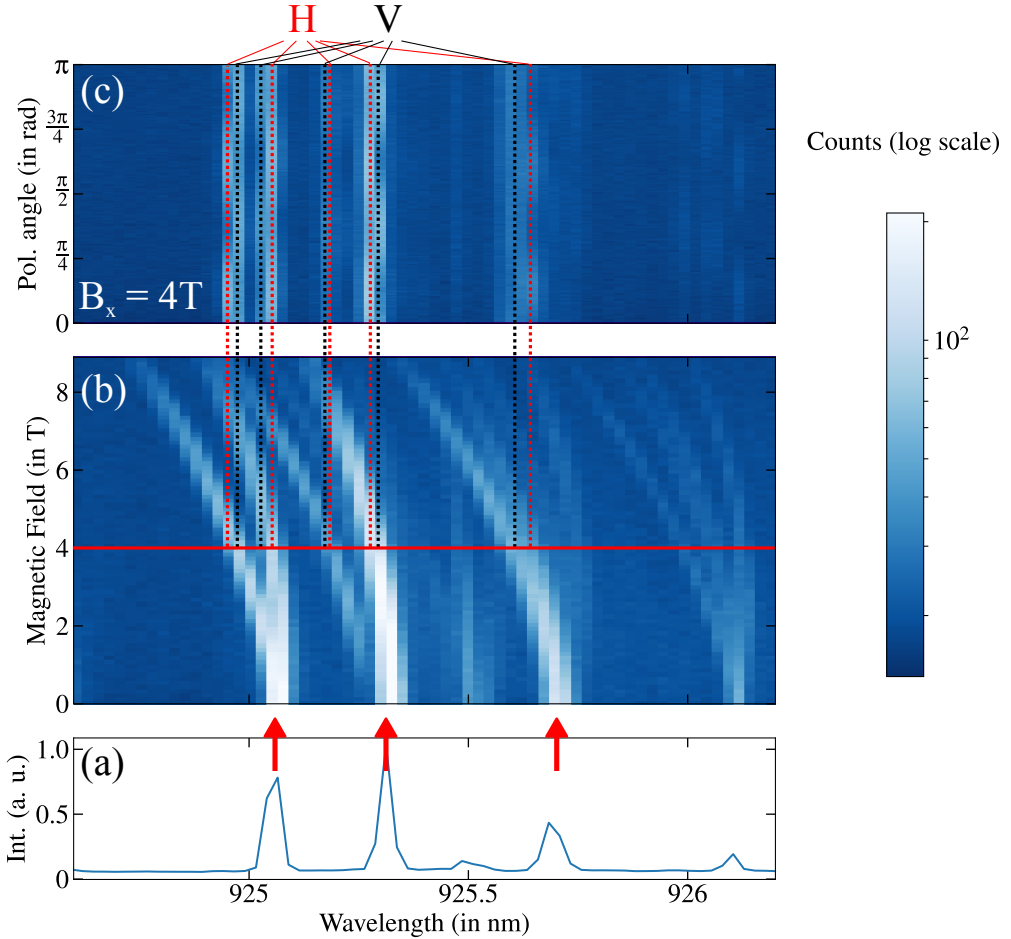


Figure 4.3: (a) Quantum dot photoluminescence under 850-nm non resonant laser observed on a spectrometer at 0 magnetic field (without polarization selection). (b) Photoluminescence of the same quantum dot under in-plane magnetic field. The optical transitions observed in (a) are now Zeeman-splittered (without polarization selection). (c) Quantum dot photoluminescence with 4T in-plane magnetic field observed for different polarizations. "Pol. angle" represents the angle read on the half waveplate before the polarizer. Some optical transitions at 4T have also a polarization splitting, highlighted by the dashed white (corresponding to horizontal polarization) and black (vertical) line.

plained by the Landé factor difference between an electron and a hole [73, 209]. The hole transverse Landé factor is generally much smaller than the electron Landé factor. The typical electron Landé factor, $g_e \approx 0.4$ [210], results in a strong Zeeman splitting of the trion spin states (that is equivalent to its electron spin states) while a smaller hole Landé factor results in a smaller splitting for the hole spin states. Such difference of Zeeman splittings implies that $|\uparrow\downarrow\uparrow_x\rangle \rightarrow |\uparrow_x\rangle$ and $|\uparrow\downarrow\uparrow_x\rangle \rightarrow |\downarrow_x\rangle$ (respec-

tively $|\downarrow\uparrow\downarrow_x\rangle \rightarrow |\uparrow_x\rangle$ and $|\downarrow\uparrow\downarrow_x\rangle \rightarrow |\downarrow_x\rangle$) have small energy difference and orthogonal polarizations as observed in the results of Fig. 4.3 (b) and (c).

4.2.2 Deterministic spin cavity matching.

With the above technique to identify the trion transition, this transition can be coupled to the fundamental cavity mode of a pillar microcavity thanks to the in-situ lithography technique. Because the in-situ lithography cryostat is not yet equipped with such magnetic field, it is not possible at the moment. To overcome this difficulty, we studied the planar cavity sample under transverse magnetic field in another cryostat, looking for general patterns in the quantum dot spectral positions. On this specific planar sample, we observed that the trion transition is the bluer transition for $\approx 60\%$ of the studied quantum dots. The sample was then placed inside the in-situ cryostat to apply the in-situ lithography procedure aiming at this bluer transition.

After the realization of electrically-contacted spin-cavity samples through the previously discussed in-situ lithography, the deterministic trion transition-cavity coupling is evaluated by repeating the procedure of trion identification under an in-plane magnetic field. The trion transition at zero magnetic field is then compared to the cavity mode energy to verify that it is indeed coupled to the cavity mode: this is what is displayed in Fig. 4.4.

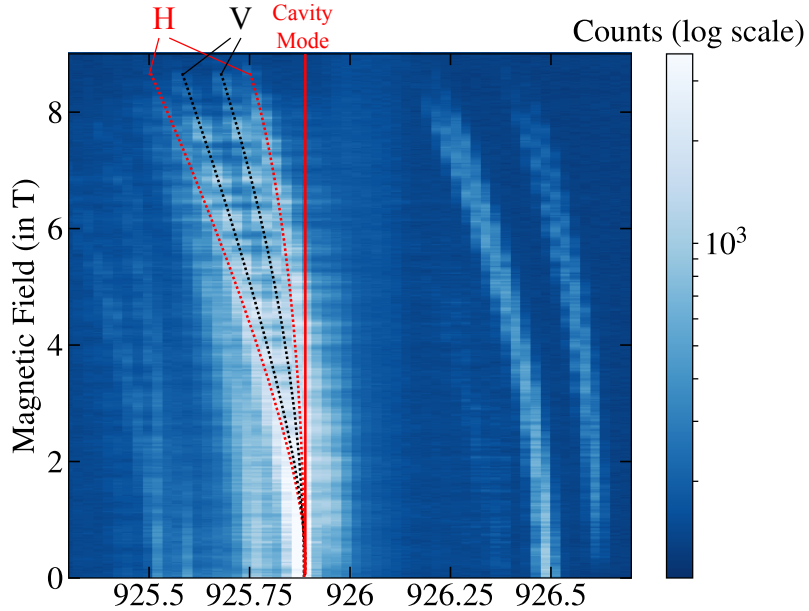


Figure 4.4: In-plane magnetic field scan of a cavity-coupled device photoluminescence. A waveplate is rotated before the spectrometer, during the magnetic field scan, to obtain polarization resolution. The trion transition is coupled to the cavity mode at 0T.

In the data plotted in Fig. 4.4, the information of the polarization and the magnetic field dependence are acquired at the same time: a set of half waveplate and polarizer is positioned before the spectrometer and is rotated with constant speed which provides the polarization information of the quantum dot photoluminescence, while the magnetic field intensity is simultaneously in-

creased. Therefore, Fig. 4.4 combines the information provided in Fig 4.3(b) and (c). It shows the photo-luminescence of a cavity-coupled quantum dot under magnetic field, at cryogenic temperature ($T = 4K$). Similar data need to be acquired but unfortunately, the Voigt lens which allows the in-plane magnetic field configuration was damaged and needed to be changed. The trion transition, characterized by the four Zeeman-split transitions, is identified at 925.9nm, which is indeed in resonance with the cavity mode. So, the in-situ lithography process indeed couples the cavity mode to the trion transition. Consequently, when a hole is populated, its spin degree of freedom will be interfaced with photons. The next step is to trap a hole inside the quantum dot with high probability.

4.3 Optical charge control of the quantum dot.

The technique developed previously deterministically couples the trion transition with a pillar microcavity. This transition appears on the quantum dot photoluminescence under non-resonant excitation, as shown in Fig. 4.4. Still, under resonant excitation, the trion transition is optically active only if a hole is trapped inside the quantum dot. Only in this case, a spin-photon interface exists. It is therefore crucial to efficiently trap a hole inside the quantum dot.

In this section, we present how the hole trapping is achieved thanks to the engineering of a new device structure and the use of a quasi-resonant optical excitation scheme. The resulting hole occupation lifetime and probability are then measured thanks to correlation measurements on the trion resonance fluorescence.

4.3.1 Hole trapping through device structure engineering.

The objective of this section is to efficiently trap a single hole inside the quantum dot for a time as long as possible. As detailed in the following, we have designed a new sample with a tunneling barrier on top of the quantum dot layer that prevents a hole confined in the quantum dot to tunnel out too quickly. An electron-hole pair is then optically generated, but the electron can quickly escape the quantum dot, while the single hole remains.

Let us first review the different hole confinement strategies that were considered and the choices that led us to the use of a tunneling barrier. The first possibility is to have a quantum dot state where a hole is permanently trapped inside the quantum dot, because of the sample residual doping: this happens by luck on at best one sample out of ten. This was for example obtained in the first generation of samples obtained by in-situ lithography, where there were no p-i-n structure and no electrical contacts [27].

A well known technique to control the charge state of quantum dots is to use a p-i-n junction [82, 211] where quantum dots are close to the doped layer so that electrons and holes can tunnel in and out. The tunneling is controlled by a bias voltage that brings the Fermi energy close to a charged quantum dot state, allowing one single charge carrier to tunnel into the quantum dot. For quantum dots coupled to microcavities, however, the free-carriers of the doped regions can absorb cavity photons leading to additional cavity losses, which are detrimental for the quality of the light-matter interaction. In this respect, the doped regions should be positioned far from the quantum dot position, where the electric field of the confined cavity mode is not intense. This strongly increases the difficulty of obtaining a Fermi level very close to the charge QD state. This is the reason why in the electrically-contacted devices used in Chap. 3, the stable quantum dot state was the neutral quantum dot: charged quantum dot states could only be obtained for a very short time and with low probability.

To increase the charge confinement time, we followed the approach developed in Finley's group [43] where a tunneling barrier is epitaxially-grown nearby the quantum dot layer to increase the hole trapping time. This solution is implemented in our device structure as seen in Fig. 4.5, where a 20nm-thick $Al_{0.1}Ga_{0.9}As$ tunneling barrier is positioned 10nm above the quantum dot layer. In Ardel et al. (2015)[43], the confinement of a hole is obtained by resonant excitation of the exciton transition: the generated electron quickly escapes the quantum dot, while the hole remains confined much longer thanks to the tunneling barrier. Such asymmetrical design should thus both increase the hole confinement time and favor the single hole state over the electron state.

In our device, the p-i-n junction and the electrical contact are still used to stabilize the electrical environment, but the doped regions are positioned far away (200nm) from the quantum dot to avoid detrimental free-carrier absorption. The counterpart of this choice is that the quantum dot charge state cannot be controlled thanks to the bias voltage and thus such spin-photon interface really requires an optical carrier injection. This is detailed in the following.

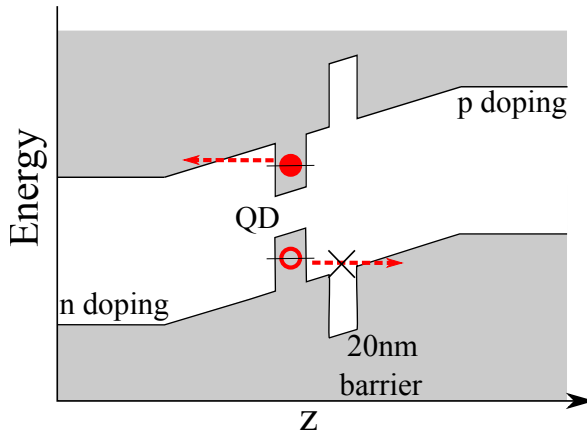


Figure 4.5: Cavity structure. A 20nm thick tunneling barrier is inserted next to the quantum dot layer on the p-doping side. Thanks to this barrier, the hole has a tunneling time much longer than the electron. When electron-hole pairs are injected in the quantum dot, the electron will eventually escape, leaving a hole trapped in the quantum dot and blocked by the tunnel barrier.

4.3.2 Quasi-resonant excitation scheme.

Resonant, quasi-resonant and non-resonant excitations.

The tunneling barrier guarantees that a hole can be trapped for a long time inside the quantum dot. Still a hole needs to be generated in the quantum dot and to do so, we use an optical carrier injection strategy.

In general, the stable quantum dot state is the neutral state whose energy levels and typical optical excitation methods are represented in Fig. 4.6 (a). A first possibility to create an electron-hole pair is to use non-resonant excitation, by exciting the material in the above-band continuum of GaAs or in the wetting layer. Another possibility is to generate an electron-hole pair by optically exciting the discrete-energy levels of the quantum dots. The lower-energy transition ("s-shell excitation") corresponds to the creation of an exciton, directly in the first excited state (previously denoted $|e\rangle$), using resonant excitation at the transition energy ω_X . Other transitions are denoted as quasi-resonant

transitions. They consist in exciting other discrete transitions, at an energy above ω_X , using for example a "p-shell" transition. Another type of quasi-resonant excitation consists in the generation of an exciton and a longitudinal optical (LO) phonon, using a laser at the energy $\omega_X + \omega_{LO}$. Both resonant, quasi-resonant and non-resonant excitation are used in various groups [43, 209, 212].

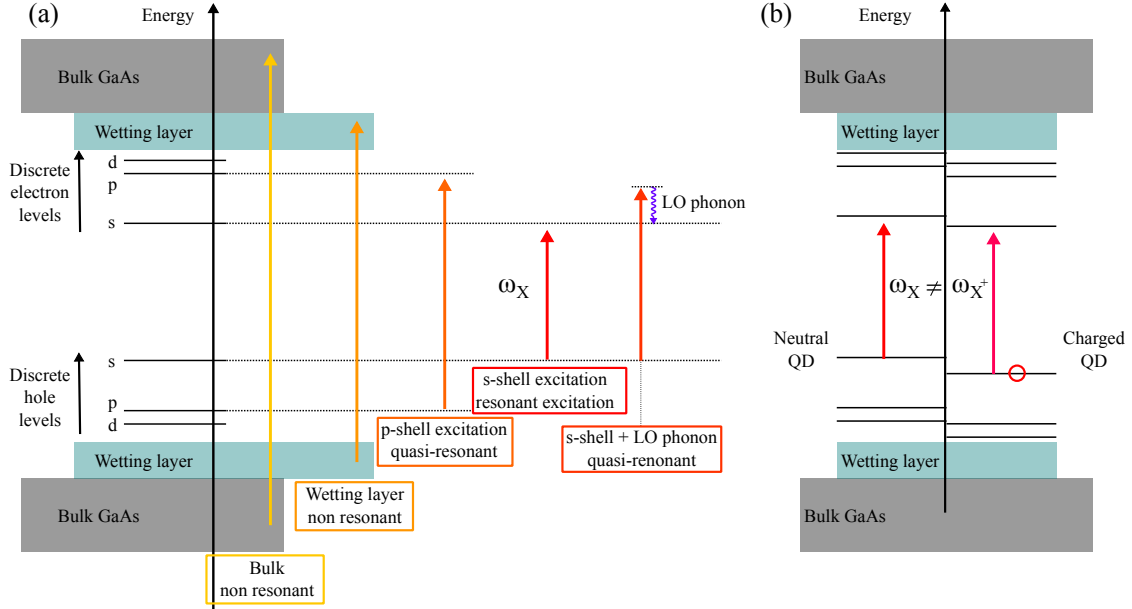


Figure 4.6: (a) Sketch of the energy levels of a neutral quantum dot with the pumping conditions: non-resonant excitation for wetting layer and bulk excitations, quasi-resonant excitation for p-shell and LO-phonon excitations, and resonant excitation at the exciton energy ω_X . (b) Comparison between the energy levels of a neutral and a singly-charged quantum dot: a hole completely modifies the discrete energy levels and the optical transition energies, including the resonant trion transition energy $\omega_{X^+} \neq \omega_X$.

In general, when an electron-hole pair is generated by quasi-resonant or non-resonant excitation, the electron and the hole non radiatively decay into the quantum dot and eventually form an exciton. Thanks to the asymmetric design of the device, the electron can tunnel out the quantum dot, thus generating a hole state. Such confined charge induces a strong modification of the electric environment by Coulomb interaction, which modifies the energies of the discrete energy levels of the quantum dot, as illustrated in Fig. 4.6 (b). This explains why the trion transition does not have the same energy as the exciton transition ($\omega_X \neq \omega_{X^+}$). But the presence of an excess hole in the QD also modifies all the other discrete energy levels, and thus all the quasi-resonant transition resonant energies.

Optical hole trapping scheme.

Thanks to the above discussion, we see that it should be possible to optically trap a hole by generating an electron-hole pair via non-resonant, quasi-resonant or resonant excitation of a neutral quantum dot. The scheme to optically trap a hole is illustrated in Fig. 4.7, using the example of quasi-resonant "p-shell" excitation. The stable quantum dot state is the crystal ground state that consists of no excess charges as shown in Fig. 4.7(a). A first laser is used to excite quasi-resonantly the quantum dot, with a laser at the energy ω_{QR} (see Fig. 4.7(b)), thus generating an electron-hole pair. As seen in Fig.

4.7(c), the two charges quickly non-radiatively decay into the fundamental exciton. If the exciton radiatively recombines by emitting a photon, the resulting state is the crystal ground state as seen in Fig. 4.7(a) and the quasi-resonant laser can generate again an electron-hole pair. Eventually, the electron escapes before the radiative recombination, while the hole is confined for a longer time, as illustrated in Fig. 4.7(d). The resulting quantum dot consists of a single hole confined in the quantum dot. It can then be optically manipulated by a second laser in resonance with the trion transition, i. e. at the energy $\omega_{X^+} \neq \omega_X$, as shown in Fig. 4.7(e). Because, the exciton and the trion transition have different energies, this second laser does not intervene in the hole trapping procedure.

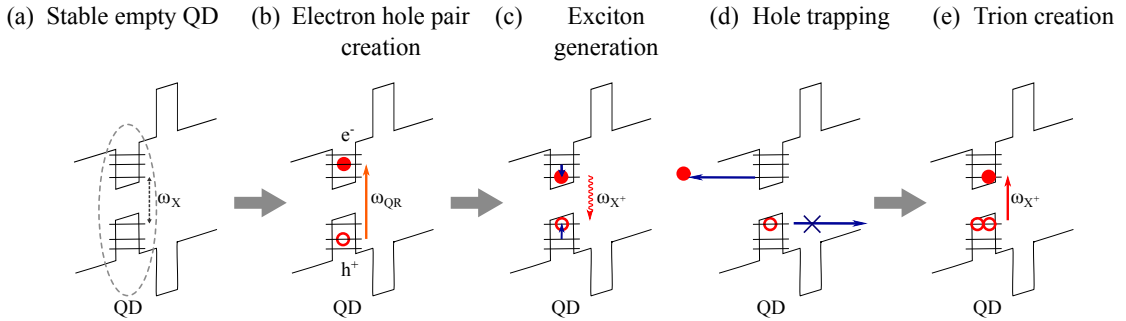


Figure 4.7: Hole trapping scheme using quasi-resonant excitation. (a) The quantum dot stable state is the empty state where the discrete energy levels of the conduction and valence bands are not populated by holes or electrons. The fundamental excitation is the exciton of energy ω_X . (b) A quasi-resonant laser creates an electron-hole pair. The laser energy ω_{QR} is chosen here to correspond to a quantum dot p-shell transition. (c) The electron and the hole non radiatively decay into the lower conduction and the upper valence energy levels respectively, thus generating an exciton that can radiatively decay and therefore, the quantum dot is in the empty state as in (a) and the quasi-resonant pumping re-create such exciton. (d) Eventually, the electron escapes the quantum dot before the radiative recombination by tunneling while the hole cannot because of the tunneling barrier. It eventually populates the quantum dot highest valence band energy level. (e) Then the quantum dot can be resonantly excited by a laser with energy ω_{X^+} ($\neq \omega_X$) corresponding to the trion transition.

Now, let us discuss the choice of the laser used for the hole trapping. A first possibility is to use a non-resonant laser. Because it is exciting an energy continuum, such non-resonant excitation generates an electron-hole pair not only when the quantum dot is in the crystal ground state but also when a hole is already confined. This can lead to the generation of another quantum dot state with two excess holes: this also needs to be avoided, as the two holes would be in a singlet state $|\uparrow\downarrow\rangle$, i. e. have no spin degree of freedom.

Another possibility is to use a laser resonant with the quantum dot excitonic transition, $\omega_{laser} = \omega_X$. However, in the context of cavity-QED with the cavity centered on the trion transition, the exciton is not in resonance with the cavity. Therefore, resonant exciton excitation requires a high laser intensity to inject photons into the cavity at a wavelength close to the trion transition: suppressing this high-intensity laser is challenging.

Therefore quasi-resonant excitation is preferred in our case. The quasi-resonant excitation wavelength that we experimentally used targets a discrete optical transition at $\lambda_{QR} = 901\text{nm}$. The exact quantum dot state that is excited is not yet clearly identified for this wavelength. It can correspond either to a p-shell excitation or to the creation of a 36meV longitudinal optical phonon in addition to the exciton. Compared to non-resonant excitation, a quasi-resonant scheme prevents the generation

of a two-hole quantum dot state: as explained in Fig. 4.6(b), if a hole is trapped, the discrete energy levels are shifted in energy due to Coulomb interaction with the trapped hole. Therefore, after generation of a hole inside the quantum dot, the optically excited non resonant transition is not active anymore, which consequently reduces the possibility of trapping two holes.

It is possible to use pulsed quasi-resonant excitations where the hole is generated directly after the pulse. We decided to work with a continuous-wave quasi-resonant laser at 901nm because of resources availability. In that case, the single hole state is produced statistically, with an occupation probability $\langle P_h \rangle$, which is the probability that the single hole state is populated at any given time. The hole trapping scheme performances are evaluated in the next section.

4.3.3 Measurement of the hole trapping efficiency.

The objective of this section is to measure the hole trapping efficiency of the scheme presented previously. The hole occupation probability and the hole trapping time are measured for three quantum dot-based spin-photon interfaces QD1, QD2, QD3 (detailed results were obtained for QD1), thanks to intensity correlation measurements of the trion cross-polarized resonance fluorescence. We show that such intensity correlations contain information on the hole occupation probability and trapping time by relating these measurements, performed at different quasi-resonant and resonant laser powers, to the brightness of the single photon emission.

Correlations measurement principle.

The correlation measurements are detailed in the following and acquired with the setup presented in Fig. 4.8:

- A spin-photon interface is excited with a CW quasi-resonant laser at $\lambda_{QR} \approx 901\text{nm}$ to generate a single-hole in the quantum dot.
- A pulsed laser, resonant to the trion transition at $\lambda_{X^+} (\approx 925\text{nm})$, is used as a probe to measure the hole occupation probability. The pulses are shaped to be 15ps long so that they are spectrally wider than the trion transition but still spectrally narrow enough not to excite the other quantum dot states. If a single hole is trapped, the trion transition is optically active and a single photon can be produced. In other cases, the trion transition is not optically active and therefore, it cannot generate a single photon. The advantage of using pulsed excitation is that the single photon source brightness can also be easily evaluated.
- The cross-polarized reflected light, which corresponds to single photons emitted by the quantum dot (assuming an ideal polarization rejection of the laser), is measured thanks to single photon detectors. The key point is that detected photons originate from the quantum dot trion transition. Consequently, the detection of a single photon is a direct signature that a single hole is indeed present in the quantum dot.
- The cross-polarized light is analyzed thanks to a Hanbury-Brown and Twiss experiment similar to the one presented in Fig. 3.4. However, in this study, we are not interested in the correlations at short delays, which are a signature of the single-photon statistics of the light source, but to the correlations at longer delays, typically of the microsecond timescale, where the charge state dynamics should appear. One should also note, that contrary to Fig. 3.5, the photons are produced here with pulsed excitation instead of continuous excitation.

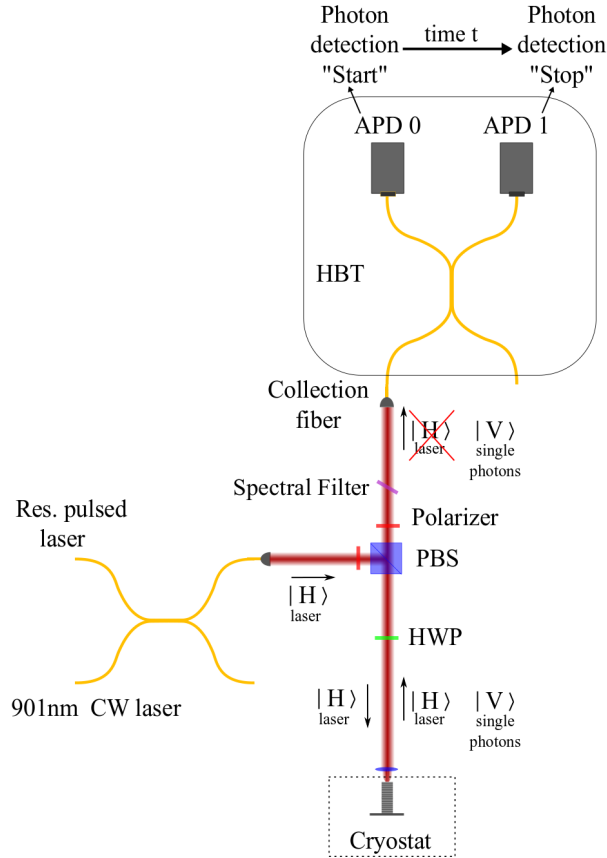


Figure 4.8: Hole trapping resonance fluorescence setup. The non-resonant CW laser and the resonant pulsed laser are set in the same spatial mode thanks to a fiber beam splitter. The laser is prepared to excite the cavity horizontal polarization axis. The emitted single photons are separated from the lasers by cross-polarization selection and by filtering out the non resonant laser thanks to a 10nm-wide bandpass spectral filter. The photons are then collected in a single-mode fiber and sent to a HBT setup. Correlations are measured between the two single-photon detectors, denoted APD0 and APD1.

Before analyzing long-delay correlations, we display in Fig. 4.9(a) a time trace of such resonance fluorescence signal, with a quasi-resonant power of $50\mu\text{W}$ and a time bin of $\Delta t = 4\mu\text{s}$. This figure clearly evidences the expected on-off behavior of the resonance fluorescence signal: when the hole is trapped, the quantum dot emits photons that are detected, while when it is not trapped, the quantum dot does not emit single photons and therefore no signal can be detected. A second histogram representing the distribution of the number of detected events per time bin is represented in Fig. 4.9(b). It also clearly displays the on/off behavior of the resonance fluorescence signal: when the hole is absent, photons are not emitted by the quantum dot and thus cannot be detected: this explains the high probability to detect zero photons per time bin. When the hole is trapped, the quantum dot emits photons that are detected with a typical Poisson distribution of parameter $\langle N \rangle$ (which coincides with a gaussian distribution centered in $\langle N \rangle$ with width $\sigma = \sqrt{\langle N \rangle}$, when $\langle N \rangle$ is sufficiently high). We extract a mean value of $\langle N \rangle = 7.9$ photons per time bin Δt which is expected given the transmission

of the setup and the efficiency of the detectors. The deviation from these two distributions, visible for $n = 1$ photon detected per time bin, is explained by the dark counts and by the imperfect laser rejection.

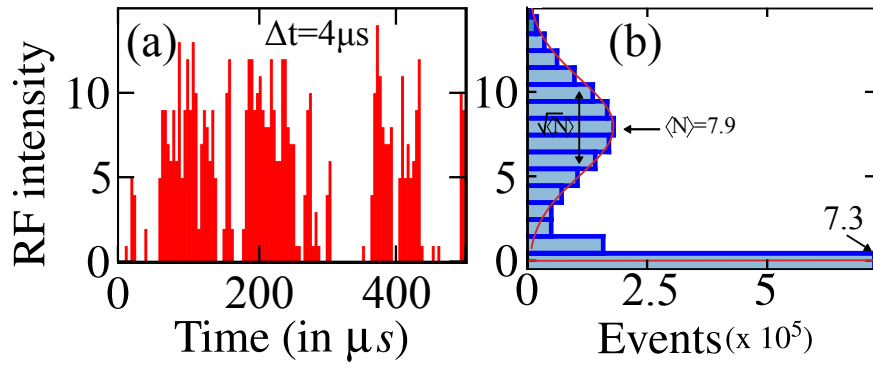


Figure 4.9: (a) Typical time trace of the resonance fluorescence signal of a quantum dot whose trion transition is resonantly excited by a pulsed laser. A second CW quasi-resonant laser (at 901nm and with $P_{QR} = 50\mu\text{W}$) is trapping the hole state. The time trace is the temporal histogram, integrated with time bin $\Delta t = 4\mu\text{s}$, recording the number of photons detected by single-photon detectors during each time bin. It shows an on/off behavior resulting from the successive presence and absence of the hole. (b) Histogram of the number of time bins corresponding to a given number of detected photons per time bin Δt , during an acquisition time of approximately 10s. It represents the intensity distribution of the single-photon source. It clearly displays the addition of a high zero detected photon probability (when the hole is not trapped) and a gaussian distribution (when the hole is trapped). When the hole is present, the intensity of the resonance fluorescence is of $\langle N \rangle = 7.9$ photons per time bin, with a width of $\sigma = 2.8 (= \sqrt{\langle N \rangle})$ which is expected for the detection of a constant signal. The dark counts and the imperfect laser rejection are certainly responsible for the deviation of these two distributions for $n = 1$ detected photon events.

We now move to the study of photon-photon correlations, using the HBT setup described in Fig. 4.8. A typical correlation measurement at short delay is displayed in Figure 4.10(a), where the two photon coincidences are displayed for different delays. It displays peaks regularly separated by a delay $T_R = 1/f$ where $f = 82\text{MHz}$ is the laser repetition rate, showing that the detected photons were produced by the resonant pulsed laser. The zero-delay peak is much smaller than the other peaks, which is a single-photon statistics signature: the quantum dot trion transition indeed generates single photons, with (ideally) not more than one photon per pulses, i. e. $g^{(2)}(0) = 0$. In Fig. 4.10(a), the continuous background between two peaks is due partly to the detector dark counts, but in majority to an imperfect filtering of the quasi-resonant laser (whose power is several orders of magnitude more intense than the resonant laser: $P_{QR} \approx 1 - 100\mu\text{W} \gg P_{X+} \approx 0.1 - 3\text{nW}$).

Figure 4.10(b) shows the same set of data for longer delays. A decay appears when observing the data at this timescale, which is the phenomenon of interest here. Figure 4.10(c) shows the intensity auto-correlations $g^{(2)}(t)$ with the same set of data at even longer times, and integrated with a time bin

corresponding to 10 laser pulses, i. e. a time bin $\Delta t = 10T_R$. At this timescale and with such a long time bin, the individual peaks are not resolved anymore, and similarly the absence of coincidence in the zero-delay peak is not observable as well, allowing us to focus on the long-timescale behavior of the autocorrelation function. Such correlation measurement clearly shows an exponential decay that can also be observed on the resonance fluorescence of other devices, as illustrated in Figure 4.10(d) and (e). The next section shows that this exponential decay is generated by the fluctuating charge state, and that it is possible to extract the hole trapping time and occupation probability out of these measurements.

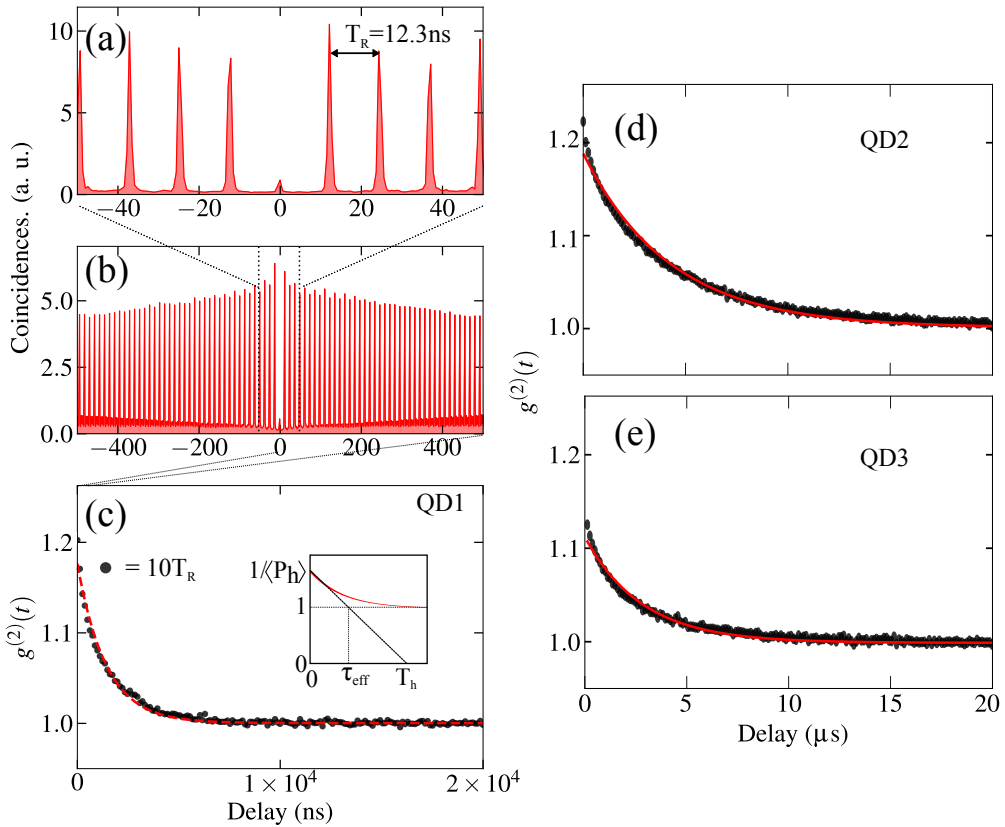


Figure 4.10: Auto-correlation measurement observed at different timescales. (a) Typical coincidences measurement of pulsed resonance fluorescence. The zero-delay peak characterizes the purity of the single photons. (b) Same data observed at longer timescale. (c) Intensity auto-correlations $g^{(2)}(t)$ of the same set of data, for even longer timescale. The pulses are no longer resolved because each point represents an integration over 10 pulses, $\Delta t = 10T_R$. The decay is observed and fitted by an exponential decay (red curve). The inset illustrates how the hole occupation probability $\langle P_h \rangle$ and the hole trapping time T_h can be deduced from such correlation measurements. (d, e) Intensity auto-correlations $g^{(2)}(t)$ repeated for other devices (QD2 and QD3).

Theoretical model of the trapping scheme.

This model aims at explaining the correlations observed in Figure. 4.10(c-e). It is based on the assumption that the quantum dot can be populated with a single hole state (denoted "h") or not (state denoted "0") (see Fig. 4.11). A more complete model that takes into account the two-hole ground state is presented in Appendix A.

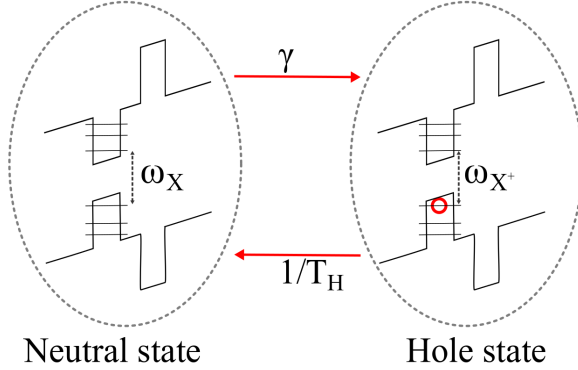


Figure 4.11: Hole trapping modelization. The quantum dot is assumed to be in two ground states corresponding to the neutral state (crystalline ground state) and to the single-hole state (the spin is not taken into account). A laser pumps the quantum dot to insert a hole with a rate γ . This hole is metastable but is tunneling out from the quantum dot at rate $1/T_H$.

The CW quasi-resonant laser at 901nm transfers the quantum dot state from "0" to "h" at a rate γ (which directly depends on the quasi-resonant power P_{QR} , used to populate the single hole state). Conversely, the hole can tunnel out from the quantum dot with a tunneling time T_H . The occupation probability of the empty state and the charged states are denoted $P_0(t)$ and $P_h(t)$ respectively .

The rate equations are:

$$\begin{aligned} \frac{dP_h(t)}{dt} &= \gamma P_0(t) - \frac{1}{T_H} P_h(t) \\ \frac{dP_0(t)}{dt} &= -\gamma P_0(t) + \frac{1}{T_H} P_h(t) \end{aligned} \quad (4.1)$$

Using $P_0 + P_h = 1$:

$$\frac{dP_h(t)}{dt} = \gamma - (\gamma + \frac{1}{T_H}) P_h(t) \quad (4.2)$$

The hole occupation probability at equilibrium is therefore given by:

$$\langle P_h \rangle = P_h(\infty) = \gamma / (\gamma + \frac{1}{T_H}) \quad (4.3)$$

Let us take, as initial time $t = 0$, the moment when a single photon has been detected in one of our photodiodes, say APD0 in the setup of Fig. 4.8. Assuming this photon was indeed generated by the trion decay, we know that at this time $t=0$, the hole is trapped inside the quantum dot with probability 1: $P_h(0) = 1$.

The hole occupation probability evolution is thus given by:

$$P_h(t) = (1 - \langle P_h \rangle) e^{-\frac{t}{\tau_{eff}}} + \langle P_h \rangle \quad (4.4)$$

with $\tau_{eff} = \left(\gamma + \frac{1}{T_h}\right)^{-1}$, the effective time characterizing the charge dynamics. The link with the $g^{(2)}(t)$ is straightforward as it is the probability to detect a photon in the second detector (APD1) at time t , conditioned to the detection at time $t = 0$ of a photon in the first detector (APD0) normalized by the uncorrelated probability of detecting a photon at any time:

$$g^{(2)}(t) = \frac{P(APD1,t|APD0,0)}{P(APD1)} \quad (4.5)$$

Because the probability to detect a photon is proportional and directly linked to the hole occupation probability, the intensity correlations at long delays are given by:

$$g^{(2)}(t) = \frac{P_h(t)}{\langle P_h \rangle} = \left(\frac{1}{\langle P_h \rangle} - 1 \right) e^{-t/\tau_{eff}} + 1 \quad (4.6)$$

This relation has been used to fit the curves in Fig. 4.10(c-e) and, as displayed in the inset of Fig. 4.10(c), it is possible to extract the hole trapping characteristics thanks to such correlation measurement. Indeed, the zero-delay value of the correlations is directly linked to the hole occupation probability $\langle P_h \rangle = \frac{1}{g^{(2)}(0)}$, and the tangent of the correlation curve at zero delay, whose equation is $y = \frac{1}{\langle P_h \rangle} \left(1 - \frac{t}{T_h} \right)$, crosses the time axis at time $t = T_h$ (and also the horizontal line $y = 1$ at time $t = \tau_{eff}$).

It is also possible to take into account the small background noise previously observed on Figure 4.10(a) and to obtain the real auto-correlation function of the quantum dot light source $g^{(2)}(t)$ deduced from the experimental one $g_{exp}^{(2)}(t)$. Let P_{QD} be the probability that a photon detected is originated from the quantum dot and $1 - P_{QD}$, the probability that it is originated from bad laser filtering or dark counts. The relation between $g_{exp}^{(2)}(t)$ and $g^{(2)}(t)$ can be calculated and gives:

$$g^{(2)}(t) = \frac{g_{exp}^{(2)}(t) - 2(1 - P_{QD}) + (1 - P_{QD})^2}{P_{QD}^2} \quad (4.7)$$

Therefore, by measuring the laser and quantum dot contributions in the total light intensity, one can measure P_{QD} and consequently, obtain a more accurate measurement of $g^{(2)}(t)$. In Fig. 4.10 (c-e) and in the subsequent ones, the corrected $g^{(2)}(t)$ is displayed, from which the occupation probability can be directly deduced through $\langle P_h \rangle = \frac{1}{g^{(2)}(0)}$.

Varying the pulsed laser intensity: Rabi oscillations.

As will be seen in the next section, the observed occupation probability $\langle P_h \rangle$ and the trapping time T_h strongly depend on the experimental conditions, among which the intensity of the resonant pulsed laser at energy ω_{X+} . The best way to characterize this intensity is to relate it to the population inversion that it allows to reach, characterized by Rabi oscillation measurements.

To describe the principle of Rabi oscillations of the trion population, the hole-trion system can be approximated to a two-level system (the spin state is indeed not relevant for this section). Under coherent excitation, this two-level system follows an oscillatory behavior back and forth from the ground state to the excited state. In the limit of very short pulses, the system would thus be coherently prepared, at the end of the pulse, in the superposition:

$$|\Psi\rangle = \cos(\Theta/2)|h\rangle + \sin(\Theta/2)|T_+\rangle \quad (4.8)$$

with $|h\rangle$, the ground singly charged hole state (disregarding its spin degree of freedom) and $|T_+\rangle$, the corresponding trion state. Θ is the pulse area proportional to the pulse intensity and to its temporal width. After the laser pulse, the excited component $|T_+\rangle$ decays by emitting a single photon: thus, the photon detection probability is directly proportional to the preparation probability of the excited state $|T_+\rangle$. With $\Theta = \pi$, the so called " π -pulse", the population inversion is maximum.

Experimentally, these Rabi oscillations are observed as a function of the pulse area¹ in Fig. 4.12, using a laser pulse width of 15ps. Oscillations up to 9π can be discriminated. As observed, the contrast of these oscillations is not perfect as the count rate of detected photons does not reach back 0 for even multiples of π . The imperfect laser polarization suppression explains partially such imperfect contrast, especially at high power. Yet the main cause of this imperfect contrast is due to the fact that pulses are not infinitely short compared to the excited state lifetime: various decoherence processes have time to occur during the pulse temporal width, preventing the quantum dot state to be prepared in a pure coherent superposition of $|h\rangle$ and $|T^+\rangle$ as in Eq. 4.8.

From this Rabi oscillation measurement, the laser intensity corresponding to complete population inversion (π -pulse) is identified as the first maximum intensity of single photon detections. The measured resonant power intensity is approximately 500pW at this π -pulse, which corresponds to nearly 2×10^6 photon detections per second. From this maximum value, we define the $\pi/2$ -pulse (respectively $\pi/3$ -pulse) as the power corresponding to half (resp. quarter) inversion of population.²

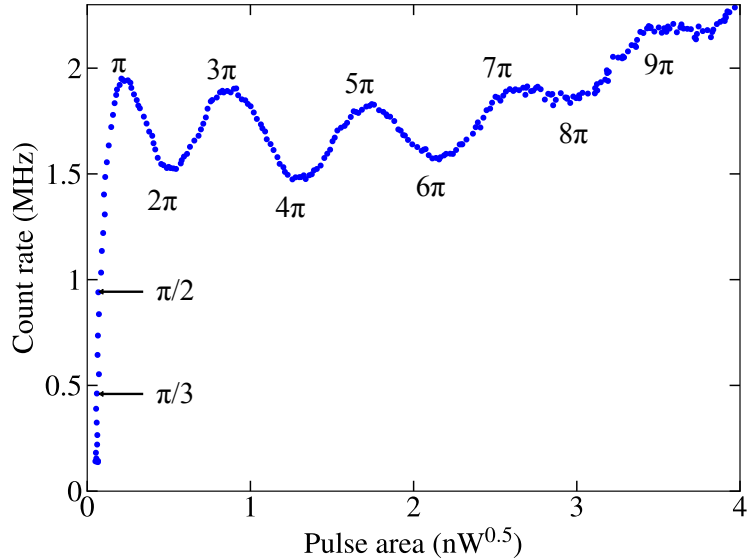


Figure 4.12: Evolution of the detected photons count-rate with the resonant laser pulse area for a pulse width of 15ps. Oscillations are observed and correspond to the Rabi oscillations of the quantum dot hole-trion states.

¹The population of the excited state depends on the amplitude of the electric field and thus of the square root of the electromagnetic field intensity. Therefore, the Rabi oscillations should be periodic over the pulse intensity.

²Indeed, with a $\Theta = \pi/2$ pulse (resp. $\Theta = \pi/3$ pulse), the excited state $|T^+\rangle$ is prepared with $\cos^2(\Theta/2) = \frac{1}{2}$ (resp. $\cos^2(\Theta/2) = \frac{1}{4}$) probability.

Laser power dependences of the hole confinement.

In this section, we study the dependence of the hole occupation probability $\langle P_h \rangle$ and trapping time T_h with the excitation conditions. On the one hand, the power P_{QR} of the quasi-resonant laser (at $\lambda_{QR} = 901\text{nm}$) is expected to influence the occupation probability $\langle P_h \rangle$, as the latter depends on the pumping rate γ (see Eq. 4.3), which increases with increasing values of P_{QR} . On the other hand, $\langle P_h \rangle$ can be degraded, when the pulse area of the resonant laser approaches π , as the trion state has a non-negligible probability to lead to an unwanted ground state with two holes, if the electron of the trion state tunnels out of the quantum dot. To characterize these effects, correlation measurements have been realized on QD1, for three different pulse areas of the resonant laser (π , $\pi/2$ and $\pi/3$ pulses), and with different quasi-resonant powers P_{QR} . Figure 4.13(a) shows the dependence of correlation measurements with the quasi-resonant power, with a resonant power fixed to π -pulse. Similarly, Figure 4.13(b) shows the dependence of correlation measurements with the resonant incoming power, with a quasi-resonant power fixed to $P_{QR} = 50\mu\text{W}$. These two curves show that the correlation timescales and the zero-delay value both depend on the incoming resonant and quasi-resonant laser intensities.

For all resonant and quasi-resonant incoming powers, the resulting correlations are fitted with an exponential decay. The hole occupation probability and trapping time are displayed in Figure 4.13(c) and (d). As expected, the hole occupation probability is increasing with the quasi-resonant power: it reaches $85 \pm 1\%$ for this specific quantum dot. The hole trapping time is higher than $20\mu\text{s}$ except at high power. This shows that the hole trapping time is always higher than the typical hole spin lifetime at zero magnetic field (which is generally around $1\mu\text{s}$). More specifically, with $300\mu\text{W}$ of non resonant power and at π -pulse, a hole is trapped $85 \pm 1\%$ of the time during on average $8\mu\text{s}$.

The dependence of the hole trapping time and occupation probability with the resonant power cannot be explained with the simple theoretical model with only zero and one hole state taken into account. A qualitative explanation can be given if considering the possibility of having a two-hole state (see Appendix A). In this case, every time a trion is generated, there is a non-zero probability that the electron tunnels out the quantum dot before the trion decays into the hole state. This leads to a two-hole state and therefore, the single-hole trapping time and occupation probability decrease with the resonant pulse power, as observed experimentally.

Similarly, the quasi-resonant power dependence of the hole trapping time cannot be explained by the simple two-state rate model, because in this case it should be constant and equal to T_H . With a model taking into account the two-hole state, the decreasing trapping time can be qualitatively explained by the trapping of a second hole due to the high quasi-resonant laser power. This should explain also why the hole occupation probability is saturating and not reaching unity with this optical trapping technique.

Figure 4.13(e) displays an evidence that the extracted timescales and probabilities are indeed characterizing the hole confinement. It shows the evolution of the polarized brightness as a function of the measured hole occupation probability. The polarized brightness B_p is the probability to detect a single photon after the first lens, in the polarization orthogonal to the polarization of the incoming resonant laser pulses, each time the source is triggered. It is measured by dividing the measured count rate CR , by the laser frequency f , the setup transmission T_{setup} (measured by independent component transmission), and the detector efficiencies η_{det} (measured by the single-photon detector company):

$$B_p = \frac{CR}{fT_{\text{setup}}\eta_{\text{det}}} \quad (4.9)$$

The measured brightness should be linearly proportional to the hole occupation probability. This is

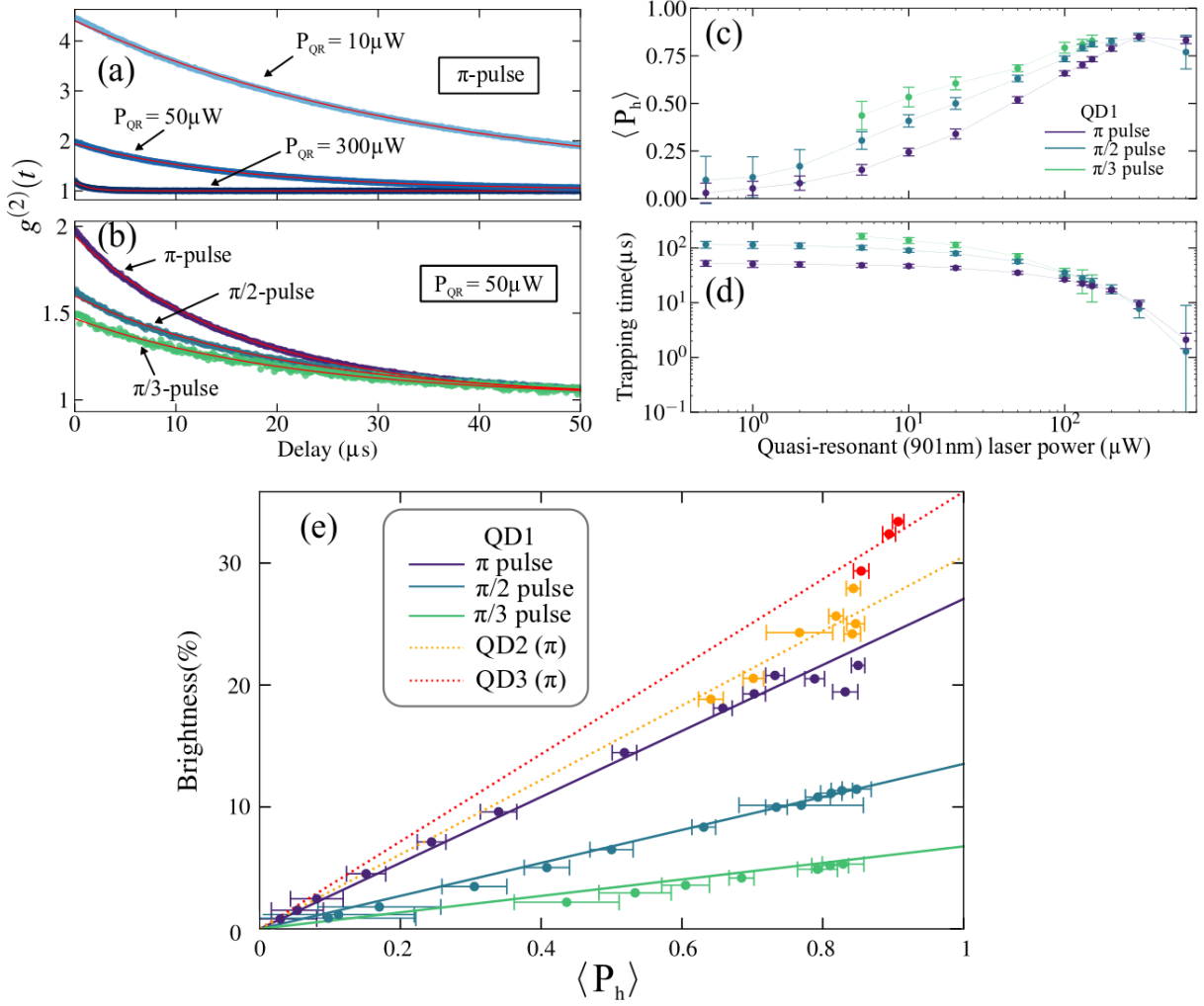


Figure 4.13: (a) Auto-correlation measurements for different incoming non resonant powers, with a fixed resonant power set to π -pulse (red curves are exponential decay fits). (b) Correlations for different incoming resonant pulse areas, at a fixed incoming quasi-resonant power set to $50\mu\text{W}$ (red curves are exponential decay fits). Extracted hole occupation probability $\langle P_h \rangle$ (c) and trapping time T_h (d) as a function of the non resonant incoming power, under three resonant pulse areas (π , $\pi/2$ and $\pi/3$ pulses). (e) Polarized brightness dependence on the hole occupation probability. Points are experimental data that are fitted with solid linear lines, showing the expected linear dependence of the single photon source brightness with the hole occupation probability. Correlation measurements have been carried out on QD1 (blue-green points and solid lines) and on QD2 (orange points and dashed line) and QD3 (red points and dashed line). The brightness measurement uncertainty is not represented on this panel but is typically of $\pm 5\%$.

indeed the case: with a single fit the data corresponding to π , $\pi/2$, $\pi/3$ pulses are fitted by 3 linear functions with relative slope $s_\pi = 26.2\%$, $s_{\pi/2} = s_\pi/2$ and $s_{\pi/3} = s_\pi/4$. For QD1, the maximum observed brightness is 21% and corresponds to 85% occupation probability.

These experiments have been repeated on two other samples, QD2 and QD3, in the polarization

tomography setup adapted in resonance fluorescence. On these two devices, a remarkably high polarized brightness have been measured: $28 \pm 5\%$ for QD2 and $33 \pm 5\%$ for QD3, equaling the state-of-the-art for quantum dot-micropillar based devices [167]. They both show similarly high hole occupation probability with $85 \pm 1\%$ for QD2 and with $91 \pm 1\%$ for QD3. These two devices are brighter than QD1, because they are measured in different cryostats: QD1 brightness was measured on a resonance fluorescence setup that has a long range objective microscope with a Numerical Aperture (NA) too small to fully collect every single photon in the first lens. On the contrary, QD2 and QD3 brightness were measured in the polarization tomography setup, that has a short range lens with sufficiently high NA , such that all the photons are collected.

Finally, we can compare below the measured brightness with the expected one. Let us start with the unpolarized brightness, which is the brightness without polarization selection: it is related to the hole occupation probability $\langle P_h \rangle$, to the photon emission into the mode β , and to the top mirror output coupling η_{top} , through $B = \langle P_h \rangle \beta \eta_{top}$ (see Sec. 1.5). On QD3, the hole occupation probability has been estimated to be $91 \pm 1\%$. By cavity reflectivity measurements, the top mirror output coupling is estimated to $\eta_{top} = 85 \pm 5\%$ thanks to a reflectivity measurement detailed in the next chapter (see Fig. 5.5). This remarkably high top mirror output coupling comes from the reduced number of pairs on the micro-pillar top DBR (14 layer pairs on the top DBR mirror compared to 28 layer pairs for the bottom mirror). The Purcell factor calculated from a lifetime measurement is $F_p = 2.5 \pm 0.4$ (assuming a photon spontaneous emission lifetime of 1ns), which leads to $\beta = 71 \pm 4\%$. The expected unpolarized brightness with independently measured parameters is therefore $B = 54 \pm 8\%$.

This value is smaller than twice the measured polarized brightness B_p , as $2B_p = 66 \pm 10\%$ for QD3, as we would have expected from the optical selection rules presented in Fig. 1.4: according to this figure, a trion state should decay into one hole state by emitting either an horizontally-polarized photon or a vertically-polarized photon, with same probability. Because only the cross-polarized resonance fluorescence is measured here, we should expect the polarized brightness to be twice less than the total brightness (without polarization selection). In fact, due to the cavity ellipticity, photons are more Purcell accelerated in the resonant cavity mode polarization than in the other, and due to this Purcell acceleration, photons are emitted more cross-polarized than co-polarized with the laser. The second hypothesis, is that the Purcell factor can be slightly underestimated if the photon spontaneous emission is in fact longer than 1ns for this quantum dot.

4.4 Device performances as a single photon source.

As discussed in Chap. 1, QD-based cavity-QED devices can operate as efficient single-photon sources, that ideally emit one and only one photon each time the source is triggered. In addition, all the emitted photons should be identical. As detailed in Sec. 1.5, single-photon sources are characterized by three crucial features that are their single-photon purity, their photon indistinguishability and their brightness. The latter has already been discussed in the previous section and the other two are evaluated in the following.

To perform as single-photon sources, each photon pulse should contain no more than 1 photon. Regarding the single-photon purity, it is evaluated by the zero-delay intensity correlations $g^{(2)}(0)$ thanks to a HBT setup (see Fig. 3.4 or sketched as Fig. 4.14(a)). Such experiment is therefore very similar to the one presented in the previous section, however, we are only interested in the zero-delay pulse, which contains information about the single-photon purity of the light source: if each pulse contains only one photon, it can only be detected by one of the two detectors presented in Fig. 4.14(a)

and thus, coincidence detections at zero delay should not be observed.

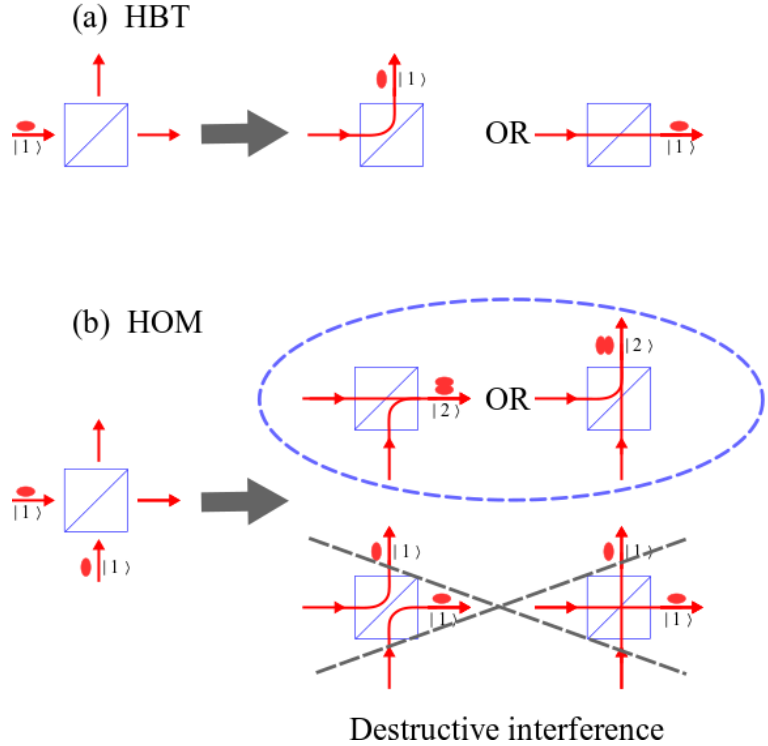


Figure 4.14: (a) Principle of a HBT experiment: one single photon is either transmitted or reflected by a 50:50 beam splitter. (b) Principle of a HOM experiment: two single photons are arriving at the same time on a 50:50 beam splitter. For indistinguishable photons, their is destructive interference that does not allow the two photons to leave the beam splitter in different output. Consequently, the two photons are leaving together the beam splitter.

Regarding the single-photon source indistinguishability, a standard way to evaluate it is by performing coalescence measurements using a Hong-Ou-Mandel setup [213], sketched in Figure 4.14(b). Such experiment is similar to an HBT experiment: it is made of a beam splitter and two single-photon detectors, but now, two single photons arrive at the same time in the two beam splitter inputs. The two photons are emitted by the quantum dot, one immediately after the other (and thus separated by the repetition period of the laser $T_R = 12.3\text{ns}$). If they are perfectly indistinguishable, it can be shown that, due to their bosonic nature, the two photons are leaving the beam splitter by the same output. Zero-delay coincidences detections on the two detectors are therefore forbidden [213].

To characterize our charged QD-cavity devices as single-photon sources, both HBT and HOM experiments have been realized on the three quantum dots, whose results are displayed in Figure 4.15. The best results are obtained for QD1, where a Fabry-Perot etalon is inserted in the collection setup to further suppress the spectrally-wide excitation laser and possible phonon side band emission. The results obtained show a good single-photon purity characterized by a small value for the $g^{(2)}(0) = 1.6 \pm 0.4\%$ (see Fig. 4.15(a)). The photon indistinguishability is also high, with an indistinguishability estimated at $V_{corr} = 99.8 \pm 0.2\%$ (corrected from the single photon purity through $V_{corr} = V_{exp} + 2g^{(2)}(0)$), similar to the state-of-the-art [167]. For the two other devices QD2 (Fig. 4.15 (c) and (d)) and QD3 (Fig. 4.15 (e) and (f)), placed in the polarization tomography setup

and without spectral filtering, $g^{(2)}(0)$ values are still reasonably small with typically 10% and high indistinguishability values. This setup is indeed not optimized for the realization of resonance fluorescence experiment as it has a bad laser rejection, thus explaining the bad $g^{(2)}(0)$ and the bad raw indistinguishabilities of Fig. 4.15 (d) and (f), but the corrected indistinguishabilities still remain high above $V_{corr} > 90\%$.

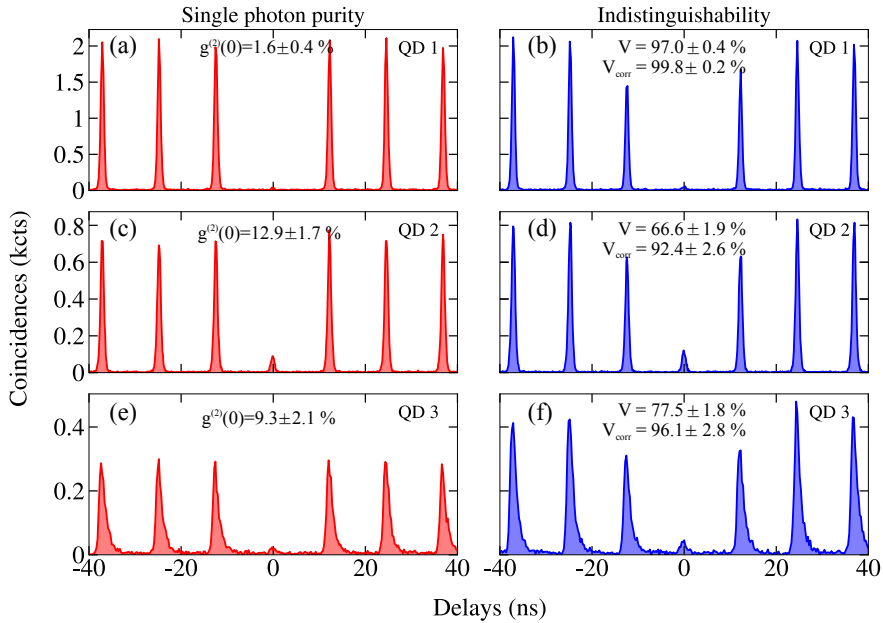


Figure 4.15: Quantum performances of the spin-photon interfaces. Single photon purity and photon indistinguishability are estimated by HBT and HOM experiments for devices QD1 (HBT(a) and HOM(b)), QD2 (c, d) and QD3 (e, f). For QD1, a Fabry-Pérot etalon was placed to better suppress the laser.

4.4.1 Quantum dot spectral fluctuations.

The indistinguishability shows that the quantum properties of the spin-photon interface are expected to be high. However, the experiment is carried out by observing the coalescence of two photons that were emitted by two successive pulses separated by $T_R = 12.3\text{ns}$. Therefore, the experiment constitutes a short-timescale measurement of the quantum properties. One should also consider, how is behaving the spin-photon interface at longer timescales. A solution is to perform coalescence between single photons whose emission is temporally-separated by a delay much longer than the incoherent processes relevant timescales [214]. This would show how the photon indistinguishability is evolving over longer timescale. Another solution, carried out in the next chapter, is to compare the spectral linewidth of the trion transition, $1/T_2$, that can be extracted from polarization-resolved reflectivity measurements (such as the one carried out in Chap. 3) and compare it to its Fourier-limited linewidth, $1/(2T_1)$, extracted from a lifetime measurement. Other techniques using noise spectroscopy [199] or long delay correlations measurements with spectrally narrower laser would

also provide information about the noise mechanism timescales.

4.5 Conclusion.

In this chapter, we have presented a technique to create spin-photon interfaces with a deterministic procedure. We have engineered a tunnel barrier that facilitates the hole confinement. We have deterministically identified the trion transition, thanks to its photoluminescence under high transverse magnetic field, and coupled it to the cavity mode of a micropillar, using the *in-situ* lithography technique. Then we have used a quasi-resonant laser to optically confine a single hole into the quantum dot with occupation probability up to $91 \pm 1\%$. Finally, we have studied the performances of the spin-photon interfaces, operating as single-photon sources, demonstrating a high polarized brightness together with a high single-photon purity and a high photon indistinguishability.

We therefore have shown that these spin-photon interfaces are efficient when operated as single-photon sources. In addition their characteristics, namely the high top mirror output coupling and its indistinguishability that can be related to a high cooperativity (if there are no spectral fluctuations), also make them promising candidates for efficient receivers of photons. In the next chapter, we explore the performances of such a spin-photon interface, operating as a receiver of photons. More specifically, we study the cavity-enhanced Kerr rotation induced by the single hole spin and demonstrate the macroscopic measurement back action induced on this spin by a single detected photon.

Chapter 5

Measurement back-action induced by a single detected photon.

5.1 Introduction: from spin noise spectroscopy to single photon back-action.

For quantum communication applications, a crucial goal is to increase the interaction between a single photon and a stationary qubit such as the spin of a singly-charged quantum dot. For example, as discussed in Chap. 1, the optical measurement of a spin is based on spin-dependent Faraday rotation which is an intrinsically small effect [15, 22]. By coupling a singly-charged quantum dot to a microcavity, the polarization rotation is enhanced by several orders of magnitude [27, 124, 192, 179, 215] and can be used to deterministically entangle a single spin with a photon emitted from another source, which can in turn be used for deterministic spin-spin or photon-photon entanglement [123, 124, 126]. The cavity-enhancement of the spin-photon interaction can also be used to quickly initialize a spin thanks to Purcell enhancement [216] or to implement quantum logic gates between a spin and a photon, as already demonstrated with photonic crystals [178].

In parallel, an experimental tool called spin noise spectroscopy [93] has emerged in the study of spin dynamics. As discussed in Sec. 1.2.4, this technique was first applied to ensembles of spins [91, 217] but, thanks to cavity enhancement which increases the sensitivity of this technique, it has also been extended to a single spin [92]. In this respect, the classical theory of spin noise spectroscopy [31] requires to be extended to the quantum regime [218] to account for the strong correlations between the single spin and the photons. Indeed, in this quantum regime, the spin macroscopically rotates the photon polarization but reciprocally, the measurement of the polarization of a single photon also drastically modifies the spin state. Such phenomenon is called the quantum measurement back-action [219, 220] of a single spin with a single detected photon.

The demonstration of such macroscopic measurement back action onto a single spin is the objective of this chapter. It is based on the polarization rotation induced by a single quantum dot, as was demonstrated in Chap. 3 (with a neutral quantum dot). However, in the present case, we use a singly-charged quantum dot deterministically coupled to a pillar microcavity, allowing a spin-dependent polarization rotation [27].

In this chapter, we first demonstrate the single-photon measurement back action onto a single spin thanks to photon correlation measurements. The experimental data are analyzed and explained with a first, simple theoretical model. This model encapsulates the main concepts of back-action but

fails to fully explain the physics of the system. We therefore present a more complete theoretical model based on the master equation, and we use it to theoretically simulate and fit the experimental results. We then show that we can use the photon correlations to study the spin dynamics and explore the behavior of a single spin under an external (longitudinal) magnetic field.

5.2 Single-photon measurement back-action on the hole spin.

In this section, the macroscopic single-photon measurement back-action on a single quantum dot spin is evidenced. The experiment is carried out by measuring the cross-correlations of the reflected light in two orthogonal polarizations. First, we show the link between these cross-correlations and the measurement back-action, using a simple theoretical model. Then, we present the experimental results and demonstrate the macroscopic single-photon measurement back-action that projects the spin in a given state with an estimated 72% probability. Finally, we discuss the limitations of the simple model introduced for this estimation.

5.2.1 Principle of photon measurement back-action on a single spin.

In the presence of a spin-dependent polarization rotation, the polarization of a photon that has interacted with a spin carries out information on the spin state. Consequently, measuring the polarization of such a photon gives access to this information on the spin state, and potentially allows to fully measure it. The measurement of a quantum system induces a strong modification of the system, through a partial or complete projection of the system density matrix. Thus, the measurement of a single photon polarization can induce such a back-action on the spin qubit. This phenomenon is detailed in the following in the context of our spin-photon interface.

As illustrated in Fig. 5.1(a), the spin-photon interface is excited with horizontally-polarized light, which corresponds to a micropillar cavity axis: consequently, the cavity does not induce any polarization rotation (as was discussed in Chap. 2). The quantum dot hole can be in two spin states $|\uparrow_z\rangle$ or $|\downarrow_z\rangle$ with a spin relaxation time T_s that takes into account incoherent spin flips between these two states. Because no transverse magnetic field is applied, $|\uparrow_z\rangle$ and $|\downarrow_z\rangle$ are the eigenstates and there is no coherent evolution between these two states. When the hole is in state $|\uparrow_z\rangle$ (respectively, $|\downarrow_z\rangle$), the incident horizontally-polarized light is reflected with rotated polarization $|\Psi_{\uparrow}\rangle$ (resp. $|\Psi_{\downarrow}\rangle$).

If the spin-dependent polarizations are orthogonal as represented in Fig. 5.1(b), the information of the spin state is completely mapped onto the polarization state. In the example of Fig. 5.1(b), when the spin is in state $|\uparrow_z\rangle$ (resp. $|\downarrow_z\rangle$), the reflected polarization is $|\Psi_{\uparrow}\rangle = |A\rangle$ (resp. $|\Psi_{\downarrow}\rangle = |D\rangle$) and therefore, the detection of a photon with anti-diagonal (resp. diagonal) polarization $|A\rangle$ (resp. $|D\rangle$) implies that the spin is in state $|\uparrow_z\rangle$ (resp. $|\downarrow_z\rangle$). Therefore, as shown in Fig. 5.1 (d) and (e), by simply measuring a photon polarization, it is possible to measure the quantum dot spin state: the photon detection induces a complete projection of the hole spin state.

Now, if the two spin-dependent polarization states $|\Psi_{\uparrow}\rangle$ and $|\Psi_{\downarrow}\rangle$ are not orthogonal, as illustrated in Fig. 5.1 (c), the spin state is not perfectly mapped onto the polarization state and therefore, the spin is only partially projected onto one of its eigenstates. This will be quantitatively discussed later on.

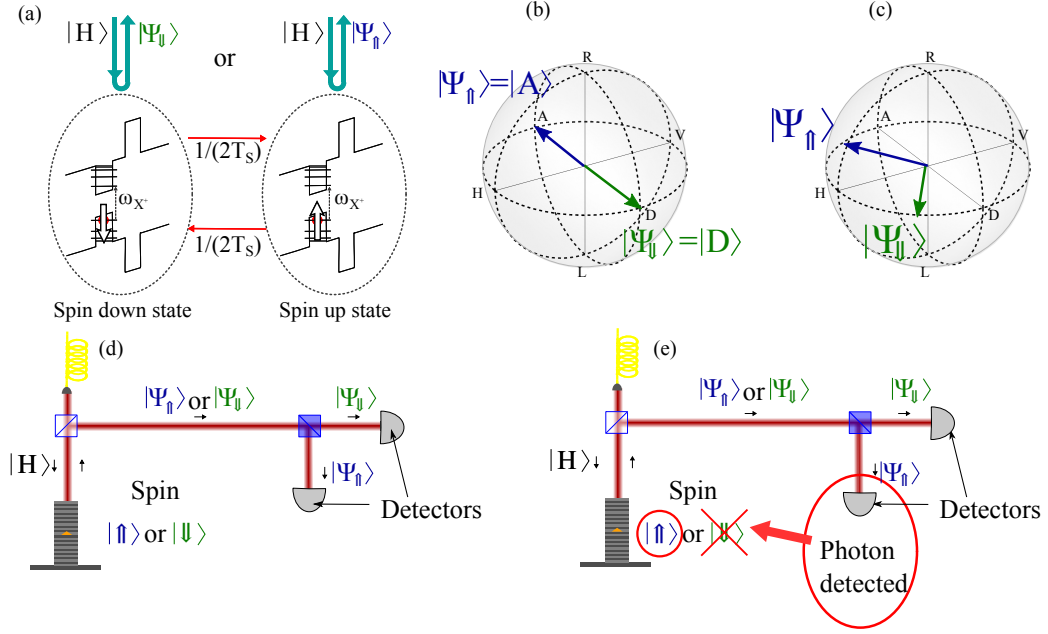


Figure 5.1: (a) The quantum dot is assumed to be either in the spin $|\uparrow_z\rangle$ or in the $|\downarrow_z\rangle$ state, with uncontrolled spin flips occurring at a rate $1/(2T_S)$. Depending on the spin state, the incident light is reflected with either $|\Psi_{\uparrow}\rangle$ or $|\Psi_{\downarrow}\rangle$ spin-dependent polarization. (b,c) Poincaré sphere representation of the ideal (b) (respectively general (c)) case where the reflected polarization states $|\Psi_{\uparrow}\rangle$ and $|\Psi_{\downarrow}\rangle$ are orthogonal (resp. not orthogonal). (d,e) Sketch of an ideal measurement back action: (d) before the measurement, the quantum dot spin is in a statistical mixture of $|\uparrow_z\rangle$ and $|\downarrow_z\rangle$ states. The horizontally-polarized incoming laser is reflected with polarization $|\Psi_{\uparrow}\rangle$ or $|\Psi_{\downarrow}\rangle$ depending on the spin state. (e) If the reflected photon is measured in polarization $|\Psi_{\uparrow}\rangle$ (respectively $|\Psi_{\downarrow}\rangle$), the spin is projected in the $|\uparrow_z\rangle$ (resp. $|\downarrow_z\rangle$) state.

5.2.2 Theory: from measurement back action to photon cross-correlations.

In order to demonstrate the single-photon back-action on a single spin state, we develop a theoretical model to explore the dynamics of the system presented in Fig. 5.1(a). The objective is to link this dynamics to correlations between photon detection events.

Spin evolution. In the model presented in Fig. 5.1 (a), the quantum dot is assumed to have a resident hole permanently trapped which has a spin that can be in either $|\uparrow_z\rangle$ with probability $P_{\uparrow}(t)$ or in $|\downarrow_z\rangle$ with probability $P_{\downarrow}(t)$, at a given time t . The spin has a relaxation time T_S and therefore the rate equations are:

$$\begin{aligned} \frac{dP_{\uparrow}}{dt}(t) &= \frac{1}{2T_S}P_{\downarrow}(t) - \frac{1}{2T_S}P_{\uparrow}(t) \\ \frac{dP_{\downarrow}}{dt}(t) &= -\frac{1}{2T_S}P_{\downarrow}(t) + \frac{1}{2T_S}P_{\uparrow}(t) \end{aligned} \quad (5.1)$$

Using $P_{\downarrow} + P_{\uparrow} = 1$:

$$\begin{aligned}\frac{dP_{\uparrow\uparrow}}{dt}(t) &= \frac{1}{2T_S} - \frac{1}{T_S}P_{\uparrow\uparrow}(t) \\ \frac{dP_{\downarrow\downarrow}}{dt}(t) &= \frac{1}{2T_S} - \frac{1}{T_S}P_{\downarrow\downarrow}(t)\end{aligned}\tag{5.2}$$

The general solution of this system, is then:

$$\begin{aligned}P_{\uparrow\uparrow}(t) &= \frac{1}{2} + \left(P_{\uparrow\uparrow}(0) - \frac{1}{2}\right)e^{-\frac{t}{T_S}} \\ P_{\downarrow\downarrow}(t) &= \frac{1}{2} + \left(P_{\downarrow\downarrow}(0) - \frac{1}{2}\right)e^{-\frac{t}{T_S}}\end{aligned}\tag{5.3}$$

These equations already show that at long delays ($t \gg T_S$), the information of the hole spin state is lost and each state has equal half probability: $P_{\uparrow\uparrow}(\infty) = P_{\downarrow\downarrow}(\infty) = \frac{1}{2}$. When the hole spin state is initialized with $P_{\uparrow\uparrow}(0) \neq P_{\downarrow\downarrow}(0) \neq 1/2$, the spin state is lost after a typical time corresponding to half the spin relaxation time, T_S .

First, let us consider what is the initial state when a photon is detected along the anti-diagonal polarization. In the case of an ideal mapping such as represented in Fig. 5.1(b), the detection of an anti-diagonally polarized photon implies that the spin is in its state $|\uparrow\downarrow_z\rangle$ with 100% probability. The initial conditions are therefore $P_{\uparrow\uparrow}(0) = 1$ and $P_{\downarrow\downarrow}(0) = 0$. The simulation of the spin evolution in time is plotted in Fig. 5.2(a) for a spin relaxation time of $T_S = 2.5\mu s$. It shows that the spin stays in the $|\uparrow\downarrow_z\rangle$ state during approximately T_S . Afterwards, the information on the spin state is lost: the spin is in a statistical mixture of $|\uparrow\downarrow_z\rangle$ and $|\downarrow\uparrow_z\rangle$.

In the more general case of spin-dependent polarizations that are not orthogonally-polarized, the detection of a photon does not project perfectly the spin state in $|\uparrow\downarrow_z\rangle$ ($P_{\uparrow\uparrow}(0) \neq 1$). The result for $P_{\uparrow\uparrow}(0) = 0.75$ and $T_S = 2.5\mu s$ is displayed in Fig. 5.2(b). It is similar to the previous case except that the contrast between $P_{\uparrow\uparrow}$ and $P_{\downarrow\downarrow}$ at times close to zero is decreased.

Cross-correlations. In order to show the measurement back-action on the spin, we calculate the intensity cross-correlations of the reflected light measured in two orthogonal polarization bases. Let us consider a diagonal/anti-diagonal measurement basis. The intensity cross-correlations between these two polarizations is given by:

$$g_{DA}^{(2)}(t) = \frac{\langle \hat{a}_D^\dagger(t)\hat{a}_A^\dagger(0)\hat{a}_A(0)\hat{a}_D(t) \rangle}{\langle \hat{a}_D^\dagger(t)\hat{a}_D(t) \rangle \langle \hat{a}_A^\dagger(0)\hat{a}_A(0) \rangle}\tag{5.4}$$

with \hat{a}_D^\dagger , \hat{a}_D and \hat{a}_A^\dagger , \hat{a}_A , the creation and annihilation operators for diagonal and anti-diagonal polarizations. It can be rewritten, in terms of probabilities, as:

$$g_{DA}^{(2)}(t) = \frac{P_{D,t|A,0}}{P_A}\tag{5.5}$$

with $P_{D,t|A,0}$ the conditional probability to detect a diagonally-polarized photon at time t , given that an anti-diagonally polarized photon was detected at time $t = 0$ and P_A the probability to detect an anti-diagonal photon without any prior condition.

Let us first consider the zero-delay cross-correlations $g_{DA}^{(2)}(0)$. In that case, it is given by the conditional probability $P_{D|A} = P_{D,0|A,0}$ (we use the shorter notation $P_{i|j}$ for the conditional probability

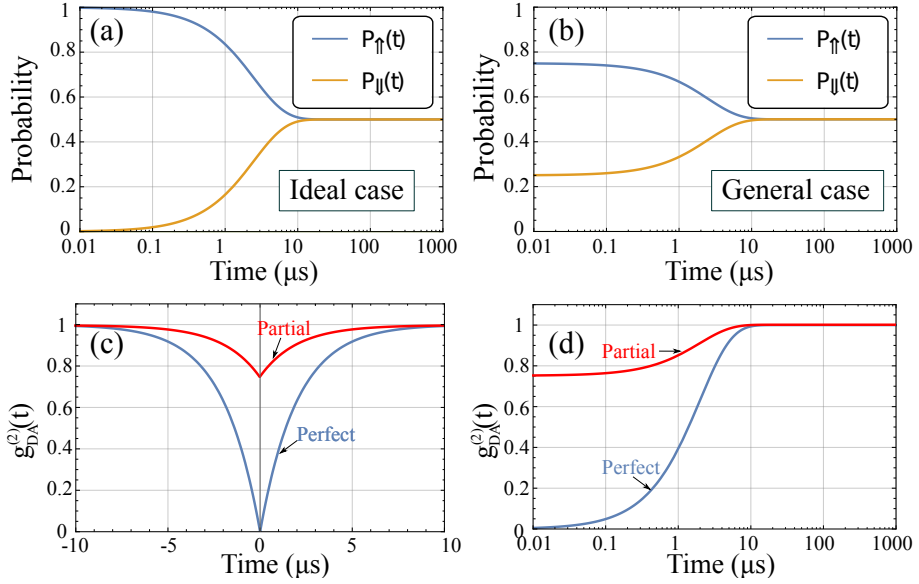


Figure 5.2: Spin state probabilities P_{\uparrow} and P_{\downarrow} evolution in time starting from perfect (a) and partial (b) initialization in spin state $|\uparrow_z\rangle$. (c) Predicted results of cross-correlations measurement in the "D/A" basis, for perfect (blue curve) and partial (red curve) spin-photon mapping. (d) Positive time ($t > 0$) part of (c) plotted in log scale.

of i given j at the same time), normalized by $P_A = 1/2$. Let us examine the link between these zero-delay cross-correlations and the single photon measurement back-action. $P_{D|A}$ can be expanded over the spin states:

$$P_{D|A} = P_{D|\uparrow} P_{\uparrow|A} + P_{D|\downarrow} P_{\downarrow|A} \quad (5.6)$$

where $P_{D|\uparrow}$ and $P_{D|\downarrow}$ are the probabilities to detect a diagonally-polarized photon given that the spin is \uparrow or \downarrow respectively. Similarly, $P_{\uparrow|A}$ and $P_{\downarrow|A}$ are the probabilities that the detection of an anti-diagonally polarized photon projects the spin in state \uparrow or \downarrow respectively. With a given photon polarization $|\Psi\rangle$, the probability to detect this photon in the diagonal polarization is: $P_{D|\Psi} = |\langle\Psi|D\rangle|^2$. The probability to detect it in the anti-diagonal polarization is: $P_{A|\Psi} = |\langle\Psi|A\rangle|^2 = 1 - P_{D|\Psi}$. These probabilities can be rewritten with the Stokes parameter $s_{DA}(|\Psi\rangle)$ for this polarization:

$$\begin{aligned} P_{D|\Psi} &= \frac{1 + s_{DA}(|\Psi\rangle)}{2} \\ P_{A|\Psi} &= \frac{1 - s_{DA}(|\Psi\rangle)}{2} \end{aligned} \quad (5.7)$$

In the ideal case $|\Psi_{\downarrow}\rangle = |D\rangle$, the Stokes parameter $s_{DA}(|\Psi_{\downarrow}\rangle)$ is one ($s_{DA}(|\Psi_{\downarrow}\rangle) = 1$) and we indeed have a unity probability to detect a photon with a diagonal polarization. In the assumption that the spin-dependent reflected polarizations are symmetric about the "H/V" axis (which holds under zero magnetic field, as detailed later in Sec. 5.3.2), we have $s_{DA}(|\Psi_{\uparrow}\rangle) = -s_{DA}(|\Psi_{\downarrow}\rangle)$. It is therefore easy to deduce the probability to detect a photon in the diagonal and anti-diagonal polarization given

the spin state:

$$\begin{aligned} P_{D|\uparrow\uparrow} &= P_{D|\Psi_{\uparrow\uparrow}} = \frac{1 + s_{DA}(|\Psi_{\uparrow\uparrow}\rangle)}{2} \\ P_{D|\downarrow\downarrow} &= P_{D|\Psi_{\downarrow\downarrow}} = \frac{1 + s_{DA}(|\Psi_{\downarrow\downarrow}\rangle)}{2} = \frac{1 - s_{DA}(|\Psi_{\uparrow\uparrow}\rangle)}{2} \\ P_{A|\uparrow\uparrow} &= P_{A|\Psi_{\uparrow\uparrow}} = \frac{1 - s_{DA}(|\Psi_{\uparrow\uparrow}\rangle)}{2} \\ P_{A|\downarrow\downarrow} &= P_{A|\Psi_{\downarrow\downarrow}} = \frac{1 - s_{DA}(|\Psi_{\downarrow\downarrow}\rangle)}{2} = \frac{1 + s_{DA}(|\Psi_{\uparrow\uparrow}\rangle)}{2} \end{aligned} \quad (5.8)$$

This shows that the relevant parameters to measure the initialization are the Stokes parameters $s_{DA}(|\Psi_{\uparrow\uparrow}\rangle)$ and $s_{DA}(|\Psi_{\downarrow\downarrow}\rangle)$.

The measurement back-action is simulated by the conditional probabilities to find the spin in a given state after a photon detection, i. e. probabilities such as $P_{\uparrow\uparrow|A}$. These conditional probabilities quantify the measurement back-action induced by a single photon detection on the hole spin. These measurement back-action probabilities can be linked to the previous ones described in Eq. 5.8 using Bayesian inference for correlated events X and Y:

$$P_{X|Y} = \frac{P_{Y|X}P_X}{P_Y} \quad (5.9)$$

We find:

$$\begin{aligned} P_{\uparrow\uparrow|A} &= \frac{P_{A|\uparrow\uparrow}P_{\uparrow\uparrow}}{P_A} = \frac{1 - s_{DA}(|\Psi_{\uparrow\uparrow}\rangle)}{2} \\ P_{\downarrow\downarrow|A} &= \frac{P_{A|\downarrow\downarrow}P_{\downarrow\downarrow}}{P_A} = \frac{1 - s_{DA}(|\Psi_{\downarrow\downarrow}\rangle)}{2} = \frac{1 + s_{DA}(|\Psi_{\uparrow\uparrow}\rangle)}{2} \end{aligned} \quad (5.10)$$

where we have used the fact that the uncorrelated probabilities are $P_A = P_D = P_{\uparrow\uparrow} = P_{\downarrow\downarrow} = 1/2$. Consequently, the zero-delayed cross-correlations $g_{DA}^{(2)}(0)$ can be expressed as:

$$g_{DA}^{(2)}(0) = \frac{P_{D|A}}{P_A} = \frac{P_{D|\uparrow\uparrow}P_{\uparrow\uparrow|A} + P_{D|\downarrow\downarrow}P_{\downarrow\downarrow|A}}{P_A} = (1 + s_{DA}(|\Psi_{\uparrow\uparrow}\rangle))(1 - s_{DA}(|\Psi_{\uparrow\uparrow}\rangle)) \quad (5.11)$$

Using Eq. 5.3 to calculate $P_{\uparrow\uparrow,t|A,0}$ and $P_{\downarrow\downarrow,t|A,0}$, it is also possible to show that the time dependence of the cross-correlations is given by:

$$g_{DA}^{(2)}(t) = 1 + (g_{DA}^{(2)}(0) - 1)e^{-\frac{t}{T_S}} \quad (5.12)$$

We thus retrieve $g_{DA}^{(2)}(t \gg T_S) = 1$, indicating that $P_{\uparrow\uparrow,t|A,0} = \frac{1}{2}$: the information acquired about the spin state at $t = 0$ has been erased by the random spin-flips. Fig. 5.2 (c) shows the cross-correlations $g_{DA}^{(2)}(t)$ for ideal and partial spin-photon mapping. For perfect spin-photon mapping, the detection of an anti-diagonal photon fully projects the spin in the $|\uparrow\downarrow_z\rangle$ state, because $s_{DA}(|\Psi_{\downarrow\downarrow}\rangle) = 1$ and $s_{DA}(|\Psi_{\uparrow\uparrow}\rangle) = -1$, thus, $P_{\uparrow\uparrow|A} = 1$ and $P_{\downarrow\downarrow|A} = 0$, so $g_{DA}^{(2)} = 0$. Immediately after the spin projection, it is not possible to detect photons in the diagonal polarization. Therefore, for a strong measurement back-action, the conditional probability $P_{D,t|A,0}$ and thus the cross-correlations $g_{DA}^{(2)}(t)$ approach zero when $t \ll T_S$, which explains the anti-correlations observed in Fig. 5.2 (c). When the measurement back-action is not perfect, the cross-correlations $g_{DA}^{(2)}(t)$ approach a non-zero value with $g_{DA}^{(2)}(0)$ given by Eq. 5.11. The same information can alternatively be displayed in a semi-logarithmic scale for

$t > 0$, as illustrated in Fig. 5.2(d): such representation is convenient in particular to represent data over different timescales.

Correlations measurement to measure the spin initialization. For a photon detection in the anti-diagonal polarization, the spin initialization is given by the Stokes parameter $s_{DA}(|\Psi_{\uparrow}\rangle)$ (Eq. 5.10) which is linked to the zero delay cross-correlations $g_{DA}^{(2)}(0)$ by Eq. 5.11. Assuming that $P_{\uparrow|A} > P_{\downarrow|A}$, the initial probabilities are plotted as a function of the zero-delay cross-correlations $g_{DA}^{(2)}(0)$ in Fig. 5.3. The measurement back-action initializes the spin in state $|\uparrow_z\rangle$ with a probability:

$$P_{\uparrow|A} = \frac{1 + \sqrt{1 - g_{DA}^{(2)}(0)}}{2} \quad (5.13)$$

Consequently, there is a direct link between the measurement back-action effect and the anti-correlations measurement. The strength of the back-action can be deduced from a cross-correlation measurement, with a perfect back-action ($P_{\uparrow|A} = 1$ and $P_{\downarrow|A} = 0$) signaled by $g_{DA}^{(2)} = 0$.

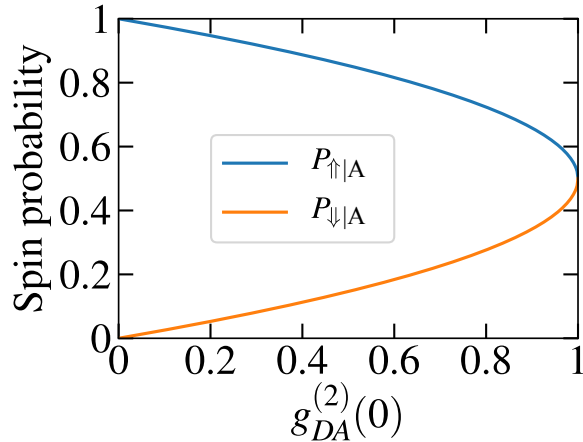


Figure 5.3: Spin projection induced by the detection of a single photon with anti-diagonal polarization, as a function of the measured zero-delay cross-correlation in the measurement "D/A" basis.

5.2.3 Classical vs quantum measurement back-action.

In all the previous discussion, we have focused on an initially unpolarized spin described by the density matrix $\rho_S = 0.5 |\uparrow_z\rangle\langle\uparrow_z| + 0.5 |\downarrow_z\rangle\langle\downarrow_z|$. We also used the word "back-action" to describe the evolution from the initial density matrix ρ_S to a new density matrix $\rho'_S \neq \rho_S$ after a photon detection. However, in the absence of coherence (purely diagonal density matrix), all the changes experienced by the density matrix can just be interpreted using classical probabilities (i. e. changes related to the information we have of the system, and not changes of the system itself). Is it actually a back action?

To illustrate this discussion we remind that, in the previous chapter, photon-photon correlation measurements were interpreted in a classical way. At any given time, the hole is either present or absent in the quantum dot, and the detection of a photon only indicates that the hole was actually present at the time the photon was emitted. In such classical configuration, we cannot say that the

photon detection modifies the system but only our knowledge of the system, and the word "back-action" clearly should not be used.

However, the situation is different with a spin qubit. Contrary to a classical system, a spin can be in more than two states: it can be in any quantum superposition of the two spin states $|\uparrow_z\rangle$ and $|\downarrow_z\rangle$, and thus point in any direction. Besides, a spin precesses about the local magnetic field, which is itself evolving in a way that depends on the spin state. In contrast to the presence or absence of a hole, we cannot state that the spin is either in state $|\uparrow_z\rangle$ or $|\downarrow_z\rangle$ at a given time.

Thus, assuming that the spin is a qubit (which we actually do not prove in this chapter), an alternative interpretation can be given to these anti-correlations $g_{DA}^{(2)}(0)$. The fact that the initial spin density matrix is depolarized ($\rho_S = 0.5 |\uparrow_z\rangle\langle\uparrow_z| + 0.5 |\downarrow_z\rangle\langle\downarrow_z|$) can be interpreted as a signature that the spin is maximally entangled with its environment. At any given time, it is possible to define complex environment states $|\text{Env}_{\uparrow}\rangle$ and $|\text{Env}_{\downarrow}\rangle$, expressed in a very large Hilbert space taking into account all the environment degrees of freedom, so that the total system (spin + environment) is in a pure quantum state of the form [87, 219]:

$$|\Psi_{S+E}\rangle = \frac{1}{\sqrt{2}} (|\uparrow_z\rangle \otimes |\text{Env}_{\uparrow}\rangle + |\downarrow_z\rangle \otimes |\text{Env}_{\downarrow}\rangle) \quad (5.14)$$

By tracing over the environment degrees of freedom, this indeed gives:

$$\rho_S = \text{Tr}_E(\rho_{S+E}) = \frac{1}{2} |\uparrow_z\rangle\langle\uparrow_z| + \frac{1}{2} |\downarrow_z\rangle\langle\downarrow_z| \quad (5.15)$$

Now, after a single photon has been reflected by the system, the total system (spin + environment + photon) is in the following state:

$$|\Psi_{S+E+P}\rangle = \frac{1}{\sqrt{2}} (|\uparrow_z\rangle \otimes |\text{Env}_{\uparrow}\rangle \otimes |\Psi_{\uparrow}\rangle + |\downarrow_z\rangle \otimes |\text{Env}_{\downarrow}\rangle \otimes |\Psi_{\downarrow}\rangle) \quad (5.16)$$

The spin is not only entangled with the environment but also with the photon. Then, if the photon is detected in the anti-diagonal polarization $|A\rangle$, the spin becomes less entangled with the environment as the new spin + environment state is of the form:

$$|\Psi'_{S+E}\rangle = \alpha |\uparrow_z\rangle \otimes |\text{Env}_{\uparrow}\rangle + \beta |\downarrow_z\rangle \otimes |\text{Env}_{\downarrow}\rangle \quad (5.17)$$

with:

$$\begin{aligned} \alpha &= \frac{\langle A | \Psi_{\uparrow} \rangle}{\sqrt{|\langle A | \Psi_{\uparrow} \rangle|^2 + |\langle A | \Psi_{\downarrow} \rangle|^2}} \neq \frac{1}{\sqrt{2}} \\ \beta &= \frac{\langle A | \Psi_{\downarrow} \rangle}{\sqrt{|\langle A | \Psi_{\uparrow} \rangle|^2 + |\langle A | \Psi_{\downarrow} \rangle|^2}} \neq \frac{1}{\sqrt{2}} \end{aligned} \quad (5.18)$$

After tracing out over the environment degrees of freedom, the new spin density matrix is simply given by:

$$\rho'_S = \text{Tr}_E(\rho'_{S+E}) = |\alpha|^2 |\uparrow_z\rangle\langle\uparrow_z| + |\beta|^2 |\downarrow_z\rangle\langle\downarrow_z| \quad (5.19)$$

With this interpretation, because $|\alpha|^2 \neq |\beta|^2 \neq 0.5$, the detection of the photon has an actual effect ("back-action") on the system as it partially disentangles it from the environment. This back-action is based on the same physical processes that are described as quantum back-action in standard

quantum mechanics textbooks [152], where pure quantum states such as $|\Psi_S\rangle = \frac{1}{\sqrt{2}}(|\uparrow_z\rangle + |\downarrow_z\rangle)$ are used. Starting from such an initial spin state, indeed, the interaction with an incoming reflected photon leads to a spin-photon entangled state of the form ($|\Psi_{S+P}\rangle = \frac{1}{\sqrt{2}}(|\uparrow_z\rangle \otimes |\Psi_{\uparrow}\rangle + |\downarrow_z\rangle \otimes |\Psi_{\downarrow}\rangle)$) [221]). Then, if the reflected photon is detected with antidiagonal polarization ($|A\rangle$), the new spin state becomes:

$$|\Psi'_S\rangle = \alpha |\uparrow_z\rangle + \beta |\downarrow_z\rangle \quad (5.20)$$

with the same values of α and β as in Eq. 5.18. As discussed in Chap. 1, the realization of such spin-photon entangled state is a major objective of this work.

In the following, we do not prepare coherent superpositions of spin states and thus do not demonstrate entanglement, yet observe photon-photon cross-correlations described by the quantity $g_{DA}^{(2)}(t)$ defined previously. In lack of a specific term, we choose to call "back-action" the corresponding change of density matrix (from ρ_S to ρ'_S), an interpretation which holds assuming that the spin is, as well known, a qubit [17, 18, 20]. We acknowledge however that additional experiments should be performed to actually prove the quantum nature of the measurement back-action using coherent superpositions of spin states.

5.2.4 Experimental evidence of the measurement back-action.

In this section, we experimentally evidence the single-photon measurement back-action induced on a single spin. To do so, we first reconstruct the reflected polarization with polarization tomography. Then, we measure the cross-correlations in the diagonal/anti-diagonal polarization basis and finally, the polarization basis dependence of the cross-correlations.

Polarization tomography with a charged quantum dot.

The reflected polarization is reconstructed thanks to the setup sketched in Fig. 5.4. The spin-photon interface has already been studied in the previous chapter (it was called QD3). It is positioned in our cryostat with the possibility to apply a magnetic field along the vertical axis (i. e. Faraday configuration). As was discussed in Chap. 4, the quantum dot needs to be prepared in its hole state, using a CW quasi-resonant laser (at 901nm) with a power of typically 4μW (the required amount of quasi-resonant power is strongly reduced when the system is not submitted to short resonant π -pulses for single-photon emission). The voltage is tuned so that the quantum dot trion transition is in resonance with the horizontal cavity mode. A second CW-tunable laser is prepared with horizontal polarization and a power of typically 8pW, to be scanned across the QD-cavity trion resonance ($\lambda_{QD} \approx 925.8\text{nm}$). The reflected resonant light is separated from the quasi-resonant pump laser by a bandpass spectral filter, and is then filtered spatially using a single-mode fiber (the interest of such spatial filtering is discussed later on). Finally, the reflected resonant light is analyzed in polarization with two single-photon detectors.

The experiment is similar to the one described in Chap. 3, in which the quantum-dot induced polarization rotation was observed with polarization tomography. However, in the present case, the quantum dot transition under study is the positive trion and not the exciton. The CW-tunable resonant laser scans in wavelength the trion transition, and the reflected light intensity is measured in the three polarization bases: "H/V", "D/A" and "R/L".

The reflectivity is presented in Fig. 5.5 (a). The cavity mode is evidenced by scanning the laser wavelength across the horizontally-polarized cavity mode and with the quantum dot tuned out

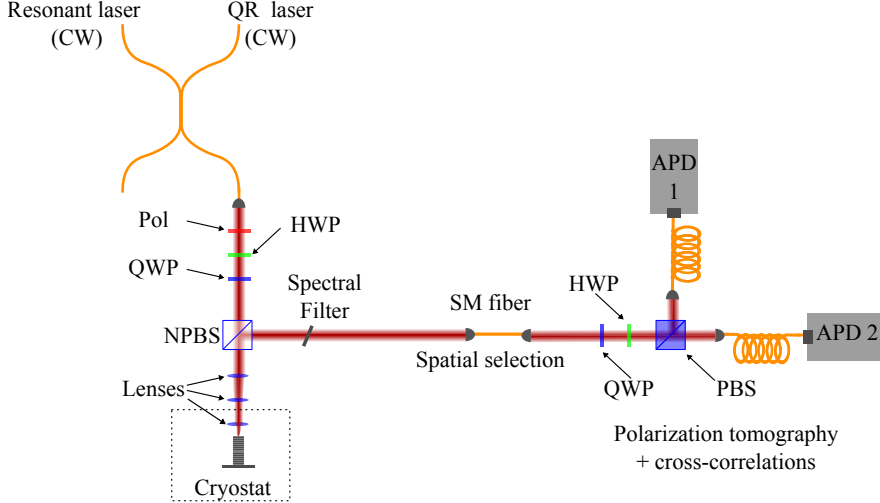


Figure 5.4: The spin-photon interface is excited both by a quasi-resonant CW laser (at 901nm), that ensures that a hole is confined inside the quantum dot, and by a horizontally-polarized CW laser resonant with the trion transition (around 925.8nm), which experiences quantum-dot induced polarization rotation. The resonant reflected light is separated from the quasi-resonant laser with a spectral filter. Then, it is spatially filtered by a single-mode fiber and its polarization is reconstructed using a polarization analyzer composed of a quarter waveplate, a half waveplate, a polarizing beam splitter, and two single photon detectors.

of the cavity. Both the cavity linewidth and the top mirror output coupling are extracted from this measurement: $\kappa = 407 \pm 5 \mu\text{eV}$ and $\eta_{top} = 84 \pm 5\%$. A second reflectivity measurement is carried out with the trion transition in resonance with the horizontally-polarized cavity mode. The laser wavelength scan is centered onto the quantum dot trion transition, and performed on a narrower energy range, to have better spectral resolution. For this second measurement, Fig. 5.5(a) shows the horizontally-polarized reflected light and the vertically-polarized scattered light. The horizontally-polarized component shows a clear reflectivity dip that evidences that the trion transition leads to a destructive interference: it is the expected quantum dot response for cavities with a high top mirror output coupling ($\eta_{top} = 84\%$ for this sample). A zoom on of the second reflectivity measurement is displayed in Fig. 5.5 (b). The fits and theoretical curves are discussed in Sec. 5.3.

The result of the polarization tomography measurement is displayed in Fig. 5.5(c), where the reflected light polarization vector is plotted in the Poincaré sphere for each incident laser wavelength. Far from the trion resonance, the reflected light has the same horizontal polarization as the incoming laser, but when the laser is tuned in resonance with the trion transition, the reflected light polarization is degraded without any rotation of polarization, i.e. $s_{DA} \approx 0$, while s_{HV} decreases down to ≈ 0.5 . The depolarization is maximum when the laser is tuned into resonance with the trion transition, with a minimum polarization purity of around 50% at $\omega_{laser} = \omega_{QD}$. The fibered spatial filtering in the setup (see Fig. 5.4) avoids the depolarization induced by non-optimal cavity coupling, as was previously discussed in Sec. 2.5 and experimentally evidenced in Sec. 2.3.4. Consequently, all the depolarization observed should be induced by the quantum dot and not by the cavity.

For a trion transition, a polarization rotation is expected, and not depolarization. Such a depo-

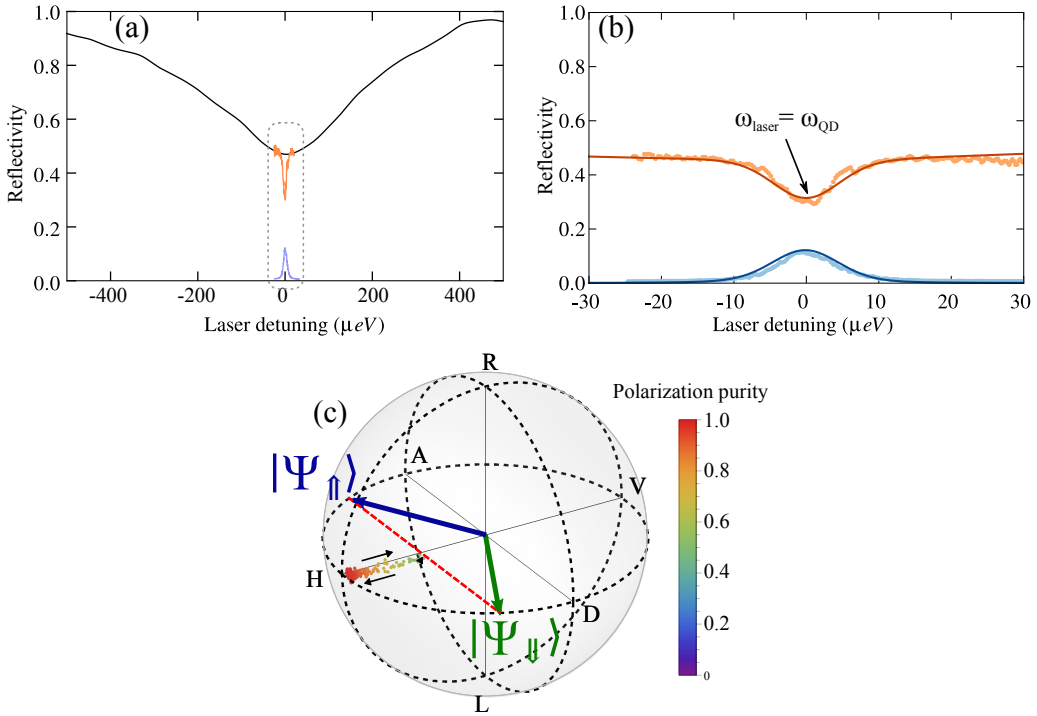


Figure 5.5: (a) Reflectivity of the spin-photon interface under horizontally-polarized excitation when the quantum dot trion transition is tuned out off (black curve) or in resonance (orange for horizontally-polarized and blue for vertically-polarized reflected light) with the cavity. (b) Reflectivity of the device with horizontal (blue) and vertical (orange) polarizations, for a laser detuning close to 0 ($\omega_{laser} = \omega_{QD}$). Solid lines represent fits simulating the QD-cavity response in both horizontal and vertical polarizations, including the effect of spectral wandering (see Sec. 5.3). (c) Polarization tomography of a charged quantum dot-cavity device. The CW laser is scanned in wavelength along the quantum dot trion resonance. At the trion resonance, there is conversion of the polarization from horizontal to vertical, without polarization rotation, thus leading to depolarization, as observed with the colorscale that represents the polarization purity. Indicative polarization states $|\Psi_{\uparrow\uparrow}\rangle$ and $|\Psi_{\downarrow\downarrow}\rangle$ in the Poincaré sphere, potentially explaining the spin depolarization when the laser is in resonance with the trion.

larization is in fact observed because the spin is not initialized in either its up ($|\uparrow\uparrow_z\rangle$) nor its down ($|\downarrow\downarrow_z\rangle$) state. Consequently, because the acquisition time (typically 10ms per wavelength) is much longer than the spin relaxation time (typically a few μs), the result of the polarization tomography measurement is an average between the two polarization vectors. In this "simple picture" model, the depolarization is explained by an averaging between two polarization states $|\Psi_{\uparrow\uparrow}\rangle$ and $|\Psi_{\downarrow\downarrow}\rangle$, sketched on the Poincaré sphere in Fig. 5.5(c) (for the wavelength that induces maximum depolarization, i.e. when $\omega_{laser} = \omega_{QD}$). From such polarization tomography, one can expect that the two pure spin-dependent polarization states should be symmetric about the "H/V" axis. These two polarizations are macroscopically different and therefore should lead to a macroscopic single-photon measurement back action on the spin, as observed in the next section.

Experimental cross-correlations.

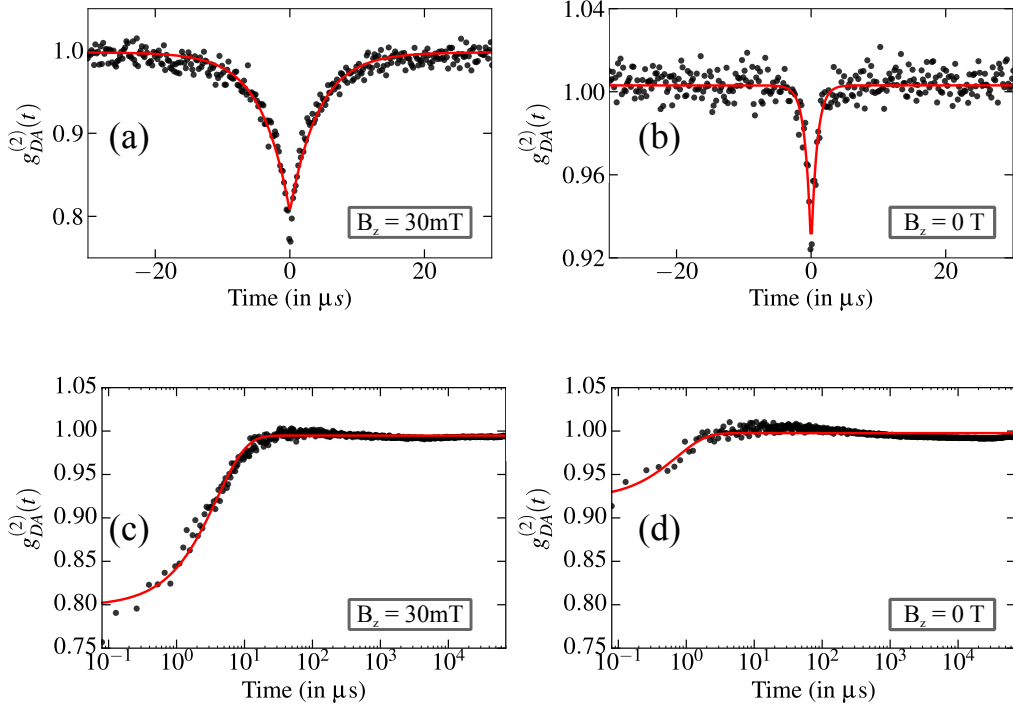


Figure 5.6: Cross-correlation measurements $g^{(2)}(t)$ in the "D/A" basis, carried out for $B_z = 30\text{mT}$ (a) and $B_z = 0\text{T}$ (b). (c, d) Same measurements plotted in logarithm scale. To be observed, the zero-delay point has been artificially put at $t = 80\text{ns}$, corresponding to the limit of the plot. The red curve corresponds to an exponential fit using Eq. 5.12.

Using the same setup (see Fig. 5.4), it is also possible to experimentally measure intensity cross-correlations in the diagonal/anti-diagonal ("D/A") basis. The laser is now in resonance with the trion transition ($\omega_{laser} = \omega_{QD}$) with an attenuated power of 8pW, ensuring that the quantum dot is excited with no more than one photon at a time (it actually corresponds to only one photon every 25ns).

Finally, the reflected resonant light is analyzed in the diagonal/anti-diagonal polarization basis. The detectors are connected to a time-correlated single photon counting module, which allows to observe the correlations between the detectors and therefore reconstruct $g_{DA}^{(2)}(t)$. Experimental cross-correlation measurements are displayed for $B_z = 0\text{T}$ and $B_z = 30\text{mT}$ in Fig. 5.6 (a) and (b) (and in semi-logarithmic scale for Fig. 5.6 (c) and (d)). They are fitted with Eq. 5.12, i. e. a monoexponential decay towards 1, to extract the zero-delay cross-correlations value $g_{DA}^{(2)}(0)$.

At $B_z = 30\text{mT}$, the observed cross-correlations show clear anti-correlations at zero delay between the two detected polarizations. The zero-delay value measured is $g_{DA}^{(2)}(0) = 80 \pm 1\%$, which corresponds to a spin initialization of $P_{\uparrow\uparrow|A} \approx 72\%$ induced by a single photon detection, according to Eq. 5.13.

At $B_z = 0\text{mT}$, the zero-delay value is higher: $g_{DA}^{(2)}(0) = 92 \pm 2\%$, which would correspond to a spin initialization induced by a single detected photon of $P_{\uparrow\uparrow|A} \approx 64\%$. From Fig. 5.6, we also observe that the experimental value is slightly smaller ($g_{DA}^{(2)}(0) \approx 76\%$ at $B_z = 30\text{mT}$) than the value extracted

by the fit, and that the spin lifetime T_S is varying with the magnetic field. These three observations are discussed in further details in Sec. 5.4.

Influence of the detection polarization basis.

So far, the cross-correlation measurements have been shown in the "D/A" basis only. Here we show an evidence that what is measured is indeed the photon-polarization measurement back-action on the spin state, by modifying the measurement basis. The spin-dependent polarization states presented in Fig. 5.5(c) are represented on the equator of the Poincaré sphere. If the measurement basis is "R/L", one should not observe any anti-correlations between the detectors, because each spin-dependent polarization can be detected with close to equal probability in each detectors: $P_{L|\uparrow} \approx P_{L|\downarrow} \approx P_{R|\uparrow} \approx P_{R|\downarrow}$, and thus $g_{RL}^{(2)}(0) \approx 1$ and subsequently, $g_{RL}^{(2)}(t) \approx 1$.

To observe this effect, the cross-correlation measurements are repeated in different polarization basis, situated on the "meridian" circle "DA/RL" of the Poincaré sphere. The polarization bases are denoted by the angle θ formed with the "R/L" measurement basis, as represented in Fig. 5.7(a). The results of the cross-correlations are all represented in Fig. 5.7(b). They are denoted $g_{\theta\bar{\theta}}^{(2)}(t)$, with the convention that $\bar{\theta}$ corresponds to the polarization state orthogonal to that corresponding to θ : for example, $\theta = 0$ (respectively $\theta = 0.5\pi$) corresponds to the polarization state $|R\rangle$ (resp. $|D\rangle$) and $\bar{\theta}$ to the polarization state $|L\rangle$ (resp. $|A\rangle$) and thus the correlations $g_{\theta\bar{\theta}}^{(2)}(t)$ are the correlations in the "R/L" basis (resp. the "D/A" basis).

We are mostly interested in the zero-delay value of the cross-correlations, $g_{\theta\bar{\theta}}^{(2)}(0)$, which is displayed in Fig. 5.7 (c) and clearly show a minimum value close to the "D/A" basis ($\theta = \pi/2$) and no anti-correlation dips close to the "R/L" basis ($\theta = 0$ and $\theta = \pi$). The small deviation of the minimum value from the "D/A" basis is due to the cavity ellipticity, which leads to $|\Psi_{\uparrow}\rangle$ and $|\Psi_{\downarrow}\rangle$ states that are not exactly in the "HVDA" plane, with small but non-zero values of $s_{RL}(|\Psi_{\uparrow}\rangle)$ and $s_{RL}(|\Psi_{\downarrow}\rangle)$.

Consequently, we have shown the macroscopic back-action induced by the detection of a single photon onto a single spin, thanks to photon cross-correlation measurements. The strength of this back-action can be controlled by choosing the measurement polarization basis. Using a simple-picture model, we can estimate that the maximum back-action induced by a single photon detection corresponds to a spin initialization with 72% probability (at 30mT, corresponding to $g_{DA}^{(2)}(0) = 0.8$), significantly higher than the average 50% probability. However, this estimation is based on the model presented in Sec. 5.2.2 which is too simple to completely tackle the complexity of the system. The next section shows the limitations of such model.

5.2.5 Discussion on the "simple picture" model.

The model presented previously gives a simple picture to understand the concepts of a cross-correlation measurement and the physical implications of a photon measurement onto the spin-photon interface. However, this system is too simple to fully explain the system, as imperfections need to be taken into account.

Imperfect hole trapping efficiency. The first limitation of this model is that it does not take into account the fact that the hole is not trapped inside the quantum dot all the time. Indeed, as demonstrated in Chap. 4, the hole occupation probability is high but never 100% in this sample. As illustrated in Fig. 5.8(a), when the quantum dot is not charged, the trion transition is not optically active and therefore, because the laser incident polarization is along the horizontal cavity axis, it is reflected

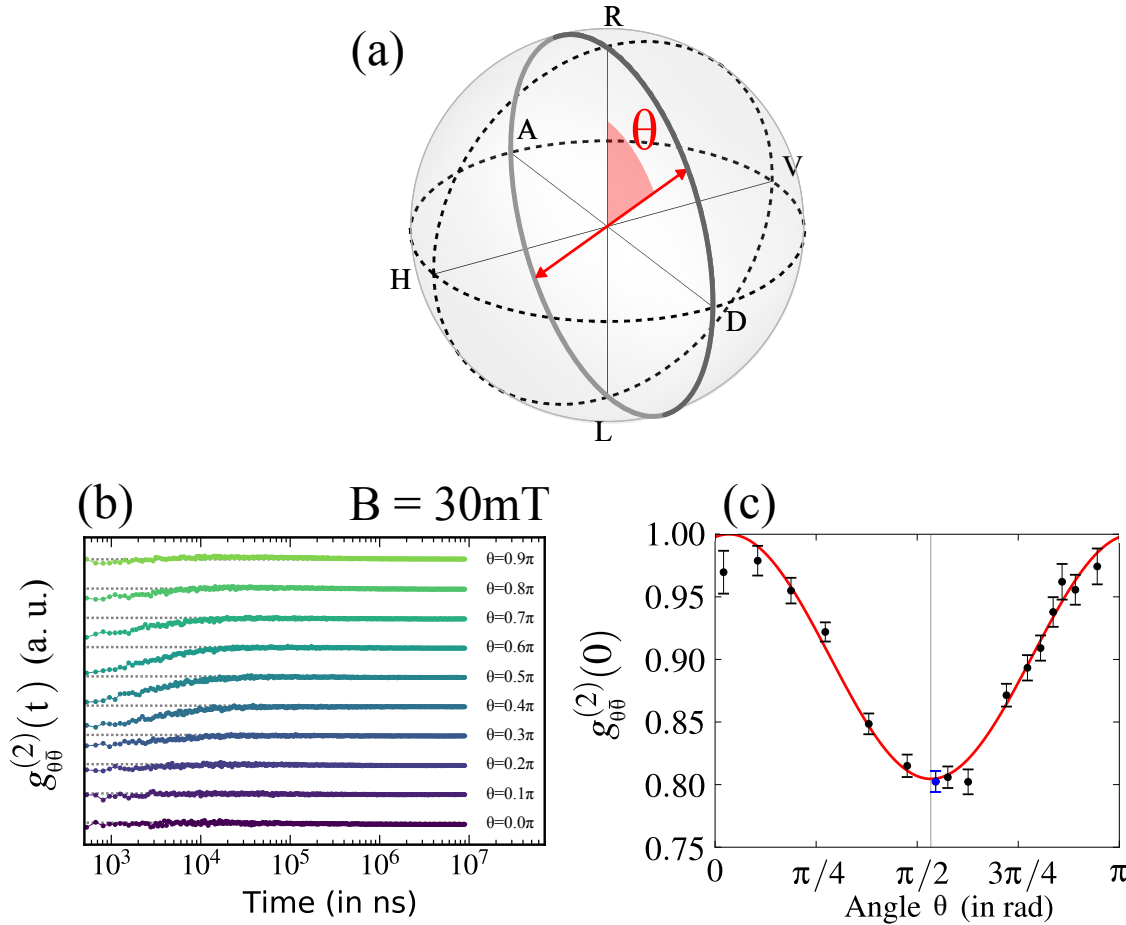


Figure 5.7: (a) Measurement basis (red arrows) in which are measured the cross-correlations $g_{\theta\bar{\theta}}^{(2)}$, characterized by the angle θ in the Poincaré sphere. (b) Cross-correlation measurements $g_{\theta\bar{\theta}}^{(2)}(t)$ repeated in different orthogonal polarization bases (denoted by their angle θ) under magnetic field $B=30\text{mT}$. The anti-correlations observed are highlighted in (c) which represents the zero-delay cross-correlations $g_{\theta\bar{\theta}}^{(2)}(0)$ for different angles, under $B=30\text{mT}$. The zero-delay cross-correlations as a function of the angle are fitted by a sine function (red curve) evidencing that they reach their minimum value for an angle close to $\pi/2$, corresponding to the "D/A" polarization basis. The blue point at $\theta = 0.55\pi$ is the polarization basis used for the cross-correlation measurement presented in Fig. 5.6.

with the same polarization state $|\Psi_0\rangle = |H\rangle$. The three possible polarization states, corresponding to the spin-dependent polarization states and the horizontal polarization obtained for an empty quantum dot, are represented in the Poincaré sphere in Fig. 5.8(b).

No correlations expected in resonance with the trion. Additionally, the cross-correlations measurement were carried out with the laser exactly in resonance with the quantum dot trion transition. However, as shown in the next section, at this specific wavelength, the reflected polarization should be the same for the two spin states ($|\Psi_\uparrow\rangle = |\Psi_\downarrow\rangle$ when $\omega_{\text{laser}} = \omega_{QD}$). Therefore, no anti-correlations

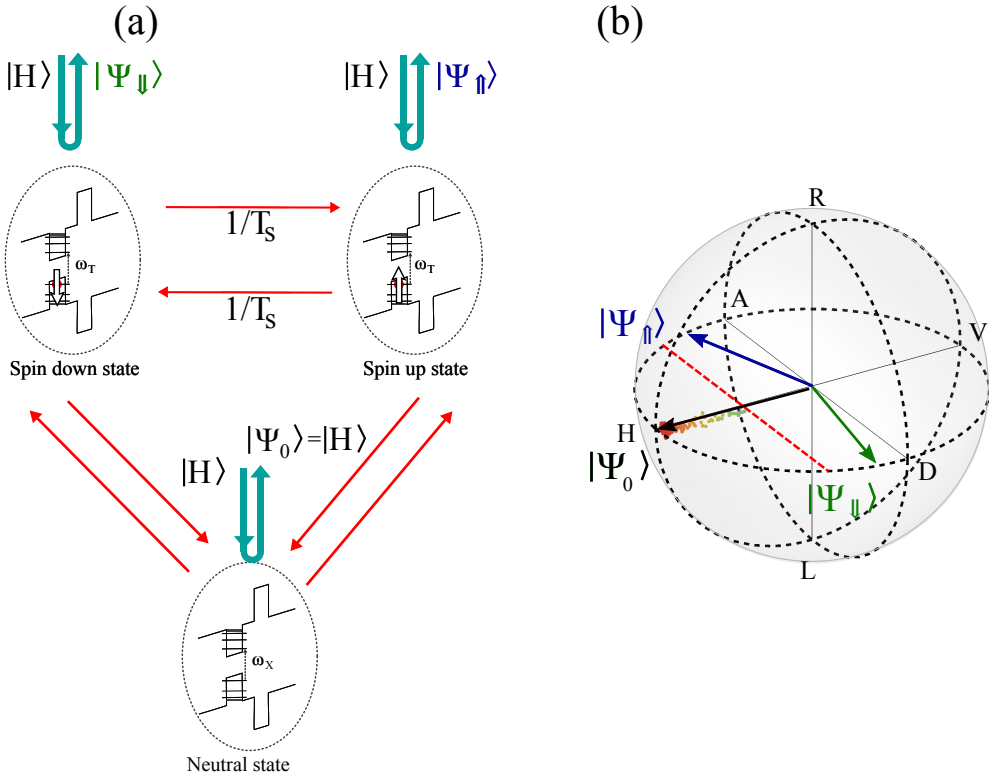


Figure 5.8: Simple model explaining the depolarization observed in the polarization tomography of a charged quantum dot. (a) The quantum dot is assumed to be either in a charged state with spin $|\uparrow_z\rangle$ or $|\downarrow_z\rangle$, or in the neutral state. Uncontrolled spin flips occur at a rate $1/T_S$. Depending on the spin state, the incident light is reflected with either $|\Psi_{\uparrow\uparrow}\rangle$ or $|\Psi_{\downarrow\downarrow}\rangle$ spin-dependent polarizations. The hole can be charged and escape the quantum dot. For the empty state, photons are reflected with horizontal polarization. (b) Polarization states $|\Psi_{\uparrow\uparrow}\rangle$ and $|\Psi_{\downarrow\downarrow}\rangle$ and $|\Psi_0\rangle = |H\rangle$ represented in the Poincaré sphere, to explain the maximum depolarization observed in the experimental data.

should be observed (since $P_{\uparrow\uparrow|A} = P_{\downarrow\downarrow|A}$), in contradiction to what is observed experimentally.

Spectral fluctuations. The third limitation is that the model does not take into account spectral fluctuations of the quantum dot. As was observed in Chap. 3, the spectral fluctuations degrade the polarization purity of the reflected light, so the spin-dependent polarization states represented in Fig. 5.8 (b), should not be represented as fixed polarization states. To know if there are spectral fluctuations, one can compare the trion transition linewidth with the Fourier-transform of the trion state lifetime. If the trion transition is wider than its Fourier-limited value, there are indeed spectral fluctuations. The trion lifetime measurement is carried out by measuring the single-photon lifetime under pulsed excitation. The result is displayed in Fig. 5.9(a): the exponential decay fit indicates a trion lifetime of $T = 380 \pm 20$ ps, which corresponds to a Fourier limited linewidth of $\Gamma = 1.7 \pm 0.1 \mu eV$. The trion transition linewidth can be observed by scanning the CW resonant laser in wavelength across the trion transition and observing its resonance fluorescence cross-polarized intensity. This is displayed in Fig. 5.9(b), and it presents a gaussian shape with standard deviation $\sigma = 4.2 \pm 0.1 \mu eV$, giving a full width at half maximum FWHM = $9.9 \pm 0.2 \mu eV$, significantly larger than the Fourier-

limited linewidth. Consequently, because the trion linewidth is broader than its Fourier-limited value, we can deduce that the trion transition is spectrally fluctuating.

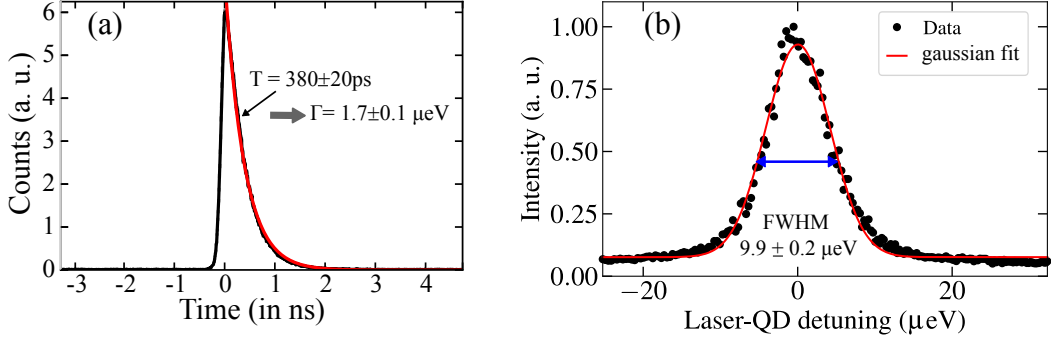


Figure 5.9: (a) Measurement of the single photon lifetime. The exponential decay is fitted with a photon lifetime of $T = 380 \pm 20\text{ps}$, which corresponds to a Fourier-transform linewidth of the trion resonance of $\Gamma = 1.7 \pm 0.1\mu\text{eV}$ (b) Measurement of the trion cross-polarized resonance fluorescence as a function of the laser energy detuning. A gaussian fit extracts a linewidth of $\text{FWHM} = 9.9 \pm 0.2\mu\text{eV}$.

In the next section, a complete model is constructed that tackles these three limitations.

5.3 Theoretical model of a charged quantum dot coupled to a cavity.

In this section, we develop an exact model that simulates realistically a charged quantum dot coupled to a cavity excited under resonant excitation. A similar model was presented in Chap. 3 for a neutral quantum dot and is adapted in this section for a charged quantum dot. We also focus on the simulation of the incoherent processes, namely the hole occupation and the spectral fluctuations. We simulate the spin-photon interface polarization response and cross-correlations with these noise models and conclude that they qualitatively and quantitatively agree with the experimental data. Finally, this exact model allows a better understanding of the limitations of the experimental measurement back-action, and indicates how to improve it.

5.3.1 Coherent evolution of a cavity-coupled charged quantum dot.

The hamiltonian presented in Chap. 3 (see more specifically Sec. 3.3.3) needs to be slightly adapted to simulate a charged quantum dot. The modifications occur on the quantum dot hamiltonian part \hat{H}_{QD} , its interaction with the cavity \hat{H}_{int} and an additional hamiltonian taking into account the quantum dot interaction with an external magnetic field \hat{H}_B .

Charged quantum dot hamiltonian. As illustrated in Fig. 5.10, the charged quantum dot is represented by a four-level system separated into two branches: the branch for circular-left (respectively circular-right) polarization composed of ground state $|\uparrow\downarrow_z\rangle$ (resp. $|\downarrow\uparrow_z\rangle$) and excited state $|\uparrow\downarrow\uparrow_z\rangle$ and $|\downarrow\uparrow\downarrow_z\rangle$. Each ground state is connected to one single excited state thanks to the operators $\hat{\sigma}_{+,R} = |\downarrow\uparrow\downarrow\rangle\langle\uparrow\downarrow|$ and $\hat{\sigma}_{+,L} = |\uparrow\downarrow\uparrow\rangle\langle\downarrow\downarrow|$ (see Fig. 5.10).

Under zero magnetic field, the two trion transitions are degenerate with energy ω_{QD} . The hamiltonian of the quantum dot alone is now:

$$\hat{H}_{QD} = \hat{H}_{QD,R} + \hat{H}_{QD,L} = (\omega_{QD} - \omega)(\hat{\sigma}_{+,R}\hat{\sigma}_{-,R} + \hat{\sigma}_{+,L}\hat{\sigma}_{-,L}) \quad (5.21)$$

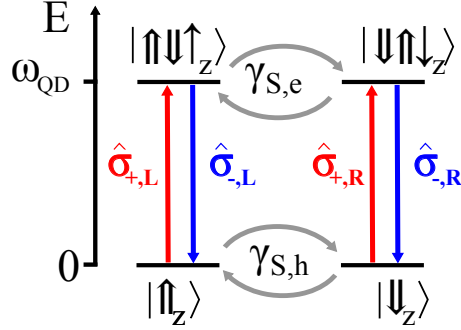


Figure 5.10: Scheme of the four level system constituted by two ground hole spin states and two excited trion states. In the model, the ground and excited states are connected through the operators $\hat{\sigma}_{+,L}$ and $\hat{\sigma}_{+,R}$. Each hole spin state is connected to one trion state through circularly-polarized photons. Incoherent spin-flips occurs at a rate $\gamma_{S,h}$ for the hole spins, and at a rate $\gamma_{S,e}$ for the trion spin states.

Interaction hamiltonian. The interaction Hamiltonian is modified to account for the circularly polarized transitions between the excited and ground states:

$$\hat{H}_{int} = \hat{H}_{int,R} + \hat{H}_{int,L} = ig(\hat{a}_R^\dagger \hat{\sigma}_{-,R} - \hat{a}_R \hat{\sigma}_{+,R}) + ig(\hat{a}_L^\dagger \hat{\sigma}_{-,L} - \hat{a}_L \hat{\sigma}_{+,L}) \quad (5.22)$$

where \hat{a}_R^\dagger and \hat{a}_L^\dagger (\hat{a}_R and \hat{a}_L) are the creation (annihilation) operators for right-handed and left-handed circularly polarized photons:

$$\begin{aligned} \hat{a}_R &= \frac{1}{\sqrt{2}} (\hat{a}_H + i\hat{a}_V), & \hat{a}_R^\dagger &= \frac{1}{\sqrt{2}} (\hat{a}_H^\dagger - i\hat{a}_V^\dagger) \\ \hat{a}_L &= \frac{1}{\sqrt{2}} (\hat{a}_H - i\hat{a}_V), & \hat{a}_L^\dagger &= \frac{1}{\sqrt{2}} (\hat{a}_H^\dagger + i\hat{a}_V^\dagger) \end{aligned} \quad (5.23)$$

Magnetic field/quantum dot interaction hamiltonian. In this chapter and for the perspectives of this thesis, an external magnetic field is used and therefore needs to be simulated in our model. The interaction hamiltonian between a spin and a magnetic field was already described in Chap. 1 by Eq. 1.4.

In the case of a charged quantum dot, the four levels have a spin degree of freedom. The ground states have a heavy hole spin with projection $S = \pm 3/2$ and a Landé-factor g_h . The excited states have two holes in a singlet and an electron, therefore have a spin equivalent to their electron's, with projection $S = \pm 1/2$ and a Landé-factor g_e .

The interaction hamiltonian for the ground states (composed of a heavy hole whose spin projection is $S = 3/2$) is:

$$\hat{H}_{B,h} = \frac{3}{2} g_h \mu_B B (\hat{\sigma}_{-,L} \hat{\sigma}_{+,L} - \hat{\sigma}_{-,R} \hat{\sigma}_{+,R}) \quad (5.24)$$

We used the fact that the populations of the ground states are given by the operators $\hat{\sigma}_{-,L}\hat{\sigma}_{+,L}$ and $\hat{\sigma}_{-,R}\hat{\sigma}_{+,R}$. In addition, we have only considered the hole longitudinal Landé factor $g_h = g_h^{\parallel}$ (which

is generally quite different from the hole transverse Landé factor g_h^\perp [73]), because the external magnetic field is only considered in Faraday configuration.

For the trion states governed by the electron spin, the interaction hamiltonian is:

$$\hat{H}_{B,e} = \frac{1}{2}g_e\mu_B B(\hat{\sigma}_{+,R}\hat{\sigma}_{-,R} - \hat{\sigma}_{+,L}\hat{\sigma}_{-,L}) \quad (5.25)$$

The total interaction hamiltonian is therefore:

$$\hat{H}_B = \hat{H}_{B,e} + \hat{H}_{B,h} \quad (5.26)$$

This hamiltonian is responsible for the Zeeman splittings between the two ground and excited states, as was already discussed in Sec. 1.1.2.

5.3.2 Theoretical polarization tomography.

With the model constructed previously, together with the collapse operator \hat{C}_{cav} simulating the cavity losses and the collapse operator \hat{C}_{sp} simulating the quantum dot spontaneous decay (see Sec. 3.3.3 for more details), it is possible to simulate an ideal spin-photon interface, which does not take into account incoherent interactions with the quantum dot environment and imperfect hole occupation probability. First, we will simulate the polarization tomography in the ideal case. Then, we will simulate incoherent processes with the environment with four different noise models and show that they have similar effects on the polarization tomography.

Simulation of an ideal spin-photon interface.

Figure 5.11 displays the simulated polarization tomographies of the reflected light in the absence of spectral fluctuations and with a quantum dot always occupied by a hole in three different spin configurations, without longitudinal magnetic field applied ($B_z = 0$). They are simulated with realistic cavity-QED parameters, chosen to be similar to the ones extracted from the fit using noise mechanisms that will be discussed later on (see Sec. 5.3.3): the cavity has a simulated top mirror output coupling of $\eta_{top} = 0.84$ and a linewidth of $\kappa = 407\mu\text{eV}$ (deduced from the cavity reflectivity in Fig. 5.5(a)), with a cavity splitting of $\omega_{c,H} - \omega_{c,V} = 77\mu\text{eV}$. The trion transition is in resonance with the horizontally-polarized cavity mode ($\omega_{QD} = \omega_{c,H}$), the light-matter interaction coupling is $g = 15.5\mu\text{eV}$, and the quantum dot spontaneous emission in bulk is $\gamma_{sp} = 0.8\mu\text{eV}$. These values are all consistent with what was extracted from the polarization tomography in Chap. 3. Contrary to Chap. 3, we assume here that there is no pure dephasing $\gamma^* = 0$, which is consistent with the good corrected indistinguishability measured with the HOM experiment in Fig. 4.15. The simulated cooperativity is $C = \frac{2g^2}{\kappa\gamma_{sp}} = 1.5$ and, together with the high top mirror output coupling, we should expect giant polarization rotation, as seen in Fig. 1.24(c).

Figure 5.11 (a) displays the polarization tomography of the reflected light when the spin is fixed in the $|\uparrow\uparrow_z\rangle$ state for different laser detunings (the colorscale shows the laser-quantum dot detuning). The top panel of this figure displays the Stokes parameters s_{HV} , s_{DA} and s_{RL} as a function of the laser-QD detuning. Far from the trion transition, $s_{HV} = 1$ and the light is reflected with the same horizontal polarization as the incident laser. However, at resonance with the trion transition ($\omega_{laser} = \omega_{QD}$), $s_{HV} = -1$ and thus the reflected light is almost vertical. As can also be seen in this figure, the other Stokes parameters are also varying for a laser wavelength close to the trion resonance, evidencing that the reflected light polarization is rotated. The middle and bottom panels display the reflected

polarizations in the Poincaré sphere, which help visualizing this polarization rotation. For all laser wavelengths, the reflected polarization is a pure polarization state and, as seen in the middle and bottom panels of Fig. 5.11(a), the reflected polarization strongly depends on the laser detuning: from red to blue detuning, the reflected light first has a similar polarization as the incident horizontal polarization, then nearly anti-diagonal polarization, vertical, nearly diagonal polarization and then again horizontal polarization. One should note that in resonance with the trion ($\omega_{laser} = \omega_{QD}$), the reflected polarization is almost vertical.

If the spin is initialized in state $|\Downarrow_z\rangle$, the reflected polarization is rotated in a very similar way, as observed in Fig. 5.11 (b). However, for a same wavelength, the reflected polarization for spin \Downarrow_z is symmetric to the reflected polarization for spin \Uparrow_z about the "H/V" basis in the Poincaré sphere. This is highlighted by the Stokes parameters represented in the top panel: The Stokes parameter s_{HV} is similar for both spin initializations, \Uparrow_z and \Downarrow_z , but the Stokes parameters s_{DA} and s_{RL} are opposite: for a given laser energy, $s_{DA}(|\Psi_{\Uparrow}\rangle) = -s_{DA}(|\Psi_{\Downarrow}\rangle)$ and $s_{RL}(|\Psi_{\Uparrow}\rangle) = -s_{RL}(|\Psi_{\Downarrow}\rangle)$. Consequently, as represented in the middle and bottom panels of Fig. 5.11 (b), from blue to red detuning, the reflected light first has a polarization close to the incident horizontal polarization, then nearly diagonal polarization, vertical, nearly anti-diagonal polarization, and then again horizontal polarization. Similarly, in resonance with the trion resonance the reflected polarization is again almost vertical. It should therefore be impossible to observe an anti-correlation dip in the cross-correlation measurement in the "D/A" basis, when $\omega_{laser} = \omega_{QD}$, because the reflected spin-dependent polarization states are both nearly vertical for this polarization (thus $s_{DA}(|\Psi_{\Uparrow}\rangle) = s_{DA}(|\Psi_{\Downarrow}\rangle) = 0$, leading to $P_{\Uparrow|A} = P_{\Downarrow|A} = 1/2$ and $g^{(2)}(0) = 1$). This will be elucidated later.

Figure 5.11 (c) shows the polarization state of the reflected light when the spin is not initialized. We observe that the reflected polarization varies from pure horizontal to pure vertical polarizations at the trion resonance, as can be seen with the Stokes parameter s_{HV} , but without any polarization rotation ($s_{RL} = s_{DA} = 0$): because the spin is in a statistical mixture, the reflected polarization for a given laser detuning is the average between the reflected polarizations for each spin state, which is therefore on the "H/V" axis of the Poincaré sphere (see middle and bottom panels of Fig. 5.11(c)), and result in depolarization without any polarization rotation. In the experimental polarization tomography (see Fig 5.5(c)), we indeed observed such depolarization but the reflected light is never vertically-polarized (s_{HV} reaches only 0.5 instead of -1, at $\omega_{laser} = \omega_{QD}$). It remains therefore necessary to explain both the anti-correlation dip observed at resonance with the trion transition (Fig. 5.6) and the limited depolarization observed experimentally in the Poincaré sphere (Fig. 5.5(c)).

Simulation of the noise mechanisms.

To theoretically explain and simulate the experimental cross-correlation measurements and the polarization tomography, we need to take into account the imperfect hole occupation probability and the trion resonance spectral fluctuations. Four different models are explored to simulate the possible noise mechanisms:

- Fast ($\lesssim 100$ ps) electric fluctuations, simulated with pure dephasing thanks to a correlated noise collapse operator as was already discussed in Sec. 3.3.4):

$$\hat{C}_{deph,e} = \sqrt{2\gamma_{elec}^*} (\hat{\sigma}_{+,R} \hat{\sigma}_{-,R} + \hat{\sigma}_{+,L} \hat{\sigma}_{-,L}) \quad (5.27)$$

- Fast ($\lesssim 100$ ps) magnetic fluctuations, simulated with pure dephasing thanks to an anti-correlated

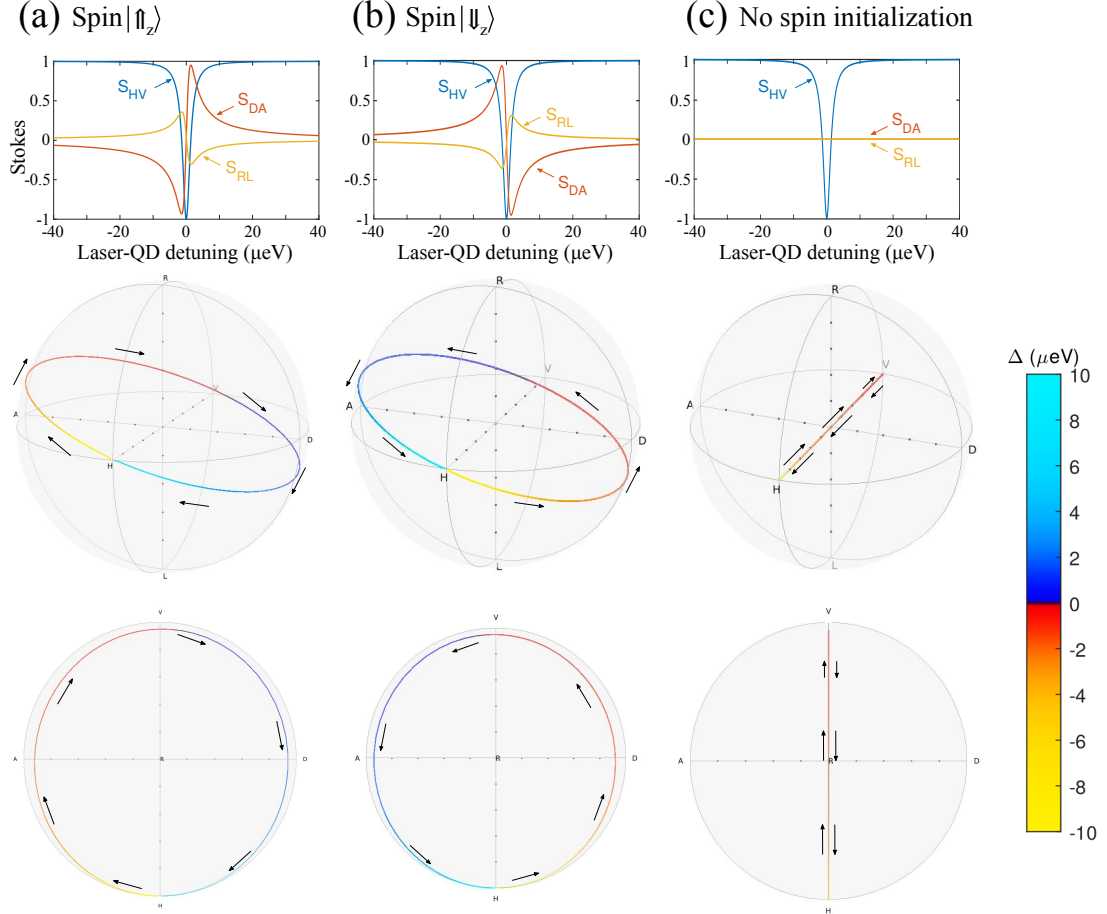


Figure 5.11: Simulated reflected polarization state in the absence of incoherent processes (therefore without spectral fluctuations and with $\langle P_h \rangle = 1$, see text for the parameters of the simulation) as a function of the laser detuning when the spin is initialized in the $|\uparrow_z\rangle$ state (a), the $|\downarrow_z\rangle$ state (b) and without spin initialization (c). The top panel represents the Stokes parameters, s_{HV} , s_{DA} and s_{RL} . The middle panel displays the simulated polarization density matrix represented in the Poincaré sphere for all laser wavelengths. The colorscale represents the laser-QD detuning ($\omega_{laser} - \omega_{QD}$). The bottom panel is the same polarization density matrix but observed from the top view of the Poincaré sphere, represented in terms of Stokes parameters (top panel) and in the Poincaré sphere (middle and bottom panels). The bottom panel of each figure is a top view of the Poincaré sphere. (a, b) When the spin is initialized, the reflected polarization is rotated and remains pure. (c) When the spin is not initialized, the reflected light is an incoherent superposition of the two spin-dependent polarization states that are symmetrical along the "H/V" axis. The reflected light polarization is therefore along the "H/V" axis and no polarization rotation is observed. The colorscale represents the laser detuning. Black arrows are represented to highlight how evolves the reflected polarization when the laser scans in wavelength the trion transition from negative to positive detuning.

noise collapse operator (see Sec. 3.3.4):

$$\hat{C}_{deph,m} = \sqrt{2\gamma_{mag}^*} (\hat{\sigma}_{+,R}\hat{\sigma}_{-,R} - \hat{\sigma}_{+,L}\hat{\sigma}_{-,L}) \quad (5.28)$$

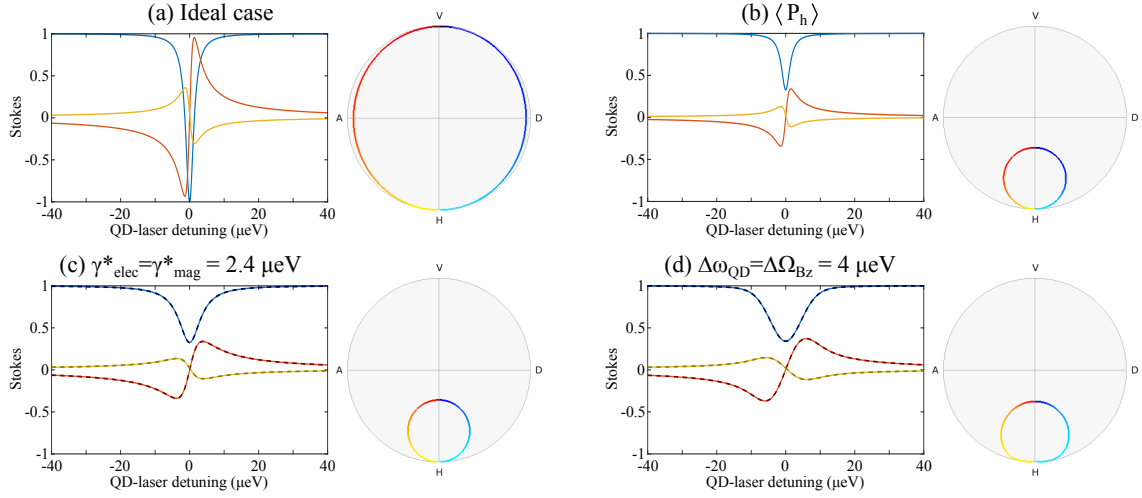


Figure 5.12: Simulated Stokes parameters and polarization tomographies with different noise models. (a) Ideal case where a single hole is always trapped inside the quantum dot and where there is no spectral fluctuations. (b) Case, where imperfect hole occupation probability is taken into account ($\langle P_h \rangle = 0.4$). (c-d) In addition to the imperfect hole occupation probability ($\langle P_h \rangle \neq 1$), the spectral fluctuations are modeled with magnetic (dashed curve) or electric (solid curve) pure dephasing (c) ($\langle P_h \rangle = 1$ and $\gamma_{elec}^* = \gamma_{mag}^* = 2.4 \mu\text{eV}$) and with slow magnetic (dashed curve) or electric (solid curve) fluctuations (d) ($\langle P_h \rangle = 0.8$ and $\Delta\Omega_{B_z} = \Delta\omega_{QD} = 3.2 \mu\text{eV}$). As can be seen, noises with magnetic or electric origin coincide in both cases. The other parameters for these simulations are discussed in the text.

- Slow electric fluctuations (occurring at timescales much longer than the relevant timescales of the system), simulated thanks to a spectral wandering of the trion transition ω_{QD} , fluctuating around an average value $\langle \omega_{QD} \rangle$, with a gaussian distribution of standard deviation $\Delta\omega_{QD}$. In such a case, both the optical transitions shown in Fig. 5.10 (from $|\uparrow_z\rangle$ to $|\uparrow\downarrow\uparrow_z\rangle$ and from $|\downarrow_z\rangle$ to $|\downarrow\uparrow\downarrow_z\rangle$) equally fluctuate with the same energy ω_{QD} .
- Slow magnetic fluctuations, simulated with fluctuations of the longitudinal magnetic field B_z , leading to a Zeeman shift Ω_{B_z} , fluctuating around zero with a gaussian distribution of standard deviation $\Delta\Omega_{B_z}$. In such a case, the optical transition from $|\uparrow_z\rangle$ to $|\uparrow\downarrow\uparrow_z\rangle$ and from $|\downarrow_z\rangle$ to $|\downarrow\uparrow\downarrow_z\rangle$ fluctuate in opposite directions around a fixed value of the average transition energy ω_{QD} : $\omega_{|\uparrow_z\rangle \rightarrow |\uparrow\downarrow\uparrow_z\rangle} = \omega_{QD} + \Omega_{B_z}$ and $\omega_{|\downarrow_z\rangle \rightarrow |\downarrow\uparrow\downarrow_z\rangle} = \omega_{QD} - \Omega_{B_z}$.

We show that any of these noise models (together with the imperfect hole occupation probability) can theoretically predict the experimental reflectivity and polarization tomography (and therefore, we cannot deduce the origin of the spectral fluctuations in that case).

Hole occupation: Let us understand first what is obtained with imperfect hole confinement, which implies a blinking of the quantum dot state, and of the device optical response. If the hole is not confined in the quantum dot, the trion transition is not optically active and therefore the incident light interacts with an empty cavity. Therefore the photons are reflected with horizontal polarization. Consequently, when the hole is confined in the quantum dot with a probability $\langle P_h \rangle$, the reflected polarization is an incoherent superposition of rotated polarization (when the hole is confined) and of horizontal polarization (when the hole is absent). To observe the effect of an imperfect hole

occupation probability, the Stokes parameters and the Poincaré sphere in the ideal case ($\langle P_h \rangle = 1$ in Fig. 5.12(a)) is compared to a partial hole occupation probability ($\langle P_h \rangle = 0.4$ in Fig. 5.12(b)), for a spin initialization in the $|\uparrow_z\rangle$ state. We observe that in that case, the amplitude of the variation of the Stokes parameters is significantly reduced, because, 60% of the time, the hole is not present and the light is reflected with horizontal polarization. We also note that the spectral width of variation of the Stokes parameters is similar to the ideal case. Therefore, the imperfect hole occupation probability cannot explain the spectral width of the trion transition discussed, in Sec. 5.2.5.

Spectral fluctuations: Contrary to the imperfect hole occupation probability, the spectral fluctuations should explain the broadening of the trion transition. These spectral fluctuations are modeled with a magnetic or electric noise occurring at either short or long timescales. Fast electric (respectively magnetic) noises are modeled with collapse operators, while slow electric (resp. magnetic) noises are modeled by repeating the simulation for different quantum dot energies ω_{QD} (resp. Zeeman shift Ω_{B_z}) and by averaging with a gaussian distribution. Fits of the experimental data are obtained with all these models and the Stokes parameters with spin initialization in the $|\uparrow_z\rangle$ state, are first plotted in Fig. 5.12 (c) and (d). We observe that the fast (respectively slow) magnetic noise gives similar results as the fast (respectively slow) electric noise. Indeed, both noise mechanisms induce fluctuations on one trion transition with respect to the other, but the spin is initialized in the spin $|\uparrow_z\rangle$ state and therefore, only the trion transition $|\uparrow_z\rangle \rightarrow |\uparrow\downarrow\uparrow_z\rangle$ is optically active. Consequently, magnetic and electric noises have the same effect on a reflectivity and a polarization tomography experiment.

In addition, it is possible to show that the fast and the slow noise mechanisms can both fit reasonably well the experimental reflectivity and the polarization tomography, as can be seen in Fig. 5.13. The fits, that also take into account the possibility of imperfect hole occupation probability ($\langle P_h \rangle \neq 1$), are all very similar and they both fit well the experimental data: all the noise mechanisms can fit the reflectivity dip of the horizontally-polarized measured reflectivity and the cross-polarized reflected (with vertical polarization), both in amplitude and in width, as can be seen in Fig. 5.13(a). Fig. 5.13(b) also displays that the noise mechanisms explain the reduced amplitude of variation of the polarization conversion, from horizontal to vertical polarization, that is observed experimentally.

The parameters extracted from these fits are:

- for the cavity, the top mirror output coupling $\eta_{top} = 84 \pm 5\%$, the cavity linewidth $\kappa = 407 \pm 5\mu\text{eV}$, and the cavity splitting $\omega_{c,H} - \omega_{c,V} = 77 \pm 3\mu\text{eV}$.
- for the quantum dot, a light matter interaction of $g = 15.5 \pm 1\mu\text{eV}$ and the quantum dot spontaneous emission in bulk $\gamma_{sp} = 0.8 \pm 0.2\mu\text{eV}$
- for the fast noise mechanism fit, a hole occupation probability of $\langle P_h \rangle = 95 \pm 5\%$ and a pure dephasing of $\gamma_{elec}^* = 2.4 \pm 0.2\mu\text{eV}$ or $\gamma_{mag}^* = 2.4 \pm 0.2\mu\text{eV}$ (depending if we simulate the electric or the magnetic pure dephasing).
- for the slow noise mechanism fit, a hole occupation probability of $\langle P_h \rangle = 80 \pm 10\%$ and a standard deviation of $\Delta\omega_{QD} = 3.2 \pm 1\mu\text{eV}$ or $\Delta\Omega_{B_z} = 3.2 \pm 1\mu\text{eV}$ (depending if we simulate the electric or the magnetic slow fluctuations).

Given the fact, that it is always possible to fit the experimental reflectivity and polarization tomography with the four different noise models, it is therefore not possible to deduce which is the dominant noise mechanism with such measurements. In the following, we are looking at the influence of each noise mechanism on a cross-correlation measurement.

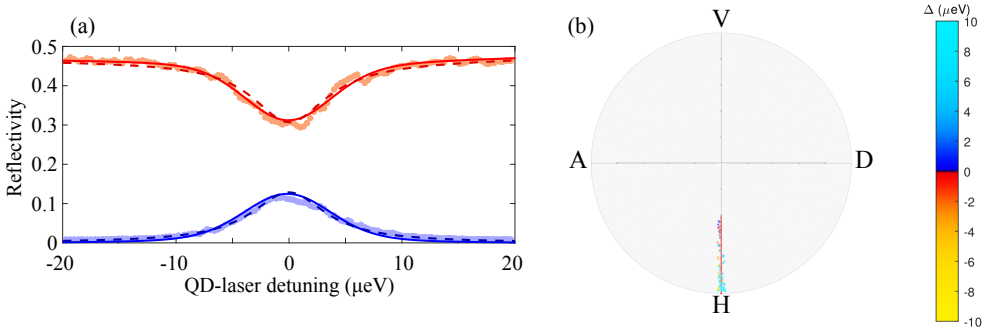


Figure 5.13: (a) Fit of the experimental reflectivity measurement using the slow (solid curve) and the fast (dashed curve) electric noise model. The measured horizontally-polarized reflectivity is represented by clear red points and the measured vertically-polarized reflectivity, by blue points. The fits are of similar quality for the different noise mechanisms. Fits with slow and fast magnetic noise mechanisms are equivalent as the one simulating slow and fast electric noise, and thus are not represented. (b) Experimental and simulated (with slow electric noise) polarization tomography as a function of the laser-QD detuning. The colorscale of the points in the Poincaré sphere represents the laser-QD detuning.

5.3.3 Consequence for the measurement back-action.

In this section, we show the influence of the different noise mechanisms on the observed cross-correlations. The objective is to understand how it is possible to predict the experimentally observed anti-correlation in the cross-correlation measurement, and thus deduce the dominant noise mechanism.

The zero-delay cross-correlation $g_{DA}^{(2)}(0)$ can be simulated with the formula given in Eq. 5.11. In order to observe anti-correlations at the trion resonance ($\omega_{laser} = \omega_{QD}$), the spin-dependent polarization states should be different: $s_{DA}(|\Psi_{\uparrow z}\rangle) \neq s_{DA}(|\Psi_{\downarrow z}\rangle)$, so that $P_{\uparrow|A} \neq P_{\downarrow|A}$ and $g_{DA}^{(2)}(0) < 1$. In resonance with the quantum dot, the two spin-dependent polarizations are both almost vertical and consequently, it should not be possible to observe anti-correlations at the trion resonance with a non-fluctuating spin-photon interface. The anti-correlation effect should therefore be induced by some incoherent processes. Fig. 5.14 displays the influence of each incoherent process onto the spin dependent polarization states.

Hole occupation probability: Let us first consider the effect of hole occupation probability, displayed in Fig. 5.14(a). When the hole is present in the quantum dot, we have an ideal spin-photon interface and almost always vertically-polarized reflected light $|\Psi_{\uparrow}\rangle = |\Psi_{\downarrow}\rangle = |V\rangle$. If the hole is absent, the light is always reflected with horizontal polarization $|\Psi_0\rangle = |H\rangle$. In all the cases, $s_{DA}(|\Psi_{\uparrow}\rangle) = s_{DA}(|\Psi_{\downarrow}\rangle) = s_{DA}(|\Psi_0\rangle) = 0$, the hole occupation probability does not have any influence onto the cross-correlation measurement.

Fast electric or magnetic noise: Let us now consider fast electric or magnetic pure dephasing, displayed in Fig. 5.14(b) and in Fig. 5.14 (c). Depending on the amount of dephasing γ^* simulated, the spin-dependent polarizations are modified and display a reduced polarization purity. This depolarization is similar to what was observed in Chap. 3, yet this time the electric or magnetic nature of the pure dephasing mechanism plays no role. Interestingly, for all values of γ^* , the spin-dependent polarizations $|\Psi_{\uparrow}\rangle$ and $|\Psi_{\downarrow}\rangle$ are identical, which means that fast electric or magnetic dephasing does

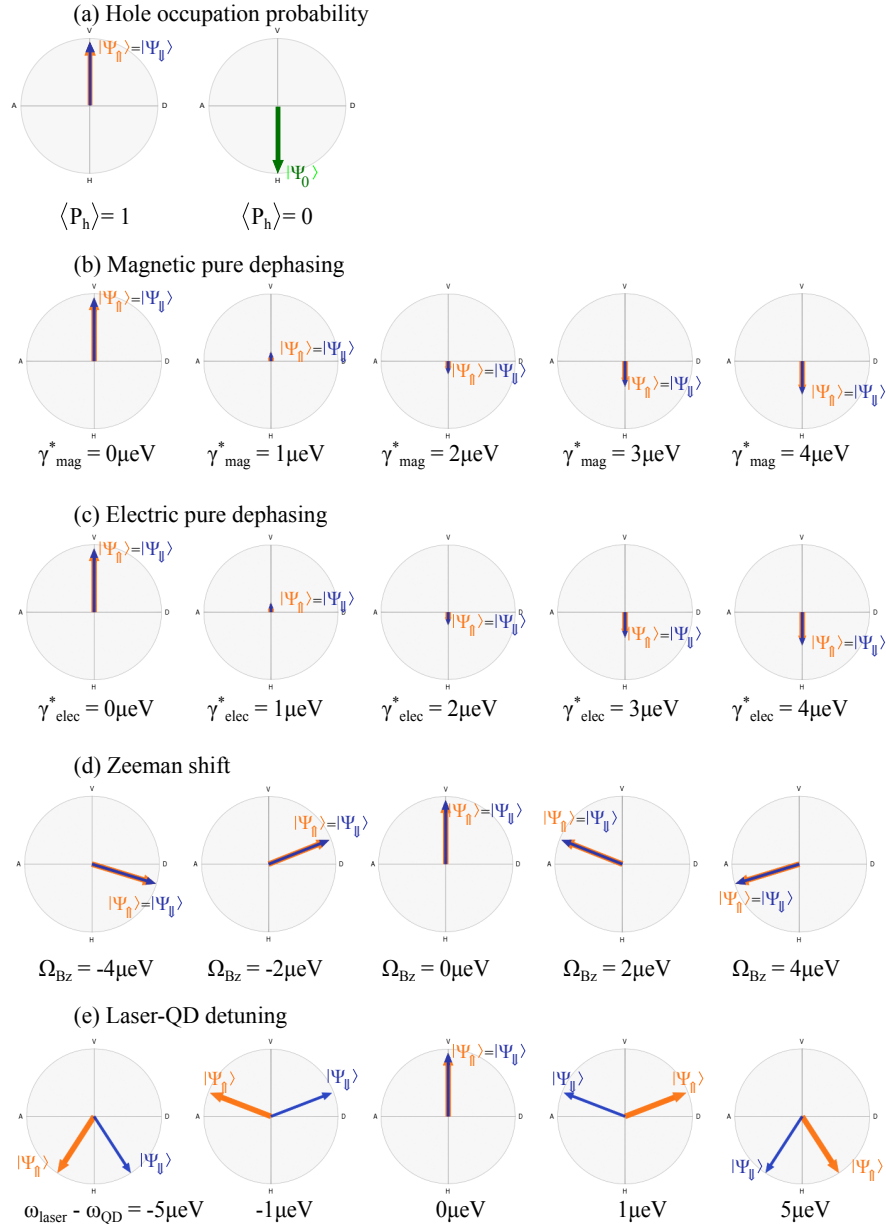


Figure 5.14: Simulated spin-dependent polarization states, for zero laser-QD detuning, for different noise mechanisms. (a) Spin-dependent polarization states for unity and zero hole occupation probabilities and without spectral fluctuations. (b, e) Spin-dependent polarization states for perfect hole occupation probability but with spectral fluctuations. (b) Case where the fluctuations are modeled by a magnetic pure dephasing term γ^*_{mag} . (c) Case where the fluctuations are modeled by an electric pure dephasing term γ^*_{elec} . (d) Spin-dependent polarization states for different Zeeman shifts Ω_{Bz} . (e) Spin-dependent polarization states for different laser-QD detunings, $\omega_{\text{laser}} - \omega_{\text{QD}}$. The blue, orange and green arrows represent the reflected polarization states for hole spin \uparrow , hole spin \downarrow and without hole confined in the quantum dot respectively.

not explain the anti-correlations observed in the cross-correlation measurements.

Slow magnetic noise: Now, let us consider the slow magnetic noise, i.e. fluctuations of the Zeeman shift Ω_{B_z} around an average value of zero, still keeping $\omega_{laser} = \omega_{QD}$. The spin-dependent polarization states for different Zeeman shifts are represented in Fig. 5.14(d): depending on the Ω_{B_z} , the spin-dependent polarization states $|\Psi_{\uparrow}\rangle$ and $|\Psi_{\downarrow}\rangle$ are rotated from the "H/V" axis but are still identical. Indeed, due to the Zeeman splitting, the laser wavelength is detuned from one transition by $+\Omega_{B_z}$ and detuned from the other transition by $-\Omega_{B_z}$, and therefore the reflected polarization is rotated in both cases. The fact that both rotations are identical comes from an interesting property of the Stokes coefficient s_{DA} , which, as illustrated in Fig. 5.11 (a) and (b), is an odd function of the laser transition detuning. Reversing the sign of the detuning, and at the same time reversing the spin state, is equivalent to reversing twice the rotation angle, and thus leave it unchanged: $s_{DA}(\uparrow, +\Omega_{B_z}) = s_{DA}(\downarrow, -\Omega_{B_z})$. Therefore, with that noise model, $|\Psi_{\uparrow}\rangle$ and $|\Psi_{\downarrow}\rangle$ are again identical, and the cross-correlations should not display an anti-correlation dip.

Slow electric noise: The last noise mechanism under study is the slow electric noise, which is displayed in Fig. 5.14(e). This figure shows the spin-dependent polarization states for different laser-quantum dot detunings ($\omega_{laser} - \omega_{QD}$), which is consistent with the fact that both $|\uparrow_z\rangle$ to $|\uparrow\downarrow\uparrow_z\rangle$ and $|\downarrow_z\rangle$ to $|\downarrow\uparrow\downarrow_z\rangle$ transitions experience the same detuning and that $s_{DA}(\uparrow, \omega_{laser} - \omega_{QD}) = -s_{DA}(\downarrow, \omega_{laser} - \omega_{QD})$. This clearly shows that the spin dependent polarization states can be different, $|\Psi_{\uparrow}\rangle \neq |\Psi_{\downarrow}\rangle$, provided that the laser is detuned from the quantum dot trion transition. Therefore, it should be possible to explain the experimental cross-correlations, with this noise model.

In the following, we will use the slow electric spectral wandering as the exclusive noise mechanism and use it to fit both the experimental polarization tomographies not only at 0T (as was done previously) but for the complete dataset including polarization tomographies with applied longitudinal magnetic fields.

Fit of the experimental set of data using spectral wandering.

Thanks to the model presented in the previous sections and simulating both the hole occupation probability and the spectral fluctuations (with a slow electric spectral wandering), it should be possible to fit all the experimental data. The complete set of data consists of the reflectivity and the polarization tomography measurements as the ones presented in Fig. 5.5, acquired not only at 0 and 30 mT but also at 10, 20, 50, 100, 200 and 500 mT. The Stokes parameters and the polarization tomographies at 30mT, 100mT and 500mT are represented in Fig. 5.15. With increasing external magnetic field, the trion transitions are Zeeman shifted, which results in a modification of the Stokes parameters (as can be seen in the left panels of Fig. 5.15). The results concerning the polarization of the reflected light are represented in the right panels of Fig. 5.15. Contrary to the polarization tomography at zero magnetic field where only depolarization was observed, with a longitudinal magnetic field, the polarization is also slightly rotated toward the anti-diagonal polarization, due to the Zeeman shift, as was already discussed in Fig. 5.14(b).

The full set of reflectivities and polarization tomographies is fitted using a single least-square method and a set of parameters consisting of the hole occupation probability $\langle P_h \rangle$, the spectral wan-

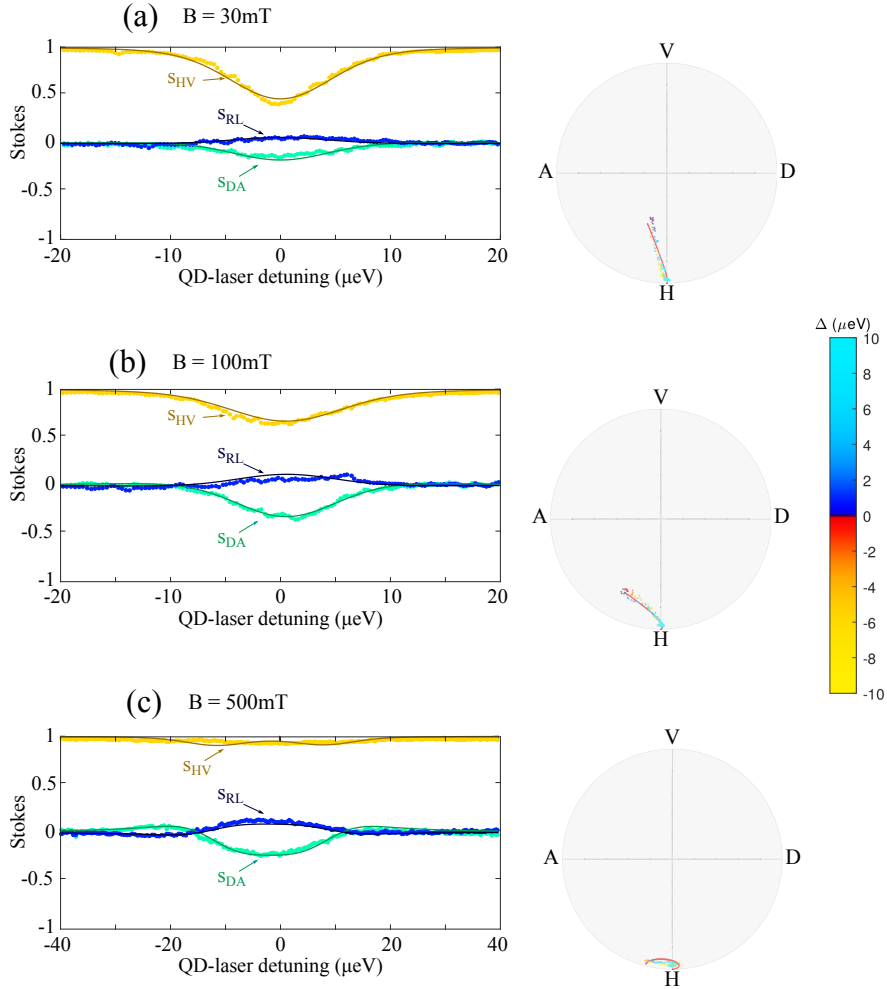


Figure 5.15: Stokes parameters (left panel) and polarization vector of the reflected light represented in the Poincaré sphere (right panel) for different laser-QD detunings, for an external magnetic field of (a) $B = 30\text{mT}$, (b) $B = 100\text{mT}$ and (c) $B = 500\text{mT}$. The colorscale represents the laser-quantum dot detuning. Points are experimental data, while solid line are fits using the slow electric noise model.

dering width $\Delta\omega_{QD}$, the light-matter coupling parameter g , the spontaneous emission rate γ_{sp} ¹. To account for the Zeeman shift induced by the external magnetic field, we consider that $\Omega_{B_z} = \mu B_z$, with $\mu = \pm\mu_B(\frac{1}{2}g_e - \frac{3}{2}g_h^{\parallel}) = 40\mu\text{eV.T}^{-1}$ (with μ_B the Bohr magneton and the \pm sign depending

¹ The ratio between the hole and the electron spin-flip rate, $\varepsilon = \frac{\gamma_{s,e}}{\gamma_{s,h}}$, is also used for this fit (it converges to a ratio $\varepsilon \approx 910^3$). It takes into account the possibility of spin pumping: when one trion transition, say $|\uparrow_z\rangle \rightarrow |\uparrow\downarrow\uparrow_z\rangle$, is resonantly excited and the other is not, it is possible to pump the spin in the $|\downarrow_z\rangle$ state, as discussed in Sec. 1.3.1. At zero magnetic field, because the resonant laser is horizontally-polarized and because the two trion transitions have the same energy, both are resonantly excited and therefore there is no spin pumping that needs to be taken into account. However, when a longitudinal magnetic field is applied, the two trion transitions have different energies $\omega_{|\uparrow_z\rangle \rightarrow |\uparrow\downarrow\uparrow_z\rangle} \neq \omega_{|\downarrow_z\rangle \rightarrow |\downarrow\uparrow\downarrow_z\rangle}$, and therefore the spin can be pumped by resonantly exciting only one trion transition. The ratio between the spin-flip rate ε is therefore only important to improve the fit of the polarization tomographies under high external magnetic field.

on the spin state). However, it is not possible to deduce independently the electron g_e and the hole longitudinal g_h^{\parallel} Landé factor.

The fit is converging for a hole occupation probability of $\langle P_h \rangle = 90 \pm 10\%$, a spectral wandering width of $\Delta\omega_{QD} = 4 \pm 1 \mu\text{eV}$, a light-matter coupling of $g = 15.5 \pm 1 \mu\text{eV}$ and a spontaneous emission rate of $\gamma_{sp} = 0.8 \pm 0.2 \mu\text{eV}$. These values are consistent with what is expected for a single-hole trapped inside a pillar microcavity. It is possible to compare the result of the theoretical model with the experimental data. In Fig. 5.5 (b), the solid lines represent the simulated reflectivity of the spin-photon interface and agree with the experimental curves. Similarly, the simulated Stokes parameters and polarization tomographies presented in 5.15 are also similar to the experimental data.

Influence of the noise spectral wandering on measurement back-action.

This section aims at having a better understanding of how the slow electric noise mechanism influences the cross-correlation measurements and the measurement back-action.

Influence on cross-correlation measurements: First, let us explain in detail why the cross-correlation measurements should display an anti-correlation dip at the trion resonance when the trion transition is fluctuating spectrally.

An experimental cross-correlation measurement is obtained with a total acquisition time of typically 15 minutes, much longer than the electrical fluctuations, but the electrical fluctuations are occurring at a timescale that is also much longer than the system dynamics timescales. Therefore, at intermediate timescale shorter than the spectral fluctuations, the spectral position of the quantum dot has a well-defined value of ω_{QD} , which corresponds to a well-defined anti-correlation dip $0 \leq g_{DA,\omega_{QD}}^{(2)}(0) \leq 1$, represented in dashed red lines in Fig. 5.16 (a) (also assuming perfect hole occupation probability). As expected, far-detuned from the quantum dot trion transition, the laser is not rotated and therefore the spin dependent reflected polarizations cannot be discriminated, leading to the absence of anti-correlation ($g_{DA}^{(2)}(0) = 1$). When the laser is tuned close to resonance, the spin-dependent polarization states $|\Psi_{\uparrow}\rangle$ and $|\Psi_{\downarrow}\rangle$ can be discriminated (see Fig. 5.12(e)), leading to a strong back-action (down to $g_{DA}^{(2)}(0) \approx 0.4$). The minimum value reached is not zero because the cross-correlations are measured in the "D/A" measurement basis, while, due to the cavity ellipticity the spin-dependent reflected polarizations are never diagonal nor anti-diagonal for all wavelengths, as can be seen in Fig. 5.11, thus s_{DA} never reaches 1 or -1 . Then, closer to the trion resonance, $g_{DA}^{(2)}(0)$ quickly increases and when the laser is completely in resonance, $\omega_{laser} = \omega_{QD}$, it reaches $g_{DA}^{(2)}(0) = 1$ which corresponds to not discriminated spin dependent polarizations (both are almost vertical for $\omega_{QD} = \omega_{laser}$).

Because the acquisition time of a cross-correlation measurement is much longer than the spectral wandering, the cross-correlation measurement result is an average with a given distribution $G(\omega_{QD})$ (assumed to be gaussian with a standard deviation, $\Delta\omega_{QD}$, as fitted in Fig. 5.5(b)) corresponding to all the spectral positions of the quantum dot. Therefore, the measured zero-delay cross-correlations are given by:

$$g_{DA}^{(2)}(0) = \int G(\omega_{QD}) g_{DA,\omega_{QD}}^{(2)}(0) d\omega_{QD} \quad (5.29)$$

which is represented with the black solid line in Fig. 5.16(a).

With the electric noise mechanism taken into account, the curve of the zero-delay cross-correlation as a function of the laser detuning is drastically different: it presents one single minimum at zero detuning, instead of a peak reaching $g_{DA}^{(2)}(0) = 1$. Therefore, we indeed have an anti-correlation dip in

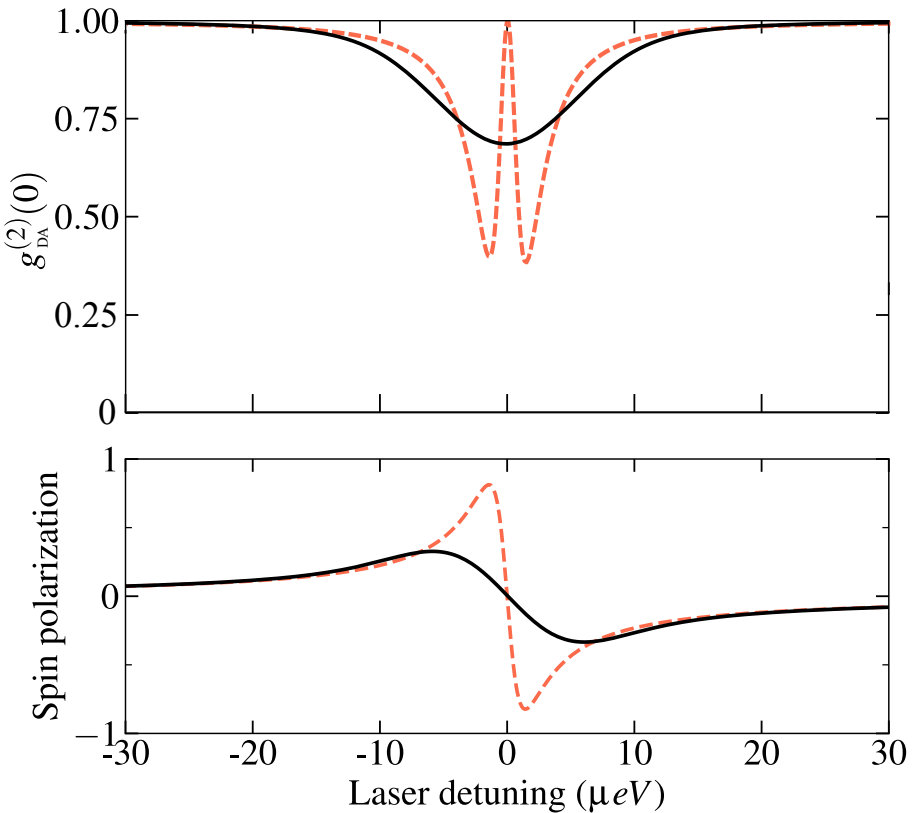


Figure 5.16: Simulated cross-correlations measurement (a) and spin polarization (b) as a function of the detuning between the trion central wavelength and the laser with imperfect hole occupation probability and spectral fluctuations (solid black curve) and in the ideal case, i. e. with 100% hole occupation probability and without incoherent processes (red dashed curve).

the theoretical predictions of the cross-correlation measurement with (in average) zero laser detuning, $\omega_{\text{laser}} = \langle \omega_{\text{QD}} \rangle$. However, the zero-delay cross-correlation expected value is 69%, much smaller than the experimentally measured value of $92 \pm 2\%$. The divergence between these two estimations is discussed in Sec. 5.4.

Influence on the measurement back action: It is also possible to study the spin polarization induced by an anti-diagonally polarized photon detection, displayed in Fig. 5.16 (b), and defined by:

$$S = \frac{P_{\uparrow\uparrow|A} - P_{\downarrow\downarrow|A}}{P_{\uparrow\uparrow|A} + P_{\downarrow\downarrow|A}} \quad (5.30)$$

Its value is zero if we have acquired no information about the spin and equal to 1 (respectively -1) if the spin is fully projected in $|\uparrow\uparrow\rangle$ (resp. $|\downarrow\downarrow\rangle$). Without spectral fluctuations, the dashed curve of Fig. 5.16 (b) shows that at resonance with the trion transition, the spin polarization is zero: the detection of an anti-diagonally-polarized photon does not project the spin in any preferred spin state. However, at timescales shorter than the spectral fluctuations (that have typical timescales above $100\mu\text{s}$ [199]), the trion resonance is well defined and can be spectrally detuned from the laser ($\omega_{\text{QD}} \neq \omega_{\text{laser}}$). When the quantum dot is detuned by a few μeV , this can constitute an efficient QND measurement of the spin, with a spin polarization that can reach $S = 0.8$, corresponding to conditional probabilities $P_{\uparrow\uparrow|A} = 90\%$

and only $P_{\downarrow|A} = 10\%$. Moreover, by choosing carefully the optimal measurement basis " $\theta/\bar{\theta}$ ", where the Stokes parameter $s_{\theta\bar{\theta}}$ is either +1 or -1, it is even possible to have a strong projective QND measurement of the spin with $P_{\uparrow|A} = 100\%$ and $P_{\downarrow|A} = 0\%$. So as predicted theoretically in Fig. 1.24(c), we have fabricated a spin-photon interface with sufficiently high top mirror coupling and cooperativity (not including spectral fluctuations), to have orthogonal spin-dependent polarizations ($\langle \Psi_{\uparrow} | \Psi_{\uparrow} \rangle = 0$, again assuming there are no spectral fluctuations), together with a reasonably high $\approx 50\%$ reflectivity.

It is therefore possible for a given QD-laser detuning to have a strong QND measurement of the spin. However, because of the spectral fluctuations, this QD-laser detuning is not controlled and at a given time, we do not know its value and therefore cannot deduce the outcome of the measurement. This is represented by the solid black curve in Fig. 5.16(b), representing the spin polarization induced by the detection of an anti-diagonally polarized photon when the spectral fluctuations are taken into account. It is similar in shape to the curve without fluctuations but its amplitude is much smaller. When the laser is in resonance with the (averaged) trion transition $\omega_{laser} = \langle \omega_{QD} \rangle$, the spin polarization is zero, showing that it is not possible to measure the spin at this energy, even though it corresponds to the maximum of anti-correlation dip. The consequence of these spectral fluctuations is therefore that the minimum of cross-correlations cannot be linked to a spin initialization anymore, contrary to what was predicted by the simple picture model presented in Sec. 5.2. Indeed, let us consider the two cases displayed for $\omega_{laser} - \omega_{QD} = \pm 1\mu\text{eV}$ in Fig. 5.14 (e). For positive or negative detuning, we indeed have different spin-dependent polarization states, that leads to anti-correlations in the cross-correlation measurement. However, the arrows representing the two spin-dependent polarization states on these two figures show that the polarization state when the spin is \uparrow at positive detuning is identical to the polarization state for spin \downarrow at negative detuning: $|\Psi_{\downarrow}(\omega_{laser} - \omega_{QD} = -1\mu\text{eV})\rangle = |\Psi_{\uparrow}(\omega_{laser} - \omega_{QD} = 1\mu\text{eV})\rangle$. Similarly, these two figures show that $|\Psi_{\downarrow}(+1\mu\text{eV})\rangle = |\Psi_{\uparrow}(-1\mu\text{eV})\rangle$. Therefore, the spin is projected into a given state in each case but because the spectral position of the trion transition at short timescale is unknown, it is not possible to know in which state it is projected. Consequently, a single-photon measurement modifies strongly the hole spin statistics at short timescales and as a result, it can be observed in the cross-correlation measurements. However, at long timescale, because of the spectral fluctuations, it is not possible to know in which state a photon measurement projects the spin at any time. Therefore, it is not possible to read out the outcome of the measurement back-action. As can be seen in Fig. 5.16 (b) however, for a suitable detuning, the detection of an anti-diagonally polarized photon with a small detuning from the trion central wavelength projects the spin. The data analysis of cross-correlation measurement with small detuning is an on-going work and is briefly discussed in the perspectives of this manuscript: it aims at the demonstration of the quantum non demolition measurement of the spin at the single-photon level, even with spectral fluctuations.

5.4 Cross-correlations under longitudinal magnetic field.

The objective of this section is to understand the magnetic field dependence of the measurement back-action that was observed in the cross-correlation measurements of Sec. 5.2.4. For different applied longitudinal magnetic fields, we observe the cross-correlations for different magnetic fields. Finally, we discuss the on-going work related to the data analysis of the results of this chapter.

5.4.1 Cross-correlations for different magnetic fields.

In Sec. 5.2.4, we have observed that the cross-correlation measurements show different anti-correlation dips at 0mT ($g_{DA}^{(2)}(0) = 92 \pm 2\%$) and at 30mT ($g_{DA}^{(2)}(0) = 80 \pm 1\%$). In this section, the cross-correlation measurement are displayed in Fig. 5.17 for different external magnetic fields. The best anti-correlations from Fig. 5.6 (obtained during another set of measurement), are also presented in blue. The behavior of the zero-delay cross-correlations with the magnetic field is the following: with increasing magnetic field, $g_{DA}^{(2)}(0)$ first decreases down to a minimum value of $\approx 86\%$ at 50mT, then it increases again with higher magnetic field. Consequently, it seems that there is experimentally an optimal magnetic field intensity in term of measurement back-action. However, as can be seen in Fig. 5.17(b), the predictions from the theoretical model does not show this minimum zero-delay cross-correlations value for an optimal magnetic field: the simulated anti-correlations are constantly decreasing with higher magnetic field, and according to the theoretical predictions, the strongest anti-correlations should be obtained at zero magnetic field. At high magnetic field, the reason why the anti-correlations should decrease with magnetic field is due to the Zeeman splitting: with increasing magnetic field, the trion transitions are more and more detuned from the laser, and as a result, their spin-dependent polarization rotation is reduced, leading to reduced anti-correlations, which is both predicted theoretically and observed experimentally in Fig. 5.17 (b). The behavior at low magnetic field is discussed in the following.

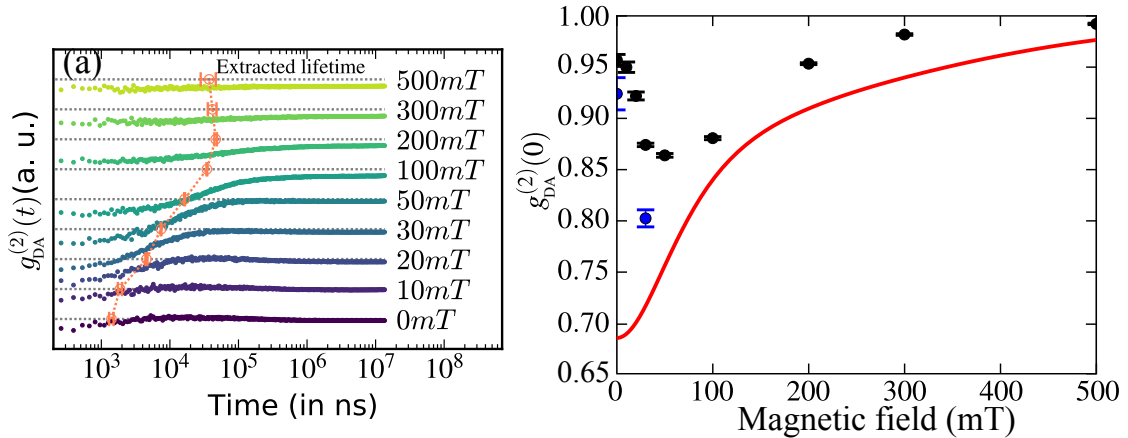


Figure 5.17: (a) Cross-correlations measurement repeated for different external magnetic fields. The extracted exponential decay timescale (corresponding to half the spin relaxation time) is plotted for each magnetic field (in coral). (b) The zero-delay cross-correlations $g_{DA}^{(2)}(0)$ as a function of the magnetic field (black points). Blue points are the best zero-delay cross-correlations values obtained from Fig. 5.6. The red curve is the simulated zero-delay cross-correlations dependence with the magnetic field. One can see that the behavior at low magnetic field is not explained by the theoretical model.

5.4.2 Carrier-spin/nuclear spins interaction at zero magnetic field.

A possible explanation for the deviation, between the experimental and expected anti-correlation dip at low magnetic field, is that a fast spin relaxation process occurs at a time shorter than the resolution of the cross-correlations measurement (which is 128ns). Such fast relaxation process

can also explain the small deviation from the exponential fit observed at zero delay in the $g_{DA}^{(2)}(t)$ curves presented in Fig. 5.6(a) and (b), where, for example at 30mT the measured zero-delay cross-correlation is $g_{DA,exp}^{(2)}(0) = 77\%$ while the fit predicts $g_{DA,fit}^{(2)}(0) = 80\%$. The spin relaxation processes are discussed in the following.

The spin evolution is indeed much more complicated than in the simple picture model where the spin relaxation was simulated by a simple exponential decay. In fact, as was discussed in Chap. 1, the hole and electron spins are deeply interacting with the $10^4 - 10^6$ quantum dot nuclear spins [70], as pictured in Fig. 1.6. The charge carrier is quickly precessing (1ns for an electron and 100ns for a hole) around the effective Overhauser field that is fluctuating at μs timescale.

Let us first consider what is happening at short timescales, for which the Overhauser field is considered random but static. Approximately one third of the time, the Overhauser field is pointing mostly in the vertical direction. In such a case, the populations of states $|\uparrow_z\rangle$ and $|\downarrow_z\rangle$, are mostly preserved, as a spin initially in state $|\uparrow_z\rangle$ will only slightly change its orientation during its precession around a mostly vertical magnetic field. However, approximately two thirds of the time, the Overhauser field is mostly in-plane, thus leading to fast precession of the spin states $|\uparrow_z\rangle$ and $|\downarrow_z\rangle$, that quickly converts the $|\uparrow_z\rangle$ state to the $|\downarrow_z\rangle$ state and vice-versa [85]. Because, the Overhauser field is random, this precession is not controlled and therefore decreases quickly the relaxation time. As a result, when no external magnetic field is applied, because the resolution of the cross-correlation measurement (128ns) is expected to be longer than the spin precession time along the Overhauser field, this effect is not resolved and induces a reduction of the anti-correlation amplitude (except one third of the time, when the Overhauser field is predominantly vertical). The situation is different in the presence of a longitudinal magnetic field ($\geq 30\text{mT}$), which forces the total field to be predominantly vertical most of the time. Therefore, this fast spin precession could explain the contrast reduced by a factor 1/3 in between the anti-correlation contrast measured at 0T, compared to that measured at 30mT.¹ It could also explain the deviation from the exponential decay towards one, observed in Fig. 5.6, as the resolution is of the same order as the expected spin-flips timescale.

In addition, the reason why the theoretical fit is always over-estimating the anti-correlation dip in comparison to experiment is not completely understood yet. This over-estimation might be due either to an over-estimation of the hole occupation probability (extracted from the fit of the reflectivity and polarization tomography curves, as discussed in Sec. 5.3.3) or to the assumption of our model that the quantum dot is only experiencing slow electric noise which is the only noise mechanism that induces an anti-correlation dip. If other noise mechanisms such as slow magnetic noise are also taken into account, it should reduce the anti-correlation estimation: realizing simulations using combinations of two noise mechanisms is still an on-going work and is not presented in this manuscript.

¹In fact, this explanation is oversimplified. In reality, we should first take into account the fact that the hole Overhauser field distribution is strongly anisotropic [82], as already discussed in Sec. 1.2.2, and is generally oriented most of the time in the vertical direction. So, most of the time the Overhauser field is oriented in the vertical direction and is not inducing spin flips onto the hole spin state, thus reducing the expected deviation from the fit and the measured anti-correlation dip at 0T. Another effect that should be taken into account is that the resonant laser can optically generate a trion that has an electron spin. This electron spin is sensitive to the nuclei via an isotropic Overhauser field that leads to much faster ($\approx 1\text{ns}$) spin precession than for the hole. Consequently, this effect should increase the deviation between the measured and simulated anti-correlation dip at 0T. In the overall, the hyperfine interaction of nuclei with the electron spin, and not with the hole spin state, might be the dominant mechanism that explains the deviation between the simulated and measured anti-correlation dips, at low magnetic fields.

5.4.3 Spin relaxation processes with external longitudinal magnetic field.

In all the cross-correlations presented in this chapter, we have focused on the anti-correlation amplitude at zero delay as it is a quantification of the measurement back-action, which is the main topic addressed in this chapter. However, the spin relaxation time is another quantity that can be extracted from such cross-correlations measurement. The cross-correlation measurements were fitted using Eq. 5.12 and the extracted spin relaxation time T_S is displayed on Fig. 5.17(a) for all magnetic fields. In these experiments, we do not focus on the fast spin relaxation time induced by a transverse Overhauser field (that cannot be resolved) but to the other spin-flip processes at $> 0.5\mu\text{s}$ timescale.

This spin relaxation time is of the order of a few μs at low magnetic field and quickly increases for a magnetic field from 0 to 100mT. Then it reaches a plateau at 100mT with a maximum spin relaxation time of $T_S = 100\mu\text{s}$. Such behavior has already been observed using spin noise spectroscopy of a single hole spin [92] even though the saturation was obtained at lower magnetic field (typically 30mT). This high spin relaxation time is similar to the state-of-the-art for a quantum dot carrier spin [16, 222, 92]. In the present case, it certainly corresponds to the hole trapping time which is the theoretically achievable upper bound for this device.

5.5 Conclusion.

In this chapter, we have demonstrated a macroscopic measurement back-action induced by a single photon on a single spin, using photon cross-correlation measurement. Using a simple model, it is possible to expect a spin projection with 72% probability after a single detected photon, significantly higher than the prior average 50% probability. Such spin projection induced by a single photon demonstrate the strong interaction obtained between a single spin and a single photon thanks to our spin-photon interface.

Such measurement back-action is based on the cavity-enhanced Kerr rotation which, given the expected top mirror output coupling and cooperativity (without spectral fluctuations) of our spin-photon interface, should provide macroscopic polarization rotation and even orthogonal spin-dependent polarization states ($\langle \Psi_{\uparrow} | \Psi_{\downarrow} \rangle = 0$), for a given laser detuning. Such orthogonally-polarized states are required for the realization of a strong Quantum Non Demolition (QND) measurement of the single spin with one single photon.

The simulations, using a realistic model of a hole spin coupled to a cavity, provides a better understanding of this phenomenon and shows the limitations to overcome to provide a controlled measurement of a single spin with a single photon, which is a crucial step toward the implementation of entanglement between a pre-existing single photon and a single spin. From another perspective, the cross-correlation measurements developed in this chapter are a promising technique for the study of spin physics and more specifically the carrier spin interaction with its nuclei.

Conclusion and Perspectives

The main objective of this work was the realization and the use of a cavity-based interface between the spin degree of freedom of a charge, confined in a quantum dot, and the polarization of a photon produced by another source. Ideally, such interface should behave as a one-dimensional atom, which means that the spin should only interact with a single external photonic channel (the cavity mode), from and into which one can efficiently collect and inject photons. Photons should therefore be efficiently injected into the cavity, optimally and coherently interact with the spin, and then be efficiently collected.

For this work, we have used quantum dots deterministically-coupled to pillar microcavities. We have first presented a polarization tomography technique to completely reconstruct the polarization state of the light reflected by the cavity-QED devices. With this technique, we have first demonstrated a near-optimal (96%) injection efficiency of photons into the pillar microcavity, together with a record measurement accuracy of the input and output couplings of the cavity mode with an external laser beam [44]. We have also completely reconstructed the macroscopic polarization rotation induced by a single quantum dot, and identified the main incoherent process that reduces the quality of the quantum dot-cavity device [176]. This result demonstrates the strong light-matter interaction in our systems, and the potential of the polarization tomography technique. However, the quantum dot state used in this result did not have a spin degree of freedom.

The deterministic assembly of a spin-photon interface and its use constituted the second part of this work. These new devices included an asymmetric tunnel barrier preventing holes to escape the quantum dot: creating an electron-hole pair, followed by the escape of the electron, could then lead to the trapping of a single hole in the quantum dot. The fabrication of these devices has benefited from the deterministic in-situ lithography technology, that deterministically couples a single quantum dot to a pillar microcavity. We improved this technique to deterministically aim at the trion transition energy, thanks to a quantum dot state identification based on its photoluminescence dependence with an external transverse magnetic field. Thanks to an optical pumping scheme, we were able to demonstrate a high occupation probability (91%) of a single hole confined in the quantum dot. Moreover, we show the interest of these devices as single-photon sources, thanks to their high output coupling (85%), allowing to efficiently collect the emitted photons. The final result of this thesis is the use of a spin-photon interface to demonstrate the macroscopic measurement back-action induced on a single spin by a single detected photon. This effect is obtained thanks to a spin-dependent polarization rotation, that is amplified to a macroscopic level in the cavity-QED device. The macroscopic measurement back-action was demonstrated with the tools of quantum optics (single photon-detectors, correlation measurements, etc) and therefore, pushes the optical spin noise spectroscopy to the quantum regime, thanks to the cavity-enhanced interaction between a single spin and the polarization of a single photon.

We present now the future developments of this work. The on-going work is dedicated to the

remaining analysis of the data presented in the previous chapter, with the objective to fully understand the noise mechanisms and the spin physics occurring in our cavity-QED device, and to demonstrate a macroscopic Quantum Non Demolition (QND) measurement [110] of a single spin with a single detected photon.

The perspectives of this work can be divided in three categories. The first axis of development of this work is to further improve the mapping of the spin qubit onto the photonic qubit, by improving the device. The QND measurement that we hope to demonstrate, has implications in the study of quantum measurements and spin physics that constitute the second axis of research. Finally, the third goal is the use of the devices presented in this work to perform and demonstrate spin-photon entanglement which can be useful for the implementation of quantum memories and quantum two-qubit gates.

On-going data analysis.

Fine understanding of the noise mechanisms and the spin physics.

We are currently working to understand and simulate better the spin physics and the noise mechanisms occurring in our spin-photon interfaces, in order to continue the data analysis presented in Chap. 5. Previously, we have constructed a model to theoretically explain the experimental reflectivity, polarization tomography and cross-correlation measurements for various external magnetic fields. We have decided first to take into account exclusively the slow electric noise to simulate the environment-induced incoherent processes. However, there are deviations between the theory and the cross-correlation measurements, in the simulated and measured zero-delay cross-correlations as a function of the magnetic field, that were presented in Fig. 5.17 (b).

This figure shows that the model fails to explain the behavior at small magnetic field and, at moderate magnetic fields, does not precisely fit the measured value of the zero-delay cross-correlations $g_{DA}^{(2)}(0)$, for values of the hole occupation probability that fit also well the reflectivity. This might be solved by fitting the data with combined noise such as slow electric and magnetic noises. Indeed, both noise types are broadening the trion linewidth but only the slow electric noise decreases the zero-delay cross-correlation value. So, it might be possible to better reproduce the zero-delay cross-correlations and, at the same time, to explain the trion linewidth broadening.

The small external magnetic field behavior of the cross-correlations has been qualitatively explained in Sec. 5.4, by a limited time resolution of the experiment that prevents from resolving the spin-flips induced by the fast precession around the Overhauser field, when the latter happens to be pointing predominantly in an in-plane direction. However, the respective roles of the spin-flips and of the electron spin-flips (in the trion states), are not completely clear. We are working to understand better this phenomenon. In addition, from the cross-correlation measurements as a function of the magnetic field presented in Fig. 5.17(a), we have extracted a characteristic exponential decay timescale for each applied longitudinal magnetic fields. We are currently investigating precisely which lifetime is measured thanks to this method, because we are wondering if it is dominated by the electron or hole spin relaxation time (T_1 , see Sec. 1.2.3 for more details). In addition, at high magnetic fields, the spin-dependent polarizations are both rotated towards the anti-diagonal polarization, as seen in Fig. 5.15. Consequently, for high longitudinal magnetic fields, the cross-correlation extracted timescales might also be sensitive to the hole trapping time, because the anti-diagonal reflected polarization is more probable when the hole is trapped than when it is not. As a result, it is not clear what can be extracted from these lifetime measurements, and we are working on it.

Quantum non demolition measurement of a single spin with a single detected photon.

In the previous chapter, we have demonstrated the macroscopic measurement back action induced by a single photon on a single spin but we have not yet demonstrated an actual measurement of the spin as the outcome is not defined. Indeed, to prove a spin measurement, we should tell in which state the spin is projected by the detection of a photon with a given polarization.

This problem is summarized in Fig. 5.16(b) which presents the spin polarization after a diagonally-polarized photon detection: when the laser is in resonance with the trion transition, the spin polarization is zero and therefore we do not acquire any information about the spin state after the detection of a diagonally-polarized photon. However, as can be seen, the spin polarization curve present two extrema for specific laser-QD detunings. When the laser is properly detuned from the central trion energy, it is possible to acquire information about the spin state: after the detection of a diagonally-polarized photon, the spin is projected more into the state $|\uparrow_z\rangle$ than in $|\downarrow_z\rangle$ ($P_{\uparrow_z|D} > 0.5$ and $P_{\downarrow_z|D} < 0.5$) for positive spin polarization and conversely for negative spin polarization. A second set of cross-correlation measurement have been taken with the laser detuned from the trion central wavelength and we are currently working to demonstrate the macroscopic QND measurement of a single spin with a single detected photon.

Improvement of the spin-photon interface.

The spin-photon interfaces presented in Chap. 4 have already been useful for the demonstration of the macroscopic measurement back action of Chap. 5 and are still under study as previously described. Other applications of these interfaces, related to quantum measurements and quantum computing, will be presented in the next sections. However, most of these applications would require (or at least benefit from) a better mapping of the spin qubit onto the photonic qubit.

In theory, it should be possible to reach an ideal spin-photon mapping, i. e. with perfect confinement of a single hole and without environment induced incoherent processes, as described in Sec. 5.3.2. In that ideal case, the measurement of a single photon should perfectly project the spin into a given state, and spin-photon entanglement with unity fidelity should be achieved. In our interfaces, such spin-photon mapping is not reached experimentally, because the hole is not confined with 100% efficiency, and because spectral fluctuations induce variations of the reflected polarizations $|\Psi_{\uparrow}\rangle$ and $|\Psi_{\downarrow}\rangle$. In this section, we propose solutions that need to be explored to overcome these limitations.

Improving the charge confinement technique.

The spectral fluctuations and imperfect hole confinement are probably induced by the quasi-resonant excitation technique used to trap a single hole in the quantum dot. Due to the quasi-resonant pumping scheme described in Sec. 4.3.2, which is necessary to obtain large occupation probabilities for the single hole state, electron-hole pairs are created near the quantum dot and modify their electrostatic environment, leading to spectral fluctuations.

An other hole trapping technique can be tried both to increase the hole occupation probability or to reduce the spectral fluctuations. One possibility is to design a sample where the doping is sufficiently close to the quantum dot, to be able to control electrically the charge state [42, 16, 18], by finely adjusting the Fermi energy close to the quantum dot charged state energy. We have not used this technique to avoid the absorption of cavity photons, as was previously discussed in Sec. 4.3.1.

Another possibility is to modify the pump laser conditions to confine the hole via resonant exciton pumping. During this work, we have empirically observed that the hole occupation probability and the spectral fluctuations depends strongly on the wavelength of the pump laser¹. Switching from non resonant (785nm) to quasi-resonant (901nm) excitation has already improved the hole occupation probability (from 65% to 91%) and has reduced the spectral fluctuations, dividing by two the trion linewidth. Therefore, by finding another wavelength to optically trap the hole, we might both reduce the spectral fluctuations and increase the hole occupation probability, as realized in *Ardelt et al.* (2015) [43] (Finley's group). Very recently, such resonant exciton scheme for the hole trapping has been realized in one of our spin-photon interface, with a CW pump laser. A quantitative analysis of the hole occupation probability, its confinement time and the trion linewidth need to be realized to determine if such resonant exciton pumping significantly improves the hole confinement and reduces the spectral fluctuations. Also, such exciton pumping can be used with short circularly-polarized pulsed excitation to not only confine the hole but also initialize its spin at the same time, as detailed in *Ardelt et al.* (2015) [43].

Active and passive control of the spectral fluctuations.

The voltage control of the electrically-contacted quantum dot can also be used to actively compensate the spectral fluctuations. *Kuhlmann et al.* (2013) [199] (Warburton's group) have shown that the magnetic and electric fluctuations are slow, with typical timescale above 100μs. This timescale is sufficiently long to actively stabilize the quantum dot fluctuations, using a technique presented in *Prechtel et al.* (2013) [223] (Warburton's group) and in *Hansom et al.* (2014) [224] where near Fourier-limited quantum dot linewidth were obtained. The active control is demanding as it requires an additional laser (intermittently switched off not to perturb the experiment), that generates cross-polarized QD resonance fluorescence that is measured in intensity. This intensity measurement is used in the feedback loop to control the applied voltage bias to the cavity-QED device, in order to fine-tune in real-time the wavelength of the trion transition. This feedback loop should stabilize the quantum dot at a fixed frequency while the QND measurement operates with another laser (or the same laser but at much lower power), slightly detuned from the quantum dot. A limitation of such active control is that it cannot compensate the imperfect hole occupation: indeed, there will be no signal to stabilize when the quantum dot is not charged with a single hole.

An easier possibility is to abandon the active control for a passive temporal post-selection of the data. The resonance fluorescence intensity, induced by the additional laser, would again be used to estimate the quantum dot-laser detuning in a given timeframe, and data would be acquired only when a sufficiently high intensity is recorded. This technique does not improve the characteristics of the spin photon interface but allows recording data associated to a fixed QD-laser detuning, and only when the hole is trapped inside the cavity. It can be a short-term option to use the spin-photon interface for various proof-of-concept experiments.

Quantum measurements of a single spin.

The measurement back-action demonstrated in the previous chapter, constitutes a tool that is analogous to the spin noise spectroscopy technique (see Sec. 1.2.4). Similarly to this technique, it relies on the Faraday/Kerr rotation and on the passive measurement of the noise of a signal. Due to the

¹For the purpose of brevity, these results are not detailed in this manuscript.

macroscopic polarization rotation induced by the spin-photon interface, the spin is extremely sensitive to a single photon measurement. Therefore, the classical technique of spin noise spectroscopy can be extended into a quantum regime thanks to the cavity-enhanced interfacing between the spin and the light probe. This platform should allow the study of the spin physics in a single quantum dot with unprecedentedly low excitation powers. We also hope to be able to monitor a single spin in real time. Finally, with increased sensitivity obtained thanks to the technique proposed in the previous sections, the QND measurement technique is well-suited to study the fundamental aspects of quantum measurements.

Study of the spin physics.

The study of the spin physics constitutes the shortest term application of this work. Indeed, the measurement of the cavity-enhanced single-photon measurement back action onto a single spin should facilitate the study of spin physics in a new regime of excitation that is orders of magnitude smaller than what is currently done. Indeed, the state-of-the-art single-spin noise spectroscopy technique requires 300 times more power with much longer integration time (two weeks) [92], while techniques based on optical destructive measurements of a spin generally require pulsed excitation with a power sufficient enough to populate a trion state [17, 97].

Such study is currently addressed by experiments that are currently prepared in the lab where the external magnetic field is either in Faraday configuration, to study the spin relaxation time T_1 or in Voigt configuration, where we can study the spin coherence T_2 .

Faraday configuration:

In addition to the finer understanding of the spin-flip time extracted from Fig. 5.17(a), as discussed above, another interesting aspect is the characterization of Overhauser field, whose intensity and fluctuation timescale can be determined. Indeed, the short timescale behavior of a correlation measurement should include a photonic response [218] and also the fast spin relaxation induced by the spin precession around the Overhauser field [30]. In the data presented in Chap. 5, the acquisition duration and the single photon detectors time resolution were not sufficient to observe these features. A longer integration time and the acquisition of superconducting detectors should be sufficient to observe and study these effects.

Voigt configuration:

In Voigt configuration, we should observe the precession of the spin at the Larmor frequency Ω of the spin state following its partial initialization (in, for example, $|\uparrow_z\rangle$) by one photon detection at $t = 0$. For an ideal spin projection in $|\uparrow_z\rangle$, this should lead to the coherent evolution $|\Psi(t)\rangle = \cos(\Omega t)|\uparrow_z\rangle + \sin(\Omega t)|\downarrow_z\rangle$ but even with a partial projection, we should be able to observe such spin precession and therefore access to the measurement of the spin coherence time T_2 . Indeed, the detection of a photon triggers the Larmor precession, which would lead to oscillations of $g_{DA}^{(2)}(t)$, with the same period, in a cross-correlation measurement, as theoretically predicted in *Smirnov et al. (2017)* [218]. In addition, this should not require any improvement of the device, as the contrast should be sufficient for observing the Larmor precession.

Quantum measurements.

The spin-photon interface provides a textbook illustration of the fundamental process of quantum measurement. In this platform, it is possible to control each individual measurement event, with the arrival time of incoming photons, and the projective strength of the QND measurement, through the detection polarization basis. Thanks to the measurement platform offered by the spin-photon interface, it should for example be possible to monitor the spin state in real-time and to study fundamental quantum measurement processes such as the measurement-induced decoherence and the quantum Zeno effect.

Real-time monitoring of a single spin:

Such spin-photon interface should allow the real-time monitoring of the spin in the Faraday configuration: the spin state is measured in real time thanks to the detection of photons. In other systems, such monitoring has already allowed the observation of quantum jumps between electronic [225], atomic [226] and light [227] states and with circuit-QED [228].

In addition to the macroscopic partially-projective or strongly-projective measurement, such monitoring requires that the spin lifetime is much longer than the integration time. Because each photon is reflected with the same polarization within the spin lifetime, by repeatedly measuring the spin state with multiple photon detections, the fidelity measurement of the spin induced by multiple photon detections should be higher than the one induced by a single photon measurement. Therefore, the spin should be measurable with ideally 100% fidelity. With the long spin relaxation time (above $50\mu s$) observed under longitudinal magnetic field (above 50mT), it should be possible to monitor the spin flips in real time, similarly to what was previously achieved in *Arnold et al. (2014)* [229], where the jumps of a single-charge into and from a defect were monitored in real-time at the μs timescale.

Measurement-induced decoherence and quantum Zeno effect:

It is also possible to study the fundamental effect of the measurement on the physical system. As said previously, with a moderate transverse magnetic field, the spin is precessing within its coherence time. Provided that we are able to perform strong 100% projective QND measurement, the spin is prepared in a pure state $|\uparrow_z\rangle$ at $t = 0$, and is coherently precessing overtime, within its coherence time: $|\Psi(t)\rangle = \cos(\Omega t) |\uparrow_z\rangle + \sin(\Omega t) |\downarrow_z\rangle$. In fact, the observation of this precession is conditioned to a very low incoming photon flux, to avoid strong perturbations induced by the measurement. There are two fundamental quantum measurement phenomena that limit the observation of these oscillations: the measurement-induced decoherence and the quantum Zeno effect.

The quantum Zeno effect is the freezing of the coherent quantum evolution of the spin by repeated projective measurements. Due to repeated photon measurements realized at a timescale much shorter than the spin precession period, the spin is constantly projected back into its initial state, such that the spin oscillations are not observed anymore: the spin stays frozen in its initial state during its coherence time. The demonstration of the quantum Zeno effect is challenging as it requires:

- to measure the spin state with pulses whose repetition period is at a timescale much shorter than the spin precession period.
- to collect nearly one photon for each pulse, because each photon strongly projects the spin state.

To do so, the setup needs to be optimized as much as possible in transmission, the photo-detectors must have a high detection efficiency and in addition, the QND spin measurement should be as projective as possible. This requires the improvements of the device described previously in this chapter.

Another fundamental aspect of measurement that can be studied with such platform is the decoherence induced by unread measurements. As discussed previously, the Larmor precession of the spin, and thus its coherence time can be observed with photon correlation measurements. By increasing the CW laser power, during a delay t between two measured detections, the system is in fact interacting with more and more photons that perform unread measurements. The unread measurements also induce a measurement back-action, but contrary to the case of the quantum Zeno effect where the spin precession is frozen, the measurement basis is not controlled and thus the measurement back-action is controlled. Consequently, the unread measurements reduce the spin coherence time by creating a new source of decoherence: the unread photons are creating irreversible leaks of quantum information in the environment. It is interesting for the field of quantum foundations as it provides a controllable experiment of how the system can be "observed" by its environment, from a purely quantum free evolution to a purely classical behavior.

Applications to quantum technologies.

Spin-photon entanglement.

Towards quantum information and quantum computing applications, the main perspective of this work is the demonstration of entanglement between a spin and a photon emitted by another source [124]. It relies on the realization of a coherent spin precession and the optimal spin dependent polarization rotation. A coherent precession $|\Psi(t)\rangle = \cos(\Omega t)|\uparrow\rangle + \sin(\Omega t)|\downarrow\rangle$ is prepared and a photon is interacting with the quantum dot spin exactly when the spin is in state $|\Psi\rangle = \frac{1}{\sqrt{2}}(|\uparrow\rangle + |\downarrow\rangle)$. The resulting spin-photon state is entangled: $|\Psi_{ent}\rangle = \frac{1}{\sqrt{2}}(|\uparrow\rangle|\Psi_{\uparrow}\rangle + |\downarrow\rangle|\Psi_{\downarrow}\rangle)$, which is maximally entangled provided that the polarization states $|\Psi_{\uparrow}\rangle$ and $|\Psi_{\downarrow}\rangle$ are orthogonal.

Contrary to previous demonstrations of spin-photon entanglement which were restricted to photons emitted by the quantum dot itself, in this scheme, the photon is emitted from another source. Therefore, it provides a novel form of entanglement which can be used for the cascaded entanglement of photons, the realization of quantum logic gates for one spin and one photon, for two spins or for two photons. Some of these applications are described below.

Generation of photonic cluster states.

It is also possible to generate multi-photon entangled states such as cluster states. Cluster states are multi-entangled states (such as $\frac{1}{4}(|D,H,D\rangle + |A,V,A\rangle)$, with $|D\rangle = \frac{1}{\sqrt{2}}(|H\rangle + |V\rangle)$ and $|A\rangle = \frac{1}{\sqrt{2}}(|H\rangle - |V\rangle)$), which have the interesting property of being maximally-entangled states that are resistant to photon losses: if a photon is lost, the remaining state is still a maximally-entangled cluster state. The realization of such multi-photon cluster state using the spin-photon interface presented in this work can follow two procedures. It is either possible to use a similar procedure as the one followed by Schwartz *et al.* (2016) [36] and generate multi-photon entangled states with photons emitted by the quantum dot. However, because the photons are entangled in polarization, it requires a technique to remove the laser signal. This can be realized thanks to resonant side excitation of the

cavity-QED device (which requires the elaboration of new samples) or generating photons via quasi-resonant excitation (with generation of a longitudinal optic or acoustic phonon, which preserves the photon coherence [212]) to spectrally filter the laser.

The second strategy to generate cluster states is based on the macroscopic spin-dependent polarization rotation:

- Streams of incoming single photons are generated by an external source, all with horizontal polarization (i. e. they are initially not entangled).
- The spin qubit is prepared in a pure quantum state (that can be induced by a 100% projective single photon QND measurement) and is coherently precessing about a transverse magnetic field.
- The single photons are successively interacting with the spin-photon interface with a period corresponding to one quarter the spin precession period.
- Provided that the spin-dependent polarizations are orthogonal ($\langle \Psi_{\uparrow} | \Psi_{\downarrow} \rangle = 0$), each reflected photon is maximally-entangled in polarization with all the previously reflected photons (and with the spin state), thus generating a linear cluster state.

Consequently, such technique can be used to generate a linear cluster state of photons. In addition, it can also be extended to the generation of two dimensional cluster states [119] which requires a second interaction between the photons and the quantum dot spin and thus, an efficient spin-photon interface that can operate as a photon receiver. Such two-dimensional cluster states are very important for the realization of a universal measurement-based quantum computer [117] and the development of optical quantum repeaters with applications to the transfer of entanglement over long distances [120].

Quantum logic gates.

Quantum information processing requires the development of quantum logic gates onto the spin and the photon. A first step is the implementation of single-qubit quantum operations on the single spin via coherent control (as discussed in Sec. 1.3.3). Such spin control is also important for the full characterization of the spin-photon entanglement as it allows the measurement of the spin state in any arbitrary measurement basis.

The second and more challenging step is the realization of two-qubit gates. The first two-qubit logic gate that can be implemented is a *SWAP* gate [13], which allows the perfect conversion of the spin state onto the photonic state and conversely: an incoming photon with polarization state $|\Psi_{in}\rangle = |H\rangle$ is reflected with output polarization $|\Psi_{out}\rangle = |V\rangle$ (as seen in Chap. 5) and this polarization conversion implies a spin flip, due to the optical selection rules (as seen in Fig. 1.4(f)). Such spin-photon *SWAP* gate is investigated experimentally in *Sun et al. (2016)*[178] (Wak's group) and will allow to use the spin as a quantum memory where the state of a photon can be stored and then recovered, with applications in quantum communications [125, 14].

A spin-photon interface can also be used to generate a $\sqrt{\text{SWAP}}$ gate [13] that is a universal quantum gate, which therefore it can be used as a universal building block of any quantum computing protocol (together with single-qubit operations). It therefore can be used for the deterministic realization of universal photon-photon gates [122] and for spin-spin gates [124]. The spin-spin entanglement is a challenging perspective as it requires not only that two trion transitions have similar

spectral profiles, both in wavelength and in linewidth, but also that the cavities are similar so they enhance the spin-dependent polarization rotation in a similar way. The spin-spin entanglement procedure can also be extended to an arbitrary number of spins using a single photon as an ancilla qubit [124].

In the overall, cavity-enhanced spin-photon interfaces thus show great promises for the implementation of building blocks for scalable quantum networks and photonic quantum computation.

Appendix A

Appendix: Initialization 3 level

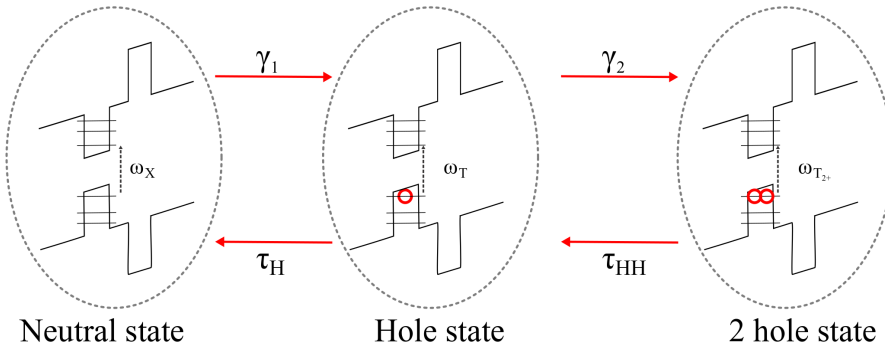


Figure A.1: Hole trapping modelization with three possible ground states. The quantum dot is assumed to be in three ground states corresponding to the neutral state (crystalline ground state), to the single-hole state (the spin is not taken into account) and to the two-hole state. A laser pumps the quantum dot to optically trap a hole in the quantum dot with a rate γ_1 . This hole is metastable but is tunneling out from the quantum dot at rate $\tau_H = 1/T_H$. From the single-hole state it is also possible to insert a second hole into the quantum dot with rate γ_1 . This second hole has a tunneling rate $\tau_{HH} = 1/T_{HH}$.

A more precise model of the single-hole trapping should take into account the possibility of trapping a second hole that makes the trion transition optically inactive. The model is presented in Fig. A.1. The rates γ_1 and γ_2 which optically traps one and two holes, depend on the resonant and non-resonant laser intensities. One can write the rate equations:

$$\begin{aligned} \frac{dP_0(t)}{dt} &= -\gamma_1 P_0(t) + \tau_H P_h(t) \\ \frac{dP_h(t)}{dt} &= \gamma_1 P_0(t) + \tau_{HH} P_{hh}(t) - (\tau_H + \gamma_2) P_h(t) \\ \frac{dP_{hh}(t)}{dt} &= \gamma_2 P_h(t) - \tau_{HH} P_{hh}(t) \end{aligned} \quad (\text{A.1})$$

With $P_0(t)$, $P_h(t)$ and $P_{hh}(t)$, the probabilities to be at time t , in the empty, one-hole and two-hole states respectively. Using the fact that $P_0(t) + P_h(t) + P_{hh}(t) = 1$ for all time, one can write:

$$\begin{aligned}\frac{dP_0(t)}{dt} &= -\gamma_1 P_0(t) + \tau_H P_h(t) \\ \frac{dP_h(t)}{dt} &= (\gamma_1 - \tau_{HH}) P_0(t) - (\tau_H + \gamma_2 + \tau_{HH}) P_h(t) + \tau_{HH}\end{aligned}\tag{A.2}$$

Which is a linear system of first order differential equations.

At equilibrium, $\frac{dP_0(t)}{dt} = \frac{dP_h(t)}{dt} = \frac{dP_{hh}(t)}{dt} = 0$ and the occupation probabilities are:

$$\begin{aligned}P_0(\infty) &= \frac{\tau_H \tau_{HH}}{D} \\ P_h(\infty) &= \frac{\gamma_1 \tau_{HH}}{D} \\ P_{hh}(\infty) &= \frac{\gamma_1 \gamma_2}{D}\end{aligned}\tag{A.3}$$

With $D = \tau_H \tau_{HH} + \gamma_1 \gamma_2 + \gamma_1 \tau_{HH}$ The negative eigenvalues of the system defines the rates:

$$\begin{aligned}\tau_1 &= +\frac{1}{2}(\tau_H + \tau_{HH} + \gamma_1 + \gamma_2) + \frac{1}{2}\sqrt{(\gamma_1 + \tau_H - \tau_{HH} - \gamma_2)^2 + 4\gamma_2 \tau_{HH}} \\ \tau_2 &= +\frac{1}{2}(\tau_H + \tau_{HH} + \gamma_1 + \gamma_2) - \frac{1}{2}\sqrt{(\gamma_1 + \tau_H - \tau_{HH} - \gamma_2)^2 + 4\gamma_2 \tau_{HH}}\end{aligned}\tag{A.4}$$

Assuming that the quantum dot cannot be populated by the two-hole state is equivalent to the two-level model discussed in Chapter 4 and should be equivalent to taking $\gamma_2 \rightarrow 0$. This is indeed the case: taking $\gamma_2 = 0$, we recover the equilibrium values of $P_0(\infty)$ and $P_h(\infty)$ of the two-level model and $P_{hh}(\infty) = 0$. The rates τ_1 is also the same as for the two-level model and $\tau_2 = \tau_{HH}$ is not relevant when the two-hole state is not populated.

The complete resolution of Eq. A.2, with a single hole trapped at time $t = 0$ as initial conditions, gives for $P_h(t)$:

$$P_h(t) = P_h(\infty) + \frac{(D - \tau_{HH} \tau_2)(\gamma_1 - \tau_1)e^{-\tau_1 t} - (D - \tau_{HH} \tau_1)(\gamma_1 - \tau_1)e^{-\tau_2 t}}{D(\tau_2 - \tau_1)}\tag{A.5}$$

Taking the evolution at short timescale $t \rightarrow 0^+$, it can be approximated by:

$$P_h(t) = 1 - (\gamma_2 + \tau_{HH})t\tag{A.6}$$

$T_S = \frac{1}{\gamma_2 + \tau_{HH}}$ is therefore the single hole trapping time, when is also taken into account the two-hole ground state. This shows that the single-hole trapping time also depends on the pump rate γ_2 that depends on the non resonant and resonant laser intensities. This therefore explains the dependences of the single-hole occupation probabilities and trapping time with the resonant and non resonant laser powers, observed in the experimental data of Figure 4.13 (c) and (d).

List of Publications

- **Boson Sampling with single-photon Fock states from a bright solid-state source.**
J. C. Loredo, M. A. Broome, P. Hilaire, O. Gazzano, I. Sagnes, A. Lemaître, M. P. Almeida, P. Senellart, A. G. White,
Physical Review Letter, 118,130503 (2016)
- **Tomography of the optical polarization rotation induced by a single quantum dot in a cavity.**
C. Antón, P. Hilaire*, C. A. Kessler, J. Demory, C. Gómez, A. Lemaître, I. Sagnes, N. D. Lanzillotti-Kimura, O. Krebs, N. Somaschi, P. Senellart, L. Lanco,*
Optica, Vol. 4, Issue 11, pp. 1326-1332 (2017)
- **Generation of non-classical light in a photon-number superposition.**
J. C. Loredo, C. Antón, B. Reznychenko, P. Hilaire, A. Harouri, C. Millet, H. Ollivier, N. Somaschi, L. De Santis, A. Lemaître, I. Sagnes, L. Lanco, A. Auffèves, O. Krebs, P. Senellart,
ArXiv:1810.05170.(2018)
- **Accurate measurement of a 96% input coupling into a cavity using polarization tomography.**
P. Hilaire, C. Antón, C. A. Kessler, A. Lemaître, I. Sagnes, N. Somaschi, P. Senellart, L. Lanco,
Appl. Phys. Lett., 112, 201101 (2018)
- **Generating multi-photon entangled states from a single deterministic single-photon source**
D. Istrati et al. in preparation.
- **Fibered semiconductor sources delivering highly indistinguishable photons beyond 4 MHz rate.**
H. Ollivier et al. in preparation.
- **Deterministic assembly of an electrically-tunable spin-photon interface based on semiconductor quantum dot.**
P. Hilaire et al. in preparation.
- **Quantum non demolition measurement of a single spin with a single photon.**
P. Hilaire et al. in preparation.

Bibliography

- [1] I. M. Georgescu, S. Ashhab, and F. Nori. “Quantum simulation”. *Reviews of Modern Physics* **86**, 153 (2014).
- [2] D. P. DiVincenzo. “The physical implementation of quantum computation”. *Fortschritte der Physik* **48**, 771–783 (2000).
- [3] H. J. Kimble. “The quantum internet”. *Nature* **453**, 1023–1030 (2008).
- [4] C. L. Degen, F. Reinhard, and P. Cappellaro. “Quantum sensing”. *Reviews of modern physics* **89**, 035002 (2017).
- [5] Q. Turchette, C. Wood, B. King, C. Myatt, D. Leibfried, W. Itano, C. Monroe, and D. Wineland. “Deterministic entanglement of two trapped ions”. *Physical Review Letters* **81**, 3631 (1998).
- [6] S. Haroche. “Nobel lecture: Controlling photons in a box and exploring the quantum to classical boundary”. *Reviews of Modern Physics* **85**, 1083 (2013).
- [7] L. Steffen, Y. Salathe, M. Oppliger, P. Kurpiers, M. Baur, C. Lang, C. Eichler, G. Puebla-Hellmann, A. Fedorov, and A. Wallraff. “Deterministic quantum teleportation with feed-forward in a solid state system”. *Nature* **500**, 319 (2013).
- [8] N. Bar-Gill, L. M. Pham, A. Jarmola, D. Budker, and R. L. Walsworth. “Solid-state electronic spin coherence time approaching one second”. *Nature communications* **4**, 1743 (2013).
- [9] D. Loss and D. P. DiVincenzo. “Quantum computation with quantum dots”. *Physical Review A* **57**, 120 (1998).
- [10] A. Imamoglu, D. D. Awschalom, G. Burkard, D. P. DiVincenzo, D. Loss, M. Sherwin, and A. Small. “Quantum information processing using quantum dot spins and cavity QED”. *Physical Review Letters* **83**, 4204–4207 (1999).
- [11] T. Jennewein, C. Simon, G. Weihs, H. Weinfurter, and A. Zeilinger. “Quantum cryprography using entangled photons”. *Physical Review Letters* **84**, 4729 (2000).
- [12] E. Knill, R. Laflamme, and G. J. Milburn. “A scheme for efficient quantum computation with linear optics”. *Nature* **409**, 46–52 (2001).
- [13] K. Koshino, S. Ishizaka, and Y. Nakamura. “Deterministic photon-photon swap gate using a λ system”. *Physical Review A* **82**, 010301 (2010).

-
- [14] N. Sangouard, C. Simon, H. De Riedmatten, and N. Gisin. “Quantum repeaters based on atomic ensembles and linear optics”. *Reviews of Modern Physics* **83**, 33 (2011).
 - [15] M. Atatüre, J. Dreiser, A. Badolato, A. Högele, K. Karrai, and A. Imamoglu. “Quantum-dot spin-state preparation with near-unity fidelity”. *Science* **312**, 551–553 (2006).
 - [16] B. D. Gerardot, D. Brunner, P. A. Dalgarno, P. Öhberg, S. Seidl, M. Kroner, K. Karrai, N. G. Stoltz, P. M. Petroff, and R. J. Warburton. “Optical pumping of a single hole spin in a quantum dot”. *Nature* **451**, 441–444 (2008).
 - [17] D. Press, K. De Greve, P. L. McMahon, T. D. Ladd, B. Friess, C. Schneider, M. Kamp, S. Höfling, A. Forchel, and Y. Yamamoto. “Ultrafast optical spin echo in a single quantum dot”. *Nature Photonics* **4**, 367–370 (2010).
 - [18] K. De Greve, P. L. McMahon, D. Press, T. D. Ladd, D. Bisping, C. Schneider, M. Kamp, L. Worschech, S. Hofling, A. Forchel, and Y. Yamamoto. “Ultrafast coherent control and suppressed nuclear feedback of a single quantum dot hole qubit”. *Nature Physics* **7**, 872–878 (2011).
 - [19] K. De Greve, L. Yu, P. L. McMahon, J. S. Pelc, C. M. Natarajan, N. Y. Kim, E. Abe, S. Maier, C. Schneider, M. Kamp, et al. “Quantum-dot spin-photon entanglement via frequency down-conversion to telecom wavelength”. *Nature* **491**, 421–425 (2012).
 - [20] W. Gao, P. Fallahi, E. Togan, J. Miguel-Sánchez, and A. Imamoglu. “Observation of entanglement between a quantum dot spin and a single photon”. *Nature* **491**, 426–430 (2012).
 - [21] J. Schaibley, A. Burgers, G. McCracken, L.-M. Duan, P. Berman, D. Steel, A. Bracker, D. Gammon, and L. Sham. “Demonstration of quantum entanglement between a single electron spin confined to an InAs quantum dot and a photon”. *Physical Review Letters* **110**, 167401 (2013).
 - [22] J. Berezovsky, M. H. Mikkelsen, O. Gywat, N. G. Stoltz, L. A. Coldren, and D. D. Awschalom. “Nondestructive optical measurements of a single electron spin in a quantum dot”. *Science* **314**, 1916–1920 (2006).
 - [23] M. Atatüre, J. Dreiser, A. Badolato, and A. Imamoglu. “Observation of faraday rotation from a single confined spin”. *Nature Physics* **3**, 101 (2007).
 - [24] A. Dousse, L. Lanco, J. Suffczyński, E. Semenova, A. Miard, A. Lemaître, I. Sagnes, C. Robin, J. Bloch, and P. Senellart. “Controlled light-matter coupling for a single quantum dot embedded in a pillar microcavity using far-field optical lithography”. *Physical Review Letters* **101**, 267404 (2008).
 - [25] O. Gazzano, S. Michaelis de Vasconcellos, C. Arnold, A. Nowak, E. Galopin, I. Sagnes, L. Lanco, A. Lemaître, and P. Senellart. “Bright solid-state sources of indistinguishable single photons”. *Nature Communications* **4**, 1425 (2013).
 - [26] N. Somaschi, V. Giesz, L. De Santis, J. C. Loredo, M. P. Almeida, G. Hornecker, S. L. Portalupi, T. Grange, C. Antón, J. Demory, C. Gómez, I. Sagnes, N. D. Lanzillotti-Kimura, A. Lemaître, A. Auffeves, A. G. White, L. Lanco, and P. Senellart. “Near-optimal single-photon sources in the solid state”. *Nature Photonics* **10**, 340–345 (2016).

-
- [27] C. Arnold, J. Demory, V. Loo, A. Lemaître, I. Sagnes, M. Glazov, O. Krebs, P. Voisin, P. Senellart, and L. Lanco. “Macroscopic rotation of photon polarization induced by a single spin”. *Nature Communications* **6**, 6236 (2015).
- [28] L. Goldstein, F. Glas, J. Marzin, M. Charasse, and G. Le Roux. “Growth by molecular beam epitaxy and characterization of InAs/GaAs strained-layer superlattices”. *Applied Physics Letters* **47**, 1099–1101 (1985).
- [29] J. Y. Marzin, J. M. Gérard, A. Izraël, D. Barrier, and G. Bastard. “Photoluminescence of single InAs quantum dots obtained by self-organized growth on GaAs”. *Physical Review Letters* **73**, 716–719 (1994).
- [30] I. Merkulov, A. L. Efros, and M. Rosen. “Electron spin relaxation by nuclei in semiconductor quantum dots”. *Physical Review B* **65**, 205309 (2002).
- [31] N. A. Sinitsyn and Y. V. Pershin. “The theory of spin noise spectroscopy: a review”. *Reports on Progress in Physics* **79**, 106501 (2016).
- [32] X. Xu, Y. Wu, B. Sun, Q. Huang, J. Cheng, D. G. Steel, A. S. Bracker, D. Gammon, C. Emery, and L. J. Sham. “Fast spin state initialization in a singly charged InAs-GaAs quantum dot by optical cooling”. *Physical Review Letters* **99**, 097401 (2007).
- [33] J. Berezovsky, M. H. Mikkelsen, N. G. Stoltz, L. A. Coldren, and D. D. Awschalom. “Picosecond coherent optical manipulation of a single electron spin in a quantum dot”. *Science* **320**, 349–352 (2008).
- [34] A. Delteil, Z. Sun, W.-b. Gao, E. Togan, S. Faelt, and A. Imamoglu. “Generation of heralded entanglement between distant hole spins”. *Nature Physics* **12**, 218–223 (2015).
- [35] R. Stockill, M. Stanley, L. Huthmacher, E. Clarke, M. Hugues, A. Miller, C. Matthiesen, C. Le Gall, and M. Atatüre. “Phase-tuned entangled state generation between distant spin qubits”. *Physical review letters* **119**, 010503 (2017).
- [36] I. Schwartz, D. Cogan, E. R. Schmidgall, Y. Don, L. Gantz, O. Kenneth, N. H. Lindner, and D. Gershoni. “Deterministic generation of a cluster state of entangled photons”. *Science* **354**, 434–437 (2016).
- [37] A. K. Nowak, S. L. Portalupi, V. Giesz, O. Gazzano, C. Dal Savio, P. F. Braun, K. Karrai, C. Arnold, L. Lanco, I. Sagnes, A. Lemaître, and P. Senellart. “Deterministic and electrically tunable bright single-photon source”. *Nat Commun* **5**, 3240 (2014).
- [38] J. Reithmaier, G. Sek, A. Löffler, C. Hofmann, S. Kuhn, S. Reitzenstein, L. Keldysh, V. Kulakovskii, T. Reinecke, and A. Forchel. “Strong coupling in a single quantum dot–semiconductor microcavity system”. *Nature* **432**, 197–200 (2004).
- [39] V. Loo, L. Lanco, A. Lemaître, I. Sagnes, O. Krebs, P. Voisin, and P. Senellart. “Quantum dot–cavity strong-coupling regime measured through coherent reflection spectroscopy in a very high-Q micropillar”. *Applied Physics Letters* **97**, 241110 (2010).

-
- [40] D. Najar, I. Söllner, P. Sekatski, V. Dolique, M. C. Löbl, D. Riedel, R. Schott, S. Starosielec, S. R. Valentin, A. D. Wieck, et al. “A gated quantum dot far in the strong-coupling regime of cavity-qed at optical frequencies”. *arXiv preprint arXiv:1812.08662* (2018).
- [41] B. Gayral, J.-M. Gérard, B. Sermage, A. Lemaitre, and C. Dupuis. “Time-resolved probing of the Purcell effect for InAs quantum boxes in GaAs microdisks”. *Applied Physics Letters* **78**, 2828–2830 (2001).
- [42] R. J. Warburton, C. Schäflein, D. Haft, F. Bickel, A. Lorke, K. Karrai, J. M. Garcia, W. Schoenfeld, and P. M. Petroff. “Optical emission from a charge-tunable quantum ring”. *Nature* **405**, 926–929 (2000).
- [43] P.-L. Ardel, T. Simmet, K. Müller, C. Dory, K. Fischer, A. Bechtold, A. Kleinkauf, H. Riedl, and J. Finley. “Controlled tunneling-induced dephasing of rabi rotations for high-fidelity hole spin initialization”. *Physical Review B* **92**, 115306 (2015).
- [44] P. Hilaire, C. Antón, C. Kessler, A. Lemaître, I. Sagnes, N. Somaschi, P. Senellart, and L. Lanço. “Accurate measurement of a 96% input coupling into a cavity using polarization tomography”. *Applied Physics Letters* **112**, 201101 (2018).
- [45] R. P. Feynman. “Simulating physics with computers”. *International journal of theoretical physics* **21**, 467–488 (1982).
- [46] J. P. Dowling and G. J. Milburn. “Quantum technology: the second quantum revolution”. *Philosophical Transactions of the Royal Society of London. Series A: Mathematical, Physical and Engineering Sciences* **361**, 1655–1674 (2003).
- [47] E. Diamanti, H.-K. Lo, B. Qi, and Z. Yuan. “Practical challenges in quantum key distribution”. *npj Quantum Information* **2**, 16025 (2016).
- [48] M. A. Nielsen and I. Chuang. “Quantum computation and quantum information”, (2002).
- [49] D. Leibfried, R. Blatt, C. Monroe, and D. Wineland. “Quantum dynamics of single trapped ions”. *Reviews of Modern Physics* **75**, 281 (2003).
- [50] H. Häffner, W. Hänsel, C. Roos, J. Benhelm, M. Chwalla, T. Körber, U. Rapol, M. Riebe, P. Schmidt, C. Becher, et al. “Scalable multiparticle entanglement of trapped ions”. *Nature* **438**, 643 (2005).
- [51] R. Barends, L. Lamata, J. Kelly, L. García-Álvarez, A. Fowler, A. Megrant, E. Jeffrey, T. White, D. Sank, J. Mutus, et al. “Digital quantum simulation of fermionic models with a superconducting circuit”. *Nature communications* **6**, 7654 (2015).
- [52] R. Ursin, F. Tiefenbacher, T. Schmitt-Manderbach, H. Weier, T. Scheidl, M. Lindenthal, B. Blauensteiner, T. Jennewein, J. Perdigues, P. Trojek, et al. “Entanglement-based quantum communication over 144 km”. *Nature physics* **3**, 481 (2007).
- [53] J. Yin, Y. Cao, Y.-H. Li, S.-K. Liao, L. Zhang, J.-G. Ren, W.-Q. Cai, W.-Y. Liu, B. Li, H. Dai, et al. “Satellite-based entanglement distribution over 1200 kilometers”. *Science* **356**, 1140–1144 (2017).

-
- [54] A. Reiserer, N. Kalb, G. Rempe, and S. Ritter. “A quantum gate between a flying optical photon and a single trapped atom”. *Nature* **508**, 237–240 (2014).
 - [55] H. De Riedmatten, M. Afzelius, M. U. Staudt, C. Simon, and N. Gisin. “A solid-state light-matter interface at the single-photon level”. *Nature* **456**, 773 (2008).
 - [56] A. Dousse, J. Suffczyński, A. Beveratos, O. Krebs, A. Lemaître, I. Sagnes, J. Bloch, P. Voisin, and P. Senellart. “Ultrabright source of entangled photon pairs”. *Nature* **466**, 217–220 (2010).
 - [57] T. D. Ladd, F. Jelezko, R. Laflamme, Y. Nakamura, C. Monroe, and J. L. O’Brien. “Quantum computers”. *Nature* **464**, 45–53 (2010).
 - [58] E. Bauer. “Phänomenologische theorie der kristallabscheidung an oberflächen. i”. *Zeitschrift für Kristallographie-Crystalline Materials* **110**, 372–394 (1958).
 - [59] D. Leonard, M. Krishnamurthy, C. Reaves, S. P. DenBaars, and P. M. Petroff. “Direct formation of quantum-sized dots from uniform coherent islands of InGaAs on GaAs surfaces”. *Applied Physics Letters* **63**, 3203–3205 (1993).
 - [60] V. Shchukin, N. N. Ledentsov, P. Kop’ev, and D. Bimberg. “Spontaneous ordering of arrays of coherent strained islands”. *Physical Review Letters* **75**, 2968 (1995).
 - [61] M. Y. Petrov, I. Ignatiev, S. Poltavtsev, A. Greilich, A. Bauschulte, D. Yakovlev, and M. Bayer. “Effect of thermal annealing on the hyperfine interaction in InAs/GaAs quantum dots”. *physical review B* **78**, 045315 (2008).
 - [62] R. C. Ashoori. “Electrons in artificial atoms”. *Nature* **379**, 413–419 (1996).
 - [63] C. Kittel, P. McEuen, and P. McEuen. *Introduction to solid state physics*, volume 8. Wiley New York, (1996).
 - [64] K. Brunner, U. Bockelmann, G. Abstreiter, M. Walther, G. Böhm, G. Tränkle, and G. Weimann. “Photoluminescence from a single GaAs/AlGaAs quantum dot”. *Physical review letters* **69**, 3216 (1992).
 - [65] E. Dekel, D. Gershoni, E. Ehrenfreund, D. Spektor, J. Garcia, and P. M. Petroff. “Multiexciton spectroscopy of a single self-assembled quantum dot”. *Physical Review Letters* **80**, 4991 (1998).
 - [66] M. Bayer, G. Ortner, O. Stern, A. Kuther, A. A. Gorbunov, A. Forchel, P. Hawrylak, S. Fafard, K. Hinzer, T. L. Reinecke, S. N. Walck, J. P. Reithmaier, F. Klopf, and F. Schäfer. “Fine structure of neutral and charged excitons in self-assembled In(Ga)As/(Al)GaAs quantum dots”. *Physical Review B* **65**, 195315 (2002).
 - [67] S. Cortez, O. Krebs, S. Laurent, M. Senes, X. Marie, P. Voisin, R. Ferreira, G. Bastard, J. Gérard, and T. Amand. “Optically driven spin memory in n-doped InAs-GaAs quantum dots”. *Physical review letters* **89**, 207401 (2002).
 - [68] A. Greilich, R. Oulton, E. A. Zhukov, I. A. Yugova, D. R. Yakovlev, M. Bayer, A. Shabaev, A. L. Efros, I. A. Merkulov, V. Stavarache, D. Reuter, and A. Wieck. “Optical control of spin coherence in singly charged (In,Ga)As/GaAs quantum dots”. *Physical Review Letters* **96**, 227401 (2006).

-
- [69] H. Drexler, D. Leonard, W. Hansen, J. Kotthaus, and P. Petroff. “Spectroscopy of quantum levels in charge-tunable InGaAs quantum dots”. *Physical Review Letters* **73**, 2252 (1994).
- [70] B. Urbaszek, X. Marie, T. Amand, O. Krebs, P. Voisin, P. Maletinsky, A. Högele, and A. Imamoglu. “Nuclear spin physics in quantum dots: An optical investigation”. *Reviews of Modern Physics* **85**, 79 (2013).
- [71] D. Krizhanovskii, A. Ebbens, A. Tartakovskii, F. Pulizzi, T. Wright, M. Skolnick, and M. Hopkinson. “Individual neutral and charged in x ga 1- x as- ga as quantum dots with strong in-plane optical anisotropy”. *Physical Review B* **72**, 161312 (2005).
- [72] R. J. Warburton. “Single spins in self-assembled quantum dots”. *Nature Materials* **12**, 483–493 (2013).
- [73] C. Testelin, F. Bernardot, B. Eble, and M. Chamarro. “Hole–spin dephasing time associated with hyperfine interaction in quantum dots”. *Physical Review B* **79**, 195440 (2009).
- [74] K. Kowalik, O. Krebs, A. Golnik, J. Suffczyński, P. Wojnar, J. Kossut, J. Gaj, and P. Voisin. “Manipulating the exciton fine structure of single cd te/ zn te quantum dots by an in-plane magnetic field”. *Physical Review B* **75**, 195340 (2007).
- [75] A. V. Khaetskii and Y. V. Nazarov. “Spin-flip transitions between zeeman sublevels in semiconductor quantum dots”. *Physical Review B* **64**, 125316 (2001).
- [76] V. I. Fal’ko, B. Altshuler, and O. Tsyplyatyev. “Anisotropy of spin splitting and spin relaxation in lateral quantum dots”. *Physical review letters* **95**, 076603 (2005).
- [77] B. Eble, C. Testelin, P. Desfonds, F. Bernardot, A. Balocchi, T. Amand, A. Miard, A. Lemaître, X. Marie, and M. Chamarro. “Hole–nuclear spin interaction in quantum dots”. *Physical Review Letters* **102**, 146601 (2009).
- [78] N. Sinitsyn, Y. Li, S. Crooker, A. Saxena, and D. Smith. “Role of nuclear quadrupole coupling on decoherence and relaxation of central spins in quantum dots”. *Physical review letters* **109**, 166605 (2012).
- [79] M. Gaudin. “Diagonalisation d’une classe d’hamiltoniens de spin”. *Journal de Physique* **37**, 1087–1098 (1976).
- [80] G. Chen, D. L. Bergman, and L. Balents. “Semiclassical dynamics and long-time asymptotics of the central-spin problem in a quantum dot”. *Physical Review B* **76**, 045312 (2007).
- [81] E. Barnes, Ł. Cywiński, and S. D. Sarma. “Nonperturbative master equation solution of central spin dephasing dynamics”. *Physical review letters* **109**, 140403 (2012).
- [82] J. H. Prechtel, A. V. Kuhlmann, J. Houel, A. Ludwig, S. R. Valentin, A. D. Wieck, and R. J. Warburton. “Decoupling a hole spin qubit from the nuclear spins”. *Nature Materials* **15**, 981–986 (2016).
- [83] S. Crooker, J. Brandt, C. Sandfort, A. Greilich, D. Yakovlev, D. Reuter, A. Wieck, and M. Bayer. “Spin noise of electrons and holes in self-assembled quantum dots”. *Physical Review Letters* **104**, 036601 (2010).

-
- [84] P.-F. Braun, X. Marie, L. Lombez, B. Urbaszek, T. Amand, P. Renucci, V. Kalevich, K. Kavokin, O. Krebs, P. Voisin, et al. “Direct observation of the electron spin relaxation induced by nuclei in quantum dots”. *Physical Review Letters* **94**, 116601 (2005).
- [85] D. Brunner, B. D. Gerardot, P. A. Dalgarno, G. Wüst, K. Karrai, N. G. Stoltz, P. M. Petroff, and R. J. Warburton. “A coherent single-hole spin in a semiconductor”. *Science* **325**, 70–72 (2009).
- [86] A. G. Redfield. “On the theory of relaxation processes”. *IBM Journal of Research and Development* **1**, 19–31 (1957).
- [87] H. M. Wiseman and G. J. Milburn. *Quantum measurement and control*. Cambridge university press, (2009).
- [88] M. Glazov and E. Ivchenko. “Spin noise in quantum dot ensembles”. *Physical Review B* **86**, 115308 (2012).
- [89] R. Dahbashi, J. Hübner, F. Berski, J. Wiegand, X. Marie, K. Pierz, H. Schumacher, and M. Oestreich. “Measurement of heavy-hole spin dephasing in (inga) as quantum dots”. *Applied Physics Letters* **100**, 031906 (2012).
- [90] S. Crooker, D. Rickel, A. Balatsky, and D. Smith. “Spectroscopy of spontaneous spin noise as a probe of spin dynamics and magnetic resonance”. *Nature* **431**, 49 (2004).
- [91] M. Oestreich, M. Römer, R. J. Haug, and D. Hägele. “Spin noise spectroscopy in GaAs”. *Physical review letters* **95**, 216603 (2005).
- [92] R. Dahbashi, J. Hübner, F. Berski, K. Pierz, and M. Oestreich. “Optical spin noise of a single hole spin localized in an (inga) as quantum dot”. *Physical review letters* **112**, 156601 (2014).
- [93] V. S. Zapasskii. “Spin-noise spectroscopy: from proof of principle to applications”. *Advances in Optics and Photonics* **5**, 131–168 (2013).
- [94] E. Kawakami, P. Scarlino, D. R. Ward, F. Braakman, D. Savage, M. Lagally, M. Friesen, S. N. Coppersmith, M. A. Eriksson, and L. Vandersypen. “Electrical control of a long-lived spin qubit in a si/sige quantum dot”. *Nature nanotechnology* **9**, 666 (2014).
- [95] T. Watson, S. Philips, E. Kawakami, D. Ward, P. Scarlino, M. Veldhorst, D. Savage, M. Lagally, M. Friesen, S. Coppersmith, et al. “A programmable two-qubit quantum processor in silicon”. *Nature* **555**, 633 (2018).
- [96] J. R. Petta, A. C. Johnson, J. M. Taylor, E. A. Laird, A. Yacoby, M. D. Lukin, C. M. Marcus, M. P. Hanson, and A. C. Gossard. “Coherent manipulation of coupled electron spins in semiconductor quantum dots”. *Science* **309**, 2180–2184 (2005).
- [97] A. Bechtold, D. Rauch, F. Li, T. Simmet, P.-L. Ardel, A. Regler, K. Müller, N. A. Sinitsyn, and J. J. Finley. “Three-stage decoherence dynamics of an electron spin qubit in an optically active quantum dot”. *Nature Physics* **11**, 1005 (2015).
- [98] X. J. Wang, S. Chesi, and W. A. Coish. “Spin-echo dynamics of a heavy hole in a quantum dot”. *Phys. Rev. Lett.* **109**, 237601 (2012).

-
- [99] A. S. Bracker, E. A. Stinaff, D. Gammon, M. E. Ware, J. G. Tischler, A. Shabaev, A. L. Efros, D. Park, D. Gershoni, V. L. Korenev, and I. A. Merkulov. “Optical pumping of the electronic and nuclear spin of single charge-tunable quantum dots”. *Physical Review Letters* **94**, 047402 (2005).
- [100] B. Urbaszek, P.-F. Braun, T. Amand, O. Krebs, T. Belhadj, A. Lemaître, P. Voisin, and X. Marie. “Efficient dynamical nuclear polarization in quantum dots: Temperature dependence”. *Physical Review B* **76**, 201301 (2007).
- [101] E. Chekhovich, M. Makhonin, K. Kavokin, A. Krysa, M. Skolnick, and A. Tartakovskii. “Pumping of nuclear spins by optical excitation of spin-forbidden transitions in a quantum dot”. *Physical review letters* **104**, 066804 (2010).
- [102] E. Chekhovich, M. Makhonin, A. Tartakovskii, A. Yacoby, H. Bluhm, K. Nowack, and L. Vandersypen. “Nuclear spin effects in semiconductor quantum dots”. *Nature materials* **12**, 494 (2013).
- [103] P. Simon, B. Braunecker, and D. Loss. “Magnetic ordering of nuclear spins in an interacting two-dimensional electron gas”. *Physical Review B* **77**, 045108 (2008).
- [104] G. Éthier-Majcher, D. Gangloff, R. Stockill, E. Clarke, M. Hugues, C. Le Gall, and M. Atatüre. “Improving a solid-state qubit through an engineered mesoscopic environment”. *Physical review letters* **119**, 130503 (2017).
- [105] D. Gangloff, G. Éthier-Majcher, C. Lang, E. Denning, J. Bodey, D. Jackson, E. Clarke, M. Hugues, C. Le Gall, and M. Atatüre. “Quantum interface of an electron and a nuclear ensemble”. *Science*, eaaw2906 (2019).
- [106] D. Press, T. Ladd, B. Zhang, and Y. Yamamoto. “Complete quantum control of a single quantum dot spin using ultrafast optical pulses”. *Nature* **456**, 218–221 (2008).
- [107] M. Kroner, K. M. Weiss, B. Biedermann, S. Seidl, S. Manus, A. W. Holleitner, A. Badolato, P. M. Petroff, B. D. Gerardot, R. J. Warburton, and K. Karrai. “Optical detection of single-electron spin resonance in a quantum dot”. *Physical Review Letters* **100**, 156803 (2008).
- [108] A. Greilich, S. G. Carter, D. Kim, A. S. Bracker, and D. Gammon. “Optical control of one and two hole spins in interacting quantum dots”. *Nature Photonics* **5**, 702–708 (2011).
- [109] V. B. Braginsky, Y. I. Vorontsov, and K. S. Thorne. “Quantum nondemolition measurements”. *Science* **209**, 547–557 (1980).
- [110] P. Grangier, J. A. Levenson, and J.-P. Poizat. “Quantum non-demolition measurements in optics”. *Nature* **396**, 537–542 (1998).
- [111] Y. Takahashi, K. Honda, N. Tanaka, K. Toyoda, K. Ishikawa, and T. Yabuzaki. “Quantum nondemolition measurement of spin via the paramagnetic faraday rotation”. *Physical Review A* **60**, 4974 (1999).
- [112] A. N. Vamivakas, C.-Y. Lu, C. Matthiesen, Y. Zhao, S. Fält, A. Badolato, and M. Atatüre. “Observation of spin-dependent quantum jumps via quantum dot resonance fluorescence”. *Nature* **467**, 297 (2010).

-
- [113] K. De Greve, P. L. McMahon, L. Yu, J. S. Pelc, C. Jones, C. M. Natarajan, N. Y. Kim, E. Abe, S. Maier, C. Schneider, et al. “Complete tomography of a high-fidelity solid-state entangled spin–photon qubit pair”. *Nature communications* **4** (2013).
 - [114] N. H. Lindner and T. Rudolph. “Proposal for pulsed on-demand sources of photonic cluster state strings”. *Physical Review Letters* **103**, 113602 (2009).
 - [115] R. Raussendorf and H. J. Briegel. “A one-way quantum computer”. *Physical Review Letters* **86**, 5188 (2001).
 - [116] R. Raussendorf, D. E. Browne, and H. J. Briegel. “Measurement-based quantum computation on cluster states”. *Physical review A* **68**, 022312 (2003).
 - [117] H. J. Briegel, D. E. Browne, W. Dür, R. Raussendorf, and M. Van den Nest. “Measurement-based quantum computation”. *Nature Physics* **5**, 19 (2009).
 - [118] K. Azuma, K. Tamaki, and H.-K. Lo. “All-photonic quantum repeaters”. *Nature communications* **6**, 6787 (2015).
 - [119] H. Pichler, S. Choi, P. Zoller, and M. D. Lukin. “Universal photonic quantum computation via time-delayed feedback”. *Proceedings of the National Academy of Sciences* **114**, 11362–11367 (2017).
 - [120] D. Buterakos, E. Barnes, and S. E. Economou. “Deterministic generation of all-photonic quantum repeaters from solid-state emitters”. *Physical Review X* **7**, 041023 (2017).
 - [121] C. Cabrillo, J. Cirac, P. Garcia-Fernandez, and P. Zoller. “Creation of entangled states of distant atoms by interference”. *Physical Review A* **59**, 1025 (1999).
 - [122] S. Rosenblum, S. Parkins, and B. Dayan. “Photon routing in cavity QED: Beyond the fundamental limit of photon blockade”. *Physical Review A* **84**, 033854 (2011).
 - [123] C. Y. Hu, W. J. Munro, and J. G. Rarity. “Deterministic photon entangler using a charged quantum dot inside a microcavity”. *Physical Review B (Condensed Matter and Materials Physics)* **78**, 125318 (2008).
 - [124] C. Y. Hu, A. Young, J. L. O’Brien, W. J. Munro, and J. G. Rarity. “Giant optical Faraday rotation induced by a single-electron spin in a quantum dot: Applications to entangling remote spins via a single photon”. *Physical Review B* **78**, 085307 (2008).
 - [125] C. Hu and J. Rarity. “Loss-resistant state teleportation and entanglement swapping using a quantum-dot spin in an optical microcavity”. *Physical Review B* **83**, 115303 (2011).
 - [126] C. Y. Hu, W. J. Munro, J. L. O’Brien, and J. G. Rarity. “Proposed entanglement beam splitter using a quantum-dot spin in a double-sided optical microcavity”. *Physical Review B* **80**, 205326 (2009).
 - [127] J. M. Gérard, B. Sermage, B. Gayral, B. Legrand, E. Costard, and V. Thierry-Mieg. “Enhanced spontaneous emission by quantum boxes in a monolithic optical microcavity”. *Physical Review Letters* **81**, 1110–1113 (1998).

-
- [128] E. M. Purcell. “Spontaneous emission probabilities at radio frequencies”. *Physical Review* **69**, 681 (1946).
 - [129] P. Goy, J. M. Raimond, M. Gross, and S. Haroche. “Observation of cavity-enhanced single-atom spontaneous emission”. *Physical Review Letters* **50**, 1903–1906 (1983).
 - [130] K. J. Vahala. “Optical microcavities”. *Nature* **424**, 839–846 (2003).
 - [131] O. Painter, R. K. Lee, A. Scherer, A. Yariv, J. D. O’Brien, P. D. Dapkus, and I. Kim. “Two-Dimensional Photonic Band-Gap Defect Mode Laser”. *Science* **284** (1999).
 - [132] Y. Akahane, T. Asano, B.-S. Song, and S. Noda. “High-Q photonic nanocavity in a two-dimensional photonic crystal”. *Nature* **425**, 944–947 (2003).
 - [133] D. Englund, D. Fattal, E. Waks, G. Solomon, B. Zhang, T. Nakaoka, Y. Arakawa, Y. Yamamoto, and J. Vučković. “Controlling the spontaneous emission rate of single quantum dots in a two-dimensional photonic crystal”. *Physical Review Letters* **95**, 013904 (2005).
 - [134] T. Yoshie, A. Scherer, J. Hendrickson, G. Khitrova, H. Gibbs, G. Rupper, C. Ell, O. Shchekin, and D. Deppe. “Vacuum Rabi splitting with a single quantum dot in a photonic crystal nanocavity”. *Nature* **432**, 200 (2004).
 - [135] S. McCall, A. Levi, R. Slusher, S. Pearton, and R. Logan. “Whispering-gallery mode microdisk lasers”. *Applied Physics Letters* **60**, 289–291 (1992).
 - [136] P. Michler, A. Kiraz, C. Becher, W. V. Schoenfeld, P. M. Petroff, L. Zhang, E. Hu, and A. Imamoglu. “A Quantum Dot Single-Photon Turnstile Device”. *Science* **290**, 2282–2285 (2000).
 - [137] B. Gayral, J. M. Gérard, A. Lemaître, C. Dupuis, L. Manin, and J. L. Pelouard. “High-Q wet-etched GaAs microdisks containing InAs quantum boxes”. *Applied Physics Letters* (1999).
 - [138] B. E. Saleh, M. C. Teich, and B. E. Saleh. *Fundamentals of photonics*, volume 22. Wiley New York, (1991).
 - [139] M. Pelton, C. Santori, J. Vučković, B. Zhang, G. S. Solomon, J. Plant, and Y. Yamamoto. “Efficient source of single photons: A single quantum dot in a micropost microcavity”. *Physical Review Letters* **89**, 233602 (2002).
 - [140] S. Reitzenstein, A. Bazhenov, A. Gorbunov, C. Hofmann, S. Münch, A. Löffler, M. Kamp, J. P. Reithmaier, V. D. Kulakovskii, and A. Forchel. “Lasing in high-Q quantum-dot micropillar cavities”. *Applied Physics Letters* **89**, 051107 (2006).
 - [141] C. Arnold, V. Loo, A. Lemaître, I. Sagnes, O. Krebs, P. Voisin, P. Senellart, and L. Lanço. “Optical bistability in a quantum dots/micropillar device with a quality factor exceeding 200 000”. *Applied Physics Letters* **100** (2012).
 - [142] J. Wiersig and M. Hentschel. “Unidirectional light emission from high- Q modes in optical microcavities”. *Physical Review A* **73**, 031802 (2006).

-
- [143] T. Gutbrod, M. Bayer, A. Forchel, J. Reithmaier, T. Reinecke, S. Rudin, and P. Knipp. “Weak and strong coupling of photons and excitons in photonic dots”. *Physical Review B* **57**, 9950 (1998).
 - [144] D. Bajoni, P. Senellart, E. Wertz, I. Sagnes, A. Miard, A. Lemaître, and J. Bloch. “Polariton laser using single micropillar GaAs- GaAlAs semiconductor cavities”. *Physical Review Letters* **100**, 047401 (2008).
 - [145] A. Fainstein, N. D. Lanzillotti-Kimura, B. Jusserand, and B. Perrin. “Strong Optical-Mechanical Coupling in a Vertical GaAs/AlAs Microcavity for Subterahertz Phonons and Near-Infrared Light”. *Physical Review Letters* **110**, 037403 (2013).
 - [146] S. Anguiano, A. Bruchhausen, B. Jusserand, I. Favero, F. Lamberti, L. Lanco, I. Sagnes, A. Lemaître, N. Lanzillotti-Kimura, P. Senellart, and A. Fainstein. “Micropillar Resonators for Optomechanics in the Extremely High 19–95-GHz Frequency Range”. *Physical Review Letters* **118**, 263901 (2017).
 - [147] M. E. Reimer, G. Bulgarini, N. Akopian, M. Hocevar, M. B. Bavinck, M. A. Verheijen, E. P. A. M. Bakkers, L. P. Kouwenhoven, and V. Zwiller. “Bright single-photon sources in bottom-up tailored nanowires”. *Nature Communications* **3** (2012).
 - [148] C. Schneider, T. Heindel, A. Huggenberger, T. Niederstrasser, S. Reitzenstein, A. Forchel, S. Höfling, and M. Kamp. “Microcavity enhanced single photon emission from an electrically driven site-controlled quantum dot”. *Applied Physics Letters* **100**, 091108 (2012).
 - [149] C. Schneider, A. Huggenberger, T. Sünder, T. Heindel, M. Strauß, S. Göpfert, P. Weinmann, S. Reitzenstein, L. Worschech, M. Kamp, et al. “Single site-controlled In (Ga) As/GaAs quantum dots: growth, properties and device integration”. *Nanotechnology* **20**, 434012 (2009).
 - [150] E. T. Jaynes and F. W. Cummings. “Comparison of quantum and semiclassical radiation theories with application to the beam maser”. *Proceedings of the IEEE* **51**, 89–109 (1963).
 - [151] H. Carmichael. “An open system approach to quantum optics, vol. m 18 of lecture notes in physics”, (1993).
 - [152] C. Cohen-Tannoudji, J. Dupont-Roc, and G. Grynberg. *Atom-Photon Interactions: Basic Processes and Applications*. A Wiley-Interscience publication. Wiley, (1998).
 - [153] E. Peter, P. Senellart, D. Martrou, A. Lemaître, J. Hours, J. M. Gérard, and J. Bloch. “Exciton-photon strong-coupling regime for a single quantum dot embedded in a microcavity”. *Physical Review Letters* **95**, 067401 (2005).
 - [154] Q. A. Turchette, C. J. Hood, W. Lange, H. Mabuchi, and H. J. Kimble. “Measurement of conditional phase shifts for quantum logic”. *Physical Review Letters* **75**, 4710–4713 (1995).
 - [155] D. Valente, Y. Li, J.-P. Poizat, J.-M. Gérard, L. Kwek, M. Santos, and A. Auffèves. “Universal optimal broadband photon cloning and entanglement creation in one-dimensional atoms”. *Physical Review A* **86**, 022333 (2012).

-
- [156] A. Predojević and M. W. Mitchell. *Engineering the Atom-Photon Interaction: Controlling Fundamental Processes with Photons, Atoms and Solids*. Springer International Publishing, (2015).
 - [157] M. Varnava, D. E. Browne, and T. Rudolph. “How good must single photon sources and detectors be for efficient linear optical quantum computation?”. *Physical Review Letters* **100**, 060502 (2008).
 - [158] R. J. Glauber. “The quantum theory of optical coherence”. *Physical Review* **130**, 2529 (1963).
 - [159] L. Hanschke, K. A. Fischer, S. Appel, D. Lukin, J. Wierzbowski, S. Sun, R. Trivedi, J. Vučković, J. J. Finley, and K. Müller. “Quantum dot single-photon sources with ultra-low multi-photon probability”. *npj Quantum Information* **4**, 43 (2018).
 - [160] M. Gschrey, A. Thoma, P. Schnauber, M. Seifried, R. Schmidt, B. Wohlfeil, L. Krüger, J.-H. Schulze, T. Heindel, S. Burger, et al. “Highly indistinguishable photons from deterministic quantum-dot microlenses utilizing three-dimensional in situ electron-beam lithography”. *Nature communications* **6**, 7662 (2015).
 - [161] Y.-M. He, Y. He, Y.-J. Wei, D. Wu, M. Atature, C. Schneider, S. Hofling, M. Kamp, C.-Y. Lu, and J.-W. Pan. “On-demand semiconductor single-photon source with near-unity indistinguishability”. *Nature Nanotechnology* **8**, 213–217 (2013).
 - [162] X. Ding, Y. He, Z.-C. Duan, N. Gregersen, M.-C. Chen, S. Unsleber, S. Maier, C. Schneider, M. Kamp, S. Höfling, C.-Y. Lu, and J.-W. Pan. “On-demand single photons with high extraction efficiency and near-unity indistinguishability from a resonantly driven quantum dot in a micropillar”. *Physical Review Letters* **116**, 020401 (2016).
 - [163] H. S. Nguyen, G. Sallen, C. Voisin, P. Roussignol, C. Diederichs, and G. Cassabois. “Ultra-coherent single photon source”. *Applied Physics Letters* **99**, 261904 (2011).
 - [164] C. Matthiesen, A. N. Vamivakas, and M. Atatüre. “Subnatural linewidth single photons from a quantum dot”. *Physical Review Letters* **108**, 093602 (2012).
 - [165] D. J. P. Ellis, A. J. Bennett, S. J. Dewhurst, C. A. Nicoll, D. A. Ritchie, and A. J. Shields. “Cavity-enhanced radiative emission rate in a single-photon-emitting diode operating at 0.5 GHz”. *New Journal of Physics* **10** (2008).
 - [166] S. Ates, S. M. Ulrich, S. Reitzenstein, A. Löffler, A. Forchel, and P. Michler. “Post-selected indistinguishable photons from the resonance fluorescence of a single quantum dot in a microcavity”. *Physical Review Letters* **103**, 167402 (2009).
 - [167] P. Senellart, G. Solomon, and A. White. “High-performance semiconductor quantum-dot single-photon sources”. *Nature nanotechnology* **12**, 1026 (2017).
 - [168] J.-T. Shen and S. Fan. “Coherent single photon transport in a one-dimensional waveguide coupled with superconducting quantum bits”. *Physical Review Letters* **95**, 213001 (2005).
 - [169] A. Stute, B. Casabone, B. Brandstatter, K. Fribe, T. E. Northup, and R. Blatt. “Quantum-state transfer from an ion to a photon”. *Nature Photonics* **7**, 219–222 (2013).

-
- [170] I. Shomroni, S. Rosenblum, Y. Lovsky, O. Bechler, G. Guendelman, and B. Dayan. “All-optical routing of single photons by a one-atom switch controlled by a single photon”. *Science* **345**, 903–906 (2014).
- [171] V. Loo, C. Arnold, O. Gazzano, A. Lemaitre, I. Sagnes, O. Krebs, P. Voisin, P. Senellart, and L. Lanco. “Optical nonlinearity for few-photon pulses on a quantum dot-pillar cavity device”. *Physical Review Letters* **109**, 166806 (2012).
- [172] V. Giesz, N. Somaschi, G. Hornecker, T. Grange, B. Reznychenko, L. De Santis, J. Demory, C. Gomez, I. Sagnes, A. Lemaître, et al. “Coherent manipulation of a solid-state artificial atom with few photons”. *Nature Communications* **7**, 11986 (2016).
- [173] L. de Santis, C. Antón, B. Reznychenko, N. Somaschi, G. Coppola, J. Senellart, C. Gómez, A. Lemaître, I. Sagnes, A. G. White, L. Lanco, A. Auffeves, and P. Senellart. “A solid-state single-photon filter”. *Nature Nanotechnology, Advanced Online Publication* (2017).
- [174] D. Englund, A. Faraon, I. Fushman, N. Stoltz, P. Petroff, and J. Vučković. “Controlling cavity reflectivity with a single quantum dot”. *Nature* **450**, 857–861 (2007).
- [175] K. Srinivasan, C. P. Michael, R. Perahia, and O. Painter. “Investigations of a coherently driven semiconductor optical cavity QED system”. *Physical Review A* **78**, 033839 (2008).
- [176] C. Antón, P. Hilaire, C. A. Kessler, J. Demory, C. Gómez, A. Lemaître, I. Sagnes, N. D. Lanzillotti-Kimura, O. Krebs, N. Somaschi, et al. “Tomography of the optical polarization rotation induced by a single quantum dot in a cavity”. *Optica* **4**, 1326–1332 (2017).
- [177] A. B. Young, R. Oulton, C. Y. Hu, A. C. T. Thijssen, C. Schneider, S. Reitzenstein, M. Kamp, S. Höfling, L. Worschech, A. Forchel, and J. G. Rarity. “Quantum-dot-induced phase shift in a pillar microcavity”. *Physical Review A* **84**, 011803 (2011).
- [178] S. Sun, H. Kim, G. S. Solomon, and E. Waks. “A quantum phase switch between a single solid-state spin and a photon”. *Nature Nanotechnology* **11**, 539–544 (2016).
- [179] P. Androvitsaneas, A. B. Young, C. Schneider, S. Maier, M. Kamp, S. Höfling, S. Knauer, E. Harbord, C. Y. Hu, J. G. Rarity, and R. Oulton. “Charged quantum dot micropillar system for deterministic light-matter interactions”. *Physical Review B* **93**, 241409 (2016).
- [180] N. Stoltz, M. Rakher, S. Strauf, A. Badolato, D. Lofgreen, P. Petroff, L. Coldren, and D. Bouwmeester. “High-quality factor optical microcavities using oxide apertured micropillars”. *Applied Physics Letters* **87**, 031105 (2005).
- [181] S. Michaelis de Vasconcellos, A. Calvar, A. Dousse, J. Suffczyński, N. Dupuis, A. Lemaître, I. Sagnes, J. Bloch, P. Voisin, and P. Senellart. “Spatial, spectral, and polarization properties of coupled micropillar cavities”. *Applied Physics Letters* **99**, 101103 (2011).
- [182] M. P. Bakker, H. Snijders, W. Löffler, A. V. Barve, L. A. Coldren, D. Bouwmeester, and M. P. van Exter. “Homodyne detection of coherence and phase shift of a quantum dot in a cavity”. *Opt. Lett.* **40**, 3173–3176 (2015).

-
- [183] J. Loredo, M. Broome, P. Hilaire, O. Gazzano, I. Sagnes, A. Lemaitre, M. Almeida, P. Senellart, and A. White. “Boson sampling with single-photon fock states from a bright solid-state source”. *Physical Review Letters* **118**, 130503 (2017).
 - [184] H. Wang, Y. He, Y.-H. Li, Z.-E. Su, B. Li, H.-L. Huang, X. Ding, M.-C. Chen, C. Liu, J. Qin, et al. “High-efficiency multiphoton boson sampling”. *Nature Photonics* **11**, 361 (2017).
 - [185] C. W. Gardiner and M. J. Collett. “Input and output in damped quantum systems: Quantum stochastic differential equations and the master equation”. *Physical Review A* **31**, 3761–3774 (1985).
 - [186] D. F. Walls and G. J. Milburn. *Quantum Optics*. Springer Berlin Heidelberg, (2008).
 - [187] A. Auffèves, B. Besga, J.-M. Gérard, and J.-P. Poizat. “Spontaneous emission spectrum of a two-level atom in a very-high-Q cavity”. *Physical Review A (Atomic, Molecular, and Optical Physics)* **77**, 063833 (2008).
 - [188] J. Demory. *Initialisation de spin et rotation de polarisation Dans une boîte quantique en microcavité*. PhD thesis, Université Paris-Saclay, (2016).
 - [189] H. Snijders, J. Frey, J. Norman, M. Bakker, E. Langman, A. Gossard, J. Bowers, M. Van Exter, D. Bouwmeester, and W. Löfller. “Purification of a single-photon nonlinearity”. *Nature communications* **7**, 12578 (2016).
 - [190] J. Loredo, C. Antón, B. Reznychenko, P. Hilaire, A. Harouri, C. Millet, H. Ollivier, N. Somaschi, L. De Santis, A. Lemaître, et al. “Generation of non-classical light in a photon-number superposition”. *arXiv preprint arXiv:1810.05170* (2018).
 - [191] C. Bonato, F. Haupt, S. S. R. Oemrawsingh, J. Gudat, D. Ding, M. P. van Exter, and D. Bouwmeester. “CNOT and Bell-state analysis in the weak-coupling cavity QED regime”. *Physical Review Letters* **104**, 160503 (2010).
 - [192] D. S. Smirnov, M. M. Glazov, E. L. Ivchenko, and L. Lanco. “Theory of optical spin control in quantum dot microcavities”. *Phys. Rev. B* **92**, 115305 (2015).
 - [193] M. P. Bakker, H. Snijders, W. Löfller, A. V. Barve, L. A. Coldren, D. Bouwmeester, and M. P. van Exter. “Homodyne detection of coherence and phase shift of a quantum dot in a cavity”. *Opt. Lett.* **40**, 3173–3176 (2015).
 - [194] A. J. Bennett, J. P. Lee, D. J. P. Ellis, T. Meany, E. Murray, F. F. Floether, J. P. Griffiths, I. Farrer, D. A. Ritchie, and A. J. Shields. “Cavity-enhanced coherent light scattering from a quantum dot”. *Science Advances* **2**, e1501256 (2016).
 - [195] G. Lindblad. “On the generators of quantum dynamical semigroups”. *Communications in Mathematical Physics* **48**, 119–130 (1976).
 - [196] C. Gardiner and P. Zoller. *Quantum noise: a handbook of Markovian and non-Markovian quantum stochastic methods with applications to quantum optics*, volume 56. Springer Science & Business Media, (2004).

-
- [197] H. J. Carmichael and M. O. Scully. “Statistical methods in quantum optics 1: Master equations and Fokker-Planck equations”. *Physics Today* **53**, 78–80 (2007).
 - [198] G. Pfanner, M. Seliger, and U. Hohenester. “Entangled photon sources based on semiconductor quantum dots: the role of pure dephasing”. *Physical Review B* **78**, 195410 (2008).
 - [199] A. V. Kuhlmann, J. Houel, A. Ludwig, L. Greuter, D. Reuter, A. D. Wieck, M. Poggio, and R. J. Warburton. “Charge noise and spin noise in a semiconductor quantum device”. *Nature Physics* **9**, 570–575 (2013).
 - [200] U. Hohenester, G. Pfanner, and M. Seliger. “Phonon-assisted decoherence in the production of polarization-entangled photons in a single semiconductor quantum dot”. *Physical review letters* **99**, 047402 (2007).
 - [201] A. Hudson, R. Stevenson, A. Bennett, R. Young, C. Nicoll, P. Atkinson, K. Cooper, D. Ritchie, and A. Shields. “Coherence of an entangled exciton-photon state”. *Physical review letters* **99**, 266802 (2007).
 - [202] A. Reinhard, T. Volz, M. Winger, A. Badolato, K. J. Hennessy, E. L. Hu, and A. Imamoglu. “Strongly correlated photons on a chip”. *Nature Photonics* **6**, 93 – 96 (2011).
 - [203] A. Javadi, I. Söllner, M. Arcari, S. L. Hansen, L. Midolo, S. Mahmoodian, G. Kiršanské, T. Pregnolato, E. Lee, J. Song, et al. “Single-photon non-linear optics with a quantum dot in a waveguide”. *Nature communications* **6**, 8655 (2015).
 - [204] A. Rundquist, M. Bajcsy, A. Majumdar, T. Sarmiento, K. Fischer, K. G. Lagoudakis, S. Buckley, A. Y. Piggott, and J. Vučković. “Nonclassical higher-order photon correlations with a quantum dot strongly coupled to a photonic-crystal nanocavity”. *Physical Review A* **90**, 023846 (2014).
 - [205] A. Bennett, J. Lee, D. Ellis, I. Farrer, D. Ritchie, and A. Shields. “A semiconductor photon-sorter”. *Nature Nanotechnology* **11**, 857–860 (2016).
 - [206] T. Tiecke, J. Thompson, N. de Leon, L. Liu, V. Vuletić, and M. Lukin. “Nanophotonic quantum phase switch with a single atom”. *Nature* **508**, 241–244 (2014).
 - [207] M. Bayer, S. Walck, T. Reinecke, and A. Forchel. “Exciton binding energies and diamagnetic shifts in semiconductor quantum wires and quantum dots”. *Physical Review B* **57**, 6584 (1998).
 - [208] V. Jovanov, S. Kapfinger, M. Bichler, G. Abstreiter, and J. Finley. “Direct observation of metastable hot trions in an individual quantum dot”. *Physical Review B* **84**, 235321 (2011).
 - [209] K. Lagoudakis, K. Fischer, T. Sarmiento, P. McMahon, M. Radulaski, J. Zhang, Y. Kelaita, C. Dory, K. Müller, and J. Vučković. “Observation of mollow triplets with tunable interactions in double lambda systems of individual hole spins”. *Physical review letters* **118**, 013602 (2017).
 - [210] E. Aubry, C. Testelin, F. Bernardot, M. Chamarro, and A. Lemaître. “Anisotropic spin splitting of the electron ground state in inas quantum dots”. *Applied physics letters* **90**, 242113 (2007).

-
- [211] M. T. Rakher, N. G. Stoltz, L. A. Coldren, P. M. Petroff, and D. Bouwmeester. “Externally mode-matched cavity quantum electrodynamics with charge-tunable quantum dots”. *Phys. Rev. Lett.* **102**, 097403 (2009).
 - [212] M. Reindl, J. H. Weber, D. Huber, C. Schimpf, S. F. Covre da Silva, S. L. Portalupi, R. Trotta, P. Michler, and A. Rastelli. “Highly indistinguishable single photons from incoherently and coherently excited GaAs quantum dots”. *arXiv e-prints*, arXiv:1901.11251 (2019).
 - [213] C. K. Hong, Z. Y. Ou, and L. Mandel. “Measurement of subpicosecond time intervals between two photons by interference”. *Physical Review Letters* **59**, 2044–2046 (1987).
 - [214] J. C. Loredo, N. A. Zakaria, N. Somaschi, C. Anton, L. De Santis, V. Giesz, T. Grange, M. A. Broome, O. Gazzano, G. Coppola, et al. “Scalable performance in solid-state single-photon sources”. *Optica* **3**, 433–440 (2016).
 - [215] P. Androvitsaneas, A. Young, J. Lennon, C. Schneider, S. Maier, J. Hinchliff, G. Atkinson, E. Harbord, M. Kamp, S. Höfling, et al. “An efficient quantum photonic phase shift in a low q-factor regime”. *ACS Photonics* (2019).
 - [216] V. Loo, L. Lanco, O. Krebs, P. Senellart, and P. Voisin. “Single-shot initialization of electron spin in a quantum dot using a short optical pulse”. *Physical Review B* **83**, 033301 (2011).
 - [217] S. Poltavtsev, I. Ryzhov, M. Glazov, G. Kozlov, V. Zapasskii, A. Kavokin, P. Lagoudakis, D. Smirnov, and E. Ivchenko. “Spin noise spectroscopy of a single quantum well microcavity”. *Physical Review B* **89**, 081304 (2014).
 - [218] D. Smirnov, B. Reznychenko, A. Auffèves, and L. Lanco. “Measurement back action and spin noise spectroscopy in a charged cavity qed device in the strong coupling regime”. *Physical Review B* **96**, 165308 (2017).
 - [219] S. Haroche and J.-M. Raimond. *Exploring the quantum: atoms, cavities, and photons*. Oxford university press, (2006).
 - [220] M. Hatridge, S. Shankar, M. Mirrahimi, F. Schackert, K. Geerlings, T. Brecht, K. Sliwa, B. Abdo, L. Frunzio, S. M. Girvin, et al. “Quantum back-action of an individual variable-strength measurement”. *Science* **339**, 178–181 (2013).
 - [221] C. Y. Hu, W. J. Munro, and J. G. Rarity. “Deterministic photon entangler using a charged quantum dot inside a microcavity”. *Phys. Rev. B* **78**, 125318 (2008).
 - [222] D. Heiss, S. Schaeck, H. Huebl, M. Bichler, G. Abstreiter, J. Finley, D. Bulaev, and D. Loss. “Observation of extremely slow hole spin relaxation in self-assembled quantum dots”. *Physical Review B* **76**, 241306 (2007).
 - [223] J. H. Prechtel, A. V. Kuhlmann, J. Houel, L. Greuter, A. Ludwig, D. Reuter, A. D. Wieck, and R. J. Warburton. “Frequency-stabilized source of single photons from a solid-state qubit”. *Physical review X* **3**, 041006 (2013).
 - [224] J. Hansom, C. H. Schulte, C. Matthiesen, M. J. Stanley, and M. Atatüre. “Frequency stabilization of the zero-phonon line of a quantum dot via phonon-assisted active feedback”. *Applied Physics Letters* **105**, 172107 (2014).

- [225] W. Nagourney, J. Sandberg, and H. Dehmelt. “Shelved optical electron amplifier: Observation of quantum jumps”. *Physical Review Letters* **56**, 2797 (1986).
- [226] J. Bergquist, R. G. Hulet, W. M. Itano, and D. Wineland. “Observation of quantum jumps in a single atom”. *Physical Review Letters* **57**, 1699 (1986).
- [227] S. Gleyzes, S. Kuhr, C. Guerlin, J. Bernu, S. Deleglise, U. Hoff, M. Brune, J.-M. Raimond, and S. Haroche. “Quantum jumps of light recording the birth and death of a photon in a cavity”. *Nature* **446**, 297–300 (2007).
- [228] K. Murch, S. Weber, C. Macklin, and I. Siddiqi. “Observing single quantum trajectories of a superconducting quantum bit”. *Nature* **502**, 211–214 (2013).
- [229] C. Arnold, V. Loo, A. Lemaître, I. Sagnes, O. Krebs, P. Voisin, P. Senellart, and L. Lanço. “Cavity-enhanced real-time monitoring of single-charge jumps at the microsecond time scale”. *Physical Review X* **4**, 021004 (2014).

Sujet : Interface spin-photon en cavité.

Résumé : La réalisation d'un réseau de communication quantique nécessite la réalisation d'interfaces efficaces entre des qubits stationnaires et messagers. Une approche prometteuse pour cela est le couplage déterministe du spin d'une charge confinée dans une boîte quantique avec une cavité micro-pilier. Nous nous intéressons plus particulièrement ici au développement de portes logiques photoniques, où l'état de polarisation d'un seul photon incident est manipulé par un seul spin.

Dans ce contexte, on s'intéresse d'abord à la rotation de polarisation induite par un dispositif de boîte quantique couplée à un micro-pilier. Nous avons développé une technique de tomographie de polarisation, permettant d'analyser la matrice densité de polarisation (représentée dans la sphère de Poincaré) des photons réfléchis. On démontre une excellente efficacité d'injection des photons dans la cavité ainsi qu'une rotation de polarisation macroscopique induite par une seule boîte quantique neutre.

Pour réaliser des portes logiques photoniques efficaces, l'état fondamental de la boîte quantique doit correspondre à une boîte quantique chargée, où la charge confinée doit avoir un degré de liberté de spin, manipulable optiquement. On démontre donc la réalisation déterministe d'interfaces spin-photon, qui peuvent notamment être utilisées comme des sources de photons uniques comparables à l'état de l'art. D'autre part, nous utilisons la rotation de polarisation macroscopique induite par un spin unique pour démontrer l'action en retour induite sur l'état de spin par un unique photon détecté. Ce phénomène démontre les fortes corrélations entre l'état de spin et la polarisation d'un photon que l'on est capable d'obtenir avec de telles interfaces.

Ces résultats vont dans le sens de la réalisation d'une intrication entre un spin et un photon émis par une source extérieure, ouvrant la voie vers la réalisation de portes logiques entre photons.

Mots clés : Communication quantique, Optique quantique, Interface spin-photon

Subject : A cavity-based spin-photon interface

Abstract: The development of future quantum networks requires an efficient interface between stationary and flying qubits. A promising approach is a single spin of a charge confined in a quantum dot (QD) deterministically coupled to a micropillar cavity. Here we focus on the development of polarization-based photonic gates, whereby the polarization state of a single incoming photon is manipulated through its interaction with the spin state.

In this framework, we first investigate the polarization rotation of coherent light interacting with QD-cavity systems. We developed a polarization tomography technique allowing to analyze the polarization density matrix of the reflected photons in the Poincaré sphere. We show an excellent injection efficiency of photons into the cavity and a macroscopic rotation of polarization induced by a single neutral quantum dot.

To realize efficient photonic gates, the quantum dot fundamental state should correspond to a charged quantum dot, where the confined charge has a spin degree of freedom that can be optically addressed. We thus demonstrate the deterministic assembly of such spin-photon interfaces, that can perform as state-of-the-art single-photon sources. We then benefit from the macroscopic spin-dependent polarization rotation offered by such cavity-based spin-photon interfaces to demonstrate the macroscopic measurement back action induced on the spin by a single photon detection event. Such a phenomenon highlights the strong correlations between the spin state and the photon polarization.

These results open the way toward the realization of entanglement between a spin and a photon emitted by an external source, which is a building block for the implementation of photon-photon gates.

Keywords : Quantum communications, Quantum optics, Spin-photon interface